MAGNITUDE ESTIMATES FOR THE EARTHQUAKES ON THE NAF USING THE EMPIRICAL CODA NORMALIZATION AND INSAR METHODS

by

Gülşen Tekiroğlu

B.S., Geophysical Engineering, Istanbul Technical University, 2023

Submitted to the Kandilli Observatory and Earthquake
Research Institute in partial fulfillment of
the requirements for the degree of
Master of Science

Graduate Program in Geodesy
Boğaziçi University
2025

MAGNITUDE ESTIMATES FOR THE EARTHQUAKES ON THE NAF USING THE EMPIRICAL CODA NORMALIZATION AND INSAR METHODS

APPROVED BY:

Asst. Prof. Tülay Kaya Eken ……..…

(Thesis Supervisor)

Prof. Haluk Özener ……..…..…..…

Prof. Eşref Yalçınkaya ……..…..…

DATE OF APPROVAL:

ACKNOWLEDGEMENTS

I am deeply grateful to my thesis advisor, Assist. Prof. Tülay Kaya Eken, for her invaluable support not only in overcoming the scientific and technical challenges of this project, but also in navigating the challenges of life.

Furthermore, I extend my sincere thanks to Dr. Kevin Mayeda, a seismologist at AFTAC, for his valuable collaboration and technical support regarding the use of coda calibration utilities. I would like to express my special thanks to Prof. Haluk Özener for sharing his valuable knowledge with me and for his support throughout my graduate education. I am also very grateful to Jorge Roman-Nieves, a Geophysicist at the AFTAC, whose dedicated work was essential for this research, particularly for providing critical information regarding MT.

My sincere thanks to Assoc. Prof. Tuna Eken, Çağkan Serhun Zoroğlu, and Mısra Gedik for their help and support. They were always willing to share the workload and were ready to help whenever I needed them. I especially want to thank my dear friend, Nisan Namlı, who never once withheld her support during this process. I am grateful for the way she broadened my artistic horizons and for her unconditional friendship. I would also like to thank my exceptional mentor, Gizem İzgi, whom I met through the mentoring program at ITU. I am grateful to her for always sharing her life experiences with me, guiding me, and giving me strength with her presence. A special thank you to my dearest uncles, Bekir Faruk Demirtaş and Tahir Demirtaş, and my one and only aunt, Feyza Aladağ, for their constant encouragement and for always supporting me.

Endless thanks to my beloved mother Güzide, my sister Merve, and my little brother Ozan Alp, who never once withheld their support during this challenging process. Their love, patience, and belief in me have been my greatest source of strength on this journey.

ABSTRACT

MAGNITUDE ESTIMATES FOR THE EARTHQUAKES ON THE NAF USING THE EMPIRICAL CODA NORMALIZATION AND INSAR METHODS

This thesis presents an integrated seismological and geodetic study to improve earthquake source characterization along the North Anatolian Fault Zone (NAFZ), a region of high seismic risk and significant tectonic complexity. The primary objective is to resolve inconsistencies in regional earthquake catalogs by developing a homogeneous moment magnitude (M_w) catalog for events with magnitudes ranging from 3.5 to 6.0. To achieve this, the Coda Calibration Technique (CCT) that utilizes the stable, scattered energy of coda waves to derive robust source spectra, mitigating path and site effects common in tectonically complex areas, is applied. The calibration is fixed using independently derived M_w from moment tensor inversion for low frequencies and apparent stress (σ_A) from coda spectral ratios for high frequencies, resulting in a reliable, homogeneous M_w catalog. Second, for two specific events, the 23 November 2022 M_w 6.0 Düzce and the 18 April 2024 M_w 5.6 Tokat earthquakes, we conduct Interferometric Synthetic Aperture Radar analysis using Sentinel-1 data. The resulting coseismic deformation fields are modeled using an elastic dislocation formulation to invert for fault slip distribution, providing independent, geodetically-derived M_w estimates that validate the seismological results. A key finding of this study is the evidence for non-self-similar source scaling in the NAFZ; apparent stress is observed to increase with seismic moment, suggesting that larger earthquakes radiate energy more efficiently than smaller ones. Furthermore, the derived apparent stress values are systematically lower than in other active tectonic regions, indicating a potentially low-stress, low-seismic-efficiency environment for the fault zone. This integrated, multi-physics framework not only produces a critical, homogeneous Mw catalog for improved seismic hazard assessment but also provides fundamental new insights into the earthquake rupture physics of the NAFZ.

ÖZET

EMPİRİK KODA NORMALİZASYONU VE INSAR YÖNTEMLERİNİ KULLANARAK KAF'TAKİ DEPREMLER İÇİN BÜYÜKLÜK TAHMİNLERİ

Bu tez, yüksek sismik riske ve önemli tektonik dinamiğe sahip bir bölge olan Kuzey Anadolu Fay Zonu (KAFZ) boyunca deprem kaynak özelliklerinin daha iyi tanımlanması amacıyla bütünleşik bir sismolojik ve jeodezik çalışma sunmaktadır. Temel amaç, büyüklükleri 3.5 ile 6.0 arasında değişen depremler için homojen bir moment büyüklüğü (M_w) kataloğu geliştirerek bölgesel deprem kataloglarındaki tutarsızlıkları gidermektir. Bu amaçla, karmaşık bölgelerde yaygın olan yol ve istasyon etkilerini azaltarak, güvenilir kaynak spektrumları elde etmek amacıyla koda dalgalarının kararlı ve saçılmış enerjisini kullanan Koda Kalibrasyon Tekniği (CCT) uygulanmıştır. Kalibrasyon, düşük frekanslar için moment tensör çözümünden bağımsız olarak türetilen M_w ve yüksek frekanslar için koda spektral oranlarından elde edilen görünür gerilme (σ_A) kullanılarak sabitlenmiş ve sonuçta güvenilir, homojen bir M_w kataloğu oluşturulmuştur. İkinci olarak, 23 Kasım 2022 M_w 6.0 Düzce ve 18 Nisan 2024 M_w 5.6 Tokat depremleri olmak üzere iki özel olay için Sentinel-1 verileri kullanılarak İnterferometrik Sentetik Açıklıklı Radar (InSAR) analizi yapılmıştır. Elde edilen deprem sırasındaki kosismik deformasyon alanları, fay üzerindeki kayma dağılımını belirlemek amacıyla elastik bir dislokasyon formülasyonu kullanılarak modellenmiştir. Bu modelleme, sismolojik sonuçları doğrulayan, jeodezik olarak türetilmiş bağımsız M_w tahminleri sağlamıştır. Bu çalışmanın önemli bir bulgusu, KAFZ'da kendine benzer olmayan kaynak ölçeklenmesine dair kanıtlardır. Görünür gerilmenin sismik moment ile birlikte arttığı gözlemlenmiştir; bu durum, büyük depremlerin enerjiyi küçük olanlara göre daha verimli bir şekilde yaydığını düşündürmektedir. Ayrıca, elde edilen görünür gerilme değerleri diğer aktif tektonik bölgelere göre sistematik olarak daha düşüktür, bu da fay zonu için potansiyel olarak düşük gerilmeli ve düşük sismik verimliliğe sahip bir ortama işaret etmektedir. Bu entegre çalışma, daha iyi sismik tehlike değerlendirmesi için homojen bir Mw kataloğu oluşturur ve NAFZ deprem kırılma fiziğine dair yeni bakış açıları sunar.

TABLE OF CONTENTS

ACKNOWLEDGEMENTS iii
ABSTRACT iv
ÖZET v
LIST OF FIGURES viii
LIST OF TABLES xxi
LIST OF SYMBOLS xxii
LIST OF ACRONYMS/ABBREVIATIONS xxv
1. INTRODUCTION 1
1.1. Subject Of Thesis 1
1.2. Study Area 3
1.2.1. Tectonic Setting of Türkiye and NAFZ 5
1.3. The Earthquake Deformation Cycle 6
1.3.1. Coseismic Deformation 8
1.4. Literature Review 9
1.4.1. History of Coda Wave Studies 9
1.4.2. Coda-Derived Moment Magnitudes and Source Scaling: A Review of Global and Regional Studies 18
1.4.3. Introduction to models 19
1.4.4. Scattering Properties 20
1.4.5. Diffusion Model 22
1.4.6. Energy-Flux Model 22
1.4.7. Radiative Transfer Theory 23
1.4.8. Back-scattering Model 23
1.4.9. Early Geodetic and Geophysical Studies in the Region 26
1.4.9.1. Long-period Deformation of Anatolia 26
1.4.9.2. The M_w 6.0 Gölyaka-Düzce Seismic activity 28
1.4.9.3. DInSAR-Based Investigation and Geophysical Interpretation of the 23 November 2022 Düzce–Gölyaka Earthquake 30
2. SEISMIC DATA & METHODOLOGY 36
2.1. Dataset & Preprocessing 36

2.2. An Overview of the Methodology ……..…… 39
2.2.1. Introduction ……... 39
2.2.2. Estimation of Peak Velocity and Envelope Shape Parameters ……. 42
2.2.3. Raw Amplitude Measurements and Empirical Distance Correction … 45
2.2.4. Coda Spectral Ratio …….. 50
2.2.5. Source Spectra, Moment Magnitude, Apparent Stress and Radiated Energy
…….. 58
3. GEODETIC DATA & METHODOLOGY …….. 61
3.1. SAR Interferometry …… 61
3.2. InSAR Processing Steps ……. 68
3.2.1. SAR Interferometric Pairs …….. 68
3.2.2. Interferogram Processing …… 73
3.3. Modeling the Slip Distribution Using Elastic Dislocations …… 93
3.3.1. Forward Model …… 101
3.3.2. Inverse Model …….. 106
3.3.3. Regularization ……. 106
4. RESULTS AND INTERPRETATION …… 111
4.1. Coda-derived Seismic Moment and Moment Magnitudes ……. 111
4.2. M_L-M_w Magnitude Conversion Relation …… 116
4.3. Source Scaling: Non-self-similar Character of Seismicity in the Region ….. 117
4.4. InSAR & Elastic Dislocation Model Results ……. 119
5. CONCLUSION …… 1244
REFERENCES ……... 126
APPENDIX A …….. 1261
APPENDIX B …….. 126
APPENDIX C …….. 126

LIST OF FIGURES

Figure 1.1. The major suture zones (Okay & Tüysüz, 1999), tectonic structures (Emre et al., 2013). Relative motions of tectonic plates with respect to Eurasia are indicated by black arrows, based on data from McClusky et al. (2000), Reilinger et al. (2006), and Nocquet (2012). The rectangle shows the study area. Red arrows indicate fault movements. ……... 6

Figure 1.2. Illustration of the earthquake deformation cycle using survey markers (modified from Wright (2002)). It shows the interseismic phase as a centuries-long period of slow strain accumulation that distorts a straight marker (A-A'). The coseismic phase involves a sudden 5 m offset, while the postseismic phase shows continued strain readjustment. …….. 8

Figure 1.3. Vertical component recordings from two USGS stations captured aftershocks of the Parkfield earthquake, with coda waves indicated by black arrows on the high-gain traces (Aki, 1969). …… 10

Figure 1.4. A simplified diagram showing how a single scatterer redirects incoming wave energy in different directions (Sato et al., 2012). …… 21

Figure 1.5. (a) numerical simulation of wavefields in random media, and (b) illustration of energy transport processes in scattering environments (Sato et al., 2012). …… 22

Figure 1.6. Geometric representation of the single backscatter model with a co-located source and receiver (Sato et al., 2012). …… 24

Figure 1.7. (a) Tectonic framework of Türkiye and interseismic surface velocities in the Eurasia-fixed frame (Weiss et al., 2020). (b) and (c) Satellite data from both descending and ascending tracks show LOS velocities,

respectively. Blue indicates motion toward and red indicates motion away from the satellite (Weiss et al., 2020). …… 28

Figure 1.8. Spatial and temporal patterns of seismic activity during the six days after the Düzce earthquake. (a) Map view of seismicity. (b) Depth cross-section along profile A–A', oriented nearly orthogonal to the Karadere fault. (c) Depth cross-section along profile B–B', roughly normal to the Düzce fault. Marker size is proportional to earthquake magnitude, and color indicates the date of occurrence (Martínez-Garzón et al., 2022). ... 30

Figure 1.9. DInSAR analysis of the 23 November 2022 Gölyaka–Düzce earthquake using ascending and descending Sentinel-1A satellite data. Four Sentinel-1A SAR datasets, two pre-earthquake and two post-earthquake, were used: ascending images from 15 November to 27 November 2022, and descending images from 14 November to 26 November 2022. (Karaca et al., 2024). …… 32

Figure 1.10. DInSAR analysis of the 23 November 2022 Gölyaka–Düzce earthquake using ascending and descending satellite data. Four Sentinel-1A SAR datasets, two pre-earthquake and two post-earthquake, were used: ascending images from 15 November to 27 November 2022, and descending ones from 14 November to 26 November 2022. Active faults are shown as black lines (Emre et al., 2013; MTA) (Karaca et al., 2024). ……..…….. 33

Figure 1.11. (A) Ascending data illustrating the 23 November 2022 earthquake in Düzce. The slip distribution from MT modeling is shown, along with aftershocks and foreshocks recorded in two days period. (B) Map view of the study area. Blue and yellow stars denote the epicenters reported by KOERI and AFAD. (C) and (D) Cross-sectional profiles A–A' and B–B' display LOS displacement. (Karaca et al., 2024). …… 34

Figure 1.12. Forward modeling results showing displacements derived from the shear distribution obtained by linear inversion: (A) Modeled displacement data, (B) Corresponding unwrapped interferogram, (C) East–west displacement component, (D) Vertical displacement component, and (E) Displacement in the N–S direction. (Karaca et al., 2024). ……... 35

Figure 2.1. This map displays 151 analyzed earthquakes (Mw 3.5-6.0) from 2013-2022, including the 2024 Tokat mainshock and foreshock, recorded by KOERI and AFAD stations. ……. 38

Figure 2.2. Example stacked narrowband envelopes between 0.05-8 Hz for the 2024 Tokat-Sulusaray mainshock recorded at COAL station. …….. 38

Figure 2.3. Coda calibration methodology presented as a top-down flowchart. …… 42

Figure 2.4. Measurements of peak velocity v and envelope shape parameters b and γ as functions of epicentral distance for two frequency bands: (a) 0.7 to 1 Hz and (b) 3 to 4 Hz. In both panels, the velocity hyperbola and the corresponding shape parameters are shown along with the best-fitting averaged model curves in blue, based on Equation (2.1). Red circles indicate individual envelope measurements for each frequency band. … 44

Figure 2.5. Example coda envelope measurements within the 0.7 to 1 Hz frequency range, where the synthetic envelope (green) is superimposed on the observed $\log_{10}$ velocity envelope in nanometer-seconds (blue) for stations positioned at varying distances from the seismic source. Manual refinement is possible by adjusting the measurement end time, marked by the vertical red f-indicator. …….. 46

Figure 2.6. Example of raw, non-dimensional $\log_{10}$ coda amplitude measurements for a single event recorded at various stations across local and regional distances. Each individual frequency is subsequently used in a one-

dimensional path inversion that incorporates amplitude data from all calibration events, including the one shown here. …… 47

Figure 2.7. Path correction examples for the (a) 0.7–1 Hz (left) and (b) 3–4 Hz (right) frequency bands. The upper panels in both (a) and (b) display amplitude measurements from common events recorded at stations BOLU and COAL, which are approximately 286 kilometers apart. Red symbols represent uncorrected values, while blue symbols show the corrected amplitudes. …… 49

Figure 2.8. An example event showing the estimation of moment magnitude using regional moment tensor inversion. The observed waveforms are displayed in black, synthetic seismograms used in the inversion are shown in red, and synthetic predictions not included in the inversion are represented in blue. ……... 52

Figure 2.9. The coda spectral ratio analysis (Mayeda et al, 2007) applied to the M_w 5.59 Tokat mainshock and its M_w 4.56 foreshock. (a) MAD minimization for accurate σ_A estimates. (b) The event pair's location and stations. (c) Amplitude ratios from 33 regional stations, modeled with the Brune (1970) spectral shape. (d) The empirically determined minimum window lengths. …… 55

Figure 2.10. (a) An example of how the relative site effects vary with frequency range 0.05 to 8 Hz across different stations. The reference is station KDZE, which is situated on rock. (b) Combined influence of *T(f)* and *S(f)* corrections applied at each of the 51 stations. These correction terms are added to the distance-adjusted logarithmic coda amplitudes ($\log_{10}$) to generate the moment-rate source spectra in N-m for each event. ……. 57

Figure 2.11. (a) An example illustrating the moment-rate source spectra for a reference event with magnitude M_w 4.56, where the σ_A is quantified using coda spectral ratios and an independently determined Mw from

waveform modeling (refer to Figures 2.8 and 2.9). The left side displays both the modeled and observed radiated energy. (b) Consistent envelope amplitude measurements between 1-1.5 Hz. …….. 59

Figure 2.12. Panel (b) illustrates the moment-rate source spectra for a validation event with a magnitude of M_w 4.10, which was excluded from the site correction term estimation. The spectral analysis shows strong agreement with independently determined magnitude values, as also summarized in panel (a) on the left. ……..... 60

Figure 3.1. Sentinel-1 operational modes (adapted from ESA's website). The modes are depicted from left to right: Stripmap (SM), Interferometric Wide Swath (IW), Extra Wide Swath (EW), and Wave (WV). ……...…… 63

Figure 3.2. The geometry of the TOPSAR acquisition mode (Grassi & Francesco, 2019). …… 64

Figure 3.3. Example of the interferometric phase for an ascending orbit (T211, F0640) of ALOS PALSAR data corresponds to the April 4, 2010, El Major-Cucapah earthquake in Baja, Mexico. Each fringe represents a displacement of 11.8 cm away from the radar. The phase is overlaid on the topographic gradient (Sandwell et al., 2016). ……. 66

Figure 3.4. Map showing the location of Sentinel-1A frames from ascending orbit path 160, used for coseismic deformation analysis of the 23 November 2022 Düzce-Gölyaka event (M_w 6.0). M_w solution was retrieved from KOERI. ……..……. 70

Figure 3.5. Map showing the location of Sentinel-1A frames from descending orbit path 138, used for coseismic deformation analysis of the 23 November 2022 Düzce-Gölyaka event (M_w 6.0). M_w solution was retrieved from KOERI. …….……..….. 71

Figure 3.6. Map showing the location of Sentinel-1A frames from ascending orbit path 14, used for coseismic deformation analysis of the 18 April 2024 Tokat-Sulusaray event (M_w 5.6). M_w solution was retrieved from KOERI. ……. 72

Figure 3.7. Map showing the location of Sentinel-1A frames from descending orbit path 94, used for coseismic deformation analysis of the 18 April 2024 Tokat-Sulusaray event (M_w 5.6). M_w solution was retrieved from KOERI. …… 73

Figure 3.8. Phase unwrapping involves reconstructing the absolute phase values, the original continuous phase (shown on the left) using the wrapped phase values (shown on the right) (ESA, 2007). ..…….. 77

Figure 3.9. The zenith delays for ascending data for two distinct dates. …… 78

Figure 3.10. Slant phase delays. The left and right images represent the secondary and reference acquisitions. ……..…. 79

Figure 3.11. Differential phase delay for the November 27, 2022, and November 15, 2022 (ascending orbit) radar images. ……...…… 79

Figure 3.12. The unwrapped interferogram (left) before and (right) after application of the APS correction. Pink and black lines represent cross sections before and after the APS correction, respectively. ……... 80

Figure 3.13. The APS correction cross-sections for 1 to 4 profiles are shown in Figure 3.12. Black lines represent cross sections after APS correction, and pink ones show before the correction. ……...…...….... 80

Figure 3.14. Phase interferogram of November 23, 2022, Düzce-Gölyaka Earthquake without Tropospheric correction. ……..…. 81

Figure 3.15. Ascending unwrapped interferogram of the Düzce earthquake. It is corrected for tropospheric noise and masked for pixels with a coherence below 0.3. The earthquake's epicenter is marked with a blue star. ……... 82

Figure 3.16. The provided image consists of two maps showing the secondary zenith delay in meters on November 14, 2022, and the reference zenith delay in meters on November 26, 2022. ..……... 82

Figure 3.17. Slant phase delays. The left and right images represent the secondary and reference acquisitions. ……. 83

Figure 3.18. Differential phase delay for the November 26, 2022, and November 14, 2022 (descending orbit) data. …… ……. 83

Figure 3.19. The unwrapped interferogram (left) before and (right) after application of the APS correction. Pink and black lines represent cross sections. …. 85

Figure 3.20. The APS correction cross-sections for 1 to 4 profiles are shown in Figure 3.19. Black lines represent cross sections after APS correction, and pink ones show before the correction. ……. 84

Figure 3.21. Phase interferogram of November 23, 2022, Düzce-Gölyaka Earthquake without tropospheric correction in descending orbit. …….. 85

Figure 3.22. Descending unwrapped interferogram of the Düzce earthquake. It is corrected for tropospheric noise and masked for pixels with a coherence below 0.3. The earthquake's epicenter is marked with a blue star. ……... 86

Figure 3.23. The zenith delays for ascending data for April 16, 2024 (Secondary) and April 28, 2024 (Reference) dates. ……. 87

Figure 3.24. Slant phase delays. The secondary image (left) was acquired on April 16, 2024, and the reference image (right) on April 28, 2024. …… 87

Figure 3.25. The differential phase delay in radians. This map represents the phase difference between radar images acquired on April 28 and April 16, 2024. …….. 87

Figure 3.26. The unwrapped interferogram (left) before and (right) after tropospheric correction for the ascending data of the Tokat-Sulusaray event. Pink and black lines represent cross sections before and after the APS correction, respectively. ……..... 89

Figure 3.27. The tropospheric correction cross-sections for 1 to 4 profiles shown in Figure 3.26. Black lines represent cross sections after APS correction and pink ones shows before the correction. ……. 89

Figure 3.28. Phase interferogram of April 18, 2024 Tokat-Sulusaray Earthquake without Trophosperic correction for ascending orbit. …….. 90

Figure 3.29. Coseismic Deformation of the 2024 Tokat-Sulusaray Earthquake for ascending orbit. This unwrapped interferogram shows LOS deformation in meters, corrected for tropospheric noise and masked for pixels with a coherence below 0.3. The earthquake's epicenter is marked with a green star. ……... 90

Figure 3.30. The zenith delay [m] for the secondary and reference dates. ……... 90

Figure 3.31. Slant phase delays for descending data for the secondary (left) and reference (right) dates. …….. 90

Figure 3.32. Differential phase delay in radians. This map represents the phase difference between radar images acquired on April 22, 2024 and April 10, 2024 (descending orbit). ……. 92

Figure 3.33. The unwrapped interferogram (left) before and (right) after application of the APS correction to the descending data. Pink and black lines represent cross sections before and after the APS correction, respectively. …….…….…….…….…….…… 91

Figure 3.34. The tropospheric correction cross-sections for 1 to 4 profiles shown in Figure 3.33. Black lines represent cross sections after APS correction and pink ones shows before the correction. ……. 93

Figure 3.35. Phase interferogram of April 18, 2024, Tokat-Sulusaray Earthquake without tropospheric correction for descending orbit. ……..…….. 93

Figure 3.36. This unwrapped interferogram shows coseismic deformation of the 2024 Tokat-Sulusaray earthquake for descending orbit. Blue star represents the Tokat mainshock. ……. 97

Figure 3.37. Fault parameters that define a dislocation on a single fault in modeling. x and y are coordinates of the fault center; l is fault length, and w is fault width. z_1 is upper depth of the fault, z_2 is the lower depth. α is fault strike and θ is the fault dip, r is rake and s is slip. …….. 97

Figure 3.38. The unwrapped data, which represents a continuous map of ground displacement in meters along the satellite's LOS caused by the 23 November 2022 Düzce earthquake (M_w 6.0). ..…… 98

Figure 3.39. The unwrapped data, which represents a continuous map of ground displacement in meters along the satellite's LOS caused by the 23 November 2022 Düzce earthquake (M_w 6.0). …….. 99

Figure 3.40. Quadtree-resampled map of InSAR LOS displacement showing ground deformation. Each rectangular cell in the plot is colored based on the median LOS displacement value within that cell. The colorbar indicates

the scale of displacement in meters, with the plot's axes representing the spatial coordinates of the resampled grid. …… 99

Figure 3.41. A wrapped interferogram generated from a pair of SAR acquisitions, depicting the coseismic ground deformation in radian along the satellite's LOS caused by the 18 April 2024 Tokat earthquake (M_w 5.6). ……... 100

Figure 3.42. The unwrapped data, which represents a continuous map of ground displacement in meters along the satellite's LOS caused by the 18 April 2024 Tokat earthquake (M_w 5.6). …… 9100

Figure 3.43. Quadtree-resampled map of InSAR LOS displacement showing ground deformation caused by the 18 April 2024 Tokat earthquake. Each rectangular cell in the plot is colored based on the median LOS displacement value within that cell. The colorbar indicates the scale of displacement in meters. …….. 100

Figure 3.44. Quadtree-resampled map of InSAR LOS displacement due to Düzce-Gölyaka Earthquake 2022. A scatter plot showing the ground deformation from the interferogram, with data points representing the focal points of a quadtree grid. The color map indicates the LOS displacement in meters. ……..…… 100

Figure 3.45. Quadtree-resampled map of InSAR LOS displacement due to Tokat-Sulusaray Earthquake 2024. A scatter plot showing the ground deformation from the interferogram, with data points representing the focal points of a quadtree grid. The color map indicates the LOS displacement in meters. ……..….. 101

Figure 3.46. Comparison of InSAR data, forward model, and residuals for model optimization. The data, shown in the left panel, have been corrected for

a nuisance parameter that can bias the misfit calculation. The center panel displays the forward model's predicted displacement field. The right panel shows the residuals, representing the difference between the corrected data and the model. …….. 103

Figure 3.47. InSAR data, inverse model, and residuals for deformation analysis are shown from left to right in meters. The left panel shows the LOS displacement data. The center panel displays the predicted displacement field from the best-fit inverse model. The right panel visualizes the residuals. ……. 106

Figure 3.48. InSAR data, inverse model, and residuals for deformation analysis are shown from left to right for the Düzce earthquake. The left panel shows the LOS displacement data. The center panel displays the predicted displacement field from the best-fit inverse model. The right panel visualizes the residuals. All displacements are in meters, and the plots are shown in a UTM coordinate system. ……. 105

Figure 3.49. InSAR data, inverse model, and residuals for deformation analysis are shown from left to right for the Tokat earthquake. The left panel shows the LOS displacement data. The center panel displays the predicted displacement field from the best-fit inverse model. InSAR data, inverse model, and residuals for deformation analysis are shown from left to right for Tokat earthquake. The right panel visualizes the residuals. ……... 106

Figure 3.50. Roughness against misfit for Düzce earthquake. Models that lie between the extremes, around the elbow of the graph, achieve a balance by fitting the data well without being overly rough. The selected κ, shown as a red circle, is 0.05. ……... 108

Figure 3.51. Slip distribution model obtained for the Düzce Earthquake. The x-axis shows the strike distance (in km) and the y-axis shows the down-dip distance. The colorbar indicates slip in meters. …..... 109

Figure 3.52. InSAR data, regularized inverse model, and residuals for deformation analysis of the Düzce Earthquake are shown from left to right. The left panel shows the LOS displacement data. The center panel displays the predicted displacement field from the best-fit inverse model. The right panel visualizes the residuals. Total squared penalty is 0.00908 m^2. …. 108

Figure 3.53. Roughness against misfit for the Tokat-Sulusaray earthquake. Models that lie between the extremes, around the elbow of the graph, achieve a balance by fitting the data well without being overly rough. The selected κ, shown as a red circle, is 0.05. …….. 110

Figure 3.54. Slip distribution model obtained for the Tokat Earthquake. The x-axis shows the along-strike distance (in km) and the y-axis shows the down-dip distance. The colorbar indicates slip in meters. …… 109

Figure 3.55. InSAR data, regularized inverse model, and residuals for deformation analysis of the Tokat-Sulusaray earthquake are shown from left to right. The left panel shows the LOS displacement data. The center panel displays the predicted displacement field from the best-fit inverse model. The right panel visualizes the residuals. Total squared penalty is 0.088469 m^2. ……... 110

Figure 4.1. Validation of coda calibration results. (a) Comparison of coda-derived M_w with reference and validation events. (b) σ_A from coda spectra for reference and validation events. (c) Relationship between coda-derived σ_A and M_0 for validation and calibration events. (d) f_c versus M_0 for two different datasets. RMS value of 0.0689 was obtained from the comparison between the coda-derived M_w's and the reference M_w's. …….. 115

Figure 4.2. Calibration parameters used in the CCT for the Central NAFZ. $v_{0,1,2}$: S-wave arrival velocity; $b_{0,1,2}$ and $\gamma_{0,1,2}$ characterize coda envelope shape;

$p_{1,2}$: path effects; station-specific constants account for site amplification and the S-to-coda transfer parameter, *T(f)*. . …… 117

Figure 4.3. The scatter plot shows the relationship between $M_{W\text{-}Coda}$ and $M_{L\text{-}KOERI}$. A 2nd-order polynomial fit (solid black line) represents the non-linear trend, with ±1σ residuals indicated by dotted lines. The 1:1 line is shown in grey. The polynomial is used because ML-KOERI saturates at higher magnitudes, making the relationship with MW-Coda nonlinear. The calculated RMS error is 0.1903. ……. 117

LIST OF TABLES

Table 2.1. Frequency bands used for coda calibration, along with the corresponding minimum window lengths required for valid data selection. ……..…….. 39

Table 3.1. Frequencies and wavelengths in InSAR system. ……..……..... 62

Table 3.2. The Sentinel-1 image pairs used in InSAR analysis.. …….…….…… 69

Table 3.3. Quadtree parameters used for the Düzce and Tokat earthquakes.…… 95

Table 3.4. Initial source parameters for forward modeling. …….. 102

Table 3.5. Fault parameters obtained from inversion. ……... 105

LIST OF SYMBOLS

A	Fault Area
A(f,t,r)	Synthetic envelope amplitude (dependent on frequency, time, and distance)
b	Intrinsic damping term
b(f,r)	Coda envelope shape parameter
b_0, b_1, b_2	Parameters characterizing the coda envelope shape
B_n	Normal (perpendicular) baseline
E	Energy
E(x,t)	Energy density (dependent on position and time)
E_R	Radiated seismic energy
f	Frequency
f_c	Corner frequency
g	Scattering power
g_0	Total scattering coefficient
h_a	Altitude of ambiguity
H	Heaviside step function
I(n,r,t)	Specific intensity (dependent on direction, position, and time)
J_0	Incident energy flux density
J_1	Scattered energy flux density
km	Kilometer
L	Fault length
m	Meter
m_b	Body wave magnitude
M_L	Local magnitude (Richter scale)
M_0	Seismic moment
M_w	Moment magnitude
N	Number density of scatterers
p_1, p_2	Path-related parameters
P(r,f)	1-D geometrical spreading and attenuation term
Qa	Anelastic attenuation quality factor

Q_c	Coda quality factor
Q_i^{-1}	Intrinsic attenuation
Q_s	Scattering attenuation quality factor
r	Epicentral distance or position vector
r_a	Radial distance in spherical coordinates
R	Site response or slant range distance
s	Slip amount
s	Second
S(f)	Site response (frequency-dependent)
T	Time
t_c	Lapse time
t_s	S-wave arrival time
T(f)	S-wave to coda wave transfer function
v(f,r)	Peak velocity (dependent on frequency and distance)
v_0,v_1,v_2	Parameters defining S-wave arrival velocity
w	Fault width
W	Source energy
$W_0(f)$	S-wave source amplitude (frequency-dependent)
x,y	Cartesian coordinates
Z_1,Z_2	Upper and lower depth of the fault
α	Strike angle
γ(f,r)	Coda envelope shape parameter
γ0,γ1,γ2	Parameters characterizing the coda envelope shape
δ	Dip angle
$\Delta\phi$	Phase difference
ϵ	Deviation parameter (in source scaling)
θ	Incidence angle or polar angle in spherical coordinates
κ	Smoothing parameter
λ	Wavelength
μ	Shear modulus (rigidity)
σ_A	Apparent stress
dσ/dΩ	Differential scattering cross-section

ϕ	Phase
ϕ_a	Azimuthal angle in spherical coordinates
ω	Angular frequency (2πf)

LIST OF ACRONYMS/ABBREVIATIONS

AFAD	General Directorate of Disaster and Emergency Management
APS	Atmospheric Phase
CCT	Coda Calibration Tool
CI	Confidence Interval
CNAFZ	Central North Anatolian Fault Zone
CNM	Coda Normalization Method
DEM	Digital Elevation Model
DInSAR	Differential Interferometric Synthetic Aperture Radar
DTAR	Distributed Target Ambiguity Ratio
E	East
EAF	East Anatolian Fault
EAFZ	East Anatolian Fault Zone
EGF	Empirical Green's Function
ESA	European Space Agency
ESD	Enhanced Spectral Diversity
ETAS	Epistemic Type Aftershock Sequence
EW	Extra Wide-swath
GACOS	Generic Atmospheric Correction Online Service
GNSS	Global Navigation Satellite System
GT	Ground Truth
HVO	Hawaiian Volcano Observatory
InSAR	Interferometric Synthetic Aperture Radar
ISCE2	InSAR Scientific Computing Environment-2
IW	Interferometric Wide-Swath
JMO	Chamber of Geological Engineers
JSON	JavaScript Object Notation
KMTJ	Kahramanmaraş Triple Junction

KOERI	Kandilli Observatory and Earthquake Research Institute
LiCSAR	Looking into Continents from Space with Synthetic Aperture Radar
LiCSBAS	LiCSAR automated Sentinel-1 InSAR processor
LOS	Line-of-Sight
MAD	Mean Absolute Deviation
MAP	Maximum A Posteriori
MDAC	Magnitude and Distance Amplitude Correction
MLTWA	Multiple Lapse Time Window Analysis
MTA	General Directorate of Mineral Research and Exploration
MTINV	Moment Tensor Inversion Toolkit
N	North
NAFZ	North Anatolian Fault Zone
NTS	Nevada Test Site
PSHA	Probabilistic Seismic Hazard Assessment
REST	Representational State Transfer?
RMS	Root Mean Square
RTT	Radiative Transfer Theory
S	South
SAC	Seismic Analysis Code
SAR	Synthetic Aperture Radar
SLC	Single-Look Complex
SM	Stripmap
SNAPHU	Statistical-cost, Network-flow Algorithm for Phase Unwrapping
SNR	Signal-to-Noise Ratio
SQL	Structured Query Language
SRTM	Shuttle Radar Topography Mission
STA/LTA	Short-Term Average/Long-Term Average
TOPSAR	Terrain Observation by Progressive Scans
UTM	Universal Transverse Mercator
VELMAP	Velocity and Strain Rate Model

W	West
WGS84	World Geodetic System 1984
WV	Wave mode

1. INTRODUCTION

1.1. Subject of Thesis

This thesis primarily seeks to address the inconsistency found in regional earthquake catalogs by employing the Coda Calibration Method (CCT) to estimate Moment Magnitude (M_w) for seismic events in the magnitude scale between 3.5 and 6.0 within the Central North Anatolian Fault Zone (CNAFZ). In addition to this approach, two selected earthquakes are analyzed for their coseismic deformation, which enables the use of Okada modeling to derive independent Mw estimates based on geodetic data. This complementary framework strengthens the reliability of magnitude assessments and facilitates a more accurate characterization of seismic source properties within the study region.

Unbiased and precise estimation of earthquake magnitudes is critical to seismic hazard analysis, particularly in areas with complex tectonism such as Türkiye. National agencies like KOERI and AFAD typically report moment magnitude (M_w) values only for earthquakes with $M_w \geq 4.0$, while local magnitude (M_L) values are provided for smaller events. However, Probabilistic Seismic Hazard Assessment (PSHA) and related applications require a complete and homogeneous earthquake catalog. The use of mixed magnitude types introduces inconsistencies, as empirical M_L–M_w conversions can lead to systematic biases, especially for small-to-moderate events.

To address this issue, this thesis proposes the use of the CCT to estimate M_w for earthquakes in the $3.5 \leq M_L \leq 6.0$ range within the CNAFZ. Coda waves, due to their reduced sensitivity to path effects and source radiation patterns, offer a robust alternative for magnitude estimation, particularly in data-scarce environments, with potential for future extension to smaller events and automated systems.

To achieve this, the study involved calculating 19 reference M_w values using waveform modeling via the MTINV (Moment Tensor Inversion Toolkit), which provided physically constrained source parameters essential for calibrating the unitless coda spectral amplitudes and tying them to absolute moment magnitudes. Additionally, the coda spectral ratio method

was applied to estimate apparent stress for two selected events (the Tokat mainshock and a nearby foreshock), recognizing this parameter's criticality for understanding high-frequency energy content and extracting information from the long-wavelength component of an earthquake's energy. Employing large-magnitude reference events with large magnitude also enabled refinement of the low-frequency spectral behavior, which is often poorly resolved in smaller earthquakes.

To further validate these results, co-seismic deformation analysis was performed for two earthquakes: the April 18, 2024, Tokat-Sulusaray (M 5.6) and November 23, 2022, Düzce-Gölyaka (M 6) using InSAR satellite data, and the observed surface displacements were modeled with the Okada (1985) elastic dislocation model. This allowed for a direct comparison between M_w values derived from waveform inversion, coda-based calibration, and geodetic modeling. The consistency among these independent methods, each based on fundamentally different physical principles, demonstrates the reliability and robustness of the geodetic and geophysical approach, particularly within this geologically complex and seismically active region.

Firstly, the results of this thesis contribute to the broader discussion on earthquake source scaling and self-similarity, with the analysis of coda-derived source parameters suggesting that large and small earthquakes may not scale uniformly, indicating potential deviations from classical self-similar models. This finding is especially important for improving the ground motion prediction and seismic hazard modeling. Secondly, by estimating surface deformation through Interferometric Synthetic Aperture Radar (InSAR) and incorporating this data into elastic dislocation modeling using Okada's mathematical expressions, this research enables a comparative analysis of geodetic and seismological approaches to earthquake source characterization. Such an integrated methodology enables a more comprehensive understanding of the consistency between geophysical and geodetic interpretations of earthquake processes across different magnitude scales.

1.2. Study Area

Türkiye is situated in one of the world's most earthquake-prone regions, shaped by complicated geodynamic interactions between major tectonic plates. It is predominantly characterized by high plateaus and mountain belts, which rise abruptly from surrounding seas, including the Mediterranean, Aegean, Black Sea, and Marmara (Figure 1.1). Over the past 400 million years, Türkiye has formed through the integration of various oceanic and continental fragments. These long-term processes, along with the continuous convergence and relative motions of neighboring plates, have resulted in the formation of several prominent shear zones and a highly active tectonic regime.

The neotectonic regime of Türkiye comprises four primary deformation provinces (Figure 1.1), each with a unique formation and developmental history. These are arisen from the westward migration of the Anatolian plate during the period of the neotectonic phase, characterized by varying motions throughout the Anatolian Peninsula: the East Anatolian Shortening Province; the North Turkish Province, characterized by gentle east-west shortening; the West Anatolian Extensional Province; the Central Anatolian Ova Province, which shows minor shortening and extension. These geological regions remain tectonically dynamic, causing the development of uplifted areas, sinking basins, and valleys constrained by faults. This process also gives rise to deeply incised river channels and terraced karstic formations (Kuzucuoğlu et al., 2019; Chang et al., 2024).

Subsequent to the Cenozoic-era closing of the Tethys Ocean, the westward movement of the Arabian and African plates against Eurasia has been the dominant force shaping the region (McKenzie, 1972). At an approximate rate of 18–25 mm/yr, the Arabian Plate is currently moving in a north-northwest direction (Figure 1.1), and the African Block advances northward at about 10 mm/yr (McClusky et al., 2000). This velocity difference is caused by two main forces: a pulling force from the African plate sinking beneath the Hellenic arc in the west, and a pushing force from compressional forces in the east. Together, these forces cause the plate to move southwestward along the North Anatolian Fault Zone (NAFZ) and the East Anatolian Fault Zone (EAFZ) (Taymaz et al., 2004).

The neotectonic period in Türkiye began in the middle Miocene, about 13 million years ago. It was initiated by the westward movement of the Anatolian Plate, which caused uneven uplift in the southern and western parts of the peninsula (Şengör et al., 1985). Since the late Miocene, the ongoing collision between the Arabian and Anatolian plates has significantly reorganized the topography, creating the complex and diverse geomorphology seen today (Şengör and Yılmaz, 1981; Erdem Bayrak et al., 2015).

The tectonic deformation across Anatolia is a result of crustal blocks interacting along major fault systems (Sançar et al., 2019). However, the specific reasons for Anatolia's westward movement are still under debate, with several competing theories (McKenzie, 1972; Chang et al., 2024). Türkiye's main tectonic boundaries are defined by the North Anatolian Fault (NAF) and the East Anatolian Fault (EAF). Two devastating earthquakes (Mw 7.8 and Mw 7.6) struck these fault lines on February 6, 2023, near the Kahramanmaraş Triple Junction (KMTJ) (Chadha, 2023; Chang et al., 2024).

The broader Anatolian–Aegean region, including the Eastern Mediterranean, has been central to the early development of plate tectonic theory, serving as a natural laboratory for numerous foundational studies (Dixon and Robertson, 1984; McKenzie, 1972; Le Pichon and Angelier, 1979; Royden, 1993). The subduction of the Tethys Ocean has dominated tectonic processes along the southern margin of Eurasia for over 200 million years (Agard et al., 2011). Since the early Miocene, roughly 20 million years ago, active tectonic deformation in the region has resulted from the interaction between the subducting Nubian oceanic lithosphere beneath the Hellenic and Cyprus arcs and the early stages of continental collision between the Arabian and Eurasian plates. This tectonic convergence has produced a broad, approximately 600-kilometer-wide deformation zone (Jolivet and Faccenna, 2000; McQuarrie and van Hinsbergen, 2013).

One of the most prominent structures accommodating this deformation is the NAFZ, a seismically active right-lateral strike-slip fault first described by Ketin (1948) and later analyzed in a plate tectonic context by McKenzie (1972). Extending for approximately 1600 kilometers, the NAFZ forms the Eurasian-Anatolian plate boundary. Due to its large seismic potential, it has been the focus of extensive geological and geophysical research. Historically, this fault has generated a series of large and destructive earthquakes. As noted

by Barka (1996), the NAFZ exhibits a pattern of westward-propagating seismicity, beginning with the 1939 Erzincan earthquake. The latest major events in this series were the 1999 İzmit (M_w 7.4) and Düzce (M_w 7.2) earthquakes, which struck the fault's western branches.

1.2.1. Tectonic Setting of Türkiye and NAFZ

The North Anatolian Fault (NAF) is a major geological structure that extends approximately 1500 km across northern Türkiye, from the Karlıova Junction in the east to the Aegean region. This fault accommodates a large portion of the Anatolian Plate's westward motion. While it follows a single path in the east, it splits into two distinct branches in the west (Barka & Kadinsky-Cade, 1988; Şengör et al., 2005). The northern branch of the fault, which moves at a slip rate of about 16 mm/yr, travels through the Adapazarı Basin and under the Sea of Marmara to the Gulf of Saros. The southern branch passes through the Geyve Basin and Lake Iznik and slips at a rate of approximately 9 mm/yr (e.g., Stein et al., 1997). These fault segments form natural boundaries between the Istanbul-Zonguldak, Armutlu-Almacık, and Sakarya zones. Additionally, InSAR data analysis has detected slow seismic slip along the NAFZ, indicating a preparatory phase for future earthquakes (Rousset et al., 2016).

The northernmost part of the western Pontides is comprised of the Istanbul-Zonguldak Zone. South of this, the Armutlu-Almacık Zone spans the Armutlu Peninsula and extends eastward toward the Almacık and Sünnice Mountains. This area is bounded by seismically dynamic fault lines, most of which have experienced rupture within the last century during major earthquakes such as the 1944 Bolu-Gerede, 1957 Abant, 1967 Mudurnu Valley, and the 1999 İzmit and Düzce events (Barka, 1992; Seyitoğlu et al., 2015). In the Late Miocene, intense volcanic activity and significant faulting fragmented the region into smaller blocks that evolved independently. One notable feature resulting from west-east extensional deformation is the Kuzuluk Basin, a complex pull-apart structure situated near the western edge of the zone (Greber, 1994; Belin et al., 2002). Further south lies the Sakarya Zone, which is bordered on the north by the Armutlu-Almacık Zone and on the south by the İzmir-Ankara Suture. The broader tectonic framework of Türkiye and the specific location of the study region are indicated in Figure 1.1.

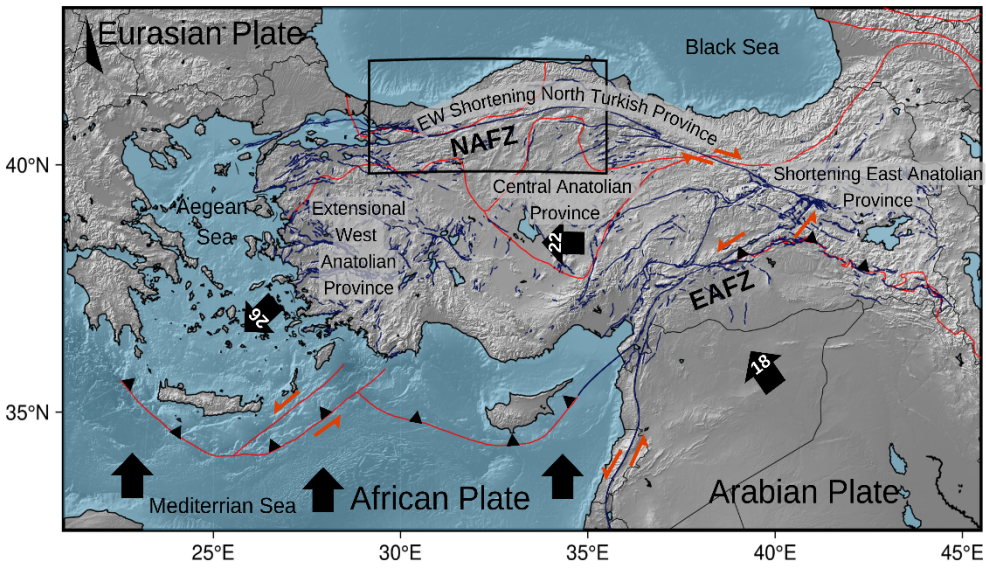


Figure 1.1. The major suture zones (Okay & Tüysüz, 1999), tectonic structures (Emre et al., 2013). Relative motions of tectonic plates with respect to Eurasia are indicated by black arrows, based on data from McClusky et al. (2000, 2003), Reilinger et al. (2006), and Nocquet (2012). The black rectangle shows the study region. Red arrows indicate fault movements.

1.3. The Earthquake Deformation Cycle

Earth deformation is a fundamental concept in the geosciences, driven by the continuous movement of tectonic plates. Earthquakes are linked to fault displacements, a phenomenon known as *stick–slip behavior.* This occurs when a fault locks and stress accumulates in the surrounding rock due to displacements at a distance. Once the stress reaches a critical level, the fault ruptures, causing an earthquake. The elastic energy stored in the adjacent rock is then partially released as heat through friction and partially radiated as seismic energy. This entire process is referred to as *elastic rebound*. The largest earthquakes can be associated with fault displacements of up to 30 meters (Turcotte et al., 2014).

Reid's elastic rebound model, developed in 1910 from displacement observations surrounding the 1906 San Francisco earthquake, was the first satisfactory explanation for the

release of accumulated elastic strain energy during seismic events. This theory is built on the cyclical accumulation and sudden release of elastic strain along an active fault, based on precise surveys near the San Andreas fault. The process can be broken down into three main stages: strain accumulation, fault locking, and sudden rupture and rebound. According to Reid's model (Figure 1.2), the earthquake deformation cycle consists of two periods: a slow build-up of elastic strain during *the interseismic phase*, after this period an abrupt rupture occurs in the *coseismic phase*.

Therefore, based on Reid's model and later discoveries, the earthquake deformation cycle is characterized by three periods: the interseismic, coseismic, and postseismic. The interseismic period is the first phase, characterized by a slow, gradual accumulation of elastic strain along a locked fault. Over decades or even centuries, the rocks near the fault are displaced as elastic energy builds up in the crust. This is followed by the coseismic phase, which is the sudden and rapid rupture of the fault. During this phase, the built-up stress reaches a critical value, causing the fault to slip and releasing the stored elastic energy as seismic waves and heat. The postseismic phase is the third and final period, involving a continued fault slip and strain readjustment that can last from days to decades following the main earthquake. In this thesis, we will focus on the co-seismic phase.

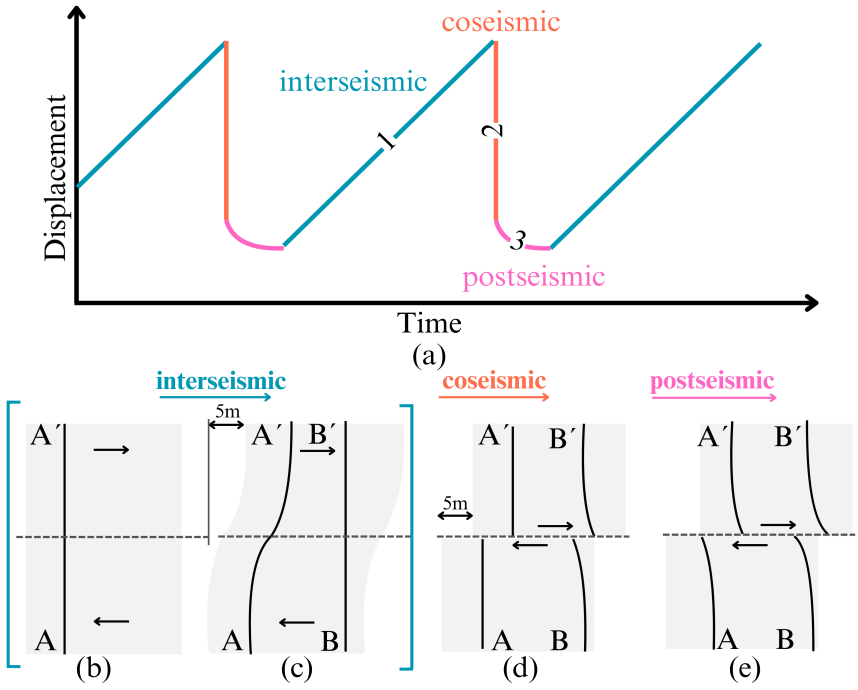


Figure 1.2. Illustration of the earthquake deformation cycle using survey markers (modified from Wright (2002)). It shows the interseismic phase as a centuries-long period of slow strain accumulation that distorts a straight marker (A-A'). The coseismic phase involves a sudden 5 m offset, while the postseismic phase shows continued strain readjustment.

1.3.1. Coseismic Deformation

For over 25 years, coseismic deformation has been measured using spaceborne SAR sensors (Boncori, 2019). Geodetic methods, such as InSAR, are used to quantify these surface displacements because they offer uninterrupted, high-resolution data across wide regions. Starting from the launches of Sentinel-1A (April 2014), Sentinel-1B (2016), and ALOS-2 (May 2014), there has been an exceptional abundance of high-quality SAR data. This data, which is characterized by low spatial and temporal baselines along with precise orbital and timing control, is highly suitable for crustal deformation studies (Boncori, 2019).

InSAR is a technique that uses radar images from satellites, such as those from the Sentinel-1 mission, to measure ground deformation before and after an earthquake. The

SAR data is processed to generate interferograms, which are visual representations of the phase difference between two temporally separated SAR acquisitions. This phase difference is proportional to the magnitude of the surface's movement caused by the seismic event (Yagüe-Martinez et al., 2016).

The generation of an interferogram is a multi-step process that transforms two complex SAR acquisitions into a single product that measures ground deformation. The workflow, particularly for Sentinel-1 TOPS mode data, is highly specialized due to the unique signal properties of the acquisition method (Grandin, 2015).

1.4. Literature Review

1.4.1. History of Coda Wave Studies

The study of coda waves began with Keiiti Aki's pioneering work in 1969, where he introduced the term to describe the later-arriving portion of high-frequency seismograms following direct seismic phases (Figure 1.3). As Figure 1.3 illustrates, coda wave amplitudes appear similar across different seismic recordings, regardless of the distance from the epicenter. Unlike direct seismic phases, their amplitudes do not significantly diminish with distance. Aki (1969) ultimately proposed that they could be effectively used to estimate seismic moment. He observed that, unlike direct waves whose amplitudes decrease with distance, they maintain consistent amplitudes and spectral properties across various stations, indicating their independence from epicentral distance. Aki attributed this behavior to incoherent scattering caused by randomly distributed heterogeneities within the Earth's lithosphere. This scattering process not only explains the uniform appearance of these later arrivals in regional seismograms but also highlights their potential as a robust tool for analyzing earthquake source characteristics, including seismic moment and excitation properties.

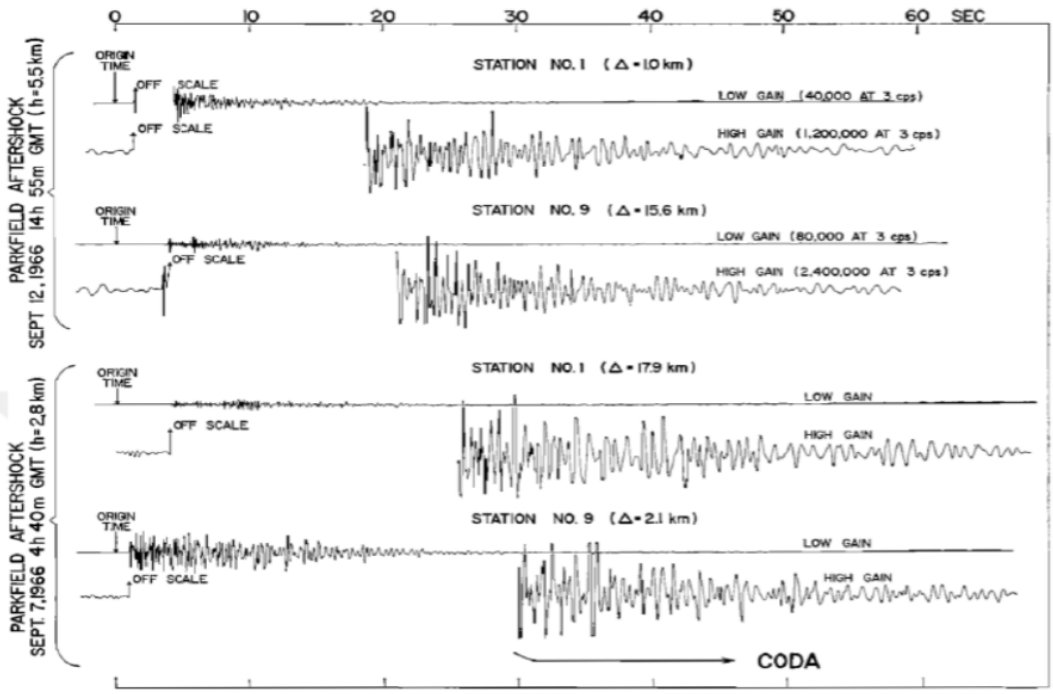


Figure 1.3. Vertical component recordings from two USGS stations captured aftershocks of the Parkfield earthquake, with coda waves indicated by black arrows on the high-gain traces (Aki, 1969).

Building on earlier work, Aki and Chouet (1975) provided compelling evidence for the backscattering model, introducing a method to interpret observed coda spectra using single-backscattering theory. Their research demonstrated that, due to their spectral characteristics, coda waves could be effectively utilized to investigate the fingerprint of earthquakes in regions such as California and Japan, as mentioned before. They further proposed two theoretical models to explain the decay pattern of coda wave amplitudes over time: the single backscattering model, which assumes weak scattering with negligible energy loss, and the diffusion model, which suggests that seismic energy spreads through the crust via a diffusion-like process. These models helped to clarify the distinctions among source effects, scattering, and attenuation. Through analyzing small local earthquakes in central California and western Japan, they concluded that coda waves originate from backscattering off randomly distributed heterogeneities in the Earth's crust. Their findings also revealed that at frequencies below 10 Hz, these waves primarily consist of backscattered surface waves, whereas at higher frequencies, they are dominated by backscattered body waves. These characteristics are specific to the seismicity of the studied regions.

Aki and his collaborators emphasized several important observations about coda waves recorded at epicentral distances less than approximately 100 km:

1. The spectral content of the later portion of local earthquake seismograms remains roughly identical across different recording stations, whereas the early arrivals often show significant variation (Aki, 1956; 1969).

2. The total duration of a local earthquake seismogram does not significantly vary with epicentral distance or azimuth within 100 km. This duration can therefore serve as a reliable proxy for earthquake magnitude (Bisztricsany, 1958).

3. The spectral energy of coda waves generated by various nearby earthquakes shows a constant temporal decay, a property that is independent of both the source-to-station distance and the propagation path (Aki, 1969; 1975).

4. For earthquakes with magnitudes below 6, the shape of narrowband coda waves remains largely unaffected by the event magnitude, indicating they are not strongly influenced by source size (Aki, 1969; 1975).

5. The excitation and amplitude of coda waves are significantly affected by the geological conditions at the recording site. For example, stations located on sedimentary ground may record amplitudes 5 to 8 times higher than those on granitic bedrock (Aki, 1969).

6. Coda waves do not propagate as conventional plane waves from the epicenter. Instead, they result from complex scattering processes within the crust (Aki et al., 1958).

Coda wave methods, initially developed to analyze clipped seismograms from large earthquakes, gained popularity due to their ability to extract source and medium information from high-gain, low-dynamic-range seismic networks (Sato et al., 2012).

Subsequent studies identified these waves as a valuable tool for quantitatively evaluating the strength of random heterogeneities within the Earth's lithosphere (Aki and Chouet, 1975; Sato, 1978). With seismometers installed in boreholes, reducing ambient seismic noise and the introduction of digital seismic networks allowing greater dynamic range, recording and modeling the full envelope of seismograms became possible. By using both the main seismic phase and the coda, a new approach enabled more detailed investigations into lithospheric heterogeneity at seismic frequencies between 1 and 30 Hz (Sato et al., 2012).

Aki and Chouet (1975) also brought in the concept of coda quality factor (Q_c), a dimensionless parameter variable quantifying the decay rate of coda wave amplitudes. While initially attributing this decay solely to anelastic attenuation within the single-scattering model framework, they later incorporated the diffusion model to account for additional energy loss from scattering. By analyzing their decay rate within specific frequency bands, they found that Q_c was not influenced by the epicentral location or the recording site for local earthquakes. This indicated that this decay behavior is largely independent of source and path effects, reinforcing the reliability of Q_c as a tool for studying attenuation characteristics within the Earth's crust.

Building on the foundational work of Aki and Chouet (1975), subsequent studies extended the application of coda wave analysis beyond Earth. Nakamura (1977) and Dainty and Toksöz (1981) applied the diffusion model to lunar seismograms, proposing that strong scattering observed in long-duration lunar records could only be explained by diffusion processes within the Moon’s lithosphere.

Observational and theoretical studies on Q_c suggest that it's a combination of two effects: anelastic attenuation, Q_a and scattering attenuation Q_s. To separate these two components and determine how they vary with frequency, several models have been developed. Some of the major approaches include the Energy Flux Model (Frankel and Wennerberg, 1987), the Radiative Transfer Theory (Wu and Aki, 1988), and the Multiple Lapse Time Window Analysis (MLTWA) (Fehler et al., 1992). These studies highlight the importance of Qc as a key parameter for understanding crustal heterogeneity and regional

tectonic activity. However, attempts to establish a consistent relationship between Q_c, Q_a, and Q_s have yielded inconclusive results.

In addition to studies on the coda quality factor, researchers have employed the Coda Normalization Method (CNM) as a practical observational technique to separate the contribution of seismic source radiation from site amplification on seismograms. Radiation from the source refers to energy as a function of frequency emitted from the earthquake source, while site amplification is influenced by near-surface geological conditions. Accurately quantifying these two components across frequencies is essential for seismic hazard assessment and earthquake characterization.

The CNM is an empirical method that does not require prior knowledge of geological structure, velocity models, or source mechanisms. Its core assumption is that, at a certain lapse time (tc), coda wave energy remains stable within a volume surrounding the source. This principle is supported by earlier findings from other researchers, who observed consistent coda decay shapes independent of source-receiver distance (Aki and Chouet, 1975).

A simple application of CNM involves comparing the normalized amplitudes of coda waves recorded at two stations. If both stations are located near the source and have similar geological conditions, their amplitudes should be nearly identical. However, differences in local geology can lead to variations in amplitude, which can be quantified by taking the ratio of the waveforms.

Phillips and Aki (1986) made further developments by analyzing digital data from more than 90 local earthquakes captured by 150 stations across Northern California. Using multiple lapse time windows, they assumed that site amplification remains consistent across different events and that coda decay shapes are unaffected by source-receiver distance or site conditions. Their results indicated that site amplification is primarily governed by local geology.

Mayeda et al. (1991) also examined site amplification across six frequency bands, noting that near-surface geological complexity can significantly affect high-frequency site

amplification. Fehler et al. (1992) analyzed local ground motion amplification within Japan's Kanto-Tokai region. They compared these aspects with magnitude residuals across various frequency bands and found a strong correlation at a central frequency of 6.0 Hz. This result highlighted that site effects are a significant contributor to magnitude residuals during earthquake magnitude estimation.

In the same year, Koyanagi et al. (1992) applied the CNM to evaluate site amplification at various locations in Hawaii using data from the Hawaiian Volcano Observatory (HVO) network. By analyzing S-coda amplitude spectra from 136 local earthquakes across the 1.5–15 Hz frequency range, they identified consistent frequency-dependent site amplification trends among stations. However, notable differences were observed due to subsurface structural variations and lava flow characteristics. Their findings suggested that regional geological trends significantly influence frequency-dependent site amplification. Additionally, the researchers compared site amplifications with magnitude residuals for the same events. They found a strong agreement within the 1.5–6.0 Hz range, confirming earlier studies by Fehler et al. (1992) and Mayeda et al. (1991).

Besides estimating site amplification, the CNM is also used to calculate seismic source radiation. Before this method was developed, Aki (1967) had explored the connection between the amplitude spectrum of seismic waves and the earthquake source size. His work demonstrated that earthquake size could be estimated using spectral density curves that vary with frequency. These curves typically exhibit a flat displacement spectrum at low frequencies, followed by a decline beyond a characteristic corner frequency. This flat portion of the spectrum was later used to calculate seismic moment, a fundamental physical parameter representing earthquake scale (Aki and Richards, 1980).

Thereafter, the amplitude of coda waves has become a valuable tool for estimating seismic moment, offering an alternative to traditional methods based on direct wave arrivals. Because these waves are representative of a volume where the energy is evenly spread, the method doesn't depend on theoretical models of source effects and wave propagation. This makes it a robust and unbiased approach for determining earthquake size.

Biswas and Aki (1984) established an empirical methodology between coda wave amplitudes, quantified at specific elapsed time and seismic moment, using data from two large Alaskan earthquakes (Rampart and St. Elias). Their findings linked the decay rate of coda amplitudes to independently estimated seismic moments.

Later, Mayeda (1993) applied the approach to estimate the scale of nuclear tests at the Nevada Test Site (NTS), measuring Lg-coda amplitudes in the 0.75–1.25 Hz range. He found that m_b magnitudes derived from Lg-coda at ~1 Hz were 3 to 4 times more stable than those obtained from direct Lg waves at the same locations.

Hartse et al. (1995) applied the technique to 27 explosions and 15 earthquakes in the southern Great Basin, introducing the concept of "type curves", which are average coda decay shapes for specific frequency bands that reflect regional scattering and attenuation characteristics.

Following this approach, Mayeda and Walter (1996) enhanced source parameter estimation by incorporating frequency-varied corrections and high-quality, three-component broadband data. They further advanced the method by applying a two-dimensional, distance-dependent scattering model to create synthetic narrowband coda envelopes, which were then linked to absolute moment-rate spectra across multiple frequency bands.

Mayeda et al. (2003) advanced a method for analyzing earthquakes in the Dead Sea Rift region. This method, which did not rely on theoretical models, incorporated S-to-coda transfer functions and accounted for the distance-dependent shape of coda envelopes. To calculate moment-rate spectra, they measured S-coda amplitudes in 14 frequency bands (0.02–8 Hz) and calibrated them against known seismic moments from reference events.

Further validation came from Eken et al. (2004), who used the same approach on local and regional earthquakes recorded at three broadband stations in Türkiye. Their results indicated a similar improvement in stability, with a standard deviation of just 0.17 in comparison to waveform modeling.

Morasca et al. (2008) also confirmed the method's reliability by applying it to events with magnitudes between 1 and 5 in the western Alps, demonstrating its effectiveness in estimating seismic moment and S-wave energy in smaller earthquakes. Yoo et al. (2011) demonstrated the effectiveness of source spectra derived from coda in estimating stable magnitude sizes and source radiation parameters for small events in the Korean Peninsula and provided further evidence for non-self-similar rupture behavior in tectonically stable regions. Gök et al. (2016) demonstrated the effectiveness of one-dimensional coda calibration techniques in estimating moment magnitudes across the Middle East, showing that reliable magnitude estimates can be achieved even in tectonically complex and data-sparse regions by utilizing extensive broadband networks. Shelly et al. (2022) benchmarked routine magnitude estimates against coda-derived Mw in the U.S. midcontinent, highlighting discrepancies in small magnitudes and validating the reliability of coda-based methods. Similarly, Morasca et al. (2022) compared direct S-wave and coda envelope methods in Central Italy, confirming the consistency of coda-derived source scaling. Most recently, Mayeda et al. (2024) and Al-Kaabi et al. (2024) validated using the Java-based tool, CCT, which applies the one-dimensional model of coda envelopes, in California and Iraq, respectively, confirming the global applicability of these techniques.

The method has also proven effective in explosion monitoring. Murphy et al. (2009) applied it to seismic data from nuclear tests, identifying distinct spectral peaks influenced by emplacement depth and geological conditions. These spectral characteristics helped distinguish explosions from natural earthquakes and improved the reliability of yield estimation.

Hoshiba (1993) introduced another significant coda wave method: the MLTWA. This technique estimates frequency-varying site amplification, assuming that coda decay pattern is driven by scattering rather than distance.

In a later study, Hoshiba (1997) used coda wave envelopes to explore the relationship between S-wave velocity and depth, concluding that velocity discontinuities influence energy density and that CNM may be insufficient for regions with depth-dependent velocity structures.

Later, Bianco et al. (2002) applied the MLTWA to the Southern Apennines region to separately quantify scattering and intrinsic attenuation (Qi^{-1}). Their results showed that, within the 2–12 Hz frequency range, total attenuation derived from coda waves (Qc^{-1}) was primarily controlled by Qi^{-1} rather than scattering.

Sens-Schönfelder and Wegler (2006) introduced a novel technique based on a physical scattering model using radiative transfer theory (RTT), which allows for the direct estimation of source parameters without relying on reference events. This method employs a joint inversion algorithm that utilizes isotropic acoustic RTT to generate synthetic coda envelopes. Unlike traditional coda normalization techniques, this approach is less susceptible to biases introduced by external reference data, such as seismic moment estimates from full waveform inversion.

This method has been successfully implemented to seismic activity related to tectonic and geothermal processes in regions such as Germany, Czechia, and the United States (Eulenfeld and Wegler, 2016; 2017). It has also been applied in Türkiye, particularly along the NAFZ, where several studies have explored its effectiveness in characterizing regional attenuation properties. In the NAFZ, Gaebler and his colleagues (2019) investigated the two- The spatial distribution of frequency-varying attenuation characteristics within the crust beneath its central segment. Their analysis was based on fitting observed and synthetic seismogram envelopes across four frequency bands, providing improved resolution of shear wave energy loss. Izgi et al. (2020) later focused on the western NAFZ, applying Acoustic Radiative Transfer Theory to invert coda wave envelopes in five frequency bands, revealing distinct attenuation patterns associated with major crustal blocks separated by the fault's branches. More recently, Izgi et al. (2024) extended this method to the Central Anatolian Plateau, where they modeled attenuation stems from intrinsic dynamics and scattering individually using a model-based approach using coda waves. Their findings highlighted the dominance of intrinsic attenuation beneath the Kırşehir Massif, suggesting the existence of a thick layer of volcanic rock and shedding light on the region's geodynamic evolution. Following this, Özkan et al. (2024) applied coda wave modeling to 303 local earthquakes in the Sea of Marmara, using data from 49 seismic stations to estimate moment magnitudes across 12 frequency bands. Their results demonstrated the stability of coda-derived

magnitudes and revealed non-self-similar rupture behavior for smaller events, leading to a better grasp of earthquake scaling and seismic risk in northwestern Türkiye.

1.4.2. Coda-Derived Moment Magnitudes and Source Scaling: A Review of Global and Regional Studies

The theoretical basis for magnitude scaling and energy release in earthquakes was established by Kanamori and Anderson (1975), who explored empirical relations in seismology. Later, Kanamori et al. (1993) and Kanamori & Rivera (2004) refined these concepts by linking static and dynamic source parameters to rupture processes and stress drop. These foundational studies provided the framework for later developments in coda-based magnitude estimation.

Mayeda et al. (2007) developed a method that uses narrow-band coda envelope amplitudes to estimate earthquake source spectra by analyzing filtered coda wave energy at specific frequencies and lapse times. This approach significantly reduces the influence of path and site effects, making it more stable than traditional direct wave methods. Their findings, particularly from the Hector Mine earthquake sequence (2007), revealed that large earthquakes may not scale uniformly with smaller ones, which challenges the assumption of self-similarity and highlighting the method's value in refining source scaling models.

Building on this, Mayeda & Malagnini (2010) applied the technique to the M_w 5.9 Wells, Nevada sequence and confirmed that coda envelopes are largely unaffected by source radiation patterns. This makes the method especially reliable for estimating moment-rate spectra and apparent stress, even in regions with sparse seismic networks.

Malagnini et al. (2014) applied the coda ratio technique to estimate corner frequencies and the apparent stress for a series of crustal events across various tectonic settings. Their analysis revealed systematic deviations from classical self-similar source scaling, a positive correlation was found between apparent stress and seismic moment. This trend suggests a progressive weakening of friction with increasing slip, a phenomenon supported by laboratory experiments conducted at seismic slip velocities. These experiments indicate that

fault slip of several tens of centimeters, typical for earthquakes with moment magnitude above 5.5, can lead to dynamic fault lubrication.

To effectively analyze coda waves within seismological studies, an understanding of their excitation models is necessary. The following chapters will therefore describe the theoretical frameworks that address how these waves are generated and propagate within the Earth.

1.4.3. Introduction to Models

The initial model for coda waves, assuming co-located seismic sources and receivers, was developed by Aki and Chouet (1975). This model was later expanded by Sato (1977a) to account for body waves and by Kopnichev (1975) for surface waves with spatially separated sources and receivers. In these phenomenological frameworks, the amplitude and shape of coda waves are primarily controlled by two key parameters: the total scattering (g0) and the attenuation of coda wave Q_c^{-1} . These parameters have been estimated globally by implementing these models to the envelopes (e.g., Jin & Aki, 2005; Nishigami, 2000).

The coda normalization method utilized in this study is a prominent technique in seismology that operates on a key assumption: long after an earthquake, the scattered energy from coda waves becomes uniformly distributed throughout the space. This principle, which builds upon the known behavior of S-coda waves, allows scientists to use data from a single seismic station to perform several crucial analyses. These include estimating relative site amplification (how much local geology affects ground shaking), identifying changes in source spectral properties (the earthquake's unique characteristics), and measuring attenuation (how wave energy is lost as it travels) (Phillips and Aki, 1986; Yoshimoto et al., 1993).

Numerous studies have documented temporal variations in coda wave properties, particularly in the attenuation parameter Q_c^{-1} , which are often associated with seismic and volcanic activity (e.g., Fehler et al., 1988). To investigate these subtle changes over time, researchers employ specialized techniques. One such method involves using earthquake doublets, pairs of nearly identical earthquakes occurring at different times to compare their

resulting wavefields (Aster et al., 1996). Another approach is the moving window cross-correlation of coda waves from events occurred within 100 km, which can detect velocity changes related to earthquake occurrences (Poupinet et al., 1984).

Following the historical context and observed characteristics of coda waves, this section, and the subsequent chapters, present various theoretical models developed to explain their generation and propagation. The discussion begins with the definition of scattering characteristics that govern wave interaction within heterogeneous media. Subsequently, the Diffusion Model, Energy-Flux Model, and Radiative Transfer Theory (RTT) are introduced, each offering distinct approaches to understanding scattered seismic wavefields. Finally, the Back-scattering Model, a fundamental scattering model essential for coda wave analysis and directly utilized in the Coda Calibration Methodology, the primary method applied in this thesis, is detailed, providing the mathematical framework for understanding energy decay over time.

1.4.4. Scattering Properties

Energy-flux density refers to the energy quantity transmitted per unit area that is oriented normal to the direction of wave propagation, per unit time (Sato et al., 2012). As depicted in Figure 1.4, consider a steady-state scenario where an incoming plane wave with a specific power density J^0 is scattered by an object, producing spherically radiating deflected waves characterized by an energy-flux density J^1. In this context, polarization effects and the division of energy into different wave components are neglected. The rate of energy scattered in a specific direction in a narrow cone space $d\Omega$ is given by $J^1r^2d\Omega$, where $r^2d\Omega$ represents the corresponding surface area element. The differential scattering cross-section is then defined the scattered energy normalized by the incident power density (Sato et al., 2012):

$$\frac{d\sigma}{d\Omega} = \frac{J^1 r^2}{j^0} \tag{1.1}$$

A randomly inhomogeneous medium can be represented as a uniform medium where waves travel at a constant velocity V_0, within which numerous point-like scatterers are embedded, as illustrated schematically in Figure 1.5. These scatterers are assumed to be

randomly and uniformly distributed in space, with isotropic properties. Each instance of scattering is described by a differential cross-section with respect to solid angle.

$$g \equiv 4\pi n \frac{d\sigma}{d\Omega}, \tag{1.2}$$

The volume scattering coefficient is determined by multiplying the number density of scatterers with the differential scattering cross-section (Aki and Chouet, 1975). This product is known as the scattering coefficient, which typically varies with frequency and scattering angle. The quantity g has units of corresponding length. However, when using the scattering coefficient to describe scattering power, it becomes impossible to differentiate between a scenario with a few strong scatterers and one with many weak scatterers.

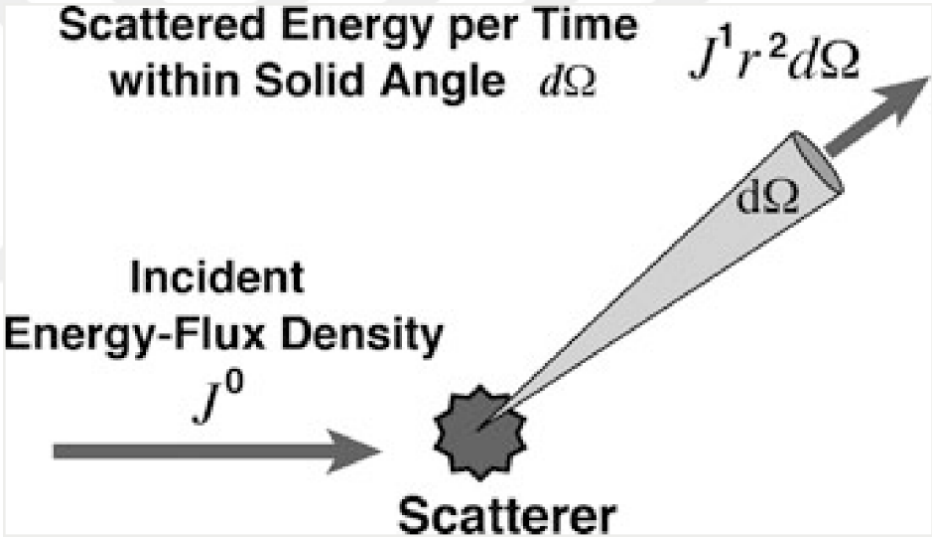


Figure 1.4. A simplified diagram showing how a single scatterer redirects incoming wave energy in different directions (Sato et al., 2012).

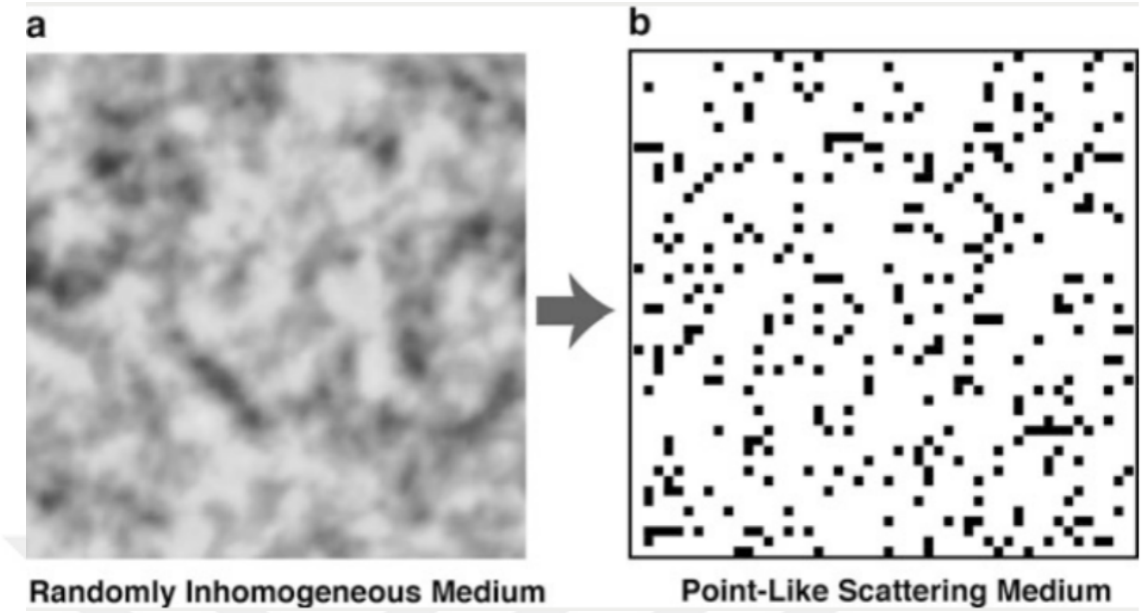


Figure 1.5. (a) numerical simulation of wavefields in random media, and (b) illustration of energy transport processes in scattering environments (Sato et al., 2012).

1.4.5. Diffusion Model

A more realistic Earth model for explaining coda waves was introduced by Sato et al. (2012), who incorporated multiple scattering processes instead of relying solely on single scattering. This approach assumes that, over long lapse times, energy diminishes and multiple scattering causes a smooth spatial field of energy density. The theoretical framework for multiple scattering is described by Morse and Feshbach (1956).

1.4.6. Energy-Flux Model

Frankel and Wennerberg (1987) introduced a model to describe the distribution of energy density over space and time. Although this model does not explicitly describe the spatial distribution of scattered wave energy, it successfully reproduces the spatiotemporal energy density observed in seismograms and incorporates the effects of multiple scattering.

1.4.7. Radiative Transfer Theory

Radiative Transfer Theory (RTT), originally introduced by Chandrasekhar (1960) to describe the propagation of light through unstable media such as the atmosphere, has since been widely adopted to characterize scattered seismic wave fields. The theory is used to model seismogram envelopes by describing the transport of S-wave energy through a heterogeneous medium. The governing principle is the Boltzmann transport equation, which formulates a energy density at a given time and location by accounting for the initial unscattered wave energy and all subsequent multiply scattered energy. the model relies on several main assumptions: the scattering of S-waves is isotropic, the earthquake source radiates energy isotropically, and the propagation occurs within a statistically homogeneous half-space (Sens-Schönfelder and Wegler, 2006). To avoid the computational expense of solving the full Boltzmann integral equation, an analytical expression for the energy density Green's function, developed by Paasschens (1997), is employed.

In the following section, we provide a comprehensive explanation of the backscattering model adopted by the coda normalization approach.

1.4.8. Back-scattering Model

Analyzing high-frequency seismograms is challenging owing to the significant influence of lateral inhomogeneities within the crustal portion of the Earth, which complicates the determination of seismic source characteristics and wave propagation paths. To address this, deterministic methods require accurate modeling of both scattering and anelastic attenuation processes along the wave path in the lithosphere. While deterministic approaches have been successfully applied to long-period surface waves assuming a laterally homogeneous lithosphere, they are inadequate when it comes to high-frequency wave analysis, which is more sensitive to crustal irregularities (Aki, 1969).

As previously discussed, Aki's seminal research demonstrated that coda wave analysis offers a reliable and straightforward statistical method for interpreting crustal structure and estimating source parameters, providing practical and effective solutions for some of the difficulties in analyzing high-frequency seismic data.

Aki and Chouet (1975) subsequently introduced the single scatter model to describe how scattered energy density evolves over time at the source position within a three-dimensional material. They examined a scenario involving a sudden, spherical release of total energy from a point source located at the origin, as depicted in Figure 1.6. In this context, the density of the incident energy flux on a scatterer located at location *z* is expressed as follows:

$$\frac{W}{4\pi r_a^2}\,\delta\left(t-\frac{r_a}{V_0}\right), \tag{1.3}$$

where w represents radiated energy, r_a and t are the radius of the sphere and travel time, and V_o is the wave velocity.

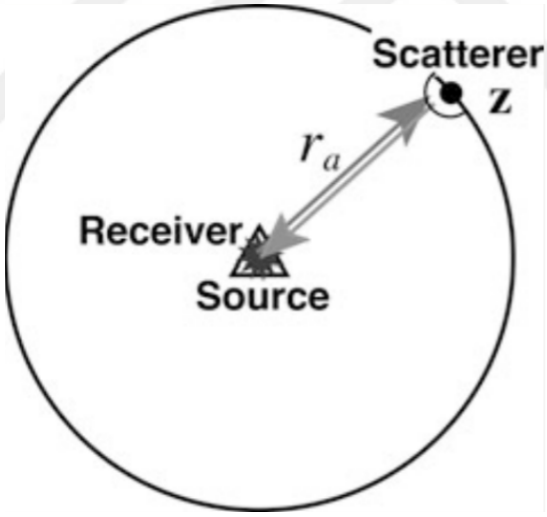


Figure 1.6. Geometric representation of the single backscatter model with a co-located source and receiver (Sato et al., 2012).

Let $r_a=|z|$. Then, the flux of energy density of the single backscattered wave returning to the origin after being generated by a scatterer at distance r_a is given by

$$\frac{W}{4\pi r_a^2}\,\delta\left(t-\frac{2r_a}{V_0}\right)\frac{1}{r_a^2}\frac{d\sigma}{d\Omega}\Big|_{\pi} \tag{1.4}$$

The delta function represents the delay in time associated with the travel from the source to the receiver and back. The subscript π denotes backscattering, as the scattering angle corresponds to that direction. Because the scatterers are assumed to be non-uniformly distributed, the resulting scattered waves are incoherent. Therefore, the total scattered wave power is calculated by summing the power contributions from each individual scattered wave. By dividing the energy flux density by the wave velocity V_0, we obtain:

$$E^1(x = 0,\ t)\ = \sum_{Scattereres} \frac{W}{4\pi r_a^2}\,\delta\left(t - \frac{2r_a}{V_0}\right)\frac{1}{r_a^2}\frac{d\sigma}{d\Omega}\Big|_\pi \frac{1}{V_0}, \tag{1.5}$$

The superscript 1 indicates that the expression refers to single scattering. By multiplying with the scatterer number density *n*, the summation over individual scatterers is replaced with an integral over all possible scatterer positions *z* throughout the entire space. This leads to the following expression for the energy density:

$$E^1(x = 0,\ t)\ = \iiint_{-\infty}^{\infty} \frac{W}{4\pi r_a^2}\,\delta\left(t - \frac{2r_a}{V_0}\right)\frac{n}{r_a^2}\ \frac{d\sigma}{d\Omega}\Big|_\pi \frac{1}{V_0}\,dz. \tag{1.6}$$

By replacing the backscattering coefficient $g_\pi = 4\pi n\left(\frac{d\sigma}{d\Omega}\right)|_\pi$into the equation above and performing the integration using spherical coordinates $(r_a, \theta_a, \varphi_a)$ where H is the Heaviside step function, we proceed with the integration. The energy density of singly scattered waves at the source diminishes proportionally proportional to one over the square of the elapsed time, meaning that the root-mean-square (RMS) amplitude of the coda decays inversely with lapse time as shown in Equation 1.7.

$$E^1(x = 0\ ,\ t) = \frac{W g_\pi}{2\pi V_0^2 t^2}\ H(t)\ \propto\ t^{-2}, \tag{1.7}$$

For practical purposes, empirical attenuation is incorporated by applying an exponential decay term at angular frequency ω, where the parameter Q_c, known as the coda attenuation factor, characterizes the level of attenuation.

$$E^1(x = 0\ ,\ t) = \frac{W g_\pi}{2\pi V_0^2 t^2}\ H(t)\ e^{-Qc^{-1}\omega t}. \tag{1.8}$$

1.4.9. Early Geodetic and Geophysical Studies in the Region

1.4.9.1. Long-period Deformation of Anatolia. Weiss et al. (2020) produced high-quality horizontal and vertical velocity fields, as well as strain rate fields, for Anatolia. The research aimed to measure current surface deformation, which is fundamental for the long-term seismic risk assessment. To achieve this, they combined approximately five years of satellite radar interferometry data from the European Space Agency's Sentinel-1 satellites with published Global Navigation Satellite System (GNSS) observations. This covered an extensive area of about 800,000 km², representing one of the largest regional interseismic measurements from InSAR to date.

The methodology involved the use of open-source, automated workflows to process the large volume of Sentinel-1 data. The LiCSAR system was used to generate interferograms, and atmospheric noise contributions were partially mitigated using the GACOS model (González et al., 2016; Yu et al., 2017; Morishita et al., 2020). Subsequently, the LiCSBAS software package was employed to extract the line of sight (LOS) displacement time series and velocities from the InSAR data. To create a full 3-D velocity field, the ascending and descending InSAR LOS velocities are decomposed into east-west and vertical components (Wright et al., 2004). Since InSAR is relatively insensitive to N-S motion, this component was constrained using an interpolated GNSS velocity field. Finally, the combined InSAR and GNSS datasets can be used in the inversion for constructing a continuous velocity and strain rate framework using the VELMAP approach (Wang & Wright, 2012).

Figure 1.7 provides the foundational tectonic context and lateral variation of the surface deformation based on the GNSS by England et al. (2016) and Nocquet et al (2012) and InSAR velocity data by Weiss et al. (2020) relative to a fixed Eurasia. Figure 1.6a displays GNSS velocity vectors, which clearly illustrate the counter-clockwise rotation implying westward motion of Anatolia. Significant tectonic features including the NAF and EAF are also shown. Figure 1.6b shows the LOS velocities from the ascending satellite tracks, where blue color indicates motion towards the satellite. The westward motion of the Anatolian plate south of the NAF is seen as a large blue region. Conversely, Figure 1.6c

presents the data from descending tracks; the same westward motion is predominantly away from the satellite's line of sight and thus appears as a large red area.

The decomposed E-W velocity field confirms the westward movement of Anatolia at a rate of 20-25 mm/year with respect to Eurasia (Weiss et al., 2020). The analysis in Weiss et al. (2020) further reveals also revealed significant vertical motions, most notably a large zone of subsidence in the Konya Basin exceeding 50 mm/year, which is attributed to groundwater extraction. This combined model of Weiss et al. (2020) shows strain rates of ≥150 nanostrain/year are observed along nearly the entire span of the NAF.

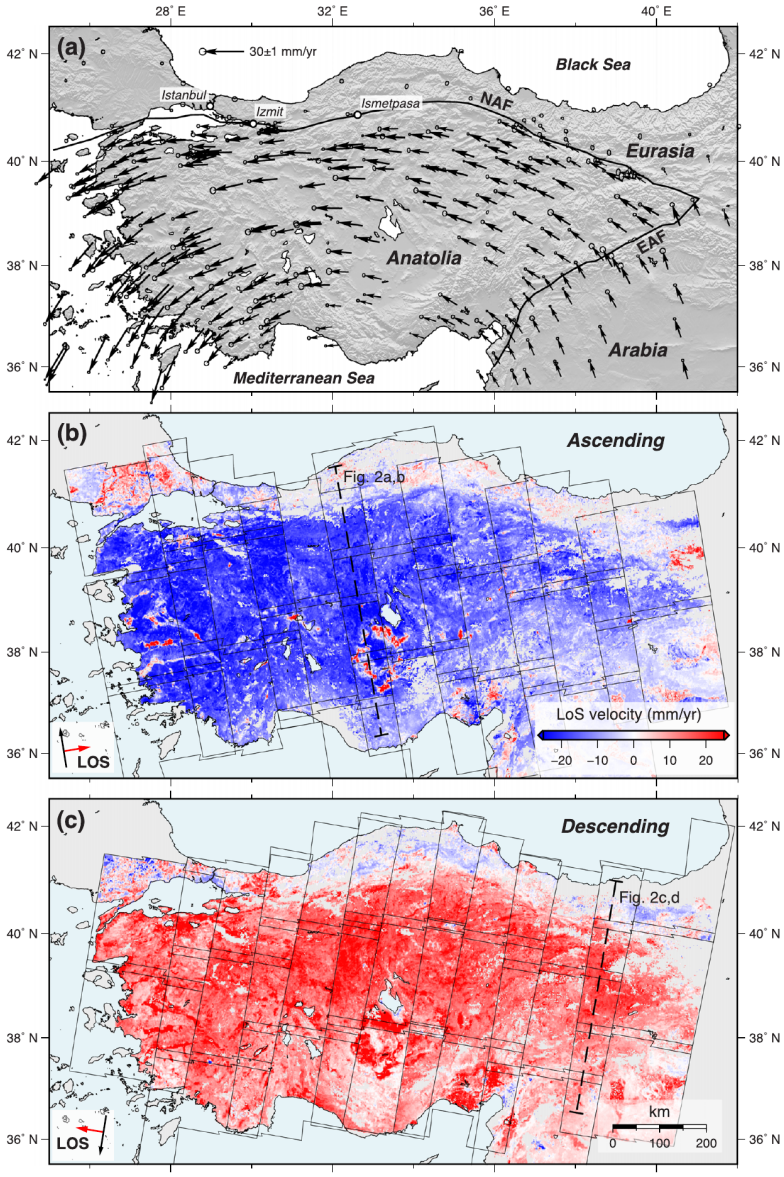


Figure 1.7. (a) Tectonic framework of Türkiye and interseismic surface velocities in the Eurasia-fixed frame (Weiss et al., 2020). (b) and (c) Satellite data from both descending and ascending tracks show LOS velocities, respectively. Blue color indicates motion toward and red indicates motion away from the satellite (Weiss et al., 2020).

1.4.9.2. The M_w 6.0 Gölyaka-Düzce Seismic Activity. Martínez-Garzón et al. (2023) analyzed the M_w 6.0 Gölyaka–Düzce earthquake, which occurred on 23 November 2022 near the rupture area of the 1999 M_w 7.1 Düzce earthquake along the NAFZ. The 2022 event is attributed to a previously unruptured segment of the Karadere fault, a subsidiary branch of the main NAFZ.

Martínez-Garzón et al. (2023) studied the spatiotemporal evolution of the seismic sequence across different scales to resolve the source characteristics of the mainshock. Using an Epistemic Type Aftershock Sequence (ETAS) model, they analyzed the long-term development of background seismic activity associated with the Karadere Fault, that has been nearly inactive since the 1999 M_w 7.1 Düzce failure but has experienced a gradual rise in the occurrence of seismic activity starting in 2000.

A high-resolution seismicity catalog based on artificial intelligence-based techniques was created for the period from one month before to six days after the mainshock using artificial intelligence-based techniques presented in Martínez-Garzón et al. (2023) reveals that a small number of events occurred within the eventual rupture segment prior to the earthquake, with no significant foreshock clustering or localization pattern (Figure 1.8).

The aftershock hypocenter distribution in the same study indicates that both the Karadere fault and the adjacent Düzce Fault, which ruptured during the 1999 earthquake, were reactivated. Initial source parameter results and analysis of the initial P-wave arrival suggest that the rupture propagated eastward, consistent with expectations from a model of a fault plane between two different materials (Martínez-Garzón et al., 2023).

According to Martínez-Garzón et al. (2023), the M_w 6.0 Gölyaka–Düzce earthquake thus demonstrates a notable case of a moderate-magnitude event with significant damage potential, occurring within a fault zone that appears to be at the beginning of the seismic cycle.

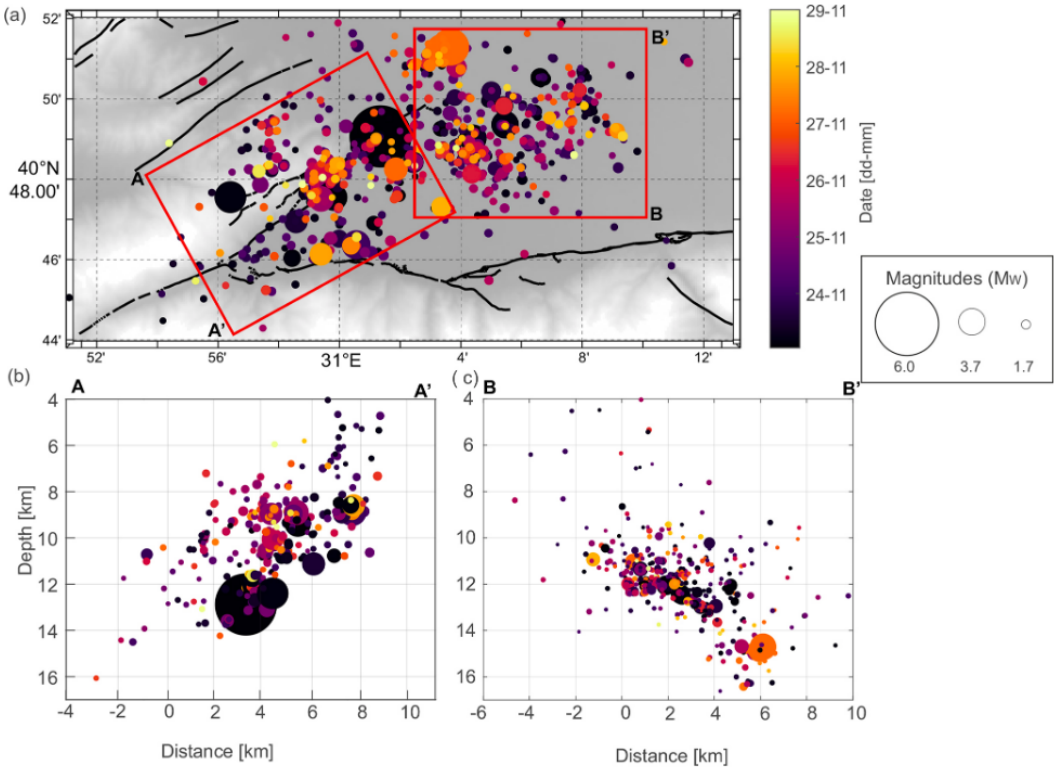


Figure 1.8. Spatial and temporal patterns of seismic activity during the six days after the Düzce earthquake. (a) Map view of seismicity. (b) Depth cross-section along profile A–A', oriented nearly orthogonal to the Karadere fault. (c) Depth cross-section along profile B–B', roughly normal to the Düzce fault. Marker size is proportional to earthquake magnitude, and color indicates the date of occurrence (Martínez-Garzón et al., 2023).

1.4.9.3. DInSAR-Based Investigation and Geophysical Interpretation of the 23 November 2022 Düzce–Gölyaka Earthquake. Karaca et al. (2024) examined the Düzce–Gölyaka earthquake that occurred on 23 November 2022 via DInSAR analysis (Figure 1.9) that employs the elastic dislocation approach for the forward modeling of surface deformation caused by the causative fault structure. Their findings showed that the northern block of the Düzce segment experienced approximately 5 centimeters of subsidence and 8 centimeters of eastward motion, while the southern block exhibited about 3 centimeters of uplift and 3 centimeters of westward displacement, implying a right-lateral strike-slip motion affecting an area of roughly 105 square kilometers in the northwestern part of the Karadere segment.

Karaca et al. (2024) further applied both nonlinear and linear inversion methods to estimate the earthquake source mechanism for a better understanding of the actual geometry of faulting. Their modelling results suggest that both inversion approaches effectively reproduce the observed surface deformation with minimal discrepancy (Karaca et al., 2024). In Karaca et al. (2024), elastic dislocation modeling (Figure 1.10) indicated that the observed deformation could be explained by slip on a single planar fault dipping to the northwest, extending to a depth of around 9.2 kilometers. Their model resulted in a slip magnitude of 0.35 meters, a moment magnitude of M_w 6.1, a strike of 264 degrees, a dip of 66 degrees, and a rake angle of minus 165 degrees, consistent with a right-lateral strike-slip fault within the upper crust.

Elastic dislocation modeling suggested that the observed deformation could be explained by slip on a single planar fault dipping to the northwest, extending to a depth of around 9.2 kilometers. The model estimated a slip magnitude of 0.35 meters and a moment magnitude of Mw 6.1. The seismic fault is estimated to have a strike of 264° with a slight southern deviation, a steep dip of 66°, and predominantly horizontal (strike-slip) movement with a rake of -165° (Karaca et al., 2024).

Moreover, the slip distribution, obtained through moment tensor modeling, highlights the fault displacement associated with the event, while seismic activity ranging from M_w 0.8 to 6.4 between 22 and 24 November 2022 provides spatial information to the rupture process. A map view of the study area shows earthquake epicenters recorded by KOERI and AFAD, distinguished by blue and yellow markers, respectively. Cross-sectional profiles perpendicular to main fault segments illustrate line-of-sight ground displacement relative to the topography, with elevation and displacement clearly differentiated (Figure 1.11). These comprehensive datasets form the foundation for understanding the seismic behavior and fault mechanics in the Gölyaka–Düzce region (Karaca et al., 2024).

The study concluded that the main rupture likely occurred on the Düzce segment, though the adjacent Karadere segment was also influenced by the event (Figure 1.12). This interpretation is supported by the DInSAR-derived deformation patterns and the distribution of foreshocks and aftershocks observed around the time of the mainshock. Moment tensor

solutions from various seismic networks also support a northward dipping fault plane that aligns with the geometry of the Düzce segment (Karaca et al., 2024).

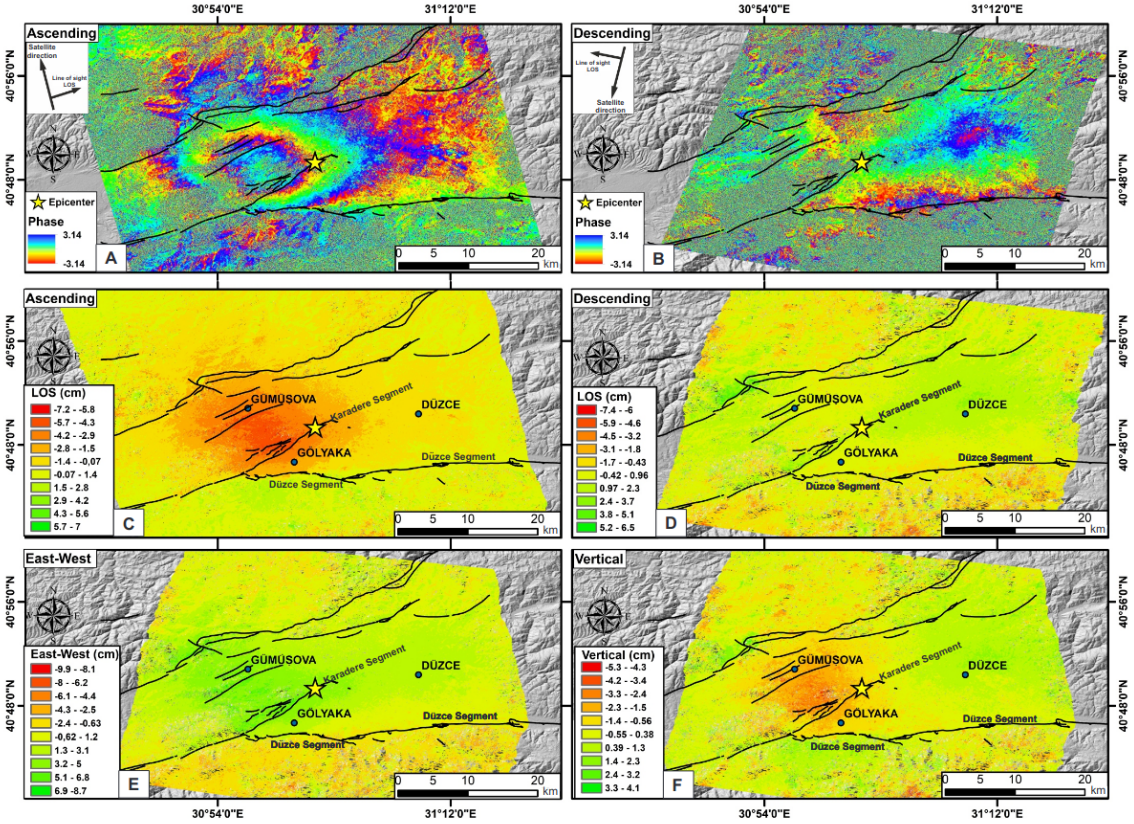


Figure 1.9. DInSAR analysis of the 23 November 2022 Gölyaka–Düzce earthquake using ascending and descending Sentinel-1A satellite data. Four Sentinel-1A SAR datasets, two pre-earthquake and two post-earthquakes, were used: ascending images from 15 November to 27 November 2022, and descending images from 14 November to 26 November 2022 (Karaca et al., 2024).

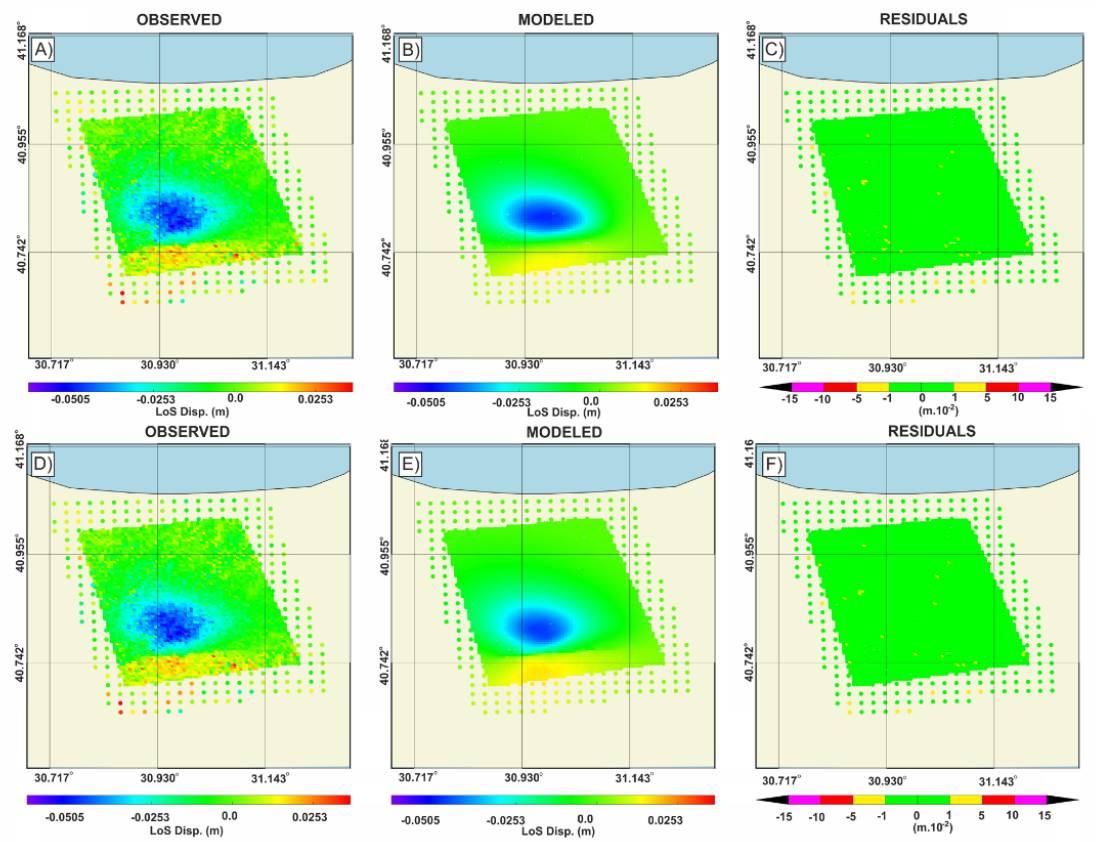


Figure 1.10. DInSAR analysis of the 23 November 2022 Gölyaka–Düzce earthquake using ascending and descending data. Four Sentinel-1A SAR datasets, two pre-earthquake and two post-earthquake, were used: ascending images from 15 November to 27 November 2022, and descending ones from 14 November to 26 November 2022. Active faults are shown as black lines (Emre et al., 2013; MTA) (Karaca et al., 2024).

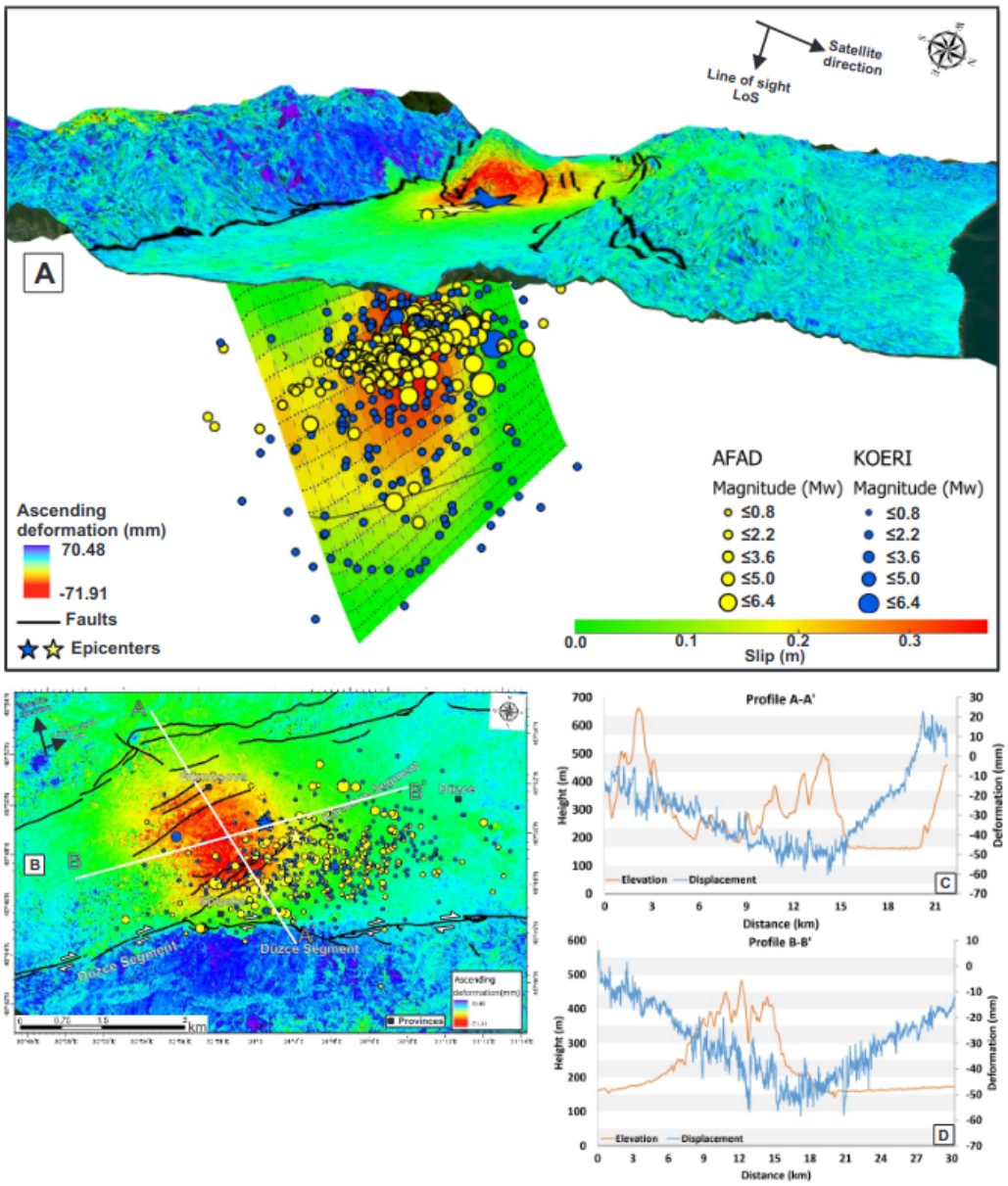


Figure 1.11. (A) Ascending data illustrating the 23 November 2022 earthquake in Düzce. The slip distribution from MT modeling is shown, along with aftershocks and foreshocks recorded in two days period. (B) Map view of the study area. Blue and yellow stars denote the epicenters reported by KOERI and AFAD. (C) and (D) Cross-sectional profiles A–A' and B–B' display line-LOS displacement (Karaca et al., 2024).

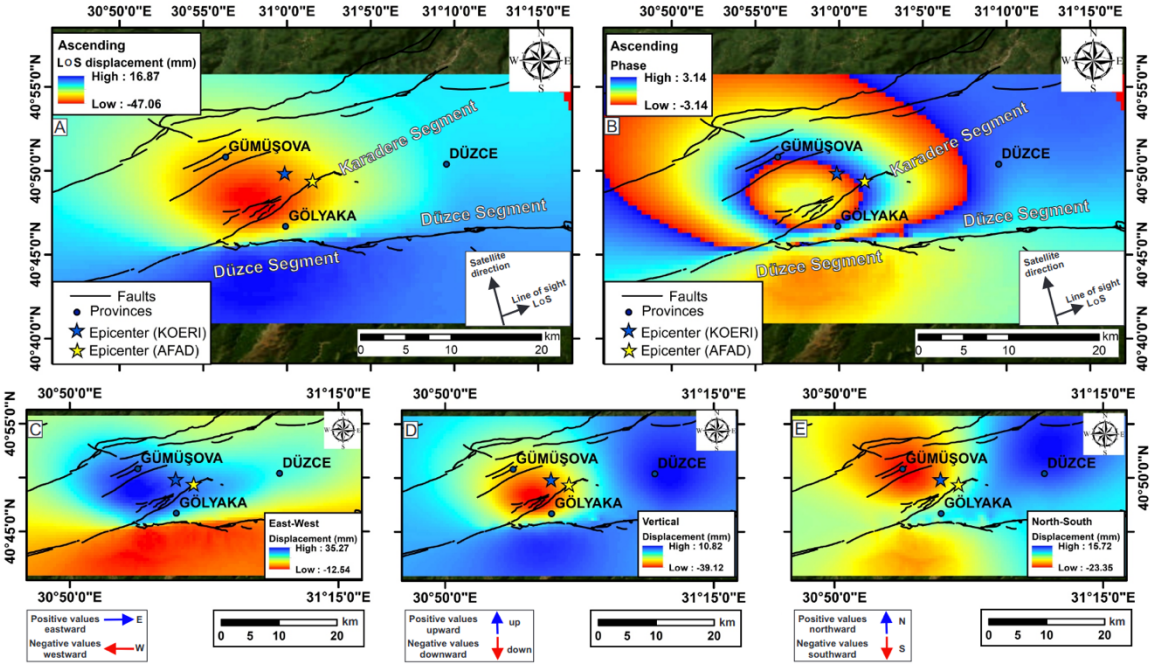


Figure 1.12. Forward modeling results showing displacements derived from the shear distribution obtained by linear inversion: (A) Modeled displacement data, (B) Corresponding unwrapped interferogram, (C) East–west displacement component, (D) Vertical displacement component, and (E) Displacement in the N–S direction. (Karaca et al., 2024).

2. SEISMIC DATA & METHODOLOGY

2.1. Dataset & Preprocessing

The data utilized in this study was obtained from 51 broadband seismometer under the operation of the KOERI and AFAD (Table A.1). Using the Java-based tool, CCT, which implements the empirical modelling of coda wave envelopes, we were able to establish the seismic source spectrum derived from coda waves to estimate the two main source parameters within the study region: M_w and σ_A.

This study analyzed 151 earthquakes, ranging from M_L 3.5 to 6.0, recorded by KOERI and AFAD stations, as depicted in Figure 2.1. The dataset primarily spans 2013 to 2022, with the addition of two 2024 earthquakes: the M_w 5.59 Tokat-Sulusaray mainshock and its M_w 4.56 foreshock. Within the dataset, 51 events with $M_L \geq 4.0$ were chosen for the empirical calibration. Among these, 39 events (32 for calibration and 7 for reference) were utilized to empirically determine seismic attenuation parameters, site terms, and source characteristics in and around the NAFZ, while the remaining 12 were set aside for validation. The remaining 99 smaller events (M_L 3.5 to < 4.0) had their magnitudes estimated using the established calibration results. Figure 2.1 illustrates the focal mechanisms of the reference and validation events, shown in black and white on the map, highlighting the region's predominant strike-slip faulting. Event depths, as reported by the KOERI catalogue and indicated by color-coding on the map, reveal that most earthquakes occurred between 1 and 15 km, with a few notable deeper events also observed.

High-sampling-rate broadband data, mostly at 100 Hz and occasionally at 50 Hz, from the horizontal components of each station contributed to generating averaged narrowband envelopes, with an example illustrated in Figure 2.2, specifically from COAL station across various frequency bands. To accurately characterize the noise level before event onset, instrument-corrected velocity waveforms in meters per second were analyzed. This analysis spanned a total duration of 1000 seconds, comprising 100 seconds prior to and 900 seconds following the origin time, consistent with the approach described by Shelly et al. (2022).

All waveforms were subjected to visual inspection to exclude low-quality data from the calibration process. Prior to this, instrument responses were removed from each raw seismogram to convert the data to units of meters per second (m s^{-1}) using SAC2000 software (Goldstein et al., 2003). Following preprocessing, horizontally stacked coda envelopes were generated utilizing the envelope function within the CCT (Barno, 2017), which employs a Hilbert transform. For each event and station, twelve narrowband envelopes were created, spanning frequencies from 0.05 to 8 Hz (Table 2.1). The envelopes were computed individually for each horizontal component. To enhance robustness in subsequent analysis, the $\log_{10}$ values of these two components were averaged and smoothed for each frequency band. The selection of these frequency bands was not arbitrary; rather, it stemmed from several early studies aimed at optimizing source spectra estimation, particularly for frequencies associated with high-frequency spectral fall-off, and ultimately based on a process of trial and error (e.g., Mayeda et al., 2007). These bands also represent the standard employed by the U.S. National Data Center's operational system, thoroughly validated over the past 20 years. The resultant narrowband coda envelopes then served as the input dataset for the calibration process.

At first, coda window lengths for various frequency bands were automatically selected and then adjusted through visual inspection of the signal envelopes. This parameter is essential for accurate calibration: shorter windows can introduce amplitude variations comparable to those in direct waves, while longer windows contribute to greater stability in the measurements (Morasca et al., 2022; Al-Kaabi et al., 2024).

To obtain stable source spectra, we used CCT, an open-source Java tool developed by Barno (2017), which builds on the methodology of Mayeda et al. (2003). CCT (Mayeda et al., 2007) calibrates high-frequency site terms by referencing both independently derived moment magnitudes and GT apparent stress estimates. This method removes the need for prior assumptions about regional source scaling and effectively separates source and site term dependencies. In this study, we modeled two events. First, we determined their moment magnitudes through independent moment tensor inversion. Then, we estimated their apparent stress, which served as a reference for calibration.

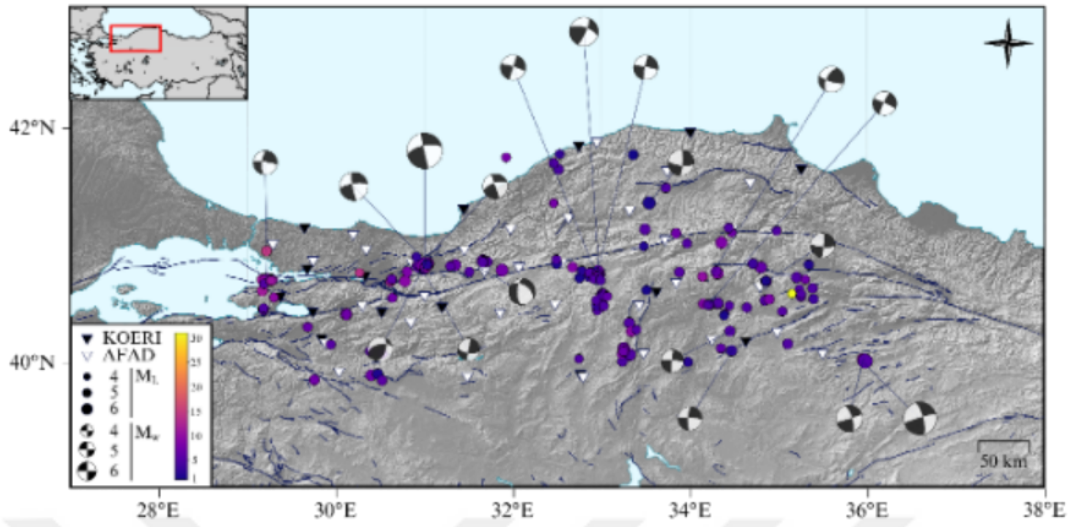


Figure 2.1. This map displays 151 analyzed earthquakes (Mw 3.5-6.0) from 2013-2022, including the 2024 Tokat mainshock and foreshock, recorded by KOERI and AFAD stations.

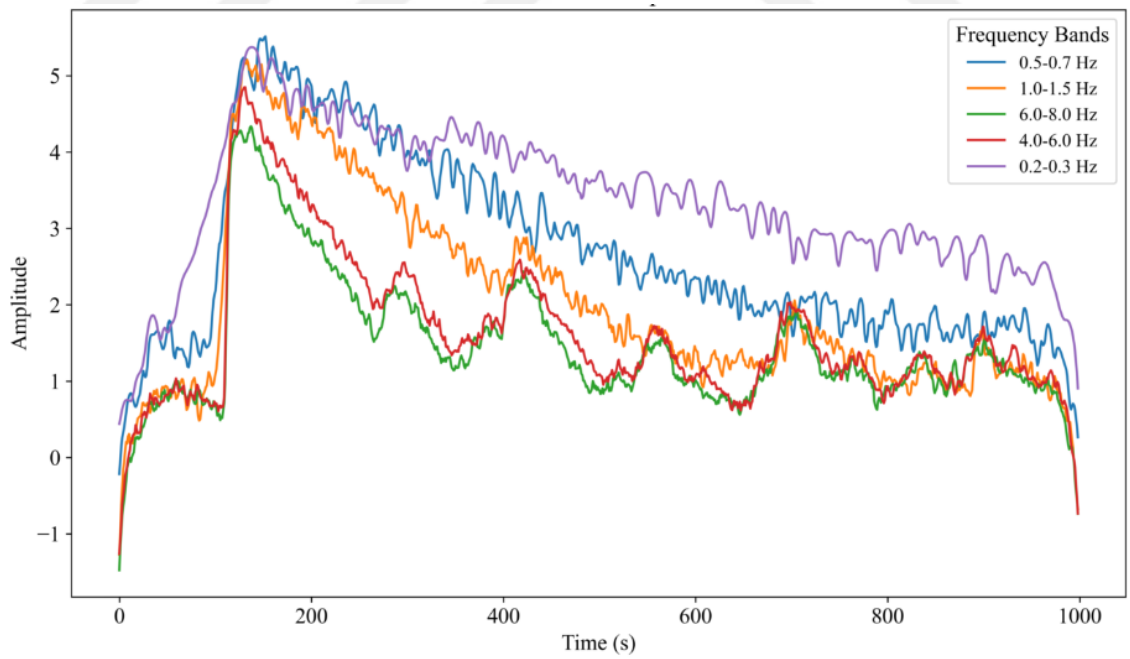


Figure 2.2. Example stacked narrowband envelopes between 0.05-8 Hz for the 2024 Tokat-Sulusaray mainshock recorded at COAL station.

Table 2.1. Frequency bands used for coda calibration, along with the corresponding minimum window lengths required for valid data selection.

Band Number	Minimum (Hz)	Maximum (Hz)	Minimum Window Length (s)
1	0.05	0.1	400
2	0.1	0.2	200
3	0.2	0.3	160
4	0.3	0.5	150
5	0.5	0.7	110
6	0.7	1	80
7	1	1.5	60
8	1.5	2	50
9	2	3	50
10	3	4	40
11	4	6	40
12	6	8	10

2.2. An Overview of the Methodology

2.2.1. Introduction

A key benefit of using coda waves for calibration is that it requires a minimal number of earthquakes and seismic stations. This is because coda waves are composed of scattered seismic energy that effectively averages out variations caused by heterogeneity of the path, seismic radiation patterns, and rupture directivity effects (Aki, 1969; Aki & Chouet, 1975). As a result, amplitude measurements from a single station using coda waves can produce results comparable to those obtained from a full network average based on direct waveforms (Mayeda & Walter, 1996).

The coda calibration technique, first introduced by Mayeda and Walter (1996) and later improved by Mayeda et al. (2003), was developed to account for regional wave propagation and local site effects in coda analysis. Its primary objective is to derive stable

and reliable source spectra across a wide range of magnitudes and epicentral distances. While the method is applicable even with a relatively limited dataset, its effectiveness largely depends on having access to high-fidelity seismic data from events with a moment magnitude of 4.5 or greater, occurring at distances on both local and regional scales.

In many calibration studies, large-magnitude events ($M_w \geq 6.0$) are often excluded. This is because their complex source processes tend to dominate the recorded waveforms, making it difficult to isolate path and site effects (Mayeda et al., 2003). In addition, such events often lead to non-linear site responses and, due to their sparse and uneven distribution, are generally unsuitable for achieving consistent regional calibration. Despite these limitations, the study includes several high-quality large events, notably the 2022 Düzce–Gölkaya sequence and the 2024 Tokat–Sulusaray mainshock with its foreshock. These events were chosen for their exceptional data quality and are used selectively, either as validation cases or as reference events within the broader calibration framework.

The following workflow was applied after selecting a calibration dataset that included 51 seismic events with magnitudes of 4.0 or higher than 4.0. These events were located at distances ranging from approximately 13 to 580 kilometers within and around the NAFZ. For this dataset, horizontally averaged coda wave envelopes were constructed across 12 narrow frequency ranges, spanning 0.05 to 8.0 Hz. The data were collected from 51 stations that spanned both local and regional distances. To evaluate the reliability of the final calibration, an independent validation dataset from the same region was also used. This validation set included events that were both smaller and larger in magnitude compared to those in the calibration dataset.

In the following, we outline the fundamental concepts and procedural steps involved in the calibration workflow applied to the NAFZ data set. A detailed overview of the calibration methodology is represented in the flowchart in Figure 2.3.

The average horizontal envelopes are matched with a synthetic model of direct-wave peak decay, enabling calibration with sparse regional networks. At each frequency f, the theoretical envelope $A(f,t,r)$ is computed based on this model:

$$A_c(f,t,r) = W_0(f) \times S(f) \times T(f) \times P(r,f) \times H(t-t_s) \times (t-t_s)^{-\gamma(f,r)} \exp\left[-b(f,r) \times (t-t_s)\right] \quad (2.1)$$

In equation (2.1), t_s is derived from the ratio of epicentral distance r to the peak velocity $v(f,r)$, where t is the elapse time relative to the event origin (in seconds), r is the distance to the earthquake epicenter (in kilometers), and f is the central frequency (in Hz). The synthetic envelope includes several components: $W_0(f)$ represents the S-wave amplitude; $S(f)$ and $T(f)$ account for site effects and the scattering-based transfer from S-waves to coda waves, respectively. $P(r,f)$ models 1-D attenuation and geometrical spreading. The Heaviside step function H defines the onset of the signal, while $b(r,f)$ and $\gamma(r,f)$ shape the coda envelope for each frequency band.

The CCT uses observed envelopes combined with a basic short-term average/long-term average method to auto-detect the highest amplitude of direct S-waves or surface waves, helping to estimate the beginning of coda decay. After detecting these phases, a visual quality control step is applied to prevent false detections caused by low signal-to-noise ratios (Barno, 2017).

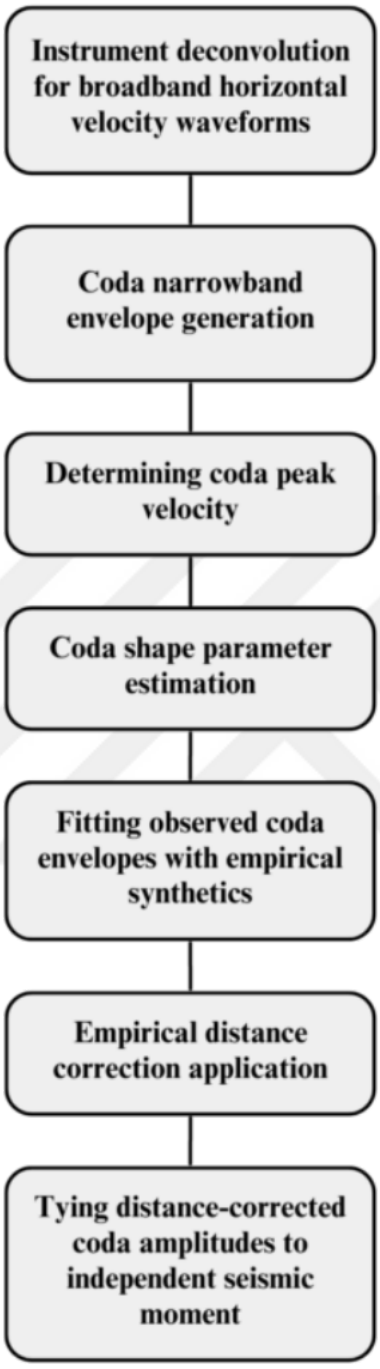


Figure 2.3. Coda calibration methodology presented as a top-down flowchart.

2.2.2. Estimation of Peak Velocity and Envelope Shape Parameters

Following a thorough inspection of the envelopes and considering that each region typically displays a distinct pattern of coda-envelope decay as noted by Sato and Fehler in

1998, the preliminary process in the calibration is to estimate the empirical parameters $v(r,f)$, $b(r,f)$, and $\gamma(r,f)$. Here, b and γ define the shape of the envelope decay using best-fit averaged model curves, while v is a path-dependent velocity term used to approximate the arrival times of direct S-waves, surface waves, and regional L_g waves corresponding to the envelope's peak amplitude.

These are simple hyperbolic functions that vary with distance and can be used to compute synthetic envelopes after the calibration process, as described by Mayeda and colleagues in 2003. Figure 2.4 indicates an example for two frequency bands, 0.7 to 1 hertz and 3 to 4 hertz, showing the velocity hyperbola along with the shape parameters b and γ, using the averaged model curves that provide the best fit. After a detailed review of the envelopes, stable empirical relationships for these parameters can be determined, as illustrated in Figure 2.4. At distances around 580 kilometers, the observed envelope shape parameters closely match the simple hyperbolic model. This result is consistent with the method's broad global application originally introduced by Mayeda and colleagues in 2003.

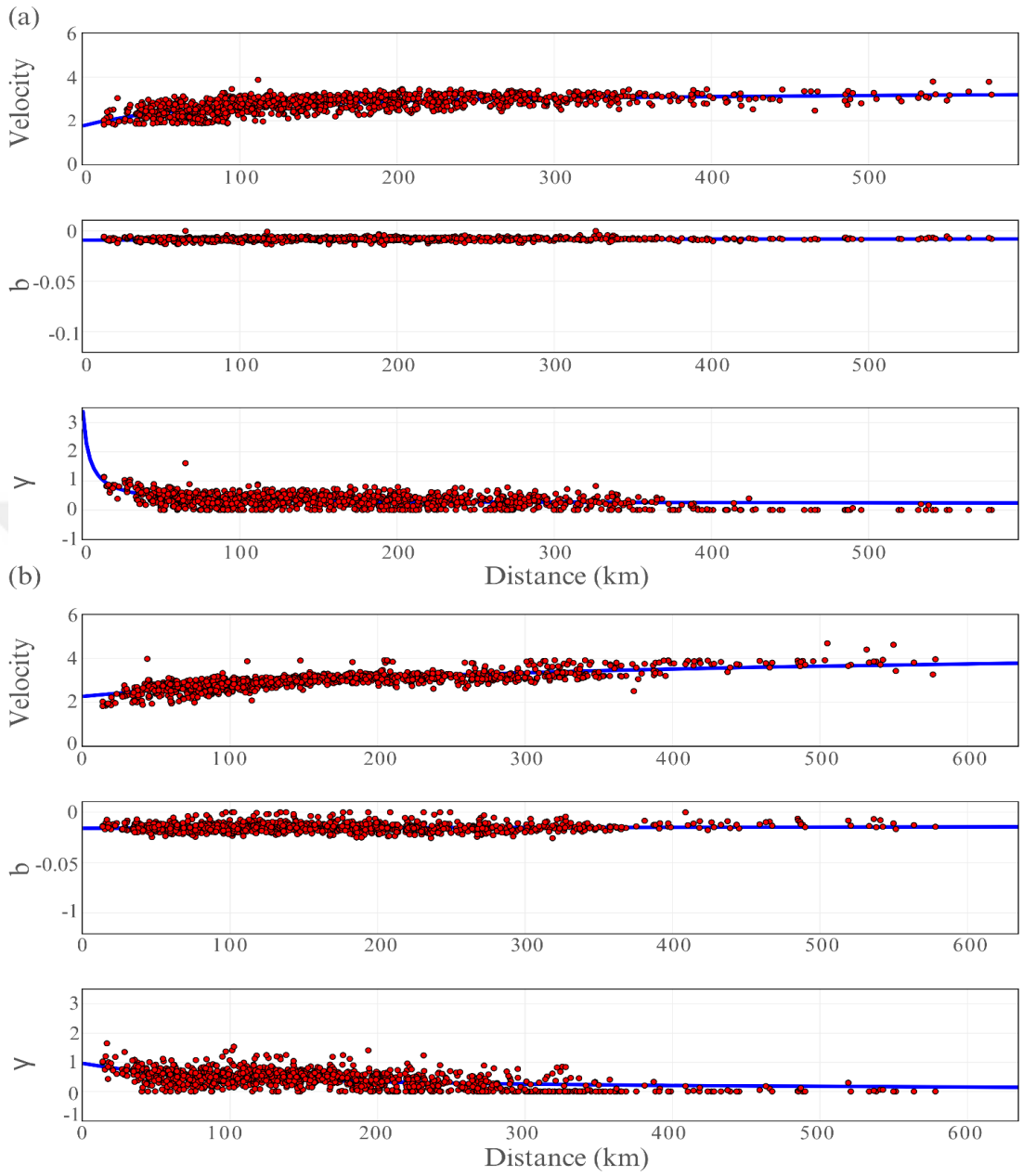


Figure 2.4. Measurements of peak velocity *v*, *b,* and *γ* as functions of epicentral distance for two frequency bands: (a) 0.7 to 1 Hz and (b) 3 to 4 Hz. In both panels, the hyperbolic velocity curve and the corresponding parameters are shown along with the averaged model curves that most accurately represent the data in blue, based on equation (2.1). Red circles indicate individual envelope measurements for each frequency band.

Once calibrated, these functions allow for the empirical creation of synthetic envelopes (Figure 2.5), which are then compared with observed envelopes to assess coda amplitudes

over both local and regional distances within a consistent calibration framework (Mayeda et al., 2003). Initially, synthetic envelopes are produced for each frequency and distance using equation (2.1), with the source, path, site, and instrument response effects set to unit values.

2.2.3. Raw Amplitude Measurements and Empirical Distance Correction

For each event-station pair, coda amplitudes are calculated across a range of frequency bands by applying a constant DC offset to the synthetic envelope. This envelope is generated based on the specific source-to-station distance and is adjusted to closely match the observed envelope using the L1 norm. At this stage, the amplitudes are still without units because corrections for site and path corrections have not yet been applied.

Even though an initial selection of recordings is performed as previously described, an additional quality control step is applied to eliminate low-quality envelopes that could introduce bias into the calibration process. This step involves evaluating amplitude measurements at specific frequencies and discarding those that do not meet established criteria, such as a minimum signal-to-noise ratio and an adequate coda window length. This is a fundamental step, as the reliability of amplitude estimates is highly dependent on the selected window length, which is itself strongly influenced by the signal-to-noise ratio (Mayeda et al., 2003).

Figure 2.5 displays the synthetic envelope in green overlaid on the observed envelope in blue between the 0.7 and 1 Hz frequency range, for stations at varying distances from the source. This figure also serves as a tool for quality control, allowing adjustments by modifying the measurement end time, which is marked by a vertical red line (Barno, 2017). Amplitude measurements are taken only within the minimum and maximum time windows defined in the calibration JSON (JavaScript Object Notation) file.

For each seismic event, the CCT automatically performs the initial coda amplitude measurements, with an example illustrated in Figure 2.6. It is important to highlight that the y-axis represents dimensionless values, as the amplitudes have not yet been corrected for one-dimensional path effects, site effects, or instrument transfer functions, as outlined in Equation 2.1.

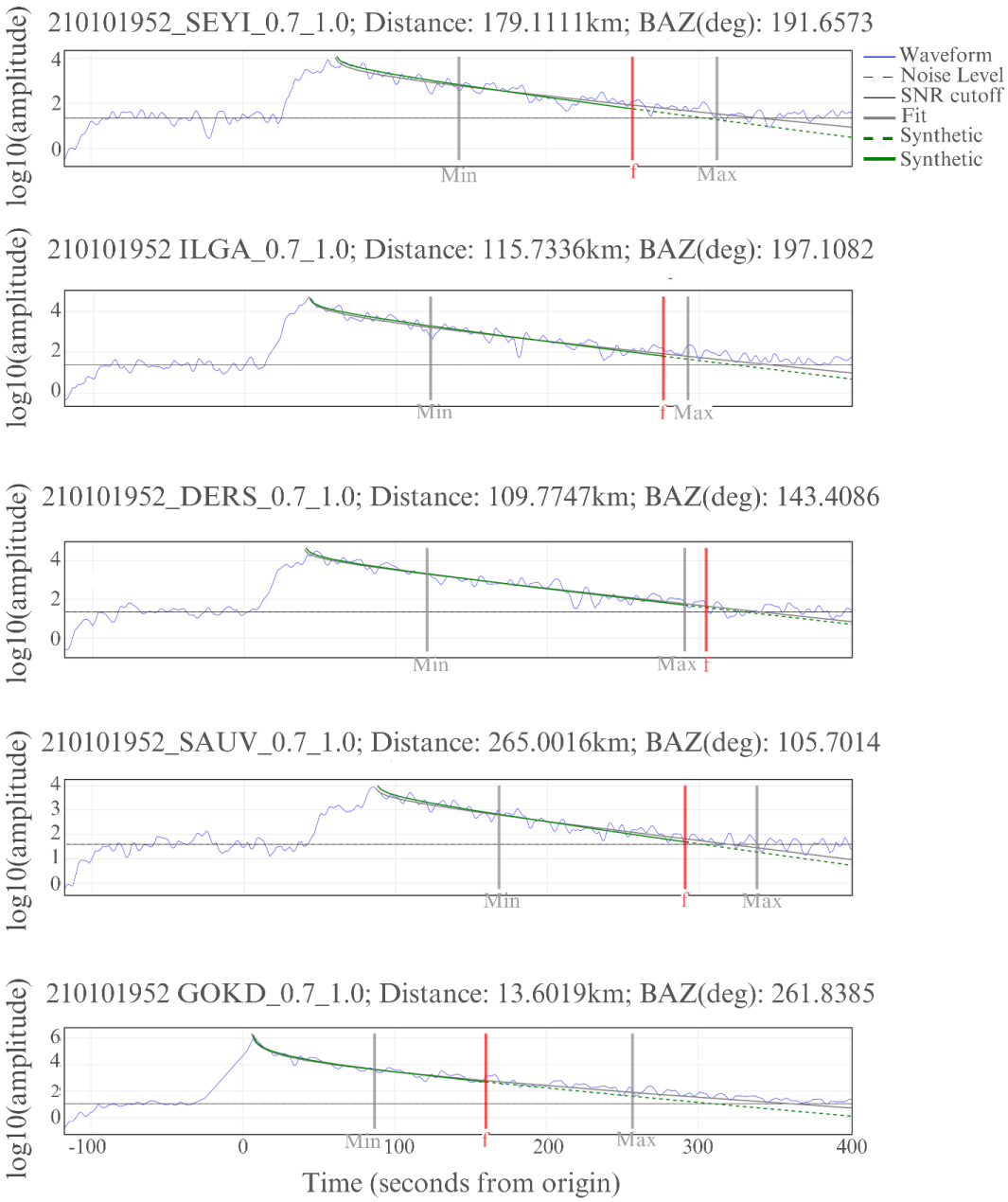


Figure 2.5. Example coda envelope measurements in the 0.7 to 1 Hz frequency range, where the synthetic envelope (green) is superimposed on the observed $\log_{10}$ velocity envelope in nanometer-seconds (blue) for stations positioned at varying distances from the seismic source. Manual refinement is possible by adjusting the measurement end time, marked by the vertical red f-indicator.

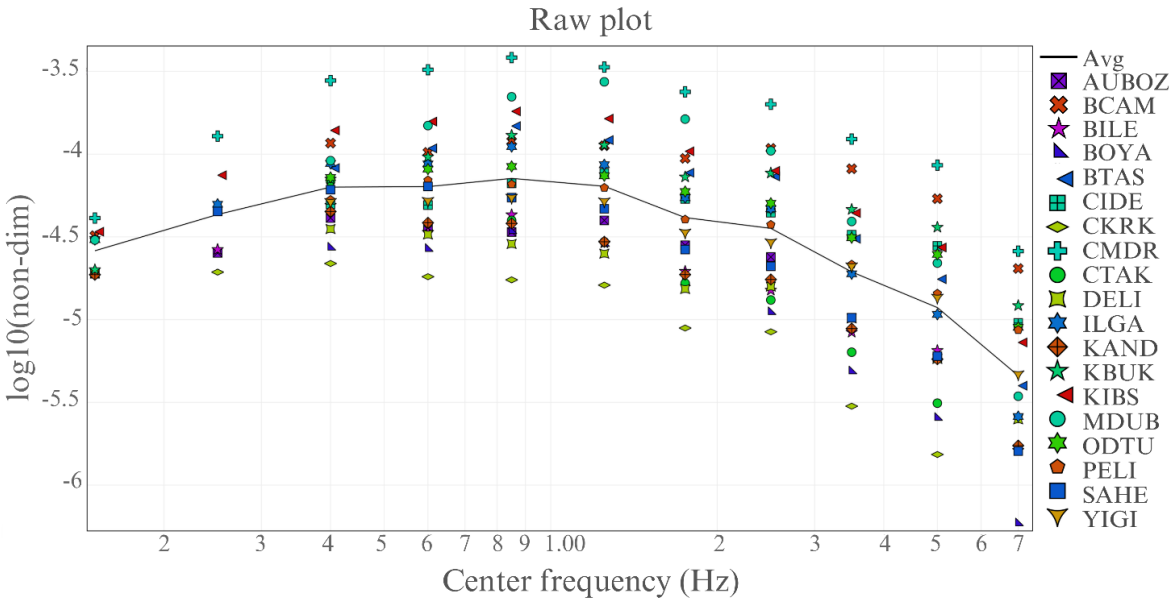


Figure 2.6. Example of raw, non-dimensional $\log_{10}$ coda amplitude measurements for a single event recorded at various stations across local and regional distances. Each individual frequency is subsequently used in a one-dimensional path inversion that incorporates amplitude data from all calibration events, including the one shown here.

Contrary to direct seismic waves, which attenuate quickly with traveled path owing to geometric spreading and energy dissipation, coda waves within local distances tend to remain relatively uniform with respect to the origin time and decay more gradually as distance increases (Aki, 1969). However, studies have also shown that coda waves can experience attenuation (Singh and Herrmann, 1983). To address this, the path calibration process focuses on empirically modeling these effects by determining parameters that reduce variability across stations for the same events. The purpose of path corrections is to reproduce the observed behavior of local and near-regional coda waves, thereby improving the accuracy of source parameter estimates.

Based on the one-dimensional path model originally introduced by Mayeda et al. (2003) and later refined by Phillips et al. (2008), we performed an inversion to determine the optimal radially symmetric 1D path correction terms for each frequency band. Figure 2.7 presents an example for the 0.7–1 Hz and 3–4 Hz bands, where the standard deviation of coda amplitudes between stations (y-axis) is plotted against interstation distance (x-axis),

comparing uncorrected (red squares) and corrected (blue circles) values. The upper panels in both (a) and (b) display amplitude measurements from common events recorded at stations BOLU and COAL, which are approximately 286 kilometers apart. Any visible DC offset is attributed to differences in relative site response and will be corrected in later steps using ground-truth reference spectra. The lower panels illustrate how standard deviation improves as a function of interstation distance (in kilometers) for all station pairs with at least five shared events. After applying the correction, the standard deviation dropped significantly from 0.33 to 0.17 in the 0.7–1 Hz band and from 0.48 to 0.19 in the 3–4 Hz band. This indicates a substantial improvement over the higher variability seen in the raw data. The corrected amplitudes show reduced scatter, with average standard deviations ranging from 0.12 to 0.24 across all frequency bands and station pairs. Notably, for this station pair, separated by approximately 286 kilometers (top lines in Figures 2.7a and 2.7b), demonstrates that the 1D path correction remains effective even in complex regional settings, as evidenced by the much lower standard deviation (less than 0.17) in the corrected amplitudes.

The final step in this process involves linking the path-corrected dimensionless amplitudes to independent source parameters, facilitating the S-to-coda transfer function and site effect corrections. For further details on this coda calibration technique, readers are referred to Mayeda et al. (2003), with additional illustration provided in Figure 2.3. Building on this methodology, the subsequent section will focus on source and site terms to demonstrate the effectiveness of this approach in and around the NAFZ.

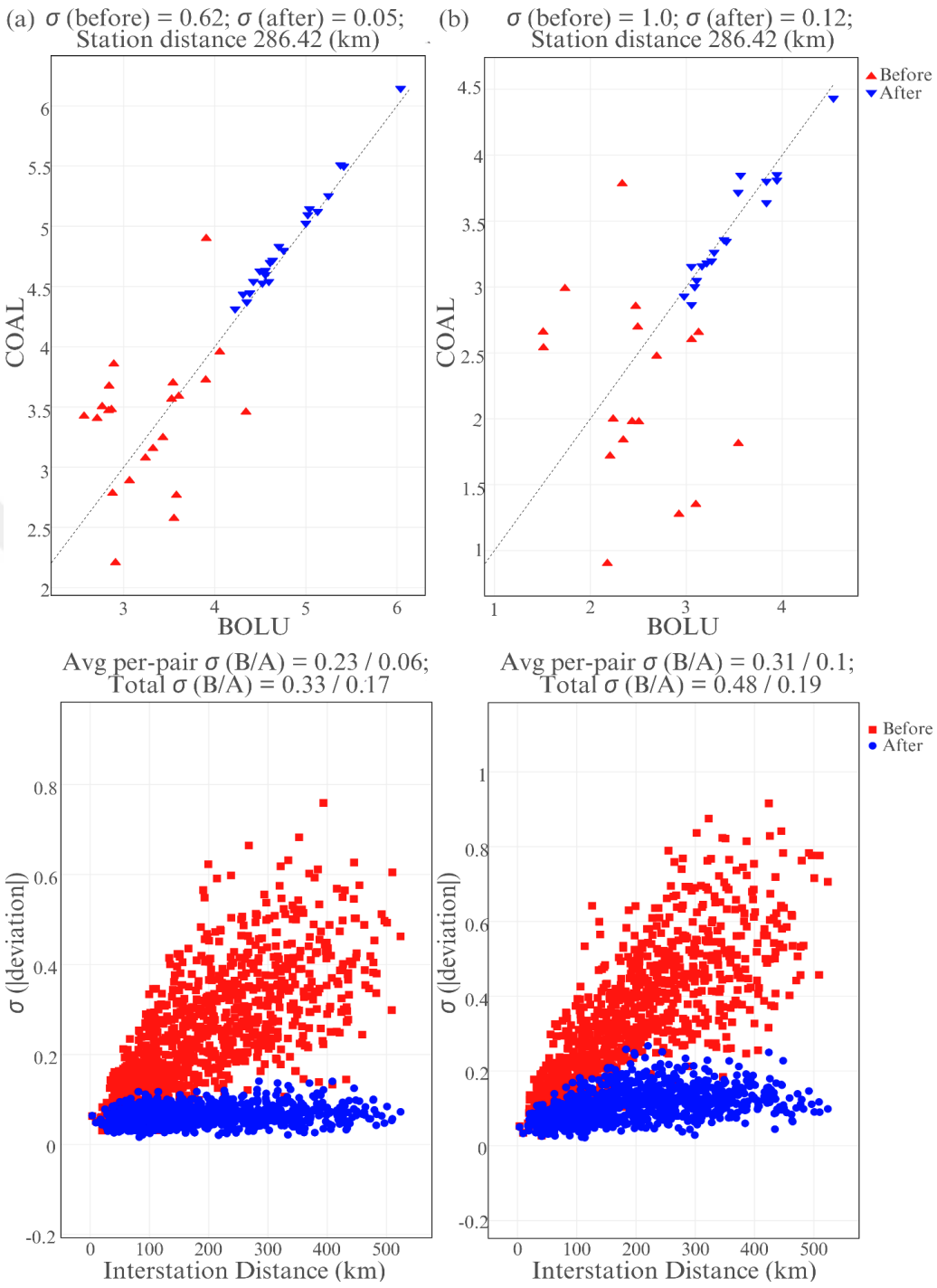


Figure 2.7. Path correction examples for the (a) 0.7–1 Hz (left) and (b) 3–4 Hz (right) frequency bands. The upper panels in both (a) and (b) display amplitude measurements from common events recorded at stations BOLU and COAL, which are approximately 286 kilometers apart. Red symbols represent uncorrected values, while blue symbols show the corrected amplitudes.

2.2.4. Coda Spectral Ratio

The coda calibration method (Mayeda & Walter, 1996; Mayeda et al., 2003) is a seismological technique that uses the independent moment magnitude of earthquakes as a reference to determine the absolute size of other seismic events. This is done by first analyzing the coda waves of an earthquake and correcting their amplitude for the distance to the recording station. The method then calibrates these relative, dimensionless amplitude measurements against the known M_w to convert them to an absolute energy scale, typically expressed in Newton-meters (N-m). The corrections are frequency-dependent, which means they are adjusted for different frequencies within the seismic spectrum to account for variations in how a station's specific geological location influences the recorded signal. This process effectively normalizes seismic recordings, allowing for consistent and stable earthquake size estimates.

Building on this, the coda spectral ratio technique (Mayeda et al., 2007) provides a stable apparent stress, which we utilize as a GT reference for constraining high-frequency site terms. In this comprehensive coda calibration procedure, both independent M_w's and σ_A's are essential for calibrating the seismic data. The independent M_w values are used to correct for long-period site effects, the influence of a specific location on low-frequency seismic waves. At the same time, coda spectral ratios from reference earthquakes provide the necessary apparent stress to correct for high-frequency site effects. This process transforms the relative, dimensionless coda amplitudes (which have already been corrected for distance) into an absolute scale, measured in N-m. Ultimately, ground truth (GT) events, which are earthquakes with reliably known properties like M_w, corner frequency (f_c), and σ_A, are vital for determining the corrections needed to convert the raw seismic recordings into a true representation of the earthquake's source energy.

This process requires independent estimates of apparent stress, which can be derived using a variety of methods. These include finite fault inversion (e.g., Taira et al., 2014), spectral ratio techniques, time-domain deconvolution (Hough, 1997), and more recent methods that utilize coda spectral ratio (Mayeda et al., 2007).

Prior knowledge of the seismic source, obtained through long-period waveform modeling, is essential for the CCT calibration process, as it helps constrain site and instrument response terms, especially for periods longer than five seconds. Because of the differences observed between the moment tensor solutions provided by KOERI and AFAD, which result from the use of different one-dimensional velocity models during inversion, we chose to compute our own moment tensors for nineteen selected events. Figure 2.8 presents an example of an independently determined moment magnitude, modeled using the MTINV software toolkit. This toolkit is a reliable resource for regional moment tensor inversion, as described by Ichinose and colleagues in 2003. Seven of these events were used as reference sources in the calibration, while the remaining twelve were used for validation purposes, as shown in Table B.1. The moment magnitudes of the other ninety-nine smaller events, with local magnitudes between 3.5 and 4.0, were then estimated using the results of this calibration. We exclusively utilized M_w solutions derived from MTINV software (Ichinose et al., 2003), comparing them with solutions from AFAD and KOERI. To avoid introducing bias due to differing crustal models and methodologies, we relied solely on the MTINV solutions throughout this process.

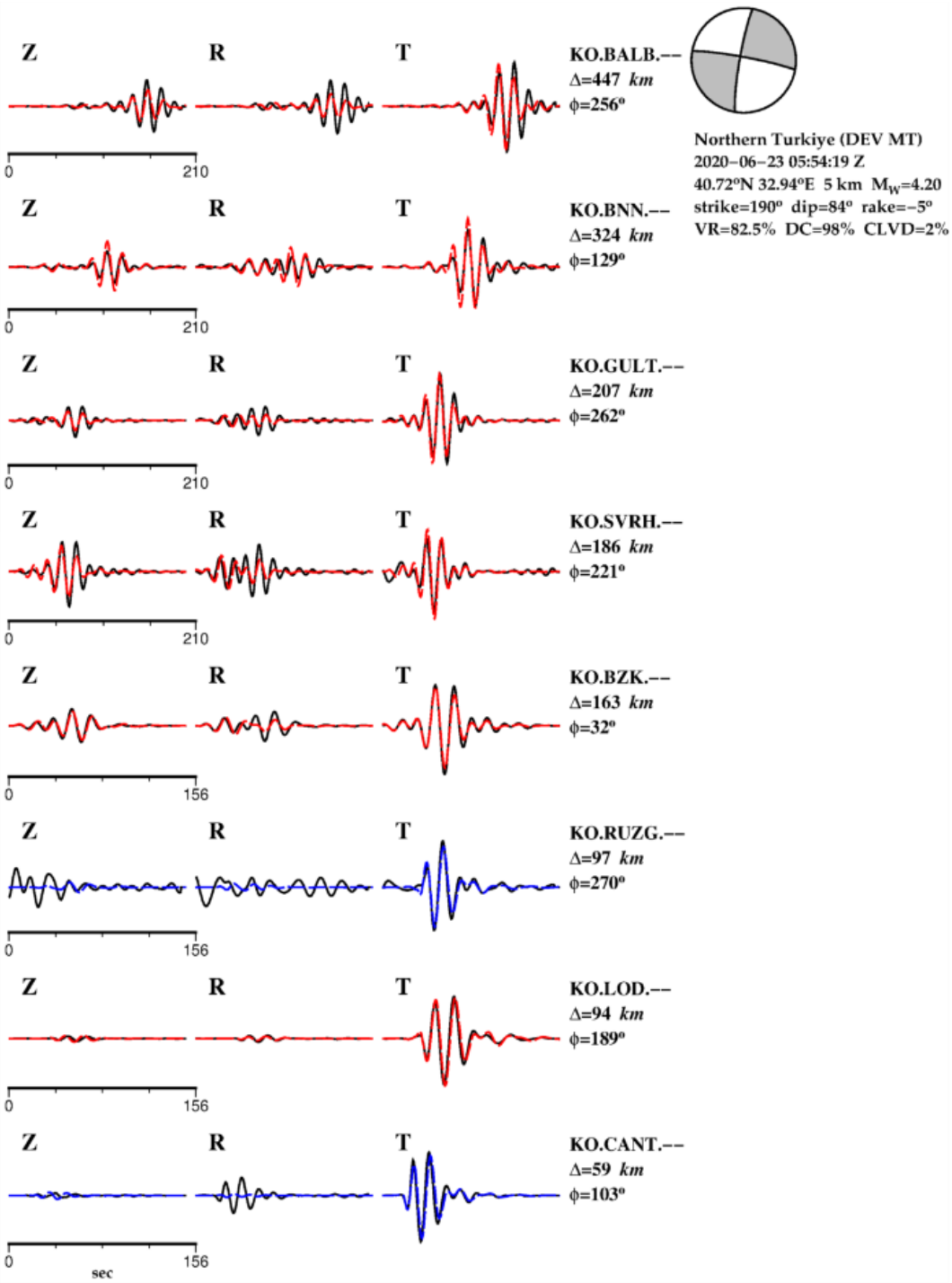


Figure 2.8. An example event showing the estimation of moment magnitude using regional moment tensor inversion. The observed waveforms are displayed in black, synthetic seismograms used in the inversion are shown in red, and synthetic predictions not included in the inversion are represented in blue.

By using multiple reference events, it is possible to derive stable and averaged site correction terms. For small earthquakes with moment magnitudes below 4.0, which cannot be accurately modeled through waveform analysis, moment estimates can be obtained from low-frequency data, typically below a few hertz, extracted from coda moment-rate spectra. In the case of very small events with magnitudes less than or equal to 2.5, the source spectra are generally assumed to be flat up to 8 Hz. These small events serve as empirically derived Green's functions (EGF), helping to extend the reliability of coda-based source spectra to lower magnitudes (e.g., Mayeda and Walter, 1996). This method, along with its regional applications, is thoroughly described by Mayeda et al. (2003).

This study introduces a refined approach for constraining high-frequency site terms by using a limited number of ground-truth reference moment-rate source spectra. These spectra are based on independently estimated apparent stress values, obtained from the spectral ratio technique originally described by Mayeda and colleagues in 2007. This method has since been applied to various regions, including Central Italy and California (Morasca et al., 2022; Mayeda et al., 2024). By using independently derived values of apparent stress and seismic moment from a selected group of reference events, we are able to estimate both the site effects and the S-to-coda transfer parameters across all frequencies for each station. This approach eliminates the assumption of the regional source scaling relationship or assignment of stress drop values to smaller events used as EGF, which can result in significant bias (as noted by Baltay et al., 2010; Baltay et al., 2011).

Corresponding Brune (1970) spectral shapes of the selected events identified by well-constrained σ_A and moment tensor solutions, as indicated in Figure 2.9, were utilized to determine the average frequency-dependent site effects and S-to-coda transfer function components, *S(f)* and *T(f),* in Equation (2.1). A hybrid usage of the reference σ_A events and the reference M_w's facilitated estimation of the average high- and long-frequency site terms, respectively, as this enabled a broadband correction valid between 0.05 and 8.0 Hz. Following Mayeda et al. (2007), we computed the σ_A using the coda spectral ratio approach. This yields accurate averaged σ_A estimates that remove common path and site effects.

Between two closely spaced events, 1 and 2, the moment-rate spectral ratio is expressed as:

$$\frac{\dot{M}_1}{\dot{M}_2} = \frac{M_{0_1}\left[1+\left(\frac{\omega}{\omega_{c_2}}\right)^2\right]^{\frac{p}{2}}}{M_{0_2}\left[1+\left(\frac{\omega}{\omega_{c_1}}\right)^2\right]^{\frac{p}{2}}} \quad (2.2)$$

M_{0i} shows the seismic moment of the event i, while p is the rate of exponential decay in the high-frequency range, a value set to 2 by the omega-square model, though the requirement for a finite energy integral dictates that p must be greater than or equal to 1.5.

Figure 2.9 illustrates the spectral ratio calculation using the Tokat mainshock (April 18, 2024, 15:11:23 UTC, M_w 5.59) and a nearby foreshock (April 17, 2024, 22:06:59 UTC, M_w 4.56). This pair, occurring approximately 3.5 km apart and recorded by 33 regional stations, is critical for the spectral ratio method as their proximity ensures that the site and path effects are essentially identical for both events, allowing them to be effectively removed in the ratio. Consequently, we achieve relatively constant source amplitude ratios, independent of azimuth and distance, since the paths and stations are common, and the coda inherently averages across source effects and the source time function.

In the next step, we model the observed source spectral ratio by performing an inversion that identifies the best-fitting Brune (1970) omega-square model. This is achieved by varying the f_c's of the two events to find the optimal match, as illustrated in Figure 2.9c. During this process, we incorporate independent moment (M_0) estimates obtained through regional moment tensor inversion using the MTINV software tool (Ichinose et al., 2003), as shown in Table A.2. These estimates help constrain the low-frequency portion of the amplitude ratio, which is essential because it is well known that solving for both relative moments and corner frequencies simultaneously in spectral ratio fitting can lead to trade-offs (e.g., Mayeda et al., 2024).

An underlying assumption in our grid search for estimating source parameters is that the network-averaged long-period coda amplitude ratio defines the low-frequency asymptote. This must align with scalar moment ratios derived from independent estimates (Walter et al., 2017). To refine the scalar moment magnitude (M_w) values, we used long-period coda spectral ratios to make slight adjustments to the independent moment tensor inversion results. Specifically, the M_w values were adjusted from 5.59 to 5.56 for the

mainshock and from 4.56 to 4.59 for the foreshock. These adjustments were applied symmetrically between the two events and helped minimize the mean absolute deviation (MAD) in the grid search. This approach accounts for minor differences caused by variations in station distribution and the frequency bands used in the two methods.

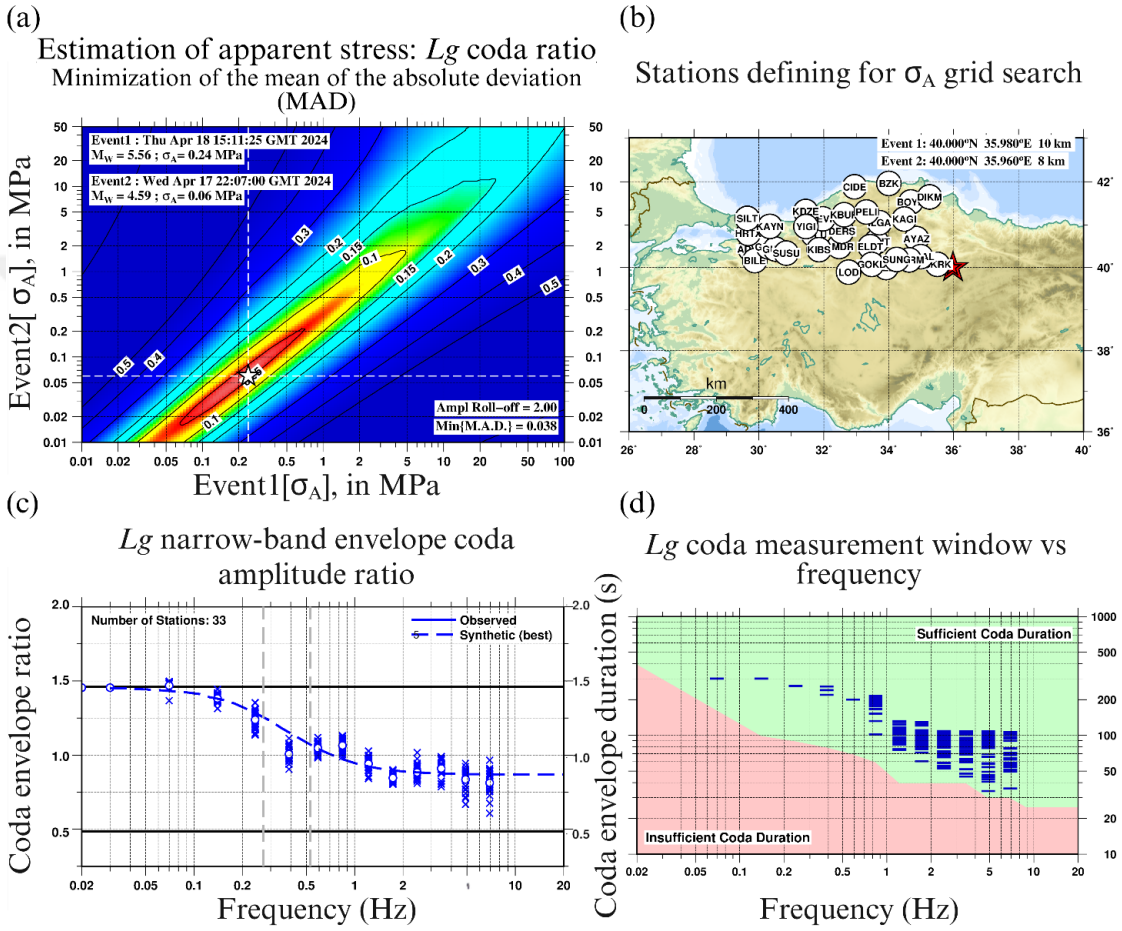


Figure 2.9. The spectral ratio technique (Mayeda et al, 2007) implemented to the M_w 5.59 Tokat mainshock and its M_w 4.56 foreshock. (a) MAD minimization for accurate σ_A estimates. (b) The event pair's location and stations. (c) Amplitude ratios from 33 regional stations, modeled with the Brune (1970) spectral shape. (d) The empirically determined minimum window lengths.

We next calculate the average correction terms for each station by referencing the modeled source spectra, which correspond to apparent stress values of 0.24 MPa for the mainshock and 0.06 MPa for the foreshock. Independent moment magnitude (M_w) estimates

from other events are used as broadband constraints, helping to eliminate potential biases in high-frequency amplitudes (above 2 Hz) by avoiding assumptions about regional source scaling. For site correction, we analyzed 51 events with $M_w \geq 4.0$, including M_w 6.06 Sarıdere-Gölyaka (Düzce) earthquake occurred on November 23, 2022 and its two largest aftershocks (M_w 4.28 and M_w 3.75), as well as the 18 April 2024 M_w 5.59 Tokat-Sulusaray event and its M_w 4.56 foreshock. These calibration events, combined with long-period and high-frequency source constraints, enabled the estimation of site correction factors for each station. Because seismic waves can be amplified or dampened by soft sediments depending on frequency, these corrections are essential for accurately separating source characteristics from observed waveforms. As shown in Figure 2.10, panel (a) provides an example of relative site amplification using station KDZE which is located on rock in Karabük taken as the reference. Panel (b) illustrates the combined correction terms for both site effects and S-to-coda energy transmission, which are applied to the distance-corrected logarithmic coda amplitudes. These corrections allow the amplitudes to be converted into source moment-rate spectra expressed in Newton-meters (Figure 2.11).

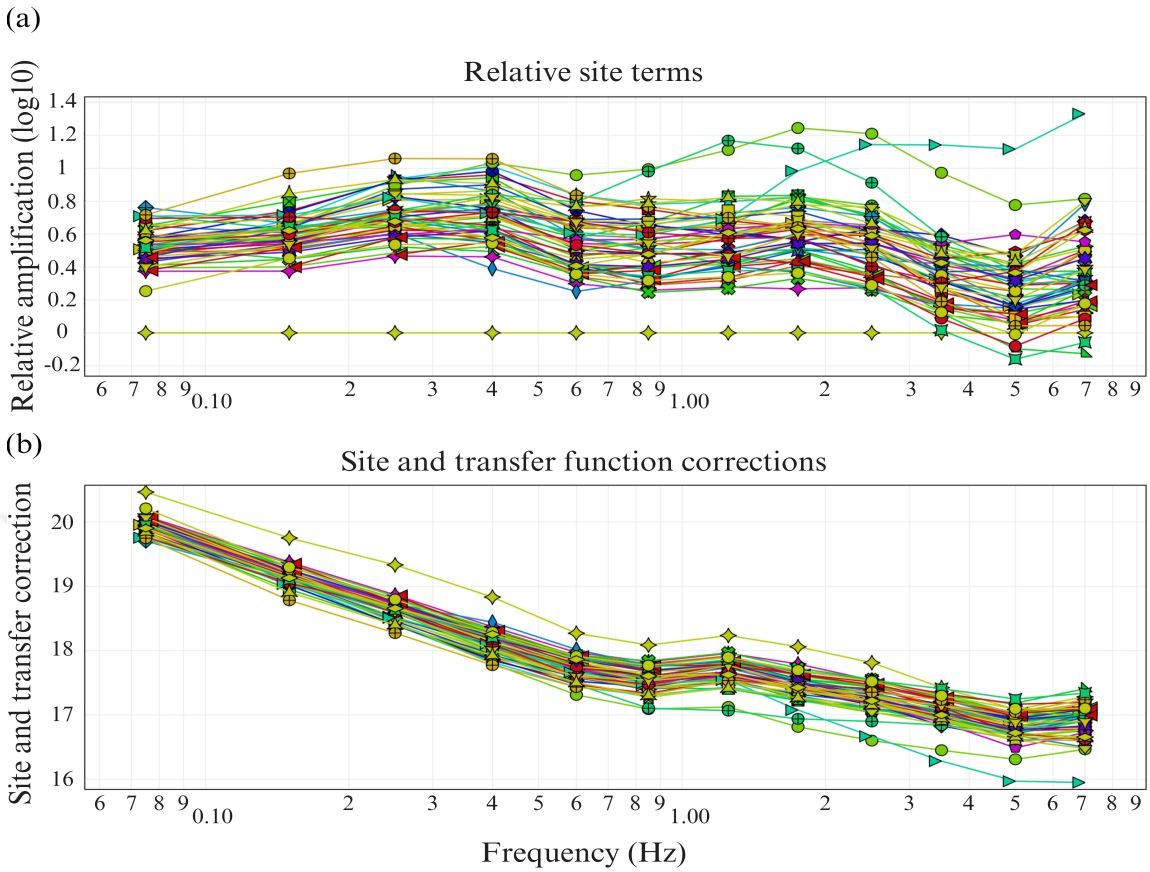


Figure 2.10. (a) An example of how the relative site effects vary with frequency range 0.05 to 8 Hz across different stations. The reference is station KDZE, which is situated on rock. (b) Combined influence of *T(f)* and *S(f)* corrections applied at each of the 51 stations. These correction terms are added to the distance-adjusted logarithmic coda amplitudes ($\log_{10}$) to generate the moment-rate source spectra in N-m for each event.

To emphasize, we used these reference events independently to constrain the broadband, frequency-dependent site terms. This approach eliminates the need to assign a fixed stress-drop value to Green's function events or to assume a uniform source scaling across the region. To assess the reliability and robustness of our final calibration parameters, we further validated them using apparent stress estimates derived from coda spectral ratios of events not included in the calibration process, along with independent moment magnitude values obtained through waveform modeling.

2.2.5. Source Spectra, Moment Magnitude, Apparent Stress, and Radiated Energy

In the final stage, we apply both the site and transfer function corrections to each amplitude that has already been adjusted for path effects. This yields moment-rate source spectra in N-m, as illustrated in Figure 2.11a and described by Mayeda et al. (2003), specifically for a ground-truth reference event with a magnitude of M_w 4.56. The panel displays both the modeled and observed radiated energy, based on 430 amplitude measurements, along with all derived source parameters. For this event, the apparent stress was quantified using coda spectral ratios and an independently determined moment magnitude from waveform modeling. The calibration process can be further refined by interactively reviewing and adjusting individual amplitude picks, as shown in Figure 2.11b.

To estimate source radiation parameters, including moment magnitude, radiated energy, apparent stress, and corner frequency, we fit the corrected spectra to the magnitude and distance amplitude correction (MDAC) spectral model (Walter and Taylor, 2001), which is based on the Brune (1970) source model. In the example from Figure 2.11a, the corner frequency is indicated by a vertical bar whose width represents the 90 percent confidence interval from the model fit, shown as a red dashed line. The CCT also calculates observed energy by converting displacement spectra into velocity squared, then integrates the high- and low-frequency portions to estimate the total radiated energy. For example, in Figure 2.11a, the extrapolated parts of the spectrum accounted for only about 11.3 percent, while the observed portion was approximately 88.7 percent of the total energy.

All estimated source parameters are saved to a database and also displayed on the spectral panel for the corresponding event. The average scatter in $\log_{10}$ amplitude is constrained to a maximum value of 1. If any outliers are identified, they can be easily reviewed, the envelope pick can be adjusted, or the data point can be removed entirely if necessary.

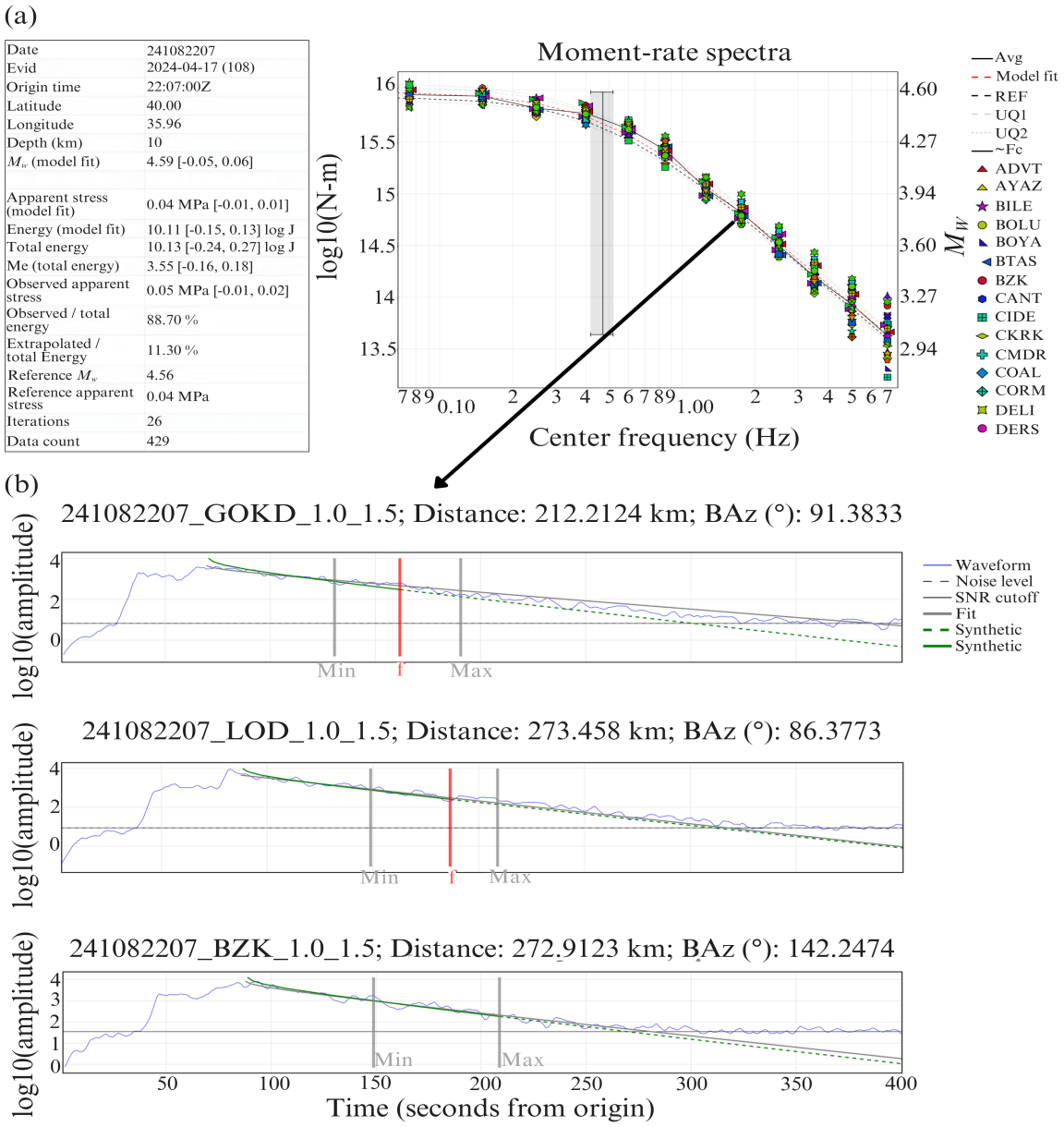


Figure 2.11. (a) An example illustrating the moment-rate source spectra for a reference event with magnitude M_w 4.56, where the σ_A is quantified using coda spectral ratios and an independently determined M_w from waveform modeling (refer to Figures 2.8 and 2.9). The left side displays both the modeled and observed radiated energy. (b) Consistent envelope amplitude measurements between 1-1.5 Hz.

Figure 2.12 indicates an example event used solely for validation and not included in the derivation of site correction factors. This figure displays both the modeled and observed radiated energy, based on 220 amplitude measurements, along with all derived source

parameters. The resulting estimates for moment magnitude (M_w) and apparent stress align closely with independently determined reference values. For this event, approximately 80.7 percent of the total radiated energy was directly observed, while the remaining 19.3 percent was estimated through extrapolation at both low and high frequencies. The model-derived parameters including moment magnitude, apparent stress, radiated energy, and corner frequency are presented along with their 90 percent confidence intervals, shown in brackets.

Additionally, the event location and the associated recording stations can be explored through an interactive map pop-up. The resulting source parameters can be exported to a file or queried from an internal database using structured query language (SQL). Final calibration parameters are stored in a calibration JSON file, as described by Mayeda et al. (2024).

(a)

Evid	161770540
Date	2016-06-25 (177)
Origin time	05:40:11Z
Longitude	40.7068
Latitude	29.2122
Depth (km)	0.01
M_w (model fit)	4.14 [-0.06, 0.05]
Apparent stress (model fit)	0.06 MPa [-0.00, 0.02]
Energy (model fit)	9.58 [-0.12, 0.19] log J
Total energy	9.56 [-0.31, 0.45] log J
Me (total energy)	3.17 [-0.20, 0.30]
Observed apparent stress	0.06 MPa [-0.02, 0.06]
Observed / total energy	80.67%
Extrapolated / total energy	19.33 %
Validation M_w	4.10
Iterations	29
Data count	217

(b)

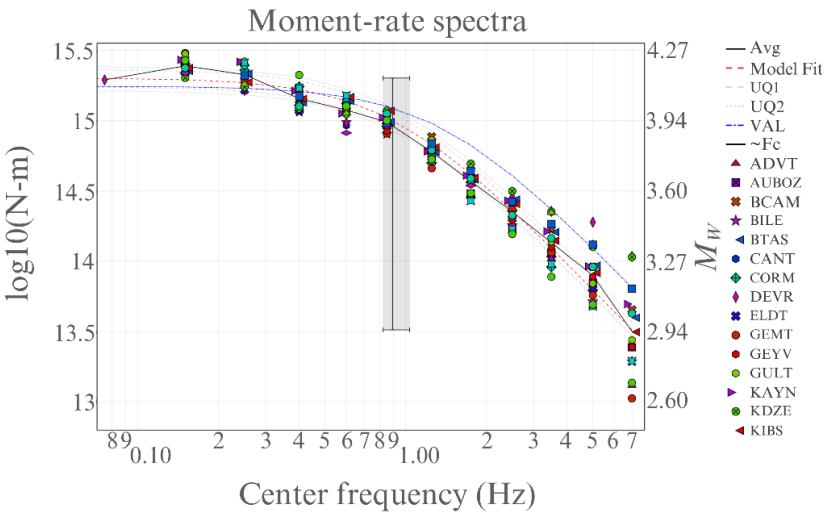


Figure 2.12**.** Panel (b) illustrates the moment-rate source spectra for a validation event with a validation magnitude of M_w 4.10, which was excluded from the site correction term estimation. The spectral analysis shows strong agreement with independently determined magnitude values, as also summarized in panel (a) on the left.

3. GEODETIC DATA & METHODOLOGY

3.1. SAR Interferometry

Operating as an active imaging method in microwave bands (Table 3.1), Synthetic Aperture Radar (SAR) stands out at acquiring high-resolution images in all weather conditions, day or night. This is made possible by using signal processing in conjunction with satellite orbital information to generate detailed images from a typically low-resolution radar system. This approach effectively creates a larger virtual antenna by consistently sequencing multiple short antenna acquisitions collected throughout the platform motion, and enables acquisition of high-resolution images.

Image created by SAR technology is essentially a two-dimensional grid of small pixels, each corresponding to a specific area on the Earth's ground. The precise location and dimensions of these resolution cells in both azimuth and slant-range coordinates are determined by the characteristics of the SAR system. Each pixel contains a measurement of the amplitude of radar energy backscattered from scatterers within that cell. While amplitude reflects the roughness of the terrain, phase information relates to the signal's travel path from the sensor to scatterers on the ground and back again, which is crucial for image formation. Differences in the distance from the radar naturally introduce different delays of time between sending and receiving the radar signal.

The Sentinel-1, a two-satellite constellation, offers robust and reliable C-band SAR imaging capabilities, with its polar-orbiting satellites continuously acquiring high-resolution data across the globe, including land, ocean, and polar regions. This comprehensive approach ensures a consistent and long-term data acquisition, which is crucial for monitoring changes over time and operational services (Torres et al, 2012).

Table 3.1. Frequencies and wavelengths in InSAR system.

Frequency Band	Frequency (GHz)	Wavelength (cm)	Applications
P	0.3 – 1	60-120	Soil moisture, Foliage penetration
L	1 – 2	15 - 30	Forestry, Agriculture
S	2 – 4	7.5 - 15	Agriculture for higher vegetation
C	4 – 8	3.75 - 7.5	Ocean, Agriculture
X	8-12	2.5-4	High resolution radar, agriculture, ocean

The mission utilizes four primary operational imaging modes (Figure 3.1). One of them is Interferometric Wide-swath (IW), which covers a swath of 250 km with a geometrical resolution of 5 × 20 meters. It operates as a ScanSAR mode, employing rapid antenna beam steering in elevation and Terrain Observation by Progressive Scans (TOPSAR) in azimuth. The Extra Wide-swath mode (EW) offers ultra-wide coverage over 400 km at a medium spatial resolution of 20 × 40 meters, also implementing a ScanSAR technique with fast beam scanning and TOPS operation (ESA, 2012). The Stripmap mode (SM) delivers the highest geometric resolution of 5 × 5 meters over an 80 km swath, extending coverage to nearly 410 km via six overlapping swaths. Finally, the Wave mode (WV) functions as a single-polarization Stripmap, acquiring 20 × 20 km sampled images at 100 km intervals.

In this thesis, we utilize the TOPSAR IW mode, which is based on the TOPS technique, an advanced form of ScanSAR, in order to generate interferograms. This is an advanced technique that enables Sentinel-1 satellites to efficiently image wide areas. This method electronically steers the radar beam from backward to forward in the azimuth direction for each burst, in addition to steering the beam in range. This forward-and-backward beam steering is crucial for eliminating image artifacts known as "scalloping"

thereby ensuring homogeneous image quality across the entire swath (Figure 3.2). The technique also takes advantage of sensor motion to optimize the overlaps between consecutive bursts and sub-swaths, which enhances acquisition efficiency and continuity (ESA, 2007). The TOPSAR mode was developed to improve the ScanSAR data quality by significantly improving image consistency while offering almost the same coverage and range resolution. A main advantage of TOPSAR is its more uniform image quality, characterized by a nearly consistent Signal-to-Noise Ratio (SNR) (ESA, 2012). This is achieved through a sweeping azimuth pattern that ensures every target on the earth is observed with the same antenna gain. For interferometric applications, bursts are precisely synchronized between different satellite passes to guarantee the alignment of image pairs (Torres et al., 2012).

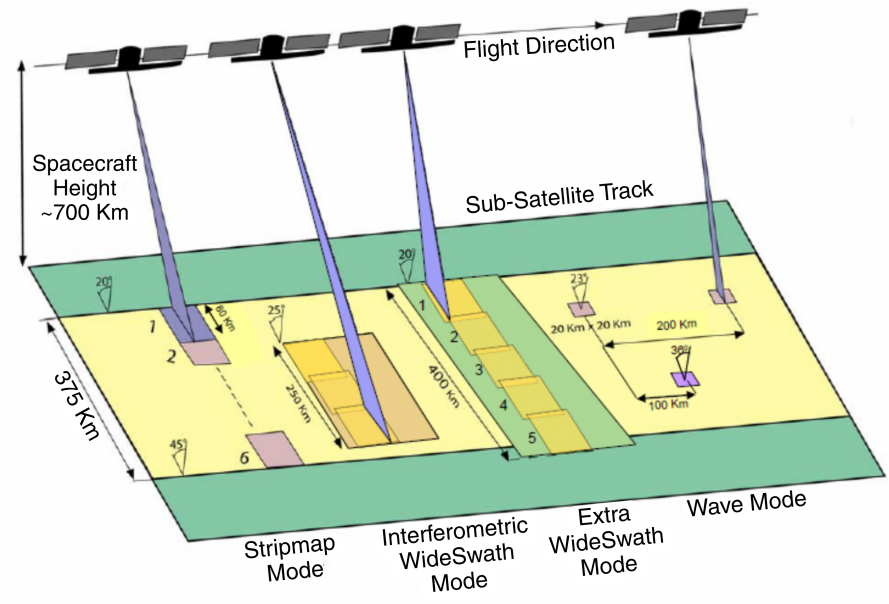


Figure 3.1. Sentinel-1 operational modes (adapted from ESA's website).

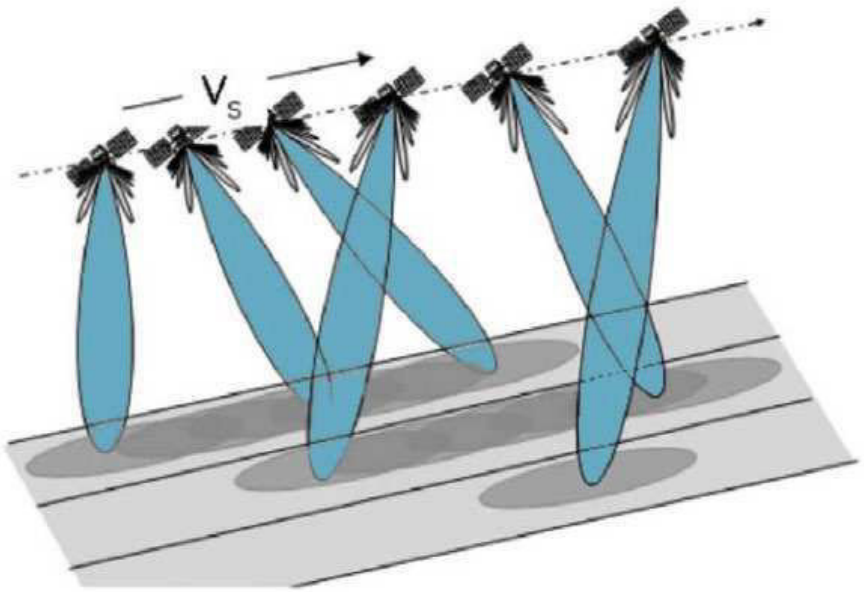


Figure 3.2. The geometry of the TOPSAR mode for data acquisition (Grassi & Francesco, 2019).

The Interferometric Synthetic Aperture Radar (InSAR) technique is based on a fundamental principle: while the phase obtained from a single SAR image does not give information about displacement in time, the difference between the phases of two images can give information about the Earth's surface. Therefore, unlike conventional SAR systems that use radar wave amplitude to generate a two-dimensional map of ground reflectivity, InSAR derives its utility from analyzing the phase information of radar signals. A prerequisite for any interferometric processing is a minimum of two SAR images, known as an interferometric pair. These images are captured from slightly offset viewing geometries over the same area at different time intervals.

In InSAR systems, the time delay (τ) between the transmitted and received signals for two acquisitions shows a phase change (ϕ). This phase change is directly and inversely proportional to the two-way travel distance (2R) of the radar signal and to the transmitted wavelength (λ):

$$\phi = \frac{4\pi}{\lambda} R \tag{3.1}$$

The interferometric phase change has two main components: one is related to the altitude difference between points on the ground, q, and the other is caused by the displacement of those points along the satellite's line of sight, s.

$$\Delta\phi = -\frac{4\pi}{\lambda}\frac{B_n q}{R sin\theta} - \frac{4\pi}{\lambda}\frac{B_n s}{R tan\theta} \quad (3.2)$$

where θ is the radiation incidence angle, B_n is the baseline perpendicular to the radar line-of-sight.

A SAR interferogram is produced by performing a pixel-based multiplication of a complex SAR image with the complex conjugate of the second image (Massonnet et al., 1998). InSAR processing is based on radar interferometry, a technique that calculates the phase difference ($\Delta\phi$) between SAR images ($\Delta\Phi = \Phi_{primary} - \Phi_{secondary}$) (Zebker et al., 1994). This process yields a new image called an interferogram, which is a visualization of the $\Delta\phi$ for each pixel on the surface. On this image, changes in the area are revealed as distinct, colored interference patterns known as fringes, which directly represent phase differences in the radar signals backscattered from Earth's surface (Figure 3.3). Each fringe effectively acts as a contour line, with each full cycle corresponding to a change in range distance of half the radar's wavelength (e.g., 2.83 cm for Sentinel-1, which operates at a C-band wavelength of 5.66 cm). This unique property makes the interferogram an effective tool for mapping subtle surface changes. Prior to the computation of displacement, a critical pre-processing step called co-registration is performed to align the secondary image's pixels with the primary image to obtain sub-pixel accuracy using cross-correlation (Hanssen, 2001).

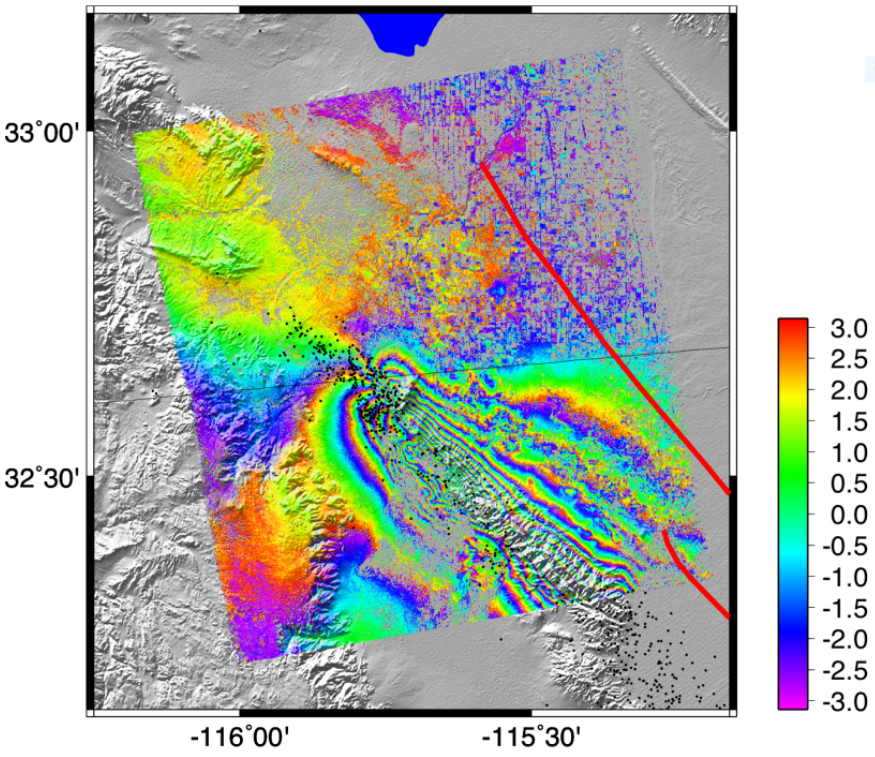


Figure 3.3. Example of the interferometric phase, superimposed on the topographic slope, for an ALOS PALSAR ascending orbit data which corresponds to the 2010, El Major-Cucapah earthquake in Mexico. The fringes imply 11.8 cm displacement away from the radar (Sandwell et al., 2016).

The calculated interferometric phase includes phase of the surface displacement ($\Delta\phi_{Disp}$) which is caused by a pixel's movement in the satellite's line-of-sight direction and several other phase contributions:

$$\Delta\Phi = \Delta\Phi_{Disp} + \Delta\Phi_{Topo} + \Delta\Phi_{Orb} + \Delta\Phi_{Atm} + \Delta\Phi_{Noise} \tag{3.3}$$

This is combined with several error terms that must be mitigated or removed during processing. These include the topographic phase ($\Delta\phi_{\text{Topo}}$), which stems from the difference in viewing geometry between the reference and secondary images and from inaccuracies in the Digital Elevation Model (DEM); the atmospheric phase ($\Delta\phi_{\text{Atm}}$), which is caused by variations in atmospheric properties like pressure, temperature, and humidity, as well as changes in the ionosphere; and the orbital phase ($\Delta\phi_{\text{Orb}}$), which results from inaccuracies in

the satellite's orbital information. Finally, there is the noise term ($\Delta\phi_{\text{Noise}}$), a residual component that accounts for pixel-scale scattering variability, thermal noise, and inaccuracies introduced during the co-registration process (ESA, 2007).

The time that passes between two SAR images can cause significant errors due to atmospheric phase contributions. These errors mainly arise from spatial variations in atmospheric water vapor, which cause heterogeneous refractivity, a quantity describing how a signal bends as it passes through a medium. As a result, any change in the amount of water vapor between the two images causes a variation in signal delay, which is recorded as an error in the InSAR data. Other factors such as liquid water, temperature and pressure gradients can also influence this delay, though to a lesser extent. Because these atmospheric effects can introduce considerable noise, they must be accurately corrected to obtain a reliable calculation of surface deformation.

The InSAR process in this study begins with the acquisition and preparation of satellite radar data (Figures 3.4-3.8) to investigate coseismic surface deformation associated with recent seismic events in Türkiye. Sentinel-1 SAR images, obtained from the Alaska Satellite Facility (ASF), were selected due to their consistent revisit time, wide coverage, and high spatial resolution. The dataset includes both ascending and descending track images covering the NAFZ, with a particular emphasis on the Düzce and Tokat regions. The selected imagery spans pre- and post-event periods of the 2022 Düzce Gölyaka and 2024 Tokat-Sulusaray earthquakes, enabling detailed analysis of ground displacement caused directly by these seismic events.

Following data acquisition, InSAR processing was conducted to generate coseismic interferograms and extract surface deformation patterns. The processing workflow was implemented using the InSAR Scientific Computing Environment-2 (ISCE2), which includes steps such as co-registration of images, interferogram generation, and phase unwrapping. InSAR, as a radar-based geodetic technique, allows for the detection of ground motion at centimeter to millimeter scale across large areas, making it highly suitable for earthquake deformation studies. This chapter outlines InSAR principles, describes the data processing methodology, and discusses the advantages and limitations of the approach, with a focus on coseismic deformation mapping through two case studies.

3.2. InSAR Processing Steps

3.2.1. SAR Interferometric Pairs

For analysis of coseismic deformation, we used radar images from the Sentinel-1 satellite. The selection of SAR images is one of the critical steps. First, we identify the coordinates of the study area, along with the corresponding track and frame numbers. This helps us to determine if satellite images are available for the specific region. If they exist, we list them by their acquisition dates and orbits. The careful selection of these images is crucial for the success of the project.

The perpendicular baseline, which is the distance between the two satellite passes, is the most crucial factor in selecting images for interferometric analysis. This baseline creates a stereoscopic effect, making the interferogram inherently sensitive to topography. The resulting phase signal includes a component directly proportional to the altitude differences across the terrain. To isolate the deformation signal of interest, this topographic phase must be calculated and removed in a process called interferogram flattening. This calculation relies on precise orbital data to determine the baseline, allowing for the generation of a phase map that is directly proportional to relative terrain altitude, with phase discontinuities resembling contour lines.

In this thesis, in order to investigate co-seismic deformation, ascending and descending data before and after the November 23, 2022, Düzce M_w 6.0 and April 18, 2024, Tokat-Sulusaray M_w 5.6 mainshocks were utilized. The characteristics of the Sentinel-1 image pairs used to study the deformations that occurred during the Tokat and Düzce Earthquakes are given in Table 3.2.

After applying flattening, the remaining phase map is directly proportional to the relative terrain altitude. As a result, the phase discontinuities in the flattened interferogram resemble topographic contour lines. The elevation difference between two adjacent discontinuities is defined as the altitude of ambiguity (h_a), a value that can be computed using the specific parameters of the interferometric pair.

Table 3.2. The Sentinel-1 image pairs used in InSAR analysis.

Interferogram	Date 1 (dd/mm/yyyy)	Orbit Direction	Date 2 (dd/mm/yyyy)
1	15/11/2022	Ascending	27/11/2022
2	14/11/2022	Descending	26/11/2022
3	16/04/2024	Ascending	28/04/2024
4	10/04/2024	Descending	22/04/2024

h_a, which is the elevation change that causes a single fringe (2π) in the flattened interferogram, is a critical parameter. A lower altitude of ambiguity means that even small elevation changes will produce a fringe. These are called topographic fringes. For example, if a mountain rises 600 meters from a flat plain within the interferogram and the altitude of ambiguity is 300 meters, the interferogram will have only two topographic fringes. If the perpendicular baseline is zero, meaning the satellite passed through the exact same point, there will be no topographic fringes at all. This parameter can be calculated as follows, given a distance of d between the two orbits:

$$h_a = \frac{\lambda R sin\theta}{2B_n} \tag{3.4}$$

For Sentinel-1, the wavelength, denoted as λ, can be taken as approximately 5.6 cm for the C-band. R, the slant range, is the average oblique distance from the satellite's antenna to a target on the ground, typically expressed in km. θ, the incidence angle, is the angle at which the radar signal from the satellite hits the Earth's surface, defined as the angle between the nadir (the point directly below the satellite) and the target. Finally, B_n, the normal or perpendicular baseline, is the component of the distance between the two satellite orbits that is perpendicular to the radar's line of sight. This relationship shows that there is an inverse proportionality between B_n and h_a.

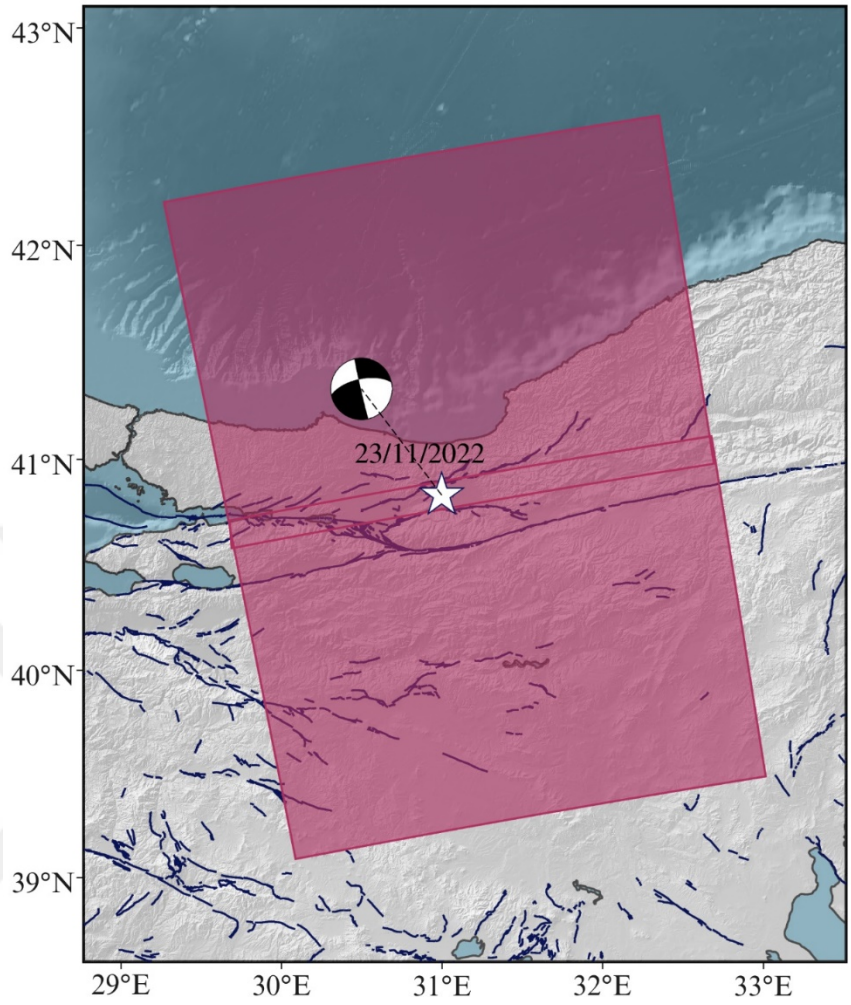


Figure 3.4. Map showing the location of Sentinel-1A frames from ascending orbit path 160, used for coseismic deformation analysis of the 23 November 2022 Düzce-Gölyaka event (M_w 6.0). M_w solution was retrieved from KOERI.

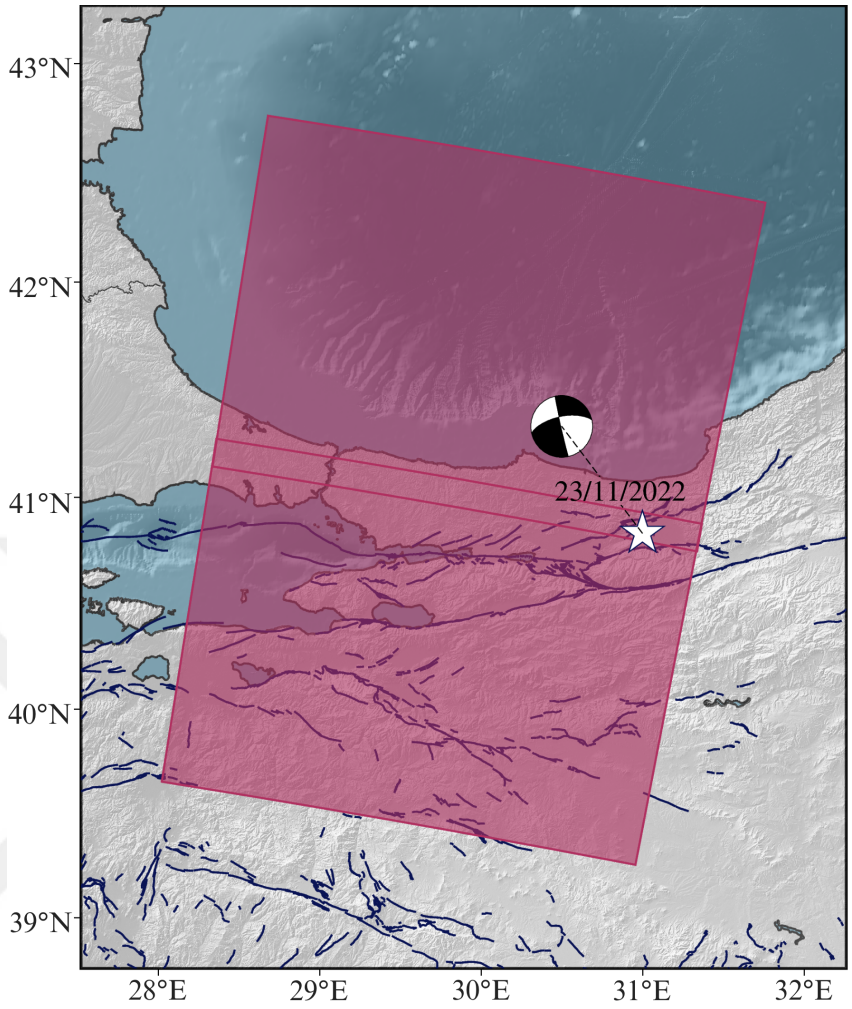


Figure 3.5. Map showing the location of Sentinel-1A frames from descending orbit path 138, used for coseismic deformation analysis of the 23 November 2022 Düzce-Gölyaka event (M_w 6.0). M_w solution was retrieved from KOERI.

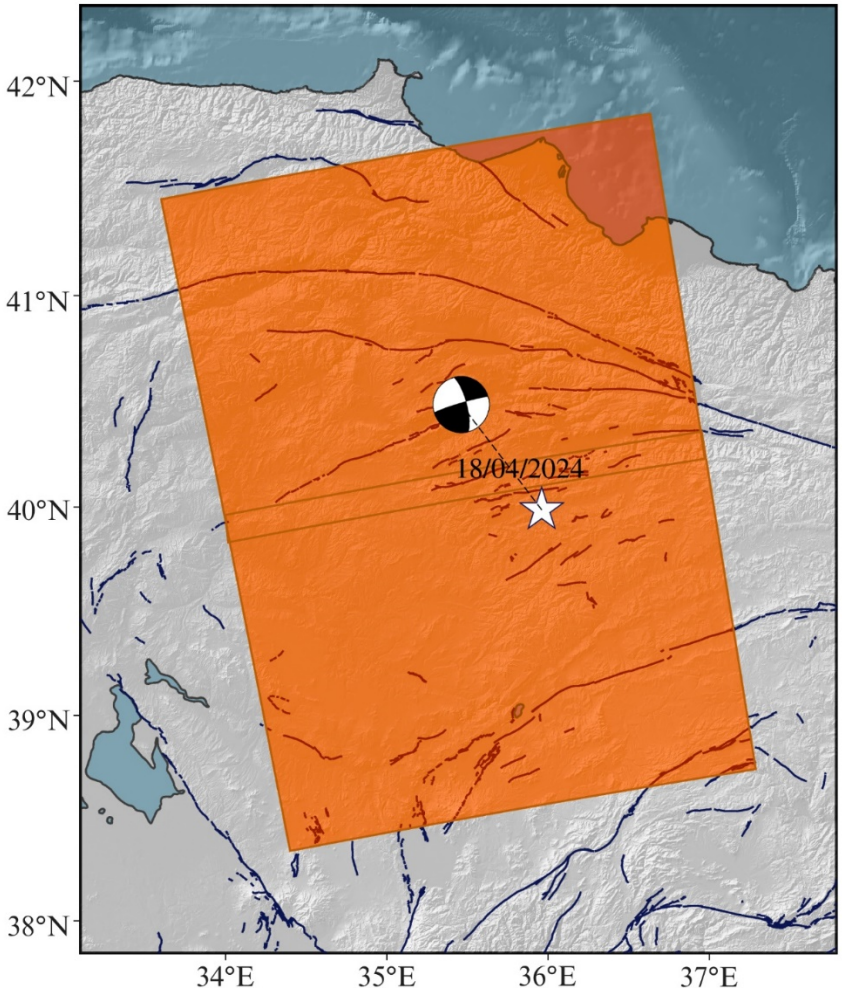


Figure 3.6. Map showing the location of Sentinel-1A frames from ascending orbit path 14, used for coseismic deformation analysis of the 18 April 2024 Tokat-Sulusaray event (M_w 5.6). M_w solution was retrieved from KOERI.

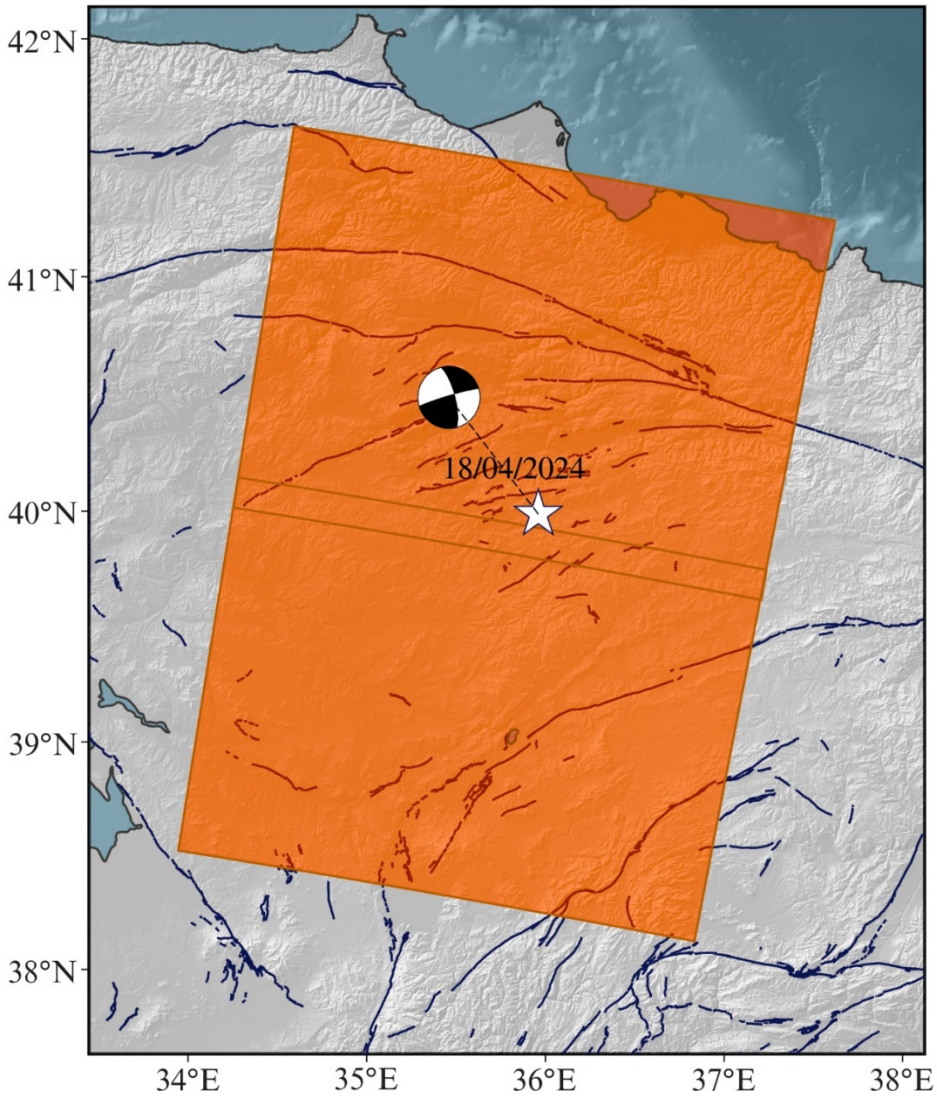


Figure 3.7. Map showing the location of Sentinel-1A frames from descending orbit path 94, used for coseismic deformation analysis of the 18 April 2024 Tokat-Sulusaray event (M_w 5.6). M_w solution was retrieved from KOERI.

3.2.2. Interferogram Processing

InSAR is an effective approach for geodetic imaging of Earth's surface displacement changes due to geodynamic processes such as earthquakes, volcanic unrest, glacier flow, and landslides (Fattahi et al., 2016). ISCE2 is a software designed for processing InSAR data. The topsApp.py is a script within the ISCE framework, used to configure and run a full InSAR workflow exclusively for Sentinel-1 TOPS mode SLC data.

The InSAR data analysis starts with the installation of a Python environment and the required dependencies, following the ISCE2 manual. For our data analysis, we acquired C-band Sentinel-1A single-look complex (SLC) data from the NASA ASF website. For a better understanding of the deformation, we selected data for both ascending and descending orbits, including acquisitions from both before and after the Düzce and Tokat earthquakes. After creating a project directory, the downloaded SAR data was organized into folders by its acquisition date. A configuration file, "*topsApp.xml*" containing the necessary parameters and paths for the processing, was then created within the project directory. Before initiating the InSAR data processing, we downloaded orbit data and a 1 arc second (~30 m) resolution digital elevation model (DEM). This DEM, from the Shuttle Radar Topographic Mission (SRTM), was utilized to flatten the data by removing the topographic phase component from the interferograms.

There are several steps required to complete the co-seismic deformation analysis using ISCE2. The ISCE2 TOPS processor takes Sentinel-1 SLC data, orbit information, and a DEM as input. Precise co-registration is essential in interferometric SAR processing to ensure that identical ground targets are aligned to the same pixel location in both images, in terms of range and azimuth (Hanssen, 2001). The co-registration procedure is typically divided into two steps: coarse and fine, to address the slow processing speed of cross-correlation techniques with large search windows. For the IW data used in this thesis, the workflow begins with identifying and extracting the overlapping regions, in other words, "*burst overlaps*" between the adjacent bursts. It then computes the initial geometrical misalignments, or "*offsets*", between a primary reference image and the secondary image, using the orbit and DEM files in the coarse co-registration step. A more precise alignment is then performed. Enhanced Spectral Diversity (ESD) is used with this aim to estimate and correct for along-track (azimuth) misregistration, followed by a similar calculation for across-track (range) misregistration as part of the fine co-registration of the images (Hanssen, 2001). ESD takes advantage of the fact that there are small, geometrically overlapping regions between adjacent bursts (Yague-Martinez et al., 2017). Once the images are co-registered in sub-pixel precision using these offsets, the individual bursts are stitched back together. This results in a stack of aligned, full-swath SLCs ready for further analysis.

Following this, the interferogram is computed. To combine two complex images interferometrically, one image's complex values must be evaluated at the pixel positions of the other by a resampling process. For precise interferogram generation, the complex images are first oversampled by a factor of two before being multiplied together. This is an essential step to reduce aliasing artifacts and enables the application of low-pass filtering to retain the resolution level of the original SLC images, making linear interpolation sufficiently accurate. Performing oversampling in the range direction before resampling the secondary image (to align it with the primary image) also makes it possible to use short, efficient interpolation kernels in the spatial domain (Hanssen, 2001).

After the resampling step, an interferogram is generated by performing a multiplication of the first image with the complex conjugate of the second co-registered image. This process reveals the phase variation between the two acquisitions, resulting in an interferometric phase image where each pixel represents this difference. The interferograms, initially generated for individual bursts, are then merged to form a single interferogram. The noise from both SAR images tends to spread across the frequency range of the interferogram, making it difficult to remove. To enhance the phase quality, a noise reduction filter is applied in the next stages. This is especially important in repeat-pass SAR acquisitions, where temporal decorrelation significantly affects coherence. In such cases, even after co-registering, aligning, interpolating, and filtering the SLC images, their convolution in the frequency domain still results in an interferogram with a noisy phase (Hassen, 2001). A common method used to reduce noise in a complex interferogram is averaging neighboring pixels. This technique, known as multi-looking, is particularly effective in minimizing uncorrelated noise sources, such as those resulting from temporal decorrelation, baseline variations, or volume scattering. However, it cannot correct for spatially correlated artifacts, like those caused by atmospheric disturbances, flattening errors, or inaccuracies in the DEM removal.

In addition to the standard pre-processing filters and complex multi-looking applied during interferogram formation, various filtering techniques have been developed to improve its quality. A notable example of this is the Goldstein filter, developed by Goldstein and Werner in 1998, which is an adaptive filter that operates in the frequency domain. In areas with high coherence and clearly visible fringes, the filter behaves like a narrow bandpass

filter, which smooths the phase and improves the signal to noise ratio. In contrast, in regions with low coherence or dominated by noise, the filter becomes broader, preserving a high density of phase residues and preventing phase unwrapping errors from spreading into decorrelated areas. The filter enhances spectral components with strong amplitudes, which represent the true signal, while suppressing weaker components associated with noise. As a result, the filter adapts to the specific characteristics of the terrain and is not applied uniformly in all directions (Hanssen, 2001).

The phase difference between two points on the flattened interferogram reflects the true difference in elevation, but only after removing any whole multiples of the height ambiguity, which correspond to full 2π phase cycles. Therefore, subsequently, the wrapped phase values, which are initially confined to a range of 0 to 2π, are converted into continuous, absolute phase values through a process known as phase unwrapping (Figure 3.8), accomplished using an algorithm like SNAPHU (Statistical-cost, Network-flow Algorithm for Phase Unwrapping) developed by Chen and Zebker (2001). SNAPHU uses generalized, nonlinear cost functions that model the probabilistic relationship between observed and unwrapped signals. The algorithm then applies network-flow optimization techniques to find an approximate solution that minimizes the total cost, effectively identifying the most probable unwrapped phase (Chen and Zebker, 2001).

The final step, geocoding, converts the deformation map from radar coordinates into a standard geographic coordinate system. This transformation uses an Earth-centered Cartesian coordinate system along with a DEM to correct geometric distortions and remove the phase effects caused by topography. The resulting geocoded interferogram accurately represents ground deformation in geodetic coordinates relative to a reference ellipsoid, making it suitable for further analysis (Hassen, 2001). The final outputs of this workflow include geocoded interferograms, unwrapped phase images, and other supporting data.

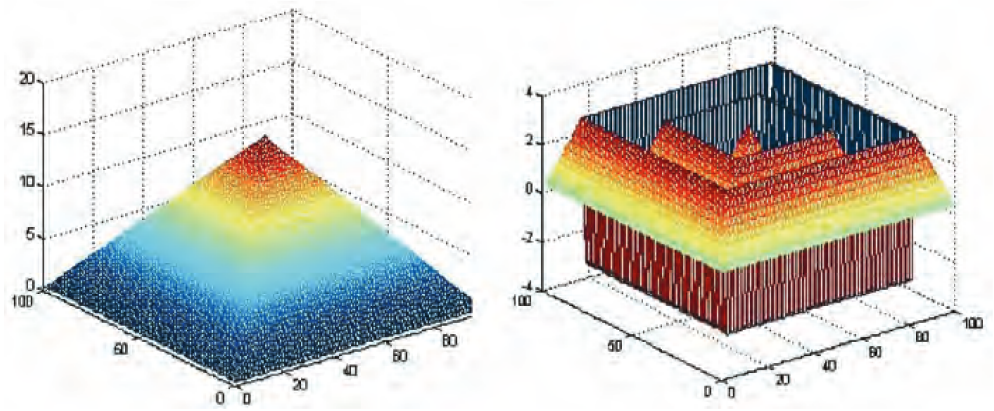


Figure 3.8. Phase unwrapping involves reconstructing the absolute phase values, the original continuous phase (shown on the left), using the wrapped phase values (shown on the right) (ESA, 2007).

Atmospheric water vapor, together with changes in temperature and pressure, may cause a delay in radar signals and can lead to interferometric errors of up to 15 to 20 centimeters, a significant error in InSAR when measuring surface movements of the Earth (e.g., Massonnet et al., 1994; Hooper et al., 2012). Therefore, these errors must be investigated in data analysis.

In this study, Sentinel-1 SAR data from S1A and S1B satellites, which operate with a six-day revisit cycle and carry C-band synthetic aperture radars with a 12-day cycle, were used to generate interferograms. The InSAR processing was performed using the ISCE software. Tropospheric corrections were applied using a Jupyter notebook to the data produced by ISCE, and these corrections were made prior to opening the interferogram. This step helped reduce phase ambiguities and improved the accuracy of phase unwrapping, especially in areas with low coherence caused by vegetation and complex topography, which can lead to geometric decorrelation.

Next, the zenith delay is projected onto the radar slant path, which is the radar's line of sight, by applying a cosine function based on the incidence angle. Simultaneously, a scaling factor is used to convert the delay from pseudo-range units into phase measurements.

$$\Phi_{slant} = \frac{-4\pi}{\lambda \cos(\theta)} d_{zenith} \tag{3.5}$$

With the tropospheric phase delay estimated for both SAR acquisitions, the next step is to calculate the differential delay. The following differential delay function takes the reference and secondary tropospheric files (APS) as inputs, along with the desired output filename.

$$\Delta\Phi_{slant} = \Phi_{reference\ slant} - \Phi_{\sec ondary\ slant} \tag{3.6}$$

The following figures (Figures 3.9-3.15) represent the data analysis for Düzce Gölyaka Earthquake 23 November, 2022, Ascending Orbit data.

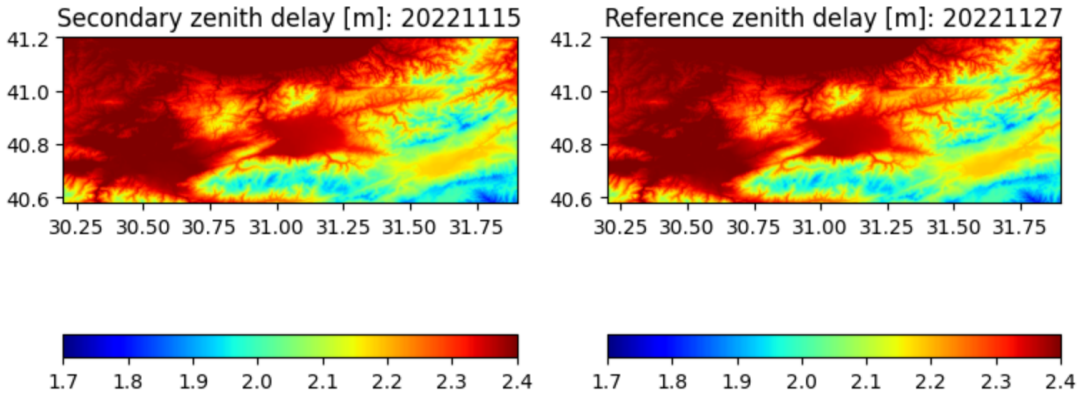


Figure 3.9. The zenith delays for ascending data for two distinct dates.

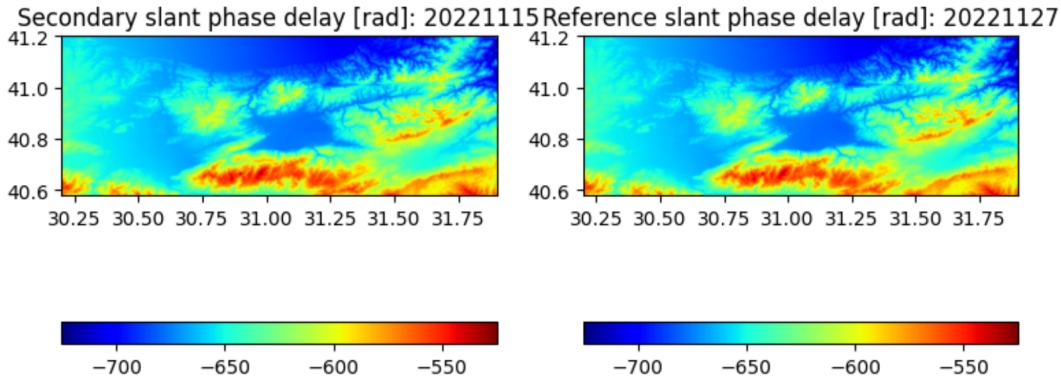


Figure 3.10. Slant phase delays. The left and right images represent the secondary and reference acquisitions.

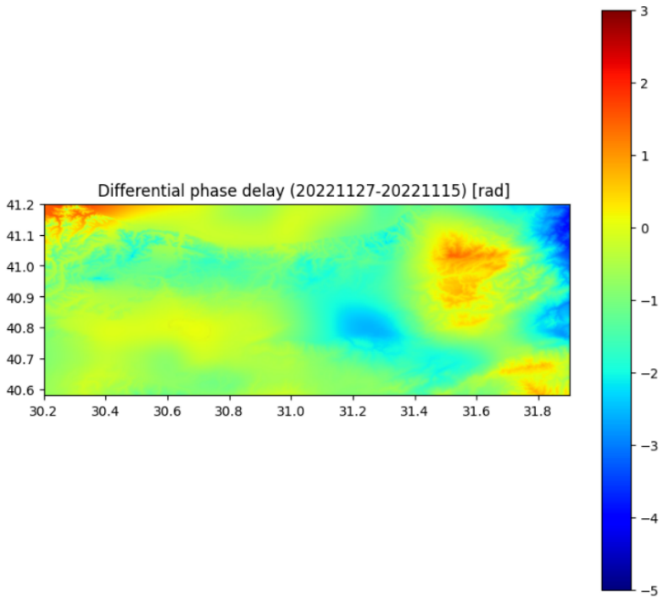


Figure 3.11 Differential phase delay for the November 27, 2022 and November 15, 2022 (ascending orbit) radar images.

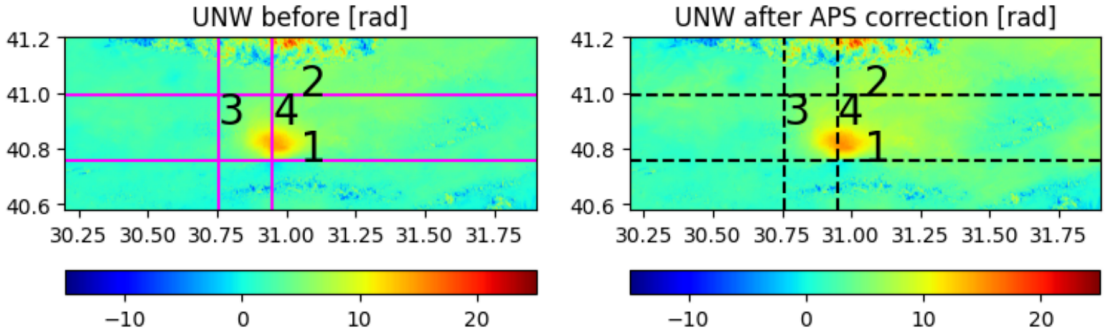


Figure 3.12. The unwrapped interferogram (left) before and (right) after application of the APS correction. Pink and black lines represent cross sections before and after the APS correction, respectively.

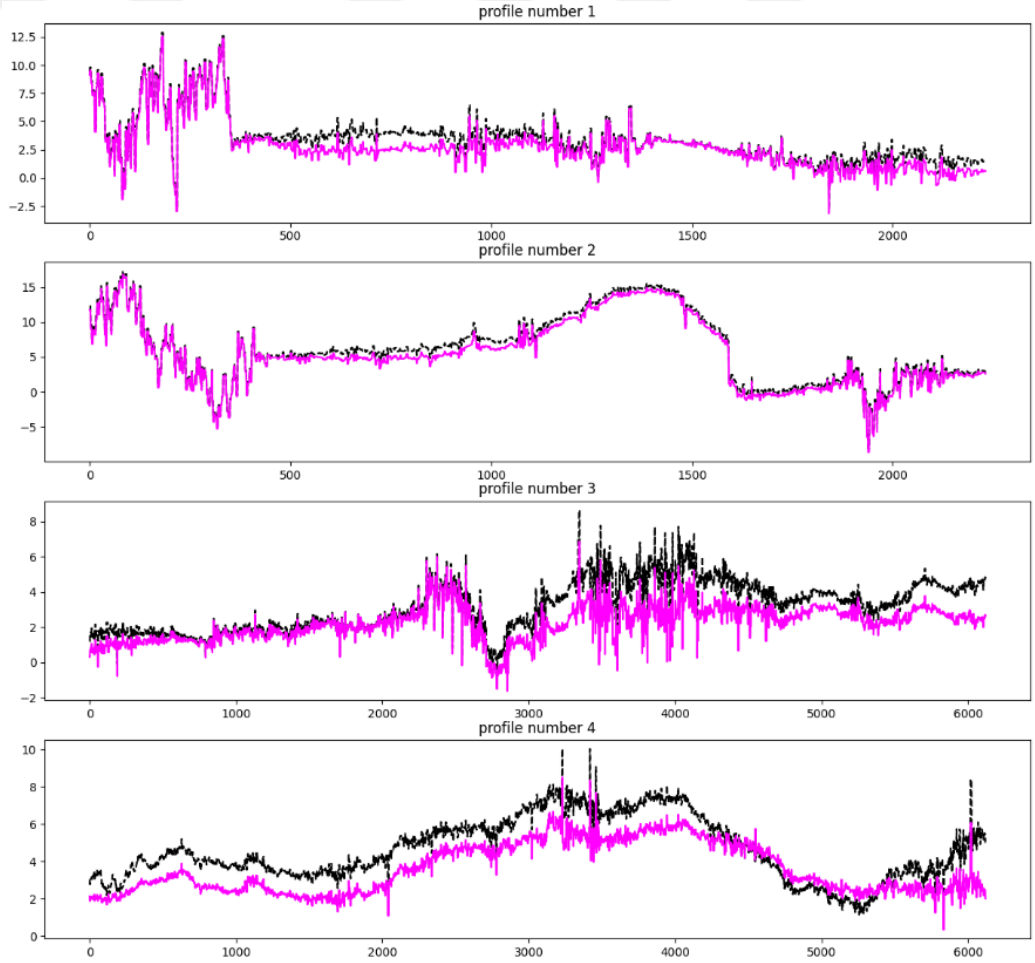


Figure 3.13. The APS correction cross-sections for 1 to 4 profiles are shown in Figure 3.12. Black lines represent cross sections after APS correction, and pink ones show before the correction.

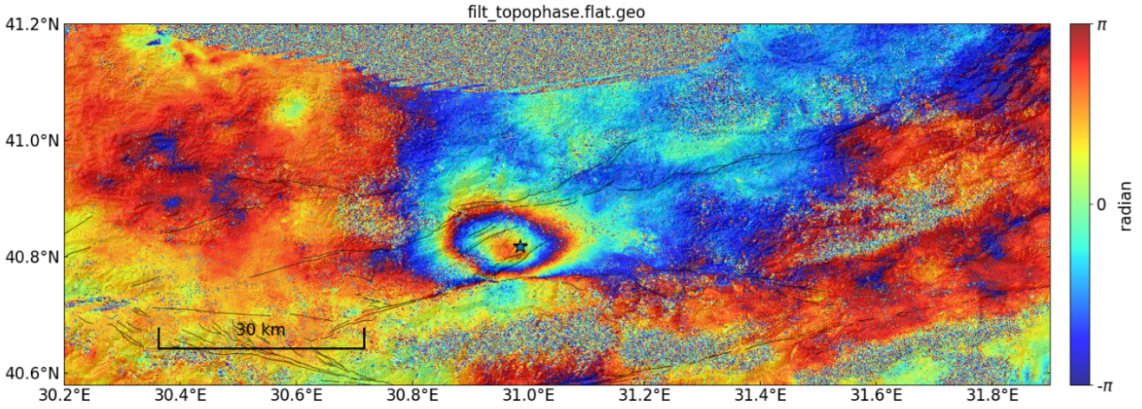


Figure 3.14. Phase interferogram of November 23, 2022, Düzce-Gölyaka Earthquake without Tropospheric correction.

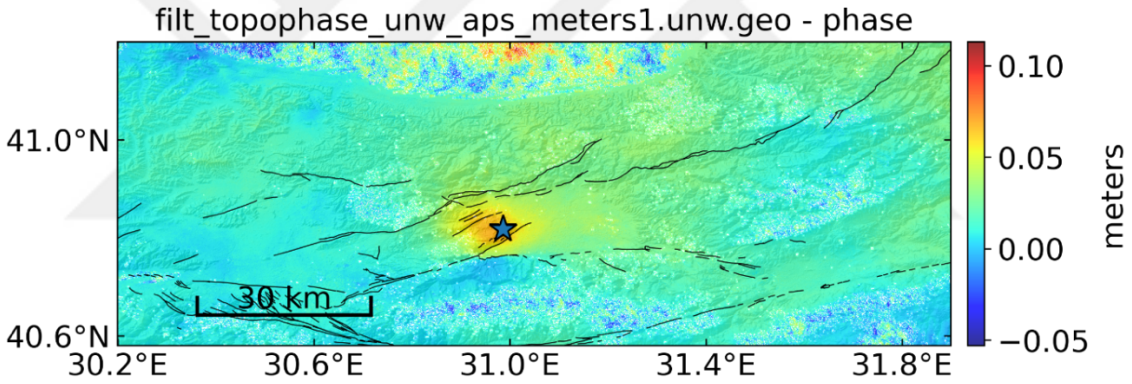


Figure 3.15. Ascending unwrapped interferogram of the Düzce earthquake. It is corrected for tropospheric noise and masked for pixels with a coherence below 0.3. The earthquake's epicenter is marked with a blue star.

The following figures from 3.16 to 3.22 represent the data analysis for Düzce Gölyaka Earthquake 23 November, 2022, Descending Orbit data.

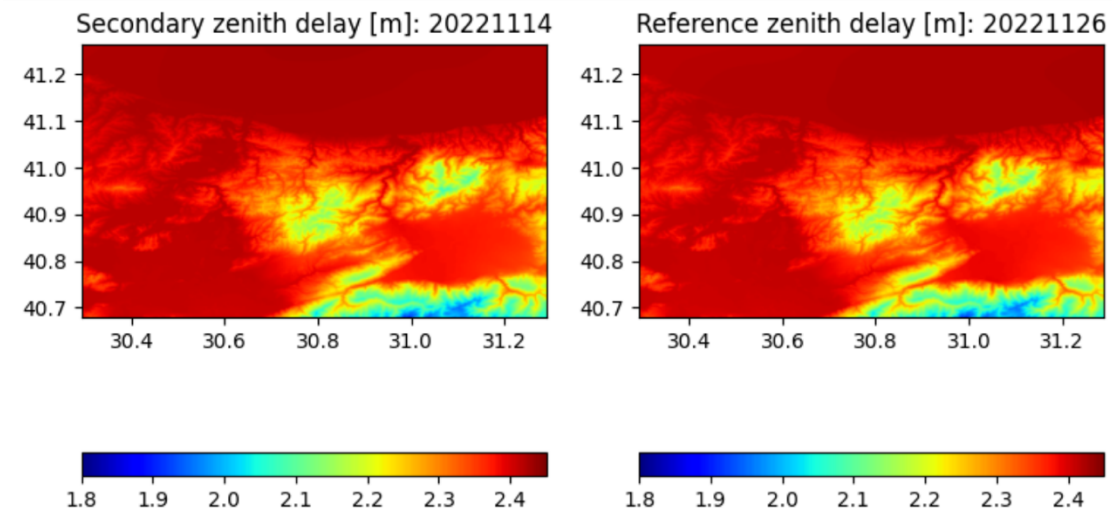


Figure 3.16. The provided image consists of two maps showing the secondary zenith delay in meters on November 14, 2022, and the reference zenith delay in meters on November 26, 2022.

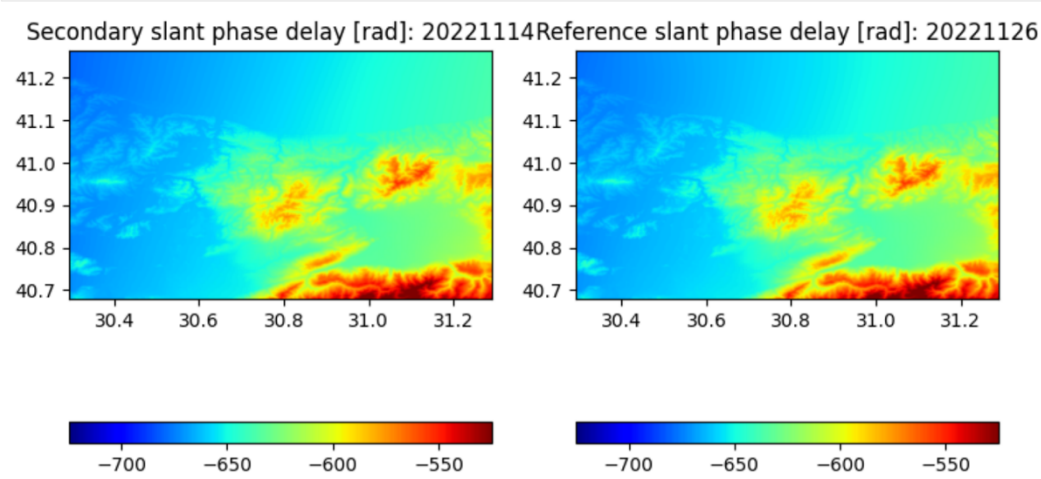


Figure 3.17. Slant phase delays. The left and right images represent the secondary and reference acquisitions.

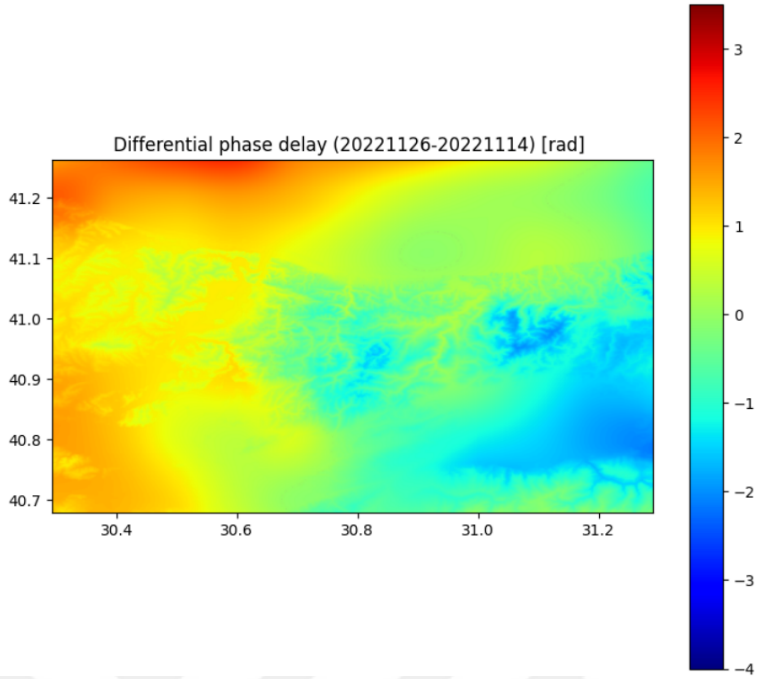


Figure 3.18. Differential phase delay for the November 26, 2022 and November 14, 2022 (descending orbit) data.

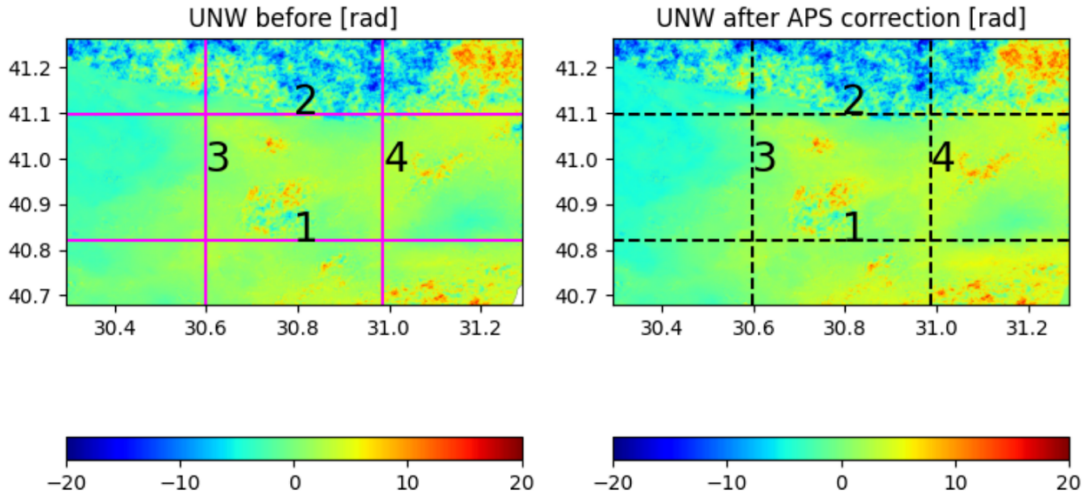


Figure 3.19. The unwrapped interferogram (left) before and (right) after application of the APS correction. Pink and black lines represent cross sections.

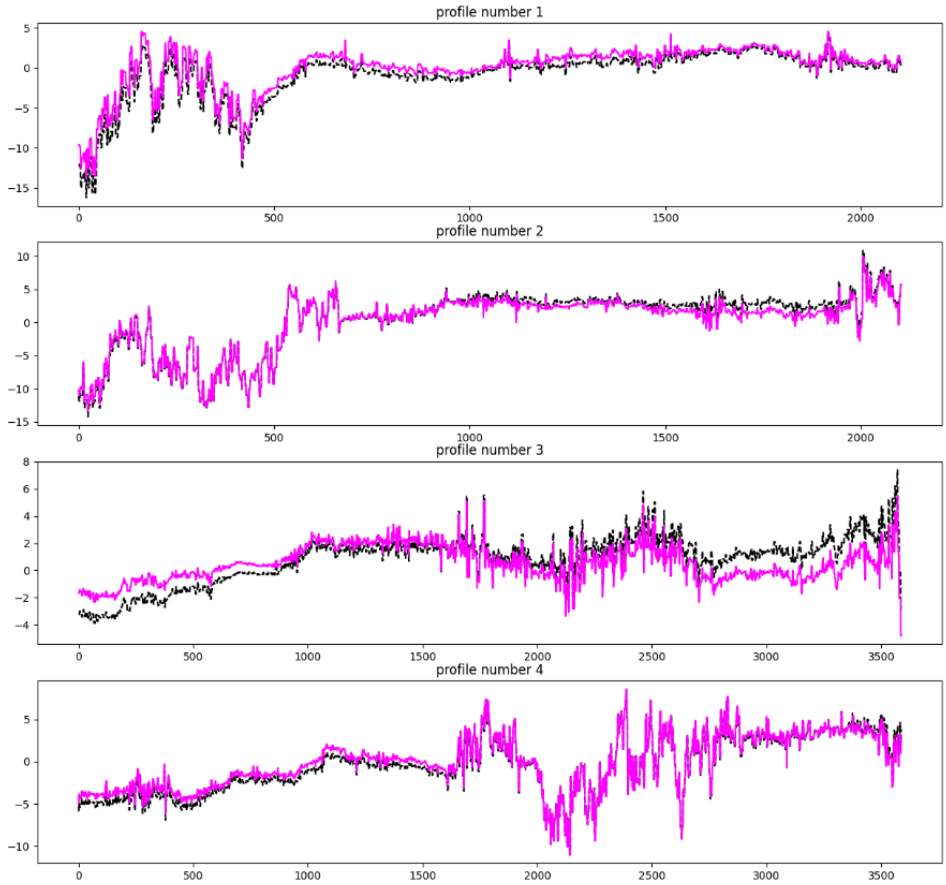


Figure 3.20. The APS correction cross-sections for 1 to 4 profiles shown in Figure 3.19. Black lines represent cross sections after APS correction and pink ones shows before the correction.

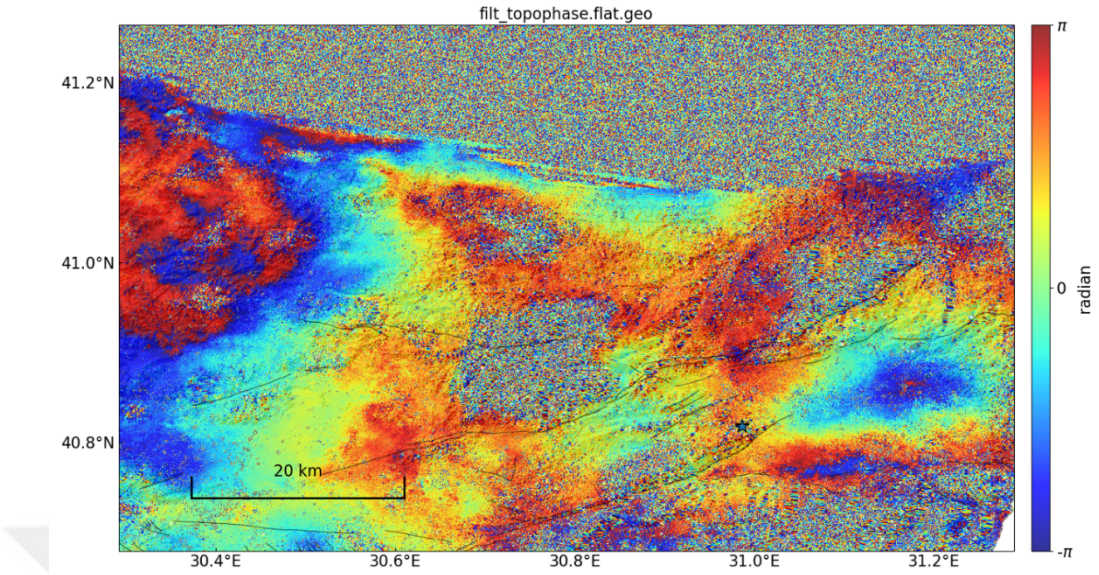


Figure 3.21. Phase interferogram of November 23, 2022 Düzce-Gölyaka Earthquake without Tropospheric correction in descending orbit.

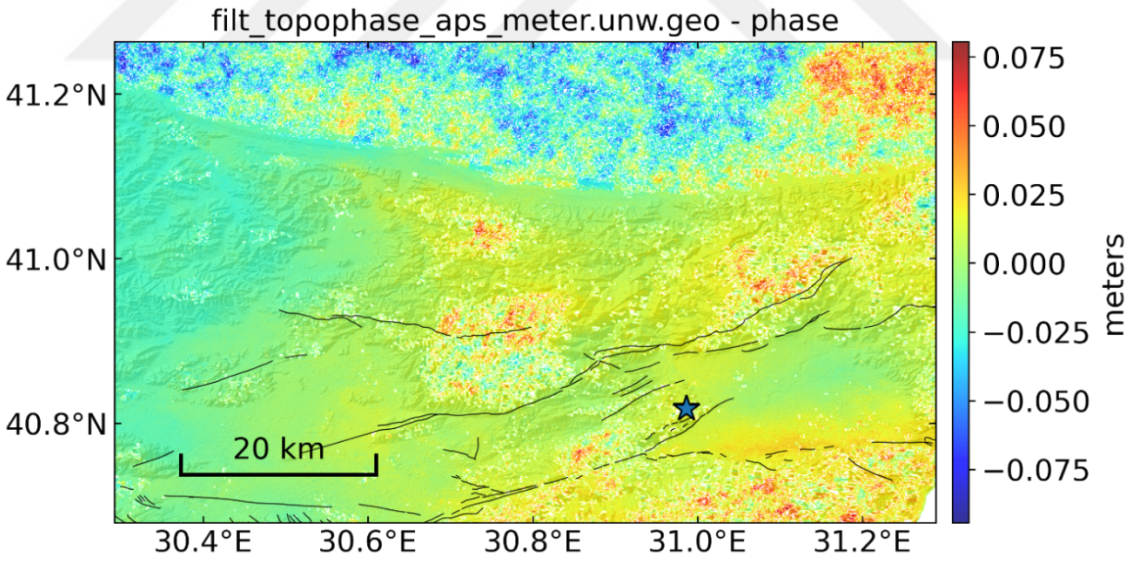


Figure 3.22. Descending unwrapped interferogram of the Düzce earthquake. It is corrected for tropospheric noise and masked for pixels with a coherence below 0.3. The earthquake's epicenter is marked with a blue star.

The following figures from 3.23 to 3.29 represent the data analysis for the Tokat-Sulusaray Earthquake (18 April 2024), Ascending Orbit data.

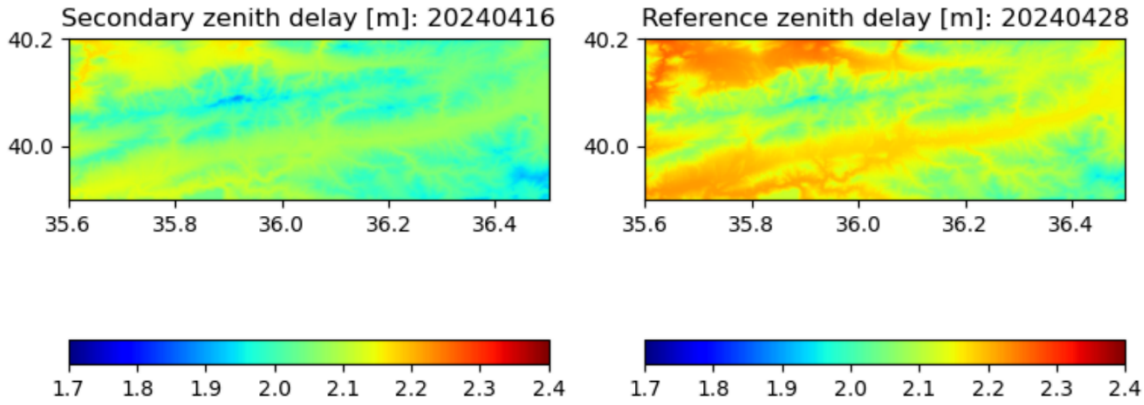


Figure 3.23. The zenith delays for ascending data for April 16,2024 (Secondary) and April 28, 2024 (Reference) dates.

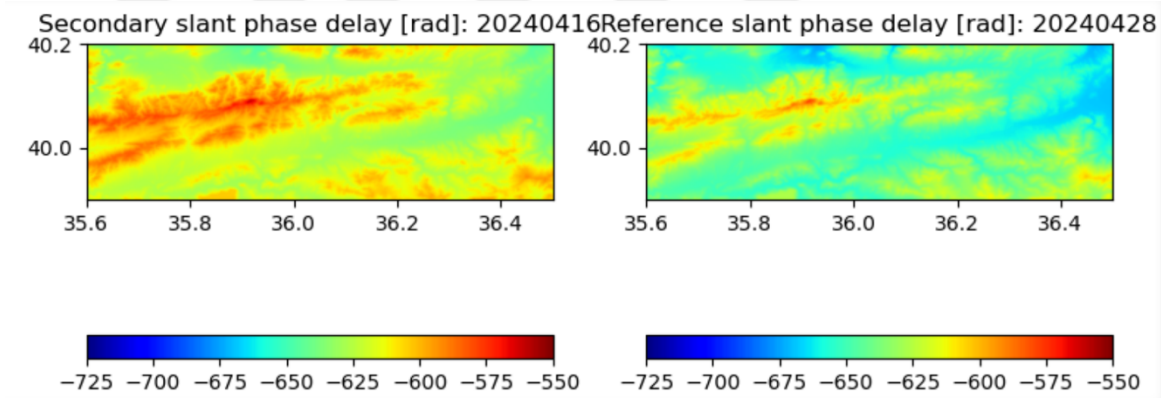


Figure 3.24. Slant phase delays. The secondary image (left) was acquired on April 16, 2024, and the reference image (right) on April 28, 2024.

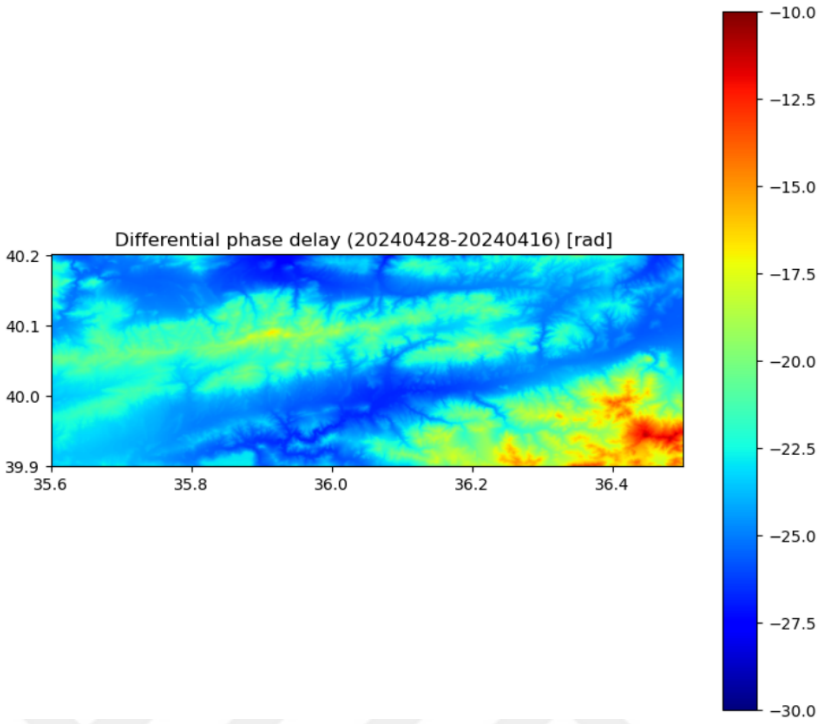


Figure 3.25. The differential phase delay in radians. This map represents the phase difference between radar images acquired on April 28, and April 16, 2024.

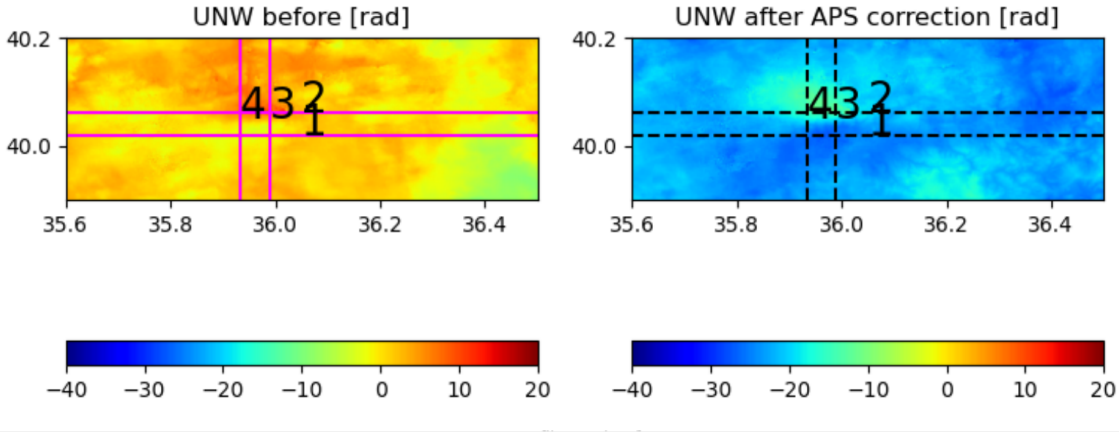


Figure 3.26. The unwrapped interferogram (left) before and (right) after tropospheric correction for the ascending data of the Tokat-Sulusaray event. Pink and black lines represent cross sections before and after the APS correction, respectively.

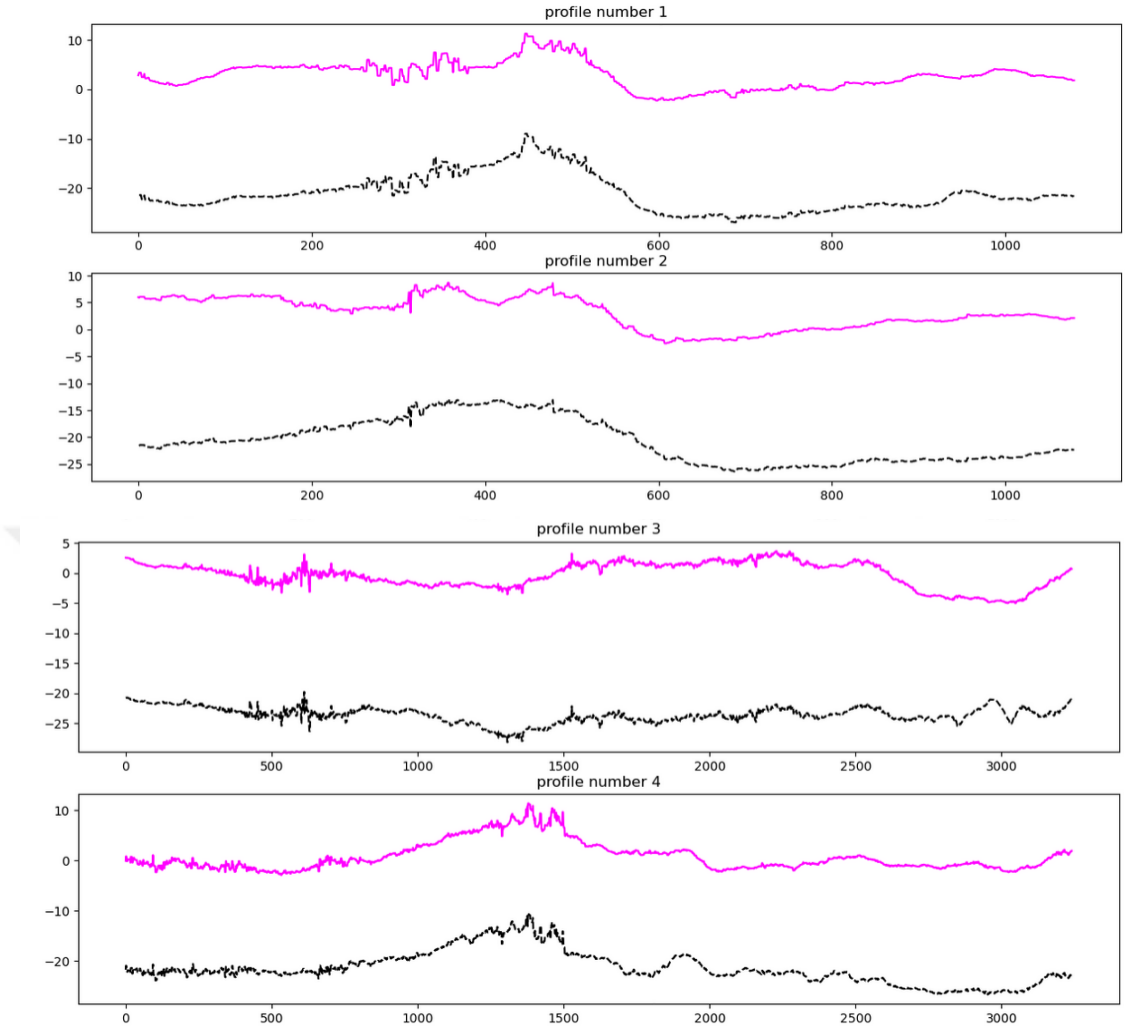


Figure 3.27. The tropospheric correction cross-sections for 1 to 4 profiles which shown in Figure 3.26. Black lines represent cross sections after APS correction, and pink ones show before the correction.

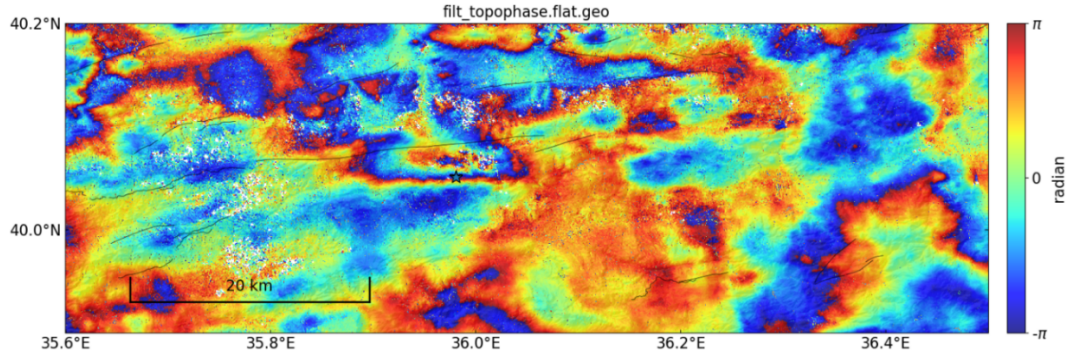


Figure 3.28. Phase interferogram of April 18, 2024, Tokat-Sulusaray Earthquake without Tropospheric correction for ascending orbit.

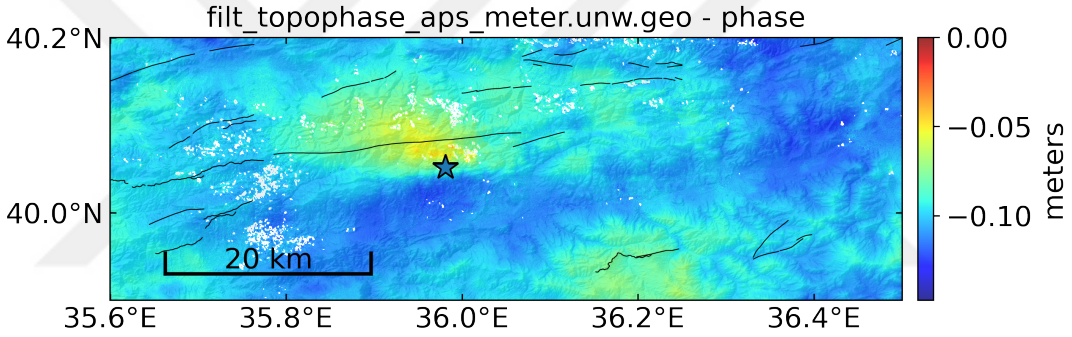


Figure 3.29. Coseismic Deformation of the 2024 Tokat-Sulusaray Earthquake for ascending orbit. This unwrapped interferogram shows LOS deformation in meters, corrected for tropospheric noise and masked for pixels with a coherence below 0.3. The earthquake's epicenter is marked with a green star.

The following figures from 3.30 to 3.36 represent the data analysis for the Tokat Sulusaray Earthquake (18 April 2024), Descending Orbit data.

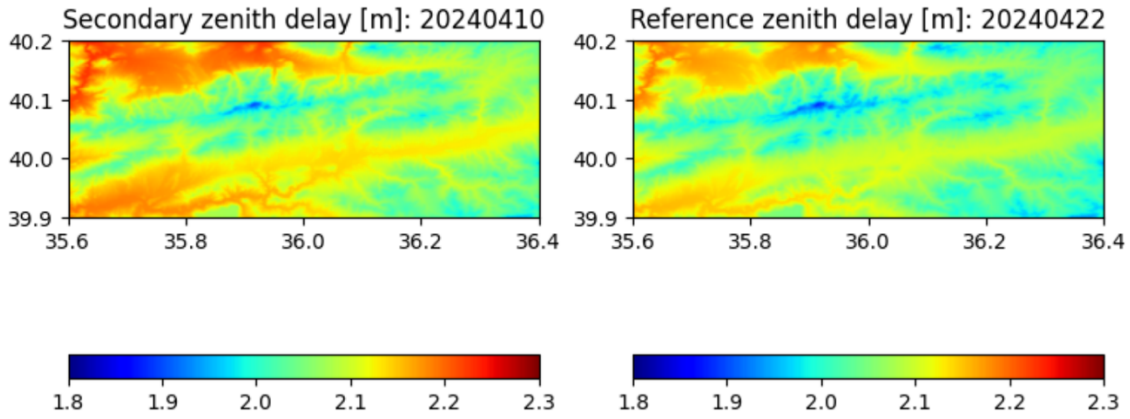


Figure 3.30. The zenith delay [m] for the secondary and reference dates.

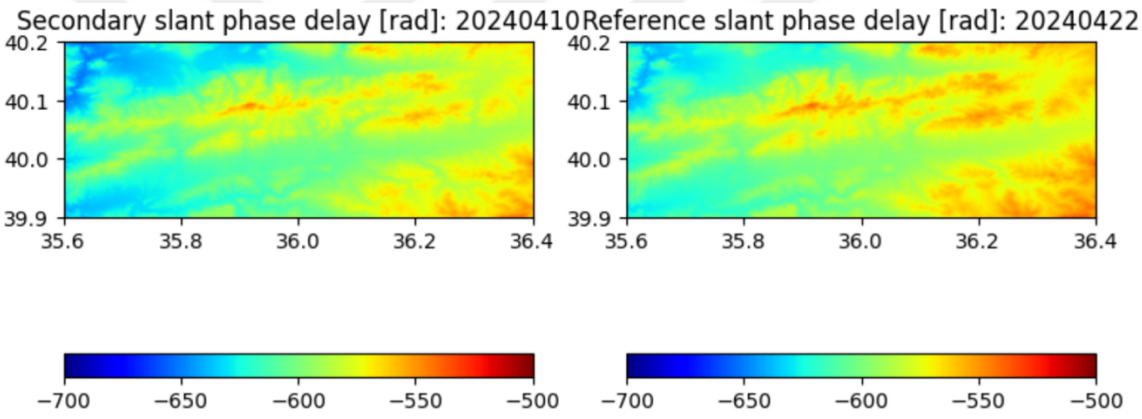


Figure 3.31. Slant phase delays for descending data for the secondary (left) and reference (right) dates.

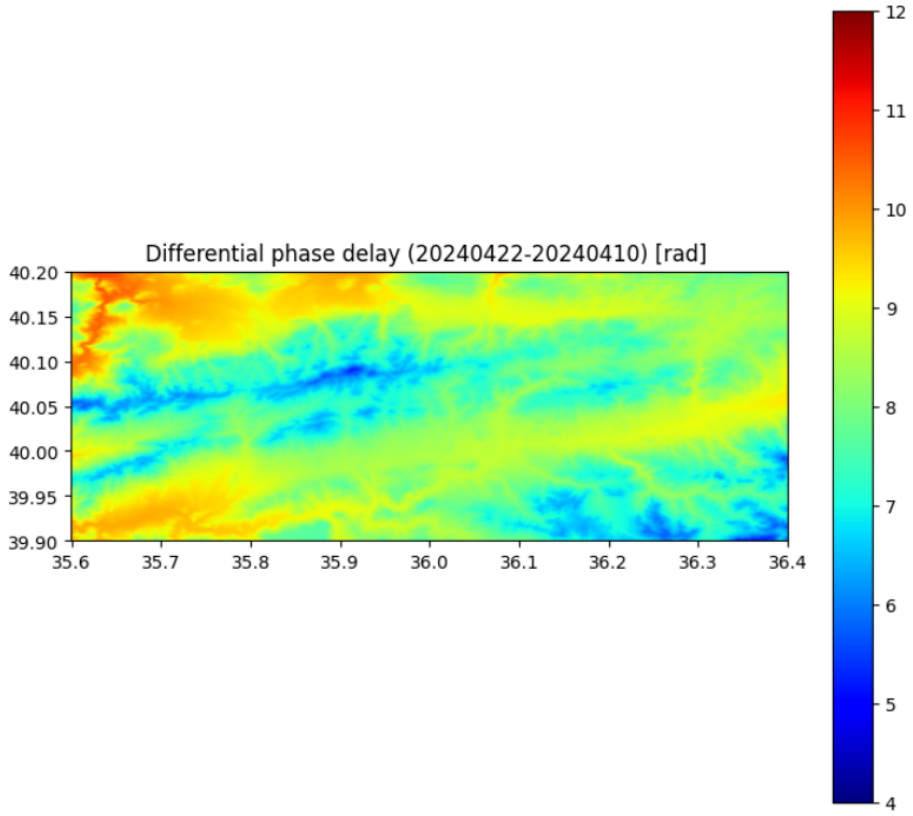


Figure 3.32. Differential phase delay in radians. This map represents the phase difference between radar images acquired on April 22, 2024 and April 10, 2024 (descending orbit).

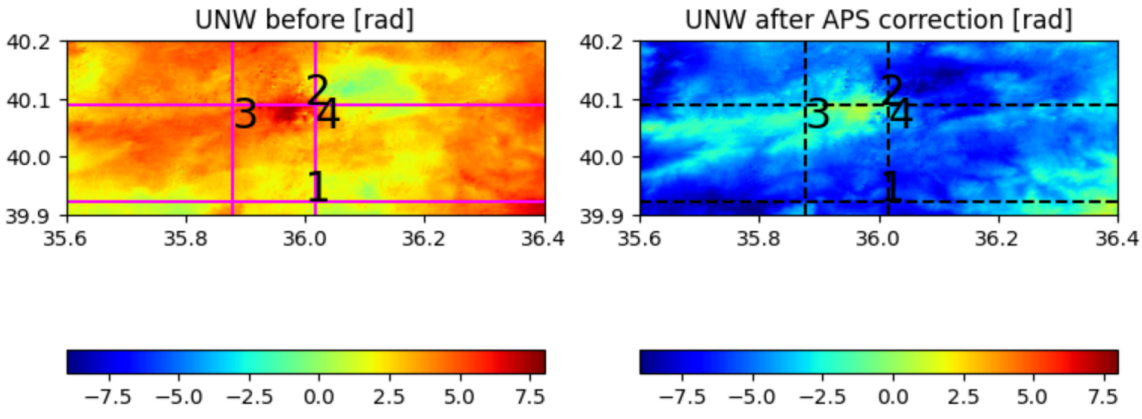


Figure 3.33. The unwrapped interferogram (left) before and (right) after application of the APS correction to the descending data. Pink and black lines represent cross sections before and after the APS correction, respectively.

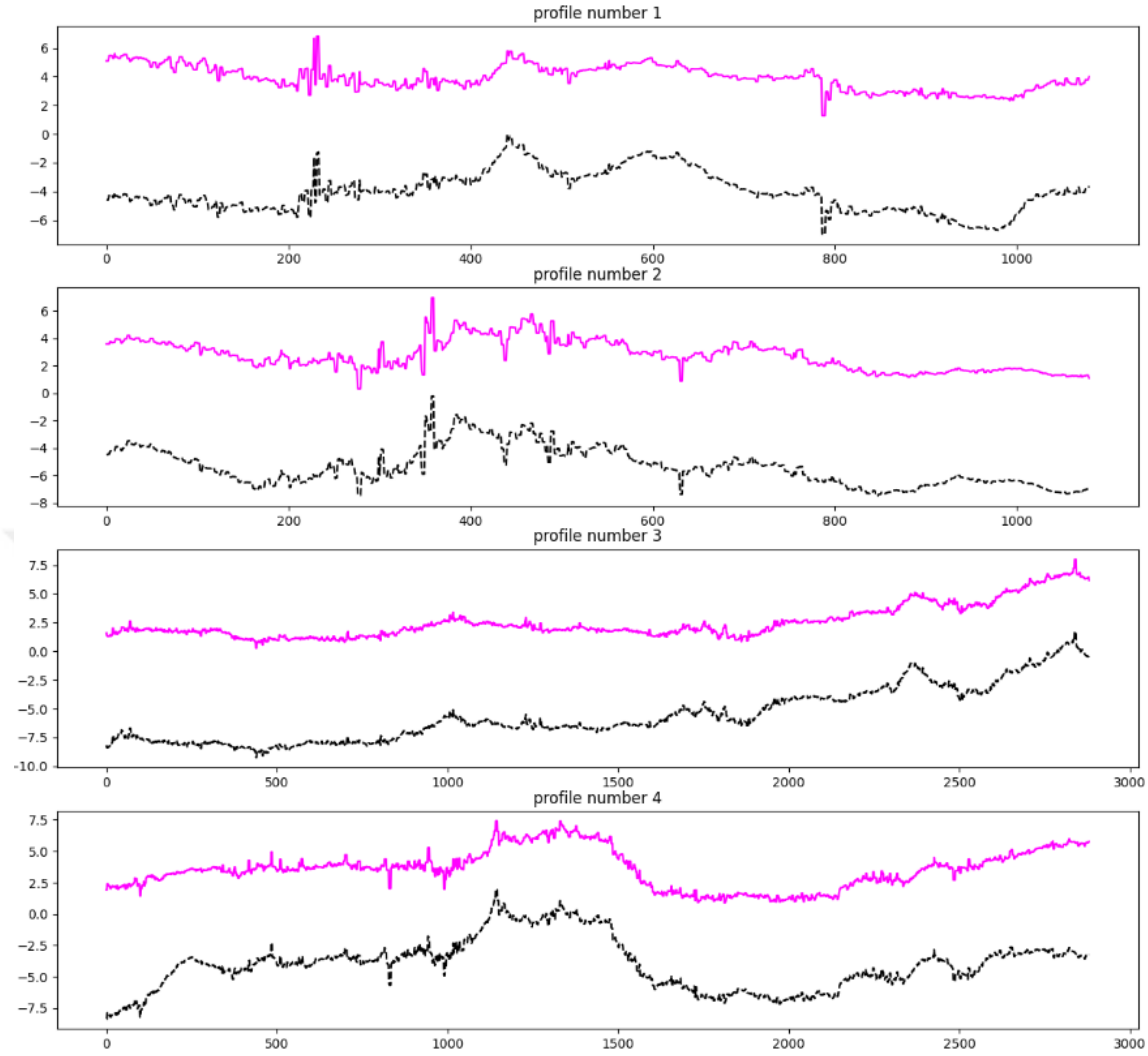


Figure 3.34. The tropospheric correction cross-sections for 1 to 4 profiles shown in Figure 3.33. Black lines represent cross sections after APS correction and pink ones shows before the correction.

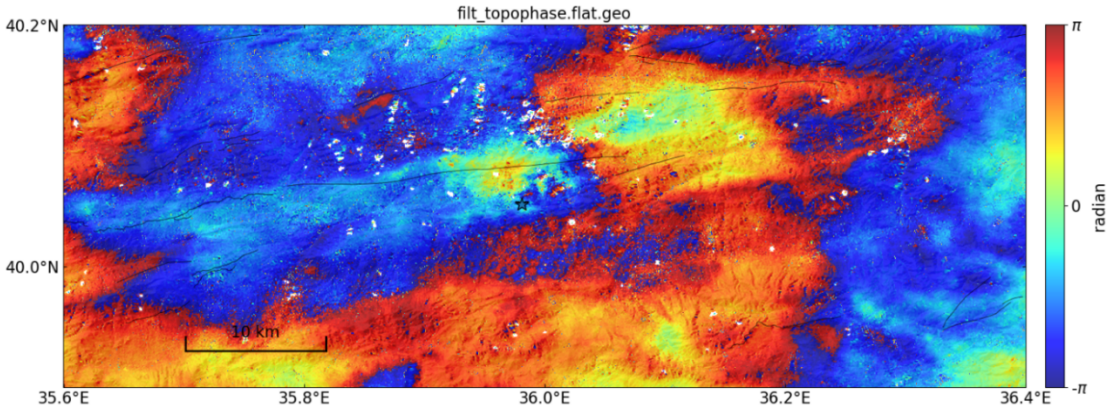


Figure 3.35. Phase interferogram of April 18, 2024, Tokat-Sulusaray Earthquake without Tropospheric correction for descending orbit.

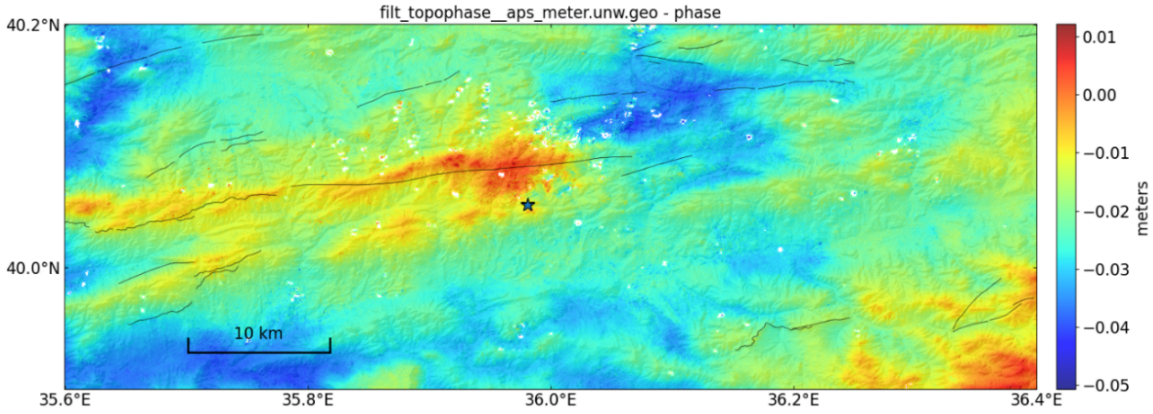


Figure 3.36. This unwrapped interferogram shows coseismic deformation of the 2024 Tokat-Sulusaray earthquake for descending orbit. Blue star represents the Tokat mainshock.

3.3. Modeling the Slip Distribution Using Elastic Dislocations

The purpose of modeling procedure in this thesis is to determine the source parameters for the earthquakes through the modeling of surface deformation derived from InSAR observations. Surface deformation due to shear or tensile opening on rectangular planes embedded in an elastic half-space is calculated using the formulas given in closed analytic form by Okada (1985). A set of 9 parameters is used for modeling. The parameters are fault

length, coordinates of the fault, upper and lower depth, strike, dip, slip and rake (Figure 3.37). One such set defines a single dislocation to describe a single fault patch. Three components of displacement (East, North and Vertical) at a point or a regular grid on the surface, due to dislocations on multiple fault patches can be calculated simply by summing the displacements resulting from each patch. Using the position of orbits surface displacement can then be projected in the direction of the radar line of sight in order to compare it with the SAR data.

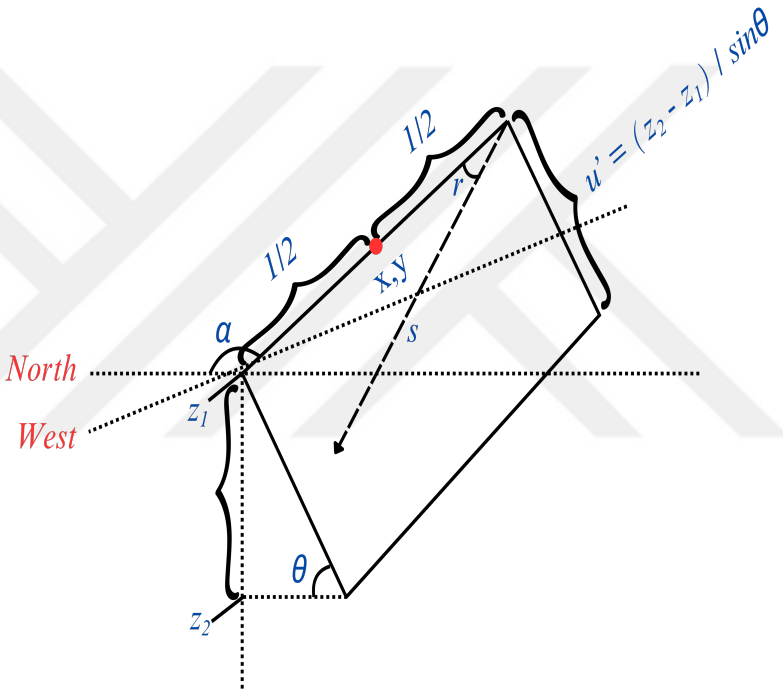


Figure 3.37. Fault parameters that define a dislocation on a single fault in modeling. x and y are coordinates of the fault center; *l* is fault length, and *w* is fault width. z_1 is upper depth of the fault, and z_2 is the lower depth. α is the fault strike and θ is the fault dip, r is rake, and s is slip.

In this thesis, the Pyrocko software suite, an open-source collection of tools designed to facilitate earthquake modeling using both seismic and InSAR data, is utilized. Two earthquakes are selected for source modeling: the M_w 6.0 Düzce-Gölyaka earthquake on November 23, and the M_w 5.6 Tokat-Sulusaray earthquake on April 18. Both events are analyzed using interferograms from ascending satellite orbits. We used only ascending orbit

data because they more accurately detected the deformation, which occurred mostly in the E–W direction. Figures from 3.38 to 3.45 represent wrapped and unwrapped interferograms, and the quadtree resampled map of the unwrapped interferogram for the Düzce and Tokat earthquakes, respectively.

First, we downsample an ISCE interferogram using quadtree decomposition. For this, we specify parameters like variance threshold, percentage of nan values allowed per tile/leaf, maximum leaf size, and minimum leaf size in degrees (Table 3.3). The optimal parameter values were obtained through a trial-and-error approach, yielding 334 and 358 leaves for the Düzce and Tokat earthquakes, respectively (Figures 3.44 and 3.45).

Table 3.3. Quadtree parameters used for the Düzce and Tokat earthquakes.

Downsample Parameters	**Düzce Earthquake**	**Tokat Earthquake**
Variance threshold	0.0052	0.006
% of nan values allowed per tile	0.05	0.2
Maximum leaf size	0.0085	0.06
Minimum leaf size	0.0001	0.001

While several modeling codes exist for the analysis of InSAR data, there is no standardized input format. Consequently, it is typically necessary to reformat data to meet the specific requirements of a given software package. At a minimum, most of these modeling applications require data point locations, displacement measurements, and LOS vector information.

An example of this reformatting process involves preparing output from a quadtree decomposition tool, such as *kite*, for use with a modeling code like *okinv*. The procedure entails several main steps: First, the centroids and average displacements from the quadtree's leaf nodes, initially in latitude-longitude coordinates, must be extracted. These geographic coordinates are then converted into a UTM system, with units expressed in kilometers. This transformation also includes converting the reference point, which for *kite* is the southwest corner of the interferogram. Following the coordinate conversion, the three components of the unit LOS vector are computed for each data point. This systematic reformatting process provides a clear framework that can be adapted to prepare data for a variety of other modeling codes as required.

The extraction of necessary information from *kite*'s output is a straightforward process. The center of each quadtree cell, identified by the variable *leaf_focal_points,* is provided in both a local coordinate system (in meters) and a geographic coordinate system. The definitions for incidence and azimuth within *kite* follow a specific convention: incidence is defined as upward-looking, toward the satellite, while azimuth is measured counter-clockwise from East. Both of these angular values are expressed in radians. This data can be readily converted to other common definitions, such as a unit LOS vector pointing from the satellite to the ground target, through simple trigonometric transformations.

Then, we compare downsampled InSAR data with model predictions and calculate penalties and residuals. For doing this, we set up initial parameters: strike, dip, rake, slip, x, y, fault length, top, and bottom. In Table 3.4, fault parameters that define a dislocation on a single fault in forward modeling is shown for the 2022 Düzce and 2024 Tokat events.

The seismic moment M_0 can be calculated by multiplying the area of fault patch (l*w) by the value of slip (s) and shear modulus (μ), that is "$M_0 = \mu * s * A$". Shear modulus, which varies typically between 30-36 GPa, is taken as 30 GPa in this study. For multiple fault patches, the total seismic moment will be the summation of the moment calculated for each patch. Moment magnitude, M_w, can be calculated using the empirical formula "$M_w = 2/3\ log\ M_0 - 6$" (Kanamori, 1977).

To model Sentinel-1 interferogram, forward modeling is used to generate a first-order model. This model is subsequently refined using a combination of trial-and-error with a conventional inversion technique. The procedure aims to fit the InSAR data, which are uniformly sampled in regions where the interferogram exhibits coherence.

The following three figures represent the wrapped-unwrapped interferogram of November 23, 2022, Düzce-Gölyaka earthquake for ascending orbit and the quadtree-resampled map of InSAR LOS displacement.

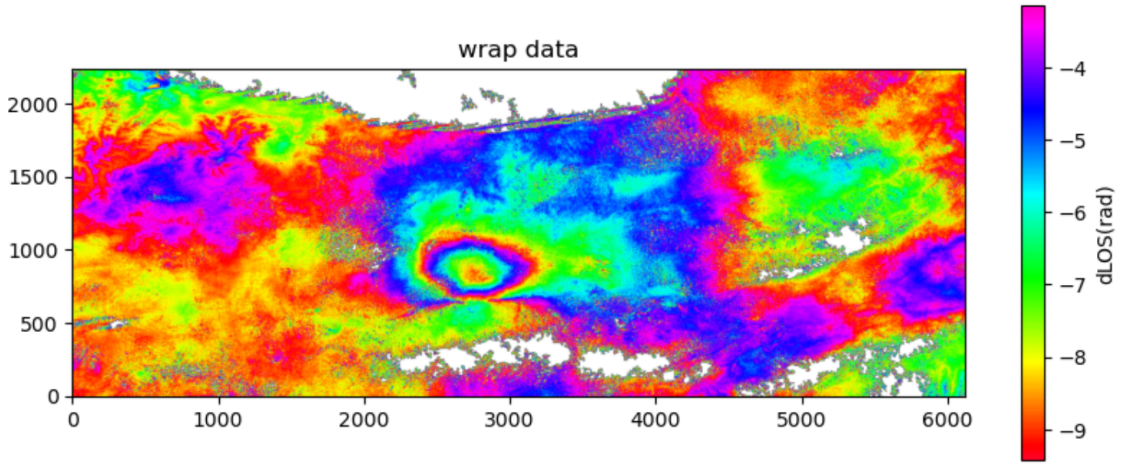


Figure 3.38. A wrapped interferogram generated from a pair of SAR acquisitions, depicting the coseismic ground deformation in radian along the satellite's LOS caused by the 23 November 2022 Düzce earthquake (M_w 6.0).

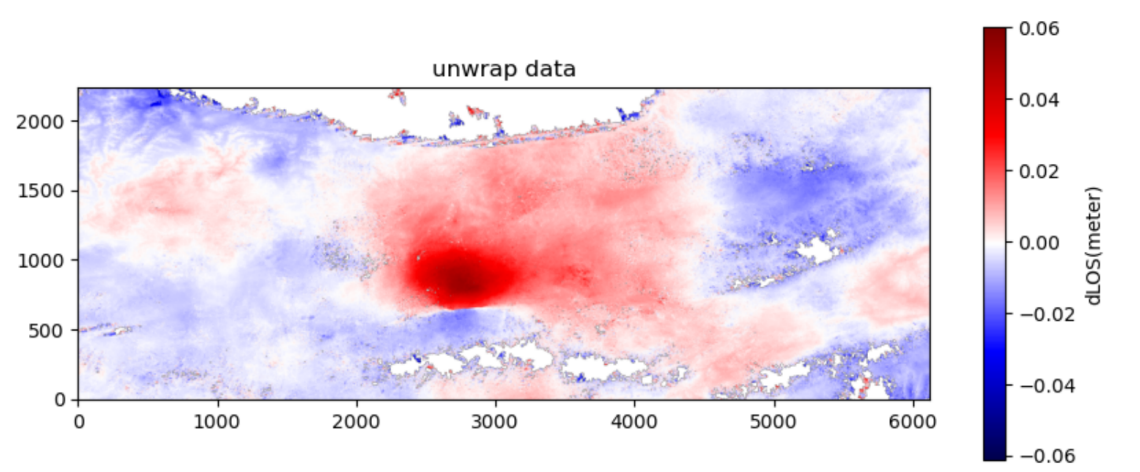


Figure 3.39. The unwrapped data, which represents a continuous map of ground displacement in meters along the satellite's LOS caused by the 23 November 2022 Düzce earthquake (M_w 6.0).

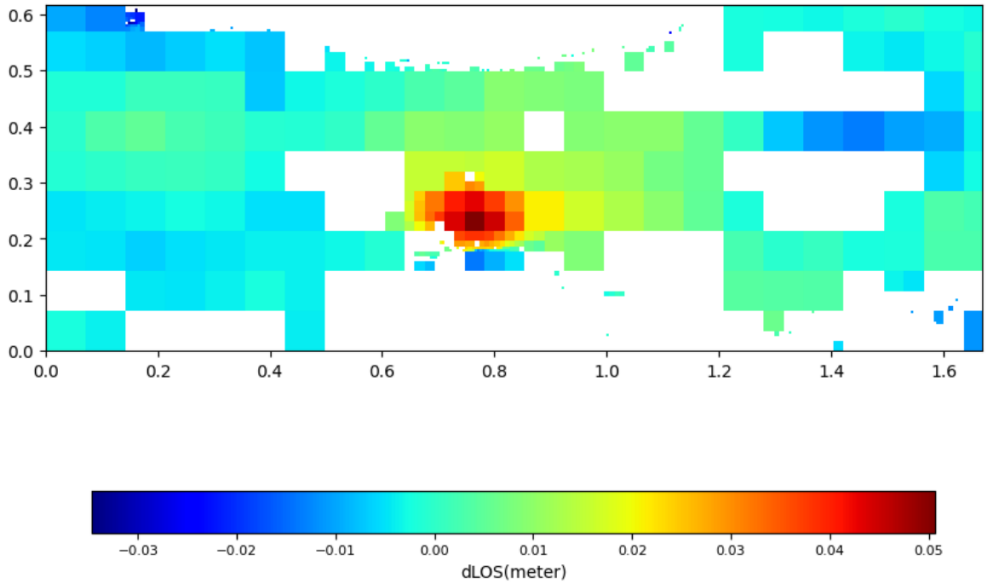


Figure 3.40. Quadtree-resampled map of InSAR LOS displacement showing ground deformation. Each rectangular cell in the plot is colored based on the median LOS displacement value within that cell. The colorbar indicates the scale of displacement in meters, with the plot's axes representing the spatial coordinates of the resampled grid.

The following three figures represent the wrapped-unwrapped interferogram of the Tokat-Sulusaray Earthquake (18 April 2024) for ascending orbit and the quadtree-resampled map of InSAR LOS displacement.

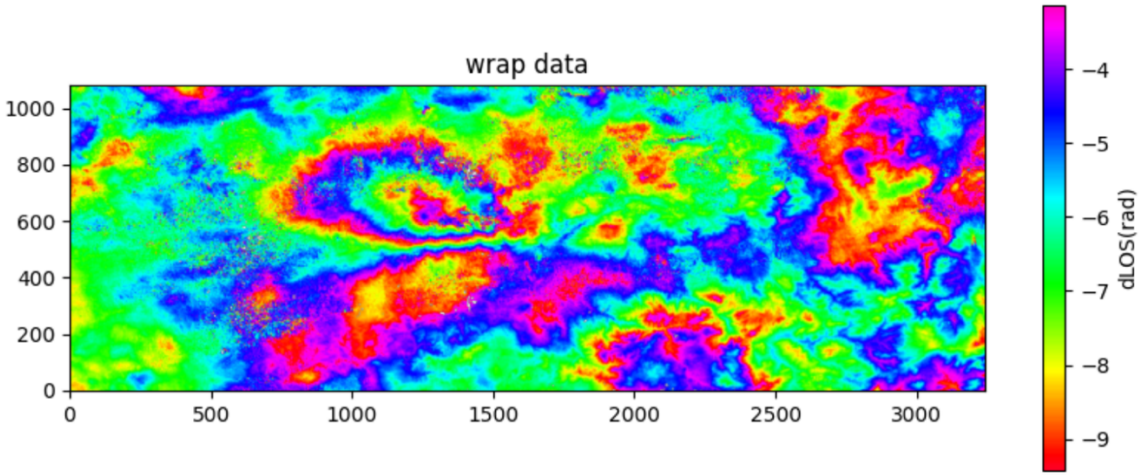


Figure 3.41. A wrapped interferogram generated from a pair of SAR acquisitions, depicting the coseismic ground deformation in radian along the satellite's LOS caused by the 18 April 2024 Tokat earthquake (M_w 5.6).

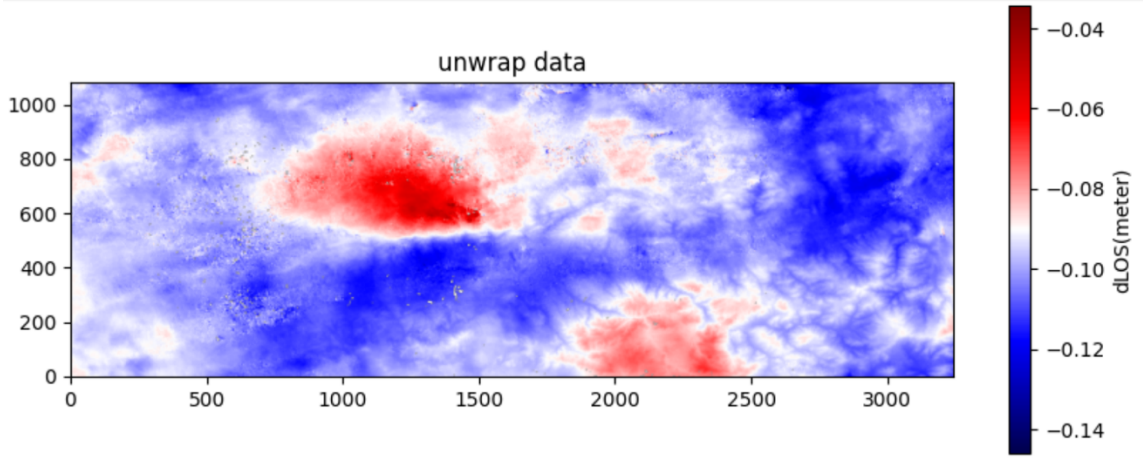


Figure 3.42. The unwrapped data, which represents a continuous map of ground displacement in meters along the satellite's LOS caused by the 18 April 2024 Tokat earthquake (M_w 5.6).

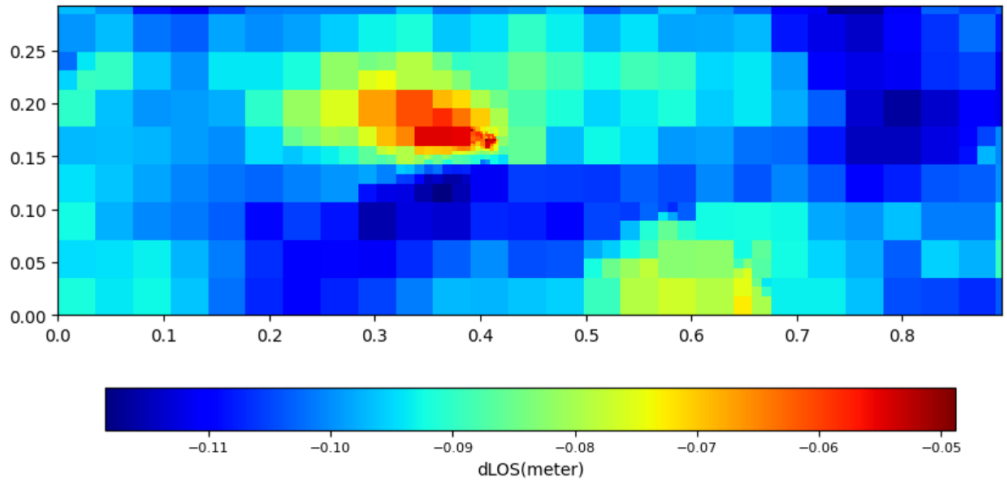


Figure 3.43. Quadtree-resampled map of InSAR LOS displacement showing ground deformation caused by 18 April 2024 Tokat earthquake. Each rectangular cell in the plot is colored based on the median LOS displacement value within that cell. The colorbar indicates the scale of displacement in meters.

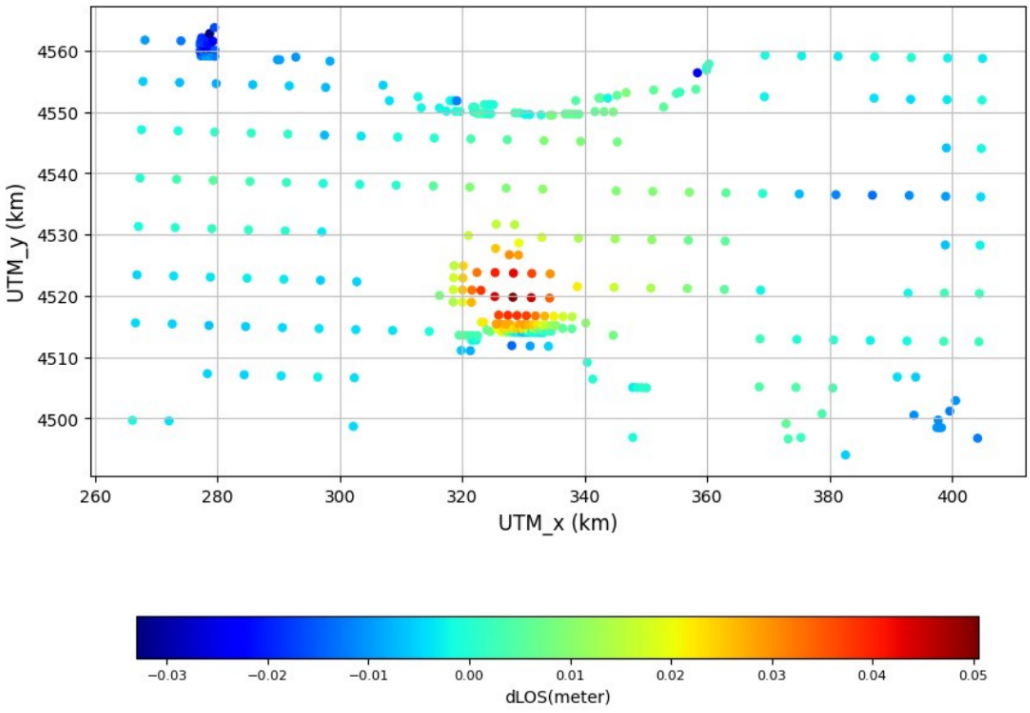


Figure 3.44. Quadtree-resampled map of InSAR LOS displacement due to Düzce-Gölyaka Earthquake 2022. A scatter plot showing the ground deformation from the interferogram, with data points representing the focal points of a quadtree grid. The color map indicates the LOS displacement in meters.

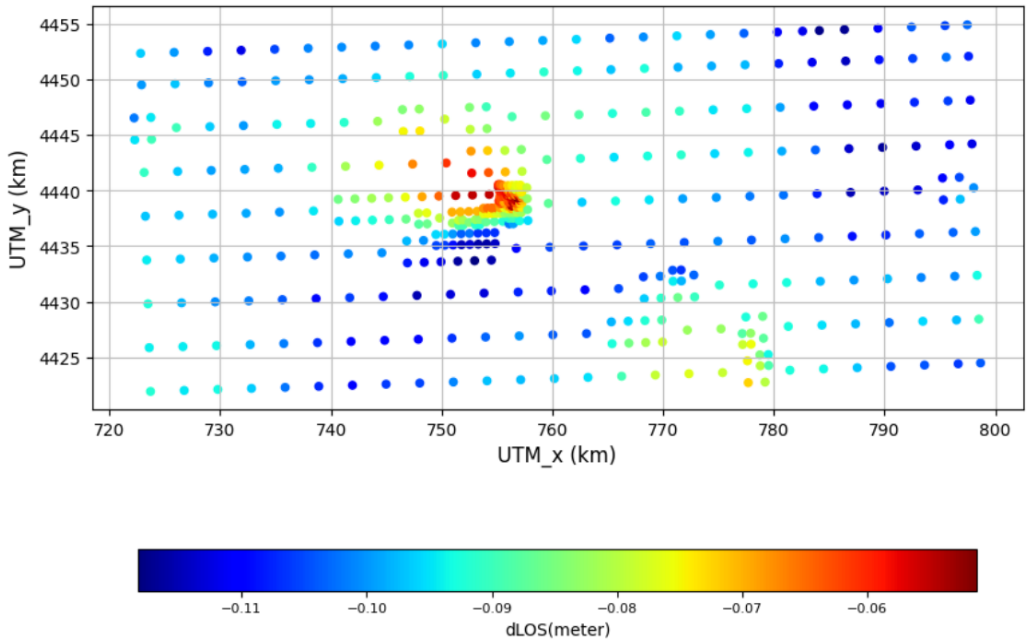


Figure 3.45. Quadtree-resampled map of InSAR LOS displacement due to Tokat-Sulusaray Earthquake 2024. A scatter plot showing the ground deformation from the interferogram, with data points representing the focal points of a quadtree grid. The color map indicates the LOS displacement in meters.

The next stage of the data processing involves exporting the output data into a file. For example, a structured format compatible with the *okinv* code is used, which consists of seven columns: the x and y coordinates (in kilometers), the LOS displacement (in meters), the x, y, and z components of the unit LOS vector, and a unique identifier for each data point. This structured output facilitates integration with subsequent modeling and analysis software.

3.3.1. Forward Model

First, we define the reference latitude and longitude values at the SW corner of the model. Then, the model is obtained by giving a vector of fault parameters, consistent with the geometry of the surface rupture (Table 3.4). For the two earthquakes, slip is predominantly strike-slip, consistent with the moment tensor solutions obtained from KOERI.

Table 3.4. Initial source parameters for forward modeling.

Okada Modeled Earthquake	November 23, 2022 Düzce Earthquake	April 18, 2024 Tokat Earthquake
Strike	252	163
Dip	62	66
Rake	-170	-24
Slip (m)	0.25	0.2
x (m)	334265	755000
y (m)	4515000	4438000
Length (m)	11000	6000
Top (m)	2500	2000
Bottom (m)	18000	14000
Elastic Parameter (GPa)	30e9	30e9

Geophysical modeling of the deformation field can be performed using an analytical solution such as the Okada model (1985), which calculates surface displacements from a rectangular dislocation source in an elastic half-space. This model uses fault geometry (Figure 3.37), and elastic parameters (e.g., shear modulus and Poisson's ratio) as inputs to compute a three-dimensional displacement field**.** The resulting 3D displacement vectors are then projected onto the one-dimensional radar LOS to enable a direct comparison with the observed InSAR deformation data (Figures 3.46 and 3.47). This projection is accomplished by applying a unit LOS vector corresponding to the location of each data point, a critical step for inverting the model to fit the measured deformation field. We used a rectangular shear fault function to obtain the model. Then, we compared the data obtained from InSAR and the forward model.

The distributions of residuals between the model and the InSAR data are represented in Figures 3.46 and 3.47 for the November 23, 2022, Düzce-Gölyaka Earthquake and April 18, 2024, Tokat-Sulusaray Earthquake. Residuals in the far field are flat, low in amplitude, and mostly negative, suggesting that the dislocation model slightly overestimates the far-field deformation caused by the earthquake. Closer to the fault trace, the residuals become noticeable (up to 15 cm in range) in both positive and negative values. These larger residuals

may reflect either local complexities in the actual deformation field or local atmospheric artefacts, which require more detailed analysis.

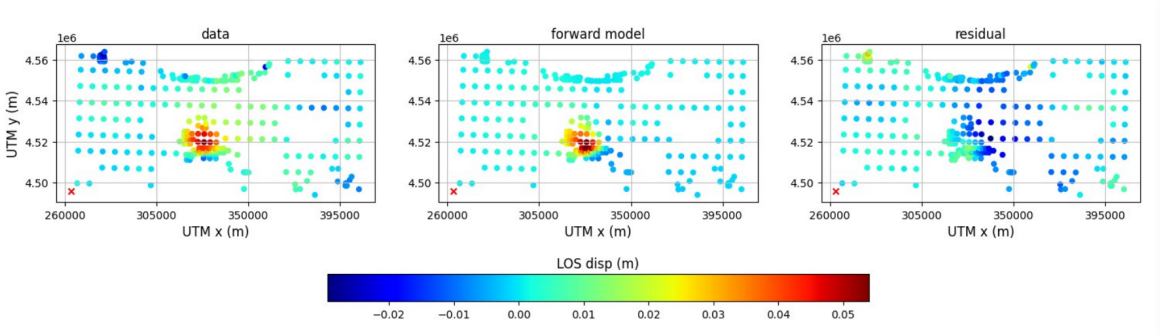


Figure 3.46. Comparison of InSAR data, forward model, and residuals for model optimization. The data, shown in the left panel, have been corrected for a nuisance parameter that can bias the misfit calculation. The center panel displays the forward model's predicted displacement field. The right panel shows the residuals, representing the difference between the corrected data and the model.

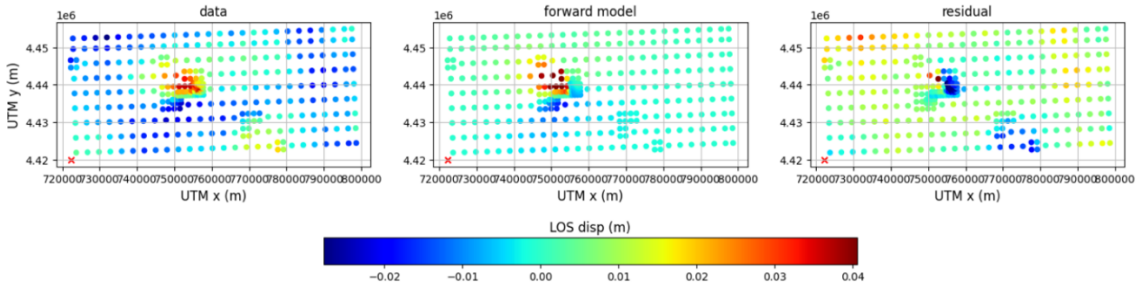


Figure 3.47. InSAR data, inverse model, and residuals for deformation analysis are shown from left to right in meters. The left panel shows the LOS displacement data. The center panel displays the predicted displacement field from the best-fit inverse model. The right panel visualizes the residuals.

In the analysis of InSAR data, another challenge is accounting for a "*nuisance parameter*" related to the unknown zero level of the unwrapped interferogram. This unknown offset arises from the arbitrary selection of a reference point during the phase unwrapping process, which may not correspond to a location of zero ground displacement. Because this offset can introduce a bias across the entire dataset, it can affect the total misfit

calculation substantially. In order to remove this effect, the mean residual (the average difference between the data and the model) is computed and then subtracted from the data. This correction shifts the dataset to align with the model's zero level, resulting in a more geophysically accurate measure of the misfit. For the Düzce-Gölyaka Earthquake, the zero-level shift was calculated as -0.00348 m and the total squared penalty as 0.027878 m^2, while for the Tokat-Sulusaray Earthquake, the zero-level shift was 0.0056 m and the total squared penalty was 0.03387 m^2.

While a single misfit value is a useful quantitative measure, a visual assessment of the residuals is essential for a comprehensive evaluation of the model. By plotting the residuals, the difference between the corrected data and the predicted displacements, we can spatially identify areas where the model fits with the observations and those where notable mismatches still exist (Figures 3.46 and 3.47). We can detect potential issues, such as poorly modeled fault complexities, or pinpoint localized noise that persists in the data, thereby indicating areas for further refinement of the geophysical model.

3.3.2. Inverse Model

A second modeling stage is essential for inferring the physical source of an observed deformation field by refining slip distributions over the fault. This process begins with a forward model as the initial solution, commonly the Okada model (1985), which analytically computes surface displacements from a rectangular dislocation in an elastic half-space. Through inversion, model parameters such as fault location, geometry, and slip are systematically adjusted to minimize the difference between the predicted displacement field and geodetic observations, for example, from InSAR analysis results (Figures 3.48 and 3.49). Fine-tuned fault geometry results are shown in Table 3.5.

Table 3.5. Fault parameters obtained from inversion.

Final fault parameters	November 23, 2022 Düzce Earthquake	April 18, 2024 Tokat Earthquake
Strike	254.4095	201.0242
Dip	61.5753	53.973
Rake	-158.0	50.343
Slip (m)	0.288	0.145
x (m)	338459.623	752596.619
y (m)	4515264.785	4438899.618
Length (m)	16999.995	9516.23
Top (m)	4847.160	10.278
Bottom (m)	13207.193	10909.996
Elastic Parameter (GPa)	30e9	30e9

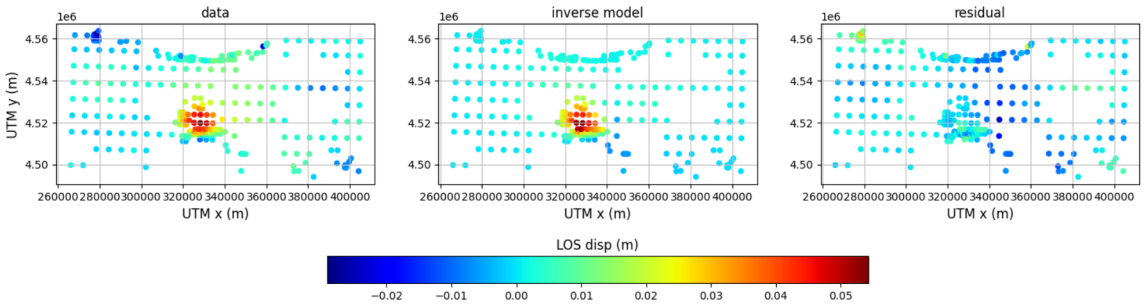


Figure 3.48. InSAR data, inverse model, and residuals for deformation analysis are shown from left to right for the Düzce earthquake. The left panel shows the LOS displacement data. The center panel displays the predicted displacement field from the best-fit inverse model. The right panel visualizes the residuals. All displacements are in meters, and the plots are shown in a UTM coordinate system.

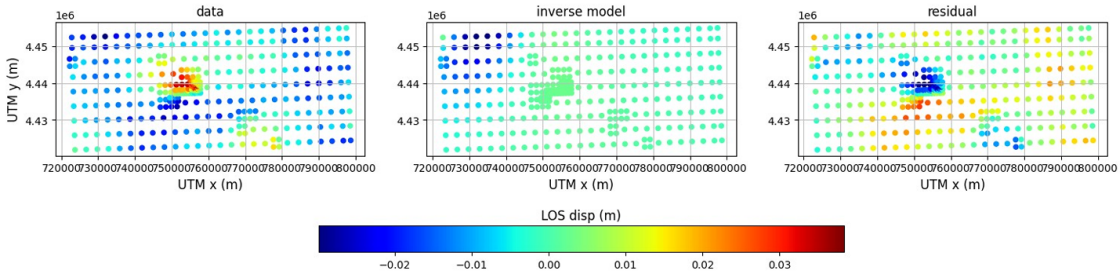


Figure 3.49. InSAR data, inverse model, and residuals for deformation analysis are shown from left to right for the Tokat earthquake. The left panel shows the LOS displacement data. The center panel displays the predicted displacement field from the best-fit inverse model. InSAR data, inverse model, and residuals for deformation analysis are shown from left to right for the Tokat earthquake. The right panel visualizes the residuals.

3.3.3. Regularization

Geophysical inversion, as applied to coseismic deformation, requires a shift from simple, uniform fault models to more complex, distributed slip models to accurately represent the true rupture process. This is achieved through a linear inversion procedure, discretizing the fault plane into a grid of smaller rectangular sub-faults. For each of these sub-faults, a forward model, such as the Okada model, is used to calculate the surface displacement at every observation point on the interferogram. These calculations produce a set of Green's functions, which are then compiled into a design matrix that links the unknown slip on each sub-fault to the observed surface displacement data.

The resulting system of equations is typically non-unique because the number of independent data points is often less than the number of unknown slip values on the sub-faults. This situation necessitates the use of regularization to obtain a stable and geophysically reasonable solution. Regularization addresses the non-uniqueness of the problem by introducing a constraint on the solution, such as requiring a smooth slip distribution. This is mathematically achieved by constructing a smoothing matrix that fine-tunes abrupt changes in slip between adjacent sub-faults. This matrix is then incorporated into the inverse problem, thereby stabilizing the solution and preventing the inversion from producing a physically unrealistic, highly fluctuating slip pattern.

The regularized inverse problem is solved by minimizing a combined objective function that includes both the data misfit (penalty) and the slip roughness, weighted by a smoothing parameter, κ. The choice of this parameter is critical, as it controls the balance between fitting the data and achieving a smooth slip distribution. A high κ value yields a very smooth model that may not accurately fit the data, while a low κ value may lead to a better data fit but an overly rough and less consistent slip distribution. To select an optimal value for κ, a common practice is to plot the total misfit against the slip roughness for a range of κ values, creating a graph known as an L-curve (Figures 3.50 and 3.53). This curve's characteristic shape, with its elbow or inflection point, visually identifies the ideal balance between model simplicity and data fidelity. The optimal value of κ is typically chosen from this elbow, as it represents a model that is not overly rough while still providing reasonable agreement with the data. Once the optimal slip distribution is determined, a final step is to plot the predicted deformation field (Figures 3.51 and 3.54) and the residuals (Figures 3.52 and 3.55) to visually confirm the quality of the inversion and identify any remaining discrepancies.

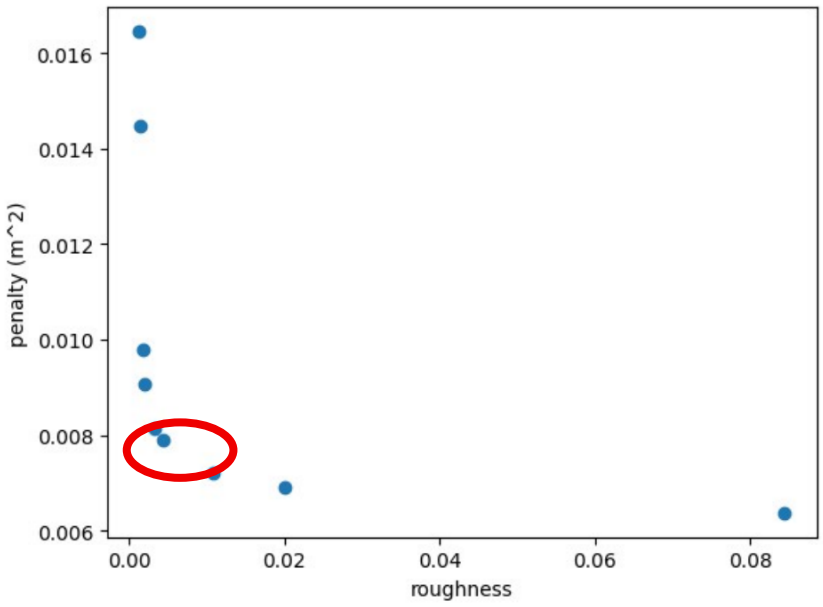


Figure 3.50. Roughness against misfit for Düzce earthquake. Models that lie between the extremes, around the elbow of the graph, achieve a balance by fitting the data well without being overly rough. The selected κ, shown as a red circle, is 0.05.

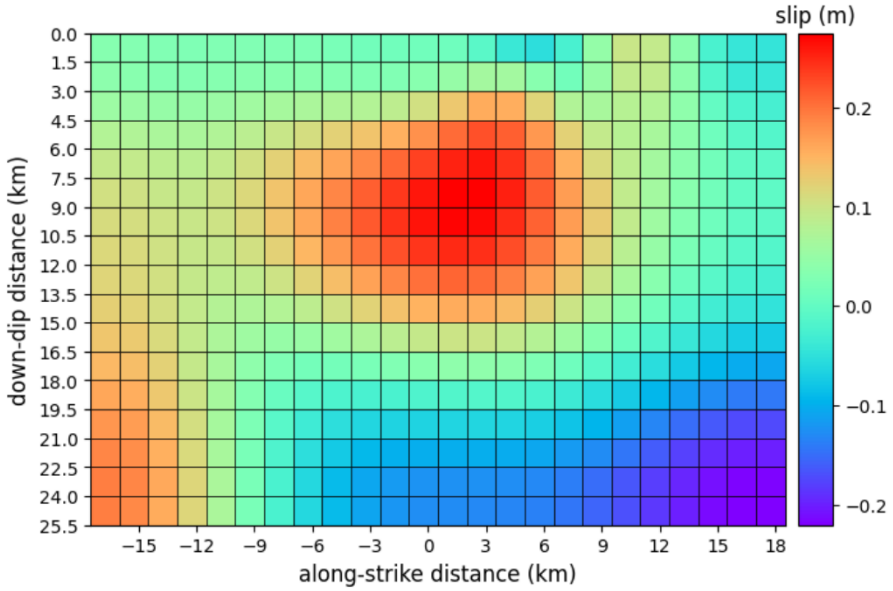


Figure 3.51. Slip distribution model obtained for the Düzce Earthquake. The x-axis shows the strike distance (in km) and the y-axis shows the down-dip distance. The colorbar indicates slip in meters.

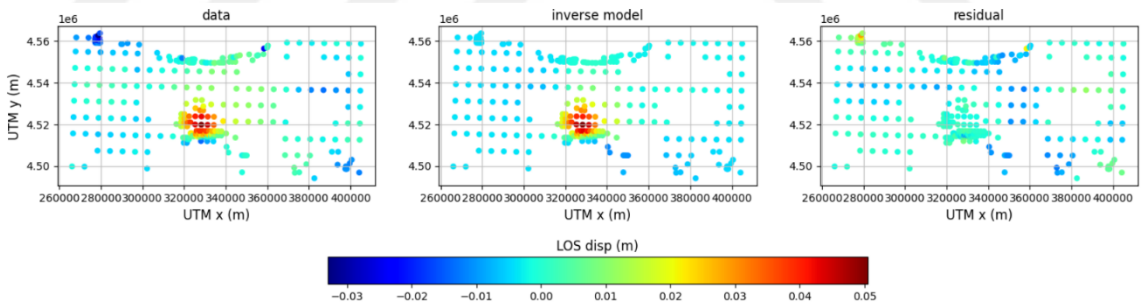


Figure 3.52. InSAR data, regularized inverse model, and residuals for deformation analysis of the Düzce Earthquake are shown from left to right. The left panel shows the LOS displacement data. The center panel displays the predicted displacement field from the best-fit inverse model. The right panel visualizes the residuals. Total squared penalty is 0.00908 m^2.

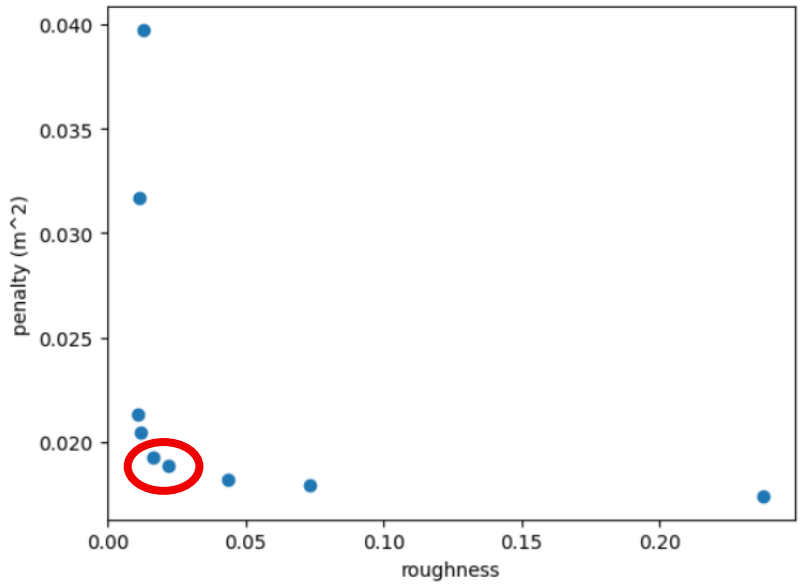


Figure 3.53. Roughness against misfit for the Tokat-Sulusaray earthquake. Models that lie between the extremes, around the elbow of the graph, achieve a balance by fitting the data well without being overly rough. The selected κ, shown as a red circle, is 0.05.

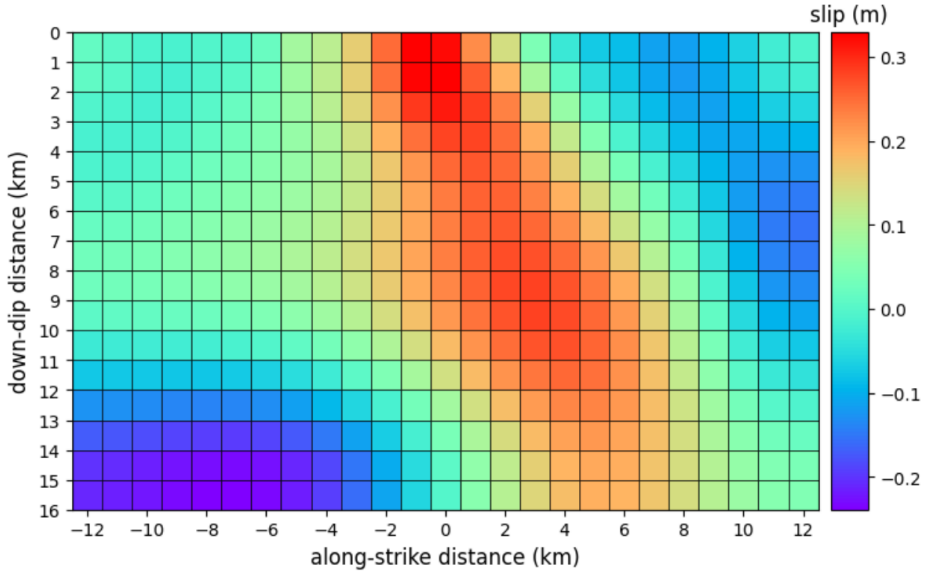


Figure 3.54. Slip distribution model obtained for the Tokat Earthquake. The x-axis shows the along strike distance (in km) and the y-axis shows the down-dip distance. The colorbar indicates slip in meters.

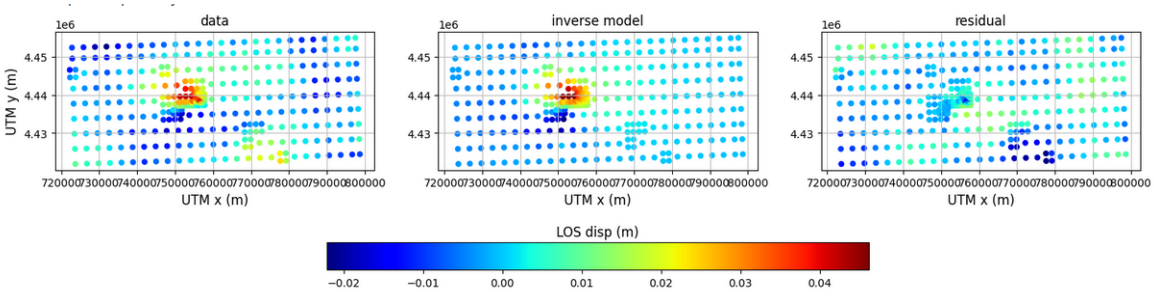


Figure 3.55. InSAR data, regularized inverse model, and residuals for deformation analysis of the Tokat-Sulusaray earthquake are shown from left to right. The left panel shows the LOS displacement data. The center panel displays the predicted displacement field from the best-fit inverse model. The right panel visualizes the residuals. Total squared penalty is 0.088469 m².

4. RESULTS AND INTERPRETATIONS

4.1. Coda-derived Seismic Moment and Moment Magnitudes

We focused on quantifying seismic energy release using $M_{w\text{-}coda}$ estimates for local to regional events of small to moderate magnitude scale (ranging from M_w 3.5 to M_w 6.06) that occurred between 2018 and 2022, including the 2024 Tokat mainshock and its foreshock sequence within and around the NAFZ. We applied the coda calibration technique using the CCT, where synthetic coda wave envelopes were empirically generated subsequent to the empirical approach described by Mayeda et al. (2003). This approach allows for the simultaneous estimation of source, path, and site effects by lowering the difference between measured and synthetic coda envelopes. It relies on a radially symmetric one-dimensional path model, which has proven effective in reducing variance for events located within a 13 to 580 km range in the study area.

Reference moment magnitudes and apparent stress values play a crucial role in determining broadband site correction terms, which are used to convert distance-corrected coda amplitudes into source spectra expressed in N-m. As in other S-wave coda applications, we stacked narrowband envelopes from the North-South and East-West components of broadband waveforms recorded at 51 seismic stations across the region. The method has also shown reliability for smaller events that are typically difficult to characterize using conventional waveform modeling, making it suitable for building a consistent M_w catalog that can support updated PSHA models (e.g., Onur et al., 2020) and routine network operations.

From the estimated source spectra, we derived source-related variables including seismic moment (M_0), Brune corner frequency (f_c), radiated energy (E), and apparent stress (σ_A). This study represents the first comprehensive catalog of moment magnitudes for earthquakes in this region during the 2018–2022 period. The resulting coda-based magnitude estimates show strong potential for supporting nationwide implementation, enabling near real-time M_w calculations. Once fully adopted across Türkiye, this methodology could offer valuable insights into earthquake source properties, such as regional variations in apparent

stress, and help achieve more precise, region-specific seismic hazard assessments in this tectonically active zone.

As observed in other applications of the CCT, the assumption of a one-dimensional path model proved highly effective, even in this tectonically complex region. Our analysis revealed that the frequency-dependent interstation standard deviations (average per station pair, see Figure 2.7) were significantly reduced to a range of 0.05 to 0.16 after applying path corrections. The most notable improvements occurred in the low-frequency range (0.05 to 0.5 Hz), where the corrected amplitudes exhibited standard deviations as low as 0.05 to 0.06. This suggests that the region behaves relatively homogeneously at longer periods. Even at higher frequencies (3 to 8 Hz), the path corrections led to substantial reductions in variability, highlighting the robustness of the coda-based approach.

These results align well with previous research. For instance, Mayeda et al. (2003) found that amplitude estimates based on coda waves exhibited three to five times less interstation variability compared to traditional direct-phase measurements such as P_g and L_g. In their study, typical coda amplitude scatter ranged from 0.07 to 0.1 across the 0.05 to 8.0 Hz frequency band, while direct-phase measurements showed significantly higher variability. Similarly, Eken et al. (2004) reported that after applying distance corrections, the interstation scatter for coda amplitudes of coda waves ranged between 0.07 and 0.15. In contrast, L_g and surface wave amplitudes showed much greater scatter, between 0.27 and 0.45, representing a three- to fourfold increase in variability.

These consistent results reinforce the effectiveness of coda waves in averaging out both source and path heterogeneities, leading to significantly more stable amplitude measurements compared to traditional direct-phase methods. The reduced scatter observed after applying corrections in this study underscores the reliability of the coda-based approach for regional seismic calibration.

Figure 4.1 summarizes the final outcomes of the coda calibration process, including the validation of M_w and σ_A, as well as the scaling behavior of σ_A and the relationship between f_c and seismic moment for events in which 65% or more of the total radiated energy was successfully measured. Panel (a) compares coda-derived M_w on the x-axis with

reference events, shown as red circles, and independent validation events, shown as black squares, indicating strong agreement with 19 waveform-based M_w values. Panel (b) shows σ_A values obtained from coda-based source spectra for both reference (red circles) and validation events (black squares), demonstrating consistent alignment between datasets. Panel (c) shows a scatter plot illustrating the relationship between coda-derived apparent stress and seismic moment for the validation dataset comprising 87 events (black squares) with magnitudes between 3.5 and 4, alongside 49 calibration events (red circles); both sets were filtered to include only events with more than 65% of the total observed energy. Panel (d) displays corner frequency versus seismic moment based on spectral fitting using the Brune (1970) model. Reference lines in panel (d) indicate constant apparent stress levels of 0.01, 0.1, and 1.0 MPa, providing context for stress variations across events.

First, the M_w values estimated from coda-derived spectra using the CCT show excellent agreement with independently obtained waveform-modeled magnitudes for 12 validation events, with an RMS value of only 0.0689. This strong correlation indicates that the method can reliably produce stable M_w estimates, even for smaller earthquakes that fall below the resolution limits of traditional waveform modeling techniques.

Second, the σ_A values derived from the coda-based source spectra also demonstrate consistency across both reference and validation events. These results remained stable regardless of the specific combination of ground-truth reference events used during calibration. This finding is consistent with previous studies, such as Mayeda et al. (2024) in southern California.

Table B.2. provides a summary of the calibration events for which at least 65% of the total measured radiated energy was analyzed in this study. For each event, it lists the earthquake origin details, including Event ID, date, time, latitude, longitude, and depth, along with key source parameters. These include the coda-derived moment magnitude (M_w) with its associated 90 percent confidence interval (CI), as well as reference and validation M_w values. The table also presents calculated apparent stress (σ_A) and corner frequency (f_c), both accompanied by their respective 90 percent confidence intervals. Additionally, reference and validation σ_A values are included for comparative purposes.

The derived values exhibit stable scaling behavior and consistency across recording stations, affirming the robustness of the calibration framework applied. The velocity coefficients v_0, v_1, and v_2 effectively captured the S-wave arrival patterns, while coda envelope characteristics shaped by parameters b_0, b_1, b_2, and γ_0, γ_1, γ_2 showed strong agreement with theoretical expectations. Path-related parameters (p_1, p_2) contributed to accurate regional propagation modeling. Corrections for site effects and wave scattering are modeled through station-specific constants, yielded high-fidelity magnitude estimates with minimal bias across varied geological conditions. All derived calibration parameters used in the estimation process are listed in Figure 4.2.

Using the CCT and utilizing shorter window lengths, we estimated source characteristics such as $M_{w\text{-}coda}$ for these smaller events ($3.5 \leq M_L < 4$), which typically have lower signal-to-noise ratios and limited usable time windows (Table B.3).

Beyond obtaining stable apparent stress (σ_A) estimates for moderate to large earthquakes within the NAFZ, the proposed methodology significantly enhances the reliability of moment magnitude (M_w) estimates for smaller events that are typically below the resolution threshold of conventional waveform modeling. This eliminates the need for converting between M_w and local, band-limited magnitude scales such as M_L or M_D, which are known to introduce systematic biases (e.g., Shelly et al., 2022). The ability to directly estimate M_w for smaller events is especially valuable for PSHA, which relies on robust and consistent M_w values. This is particularly important in regions where earthquake catalogs must be complete down to magnitudes of M_w 2 to 3, depending on the density of the seismic network (Onur et al., 2020).

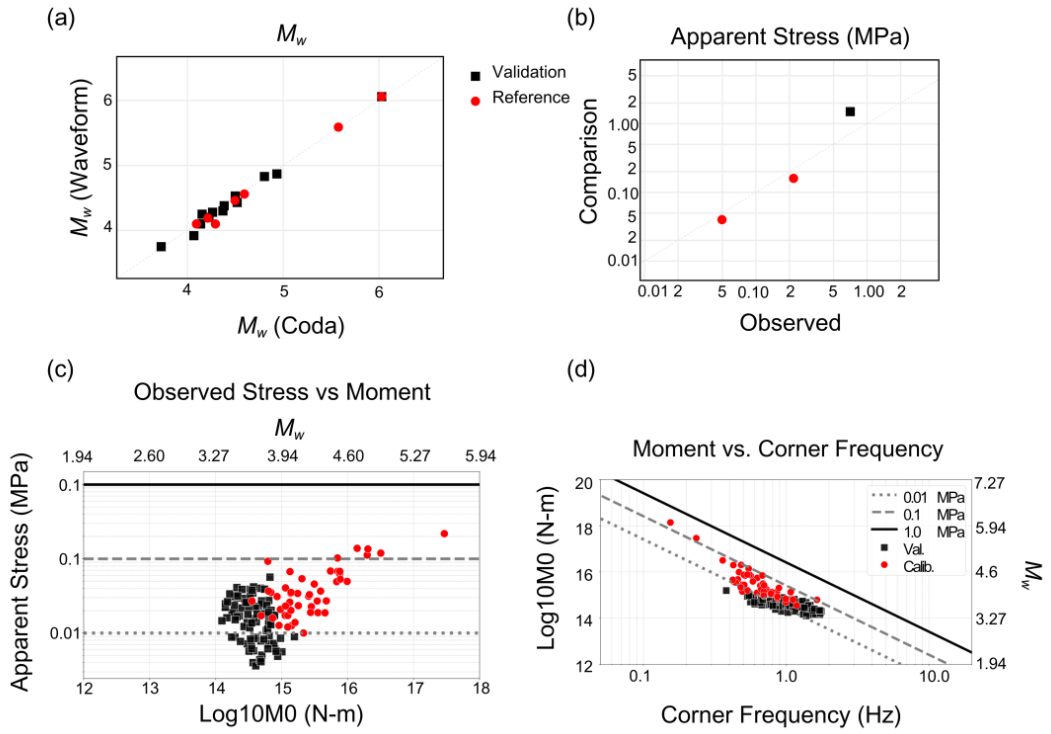


Figure 4.1. Validation of coda calibration results. (a) Comparison of coda-derived M_w with reference and validation events. (b) σ_A from coda spectra for reference and validation events. (c) Relationship between coda-derived σ_A and M_0 for validation and calibration events. (d) f_c versus M_0 for two different datasets. RMS value of 0.0689 was obtained from the comparison between the coda-derived M_w's and the reference M_w's.

Frequency		Velocity			Beta			Gamma			Length (Sec)	
Low	High	V0	V1	V2	B0	B1	B2	G0	G1	G2	Min	Max
0.02	0.03	0.00	0.00	0.00	0.00	0.00	0.00	0.00	0.00	0.00	600.0	2500.0
0.03	0.05	0.00	0.00	0.00	0.00	0.00	0.00	0.00	0.00	0.00	500.0	1500.0
0.05	0.10	2.955	3.76	1.5315	-0.0001	0.10	1499.9981	0.5015	-32.8675	101.00	400.0	1000.0
0.10	0.20	2.6836	48.852	120.1815	-0.0008	0.10	1500.00	0.4904	-41.3133	101.00	200.0	900.0
0.20	0.30	4.3824	5000.00	2184.7421	-0.0032	0.10	1500.00	0.0153	-70.4845	76.9478	160.0	700.0
0.30	0.50	3.4647	204.0852	110.5805	-0.0024	3.9842	1500.00	0.0925	-19.3861	10.4704	150.0	700.0
0.50	0.70	3.3026	117.3786	69.4187	-0.0006	9.0123	1500.00	0.2343	-11.3171	1.00	110.0	400.0
0.70	1.00	3.3899	133.6187	82.3333	-0.008	0.10	78.5754	0.2152	-14.4642	5.4394	80.0	250.0
1.00	1.50	3.4045	106.5418	60.9669	-0.011	0.10	1500.00	0.1809	-17.7367	3.8975	60.0	120.0
1.50	2.00	3.6032	163.0158	93.0708	-0.0123	0.10	1500.00	0.1952	-23.6896	7.257	50.0	120.0
2.00	3.00	3.9275	299.3341	159.8507	-0.014	0.10	1500.00	0.00	-92.9659	95.0992	50.0	100.0
3.00	4.00	4.6117	812.2724	346.315	-0.0118	6.0045	1500.00	0.0119	-96.7903	101.00	40.0	100.0
4.00	6.00	5.0853	1208.754	432.173	-0.0008	20.00	1151.8137	0.0142	-97.1099	101.00	40.0	100.0
6.00	8.00	4.8312	784.4389	297.6469	0.0005	20.00	782.0651	0.00	-65.3752	69.9972	10.0	100.0

Figure 4.2. Calibration parameters used in the CCT for the Central NAFZ. $v_{0,1,2}$: S-wave arrival velocity; $b_{0,1,2}$ and $\gamma_{0,1,2}$ characterize coda envelope shape; $p_{1,2}$: path effects; station-specific constants account for site amplification and the S-to-coda transfer parameter, *T(f)*.

4.2. M_L-M_w Magnitude Conversion Relation

Moment magnitude (M_w) is widely regarded as the most reliable and physically meaningful measure of earthquake size, as it does not saturate at higher magnitudes and is directly linked to seismic moment, which reflects the actual energy released during fault rupture (Hanks & Kanamori, 1979). In contrast, traditional earthquake magnitude scales such as M_L, m_b, and M_s tend to saturate for larger events, often resulting in significant underestimation of earthquake size (Kanamori, 1983; Scordilis, 2006). To explore this further, we compared coda-derived M_w values with catalog magnitudes ($M_{L\text{-KOERI}}$, see Equation 4.1.) for all events in our dataset. This comparison enabled us to establish a second-degree polynomial relationship through regression analysis, as illustrated in Figure 4.3.

$$M_{w-Coda} = -1.1916 \pm 0.414 \cdot M_{L-KOERI} + 0.2233 \pm 0.047 \cdot M^2{}_{L-KOERI} + 5.1370 \pm 0.893 \quad (4.1.)$$

Unlike M_w, which is directly tied to seismic moment and does not saturate at higher magnitudes, M_L is a narrowband measure centered around ~2.0 Hz and lacks a physical basis for representing earthquake size. The CCT significantly improves the accuracy of earthquake magnitude estimates, particularly for smaller events that are difficult to measure using traditional earthquake sizing methods. The primary advantage of the CCT is that it provides a reliable calculation of Mw. This approach eliminates the need for converting between different magnitude scales, such as M_L or M_D, a process known to introduce systematic biases. This not only solves the problems associated with these less-accurate empirical models but also provides high-quality data that can be used to improve them for future use when a direct M_w calculation isn't possible.

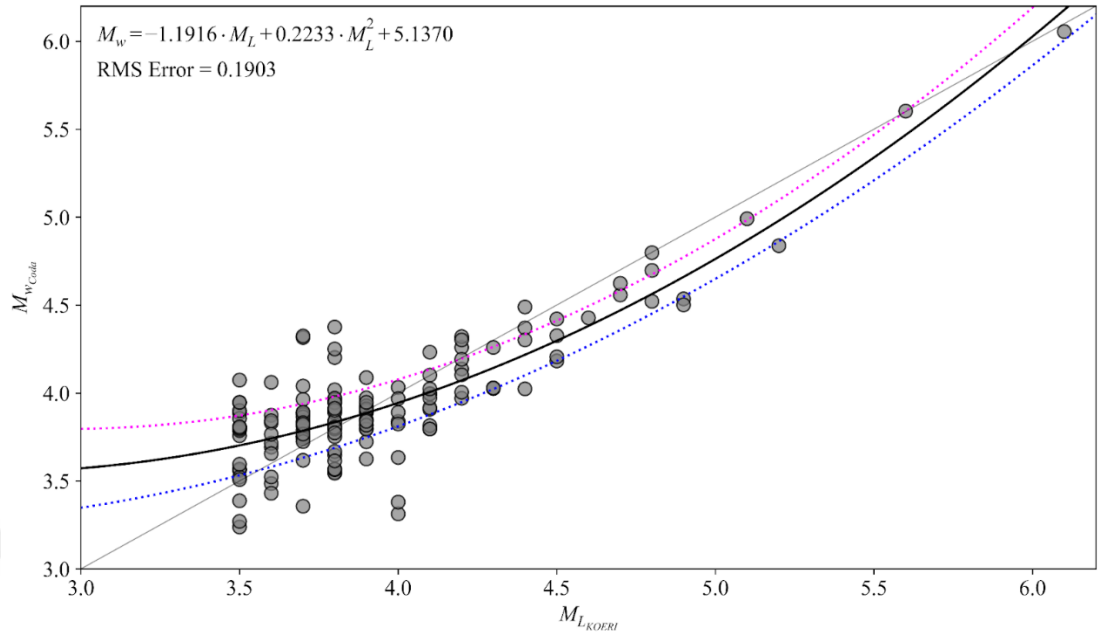


Figure 4.3. The scatter plot shows the relationship between $M_{W\text{-}Coda}$ and $_{ML\text{-}KOERI}$. A 2nd-order polynomial fit (solid black line) represents the non-linear trend, with ±1σ residuals indicated by dotted lines. The 1:1 line is shown in grey. The polynomial is used because $M_{L\text{-}KOERI}$ saturates at higher magnitudes, making the relationship with $M_{W\text{-}Coda}$ nonlinear. The calculated RMS error is 0.1903.

4.3. Source Scaling: Non-self-similar Character of Seismicity in the Region

Seismic scaling relationships serve as a critical framework for evaluating the consistency of the physical mechanisms underlying earthquakes across a broad spectrum of magnitudes. While static indicators of seismic moment, such as M_0, are well established and widely accepted within the geophysical community, dynamic parameters remain less well constrained. These dynamic measures are often highly sensitive to the analytical methodologies employed, with even identical datasets producing markedly different outcomes depending on the specific techniques applied.

The concept of self-similarity in earthquake source scaling, introduced by Aki in 1967 and expanded by Kanamori and Anderson in 1975, suggests that seismic moment (M_0) scales proportionally with the inverse cube of corner frequency *(f_c)*. This relationship implies that earthquake behavior, including radiated energy *(E_R),* remains consistent across magnitudes.

Several studies, such as those by McGarr (1999), Ide and Beroza (2001), have supported the idea that the proportion of radiated energy to seismic moment *(ER/M₀)* stays nearly constant.

However, newer research challenges the universal applicability of this scaling. Kanamori and Rivera (2004) proposed a modified relationship, $M_0 \propto f_c^{(-(3+\varepsilon))}$, with ε representing a slight deviation that better fits observed data. This model reflects more nuanced earthquake behavior, especially among smaller events or across tectonically varied regions, as shown in a study by Abercrombie (1995).

The reliability of source characterization parameters such as M_0, f_c, and E_R depends heavily on environmental complexities like wave propagation, attenuation, local geology, and radiation patterns. In this context, the observed relationship between stress drop and M_0 demonstrates internal consistency, lending credibility to these estimates. Measurements in the NAFZ reveal σ_A values and corner-frequency trends similar to those seen in central Italy (Morasca et al., 2022) and Ridgecrest (Mayeda et al., 2024), yet noticeably lower than those in more stable regions such as eastern Canada (Bent et al., 2024). This discrepancy likely stems from differing petrophysical characteristics and thermal conditions across seismogenic settings.

Consistent with findings from other regions, recent work by Mayeda et al. (2024) shows that σ_A tends to increase with earthquake magnitude, levels off around M_w 5.5, highlighting a pattern in rupture dynamics that may not conform strictly to the self-similar model.

Although the magnitude range in this dataset is somewhat limited, there is a noticeable increase in σ_A with rising magnitude, consistent with findings from Morasca et al. (2022) and Mayeda et al. (2024). This upward pattern has also been observed by Malagnini et al. (2014), and reinforced through Ridgecrest sequence analyses (Abercrombie et al., 2024) and direct wave investigations of the Amatrice sequence in Italy (Calderoni and Abercrombie, 2023). Similar behavior was noted by Yoo et al. (2011) in the Korean Peninsula using empirical coda calibration, which showed an increase in scaled energy with seismic moment.

In the western NAFZ, Özkan et al. (2024) reported non-self-similar scaling in local crustal earthquakes ranging from M_w 2.5 to M_w 5.6. Their methodology involved a physically grounded modeling approach using analytical expressions and iterative optimization to align observed and synthetic coda wave envelopes, factoring in both source and path effects.

Echoing those results, the present study which focused on central NAFZ seismic events from 2018 to 2022 with magnitudes between M_L 3.5 and M_L 6.0, shows a similar variation in seismic moment with stress drop, indicating non-self-similar behavior. This consistency across segments of the NAFZ highlights the area's intricate tectonic architecture, shaped by diverse fault characteristics and stress regimes. The variability in M_0 with respect to σ_A points to distinct rupture mechanisms across magnitudes, with larger earthquakes in this region.

Moreover, the corner frequency and moment distribution matches theoretical predictions, with events distributed along reference lines corresponding to apparent stress levels of 0.01, 0.1, and 1.0 MPa. For events with M_w between 3.5 and 6, the f_c–M_0 data from central Italy (Morasca et al., 2022) and Ridgecrest (Mayeda et al., 2024) mostly fall within the 0.1–1 MPa reference range.

Taken together, values observed in our study area tend to fall below the 0.1 MPa reference curve for events smaller than 4.6 (Figure 4.1c), suggesting that apparent stress is considerably lower than that in these comparison regions. This finding likely reflects a reduced seismic efficiency, where less energy is radiated per unit of seismic moment. The underlying cause appears to be linked to specific regional characteristics, including the local geophysical environment, fault zone properties, and broader tectonic framework.

4.4. InSAR & Elastic Dislocation Model Results

In this thesis, we produced four interferograms from two ascending and two descending orbit SAR images to study the Düzce-Gölyaka and Tokat-Sulusaray events. The first two interferograms, both with a 12-day temporal baseline, were generated from imagery acquired in November 2022 to investigate the deformation of the Düzce-Gölyaka

earthquake. Specifically, the ascending orbit on Path 160 images from November 15 and 27, and the descending orbit on Path 138 images from November 14 and 26 were chosen. The remaining two interferograms were created from April 2024 imagery to investigate the deformation due to the Tokat-Sulusaray earthquake. An interferogram from ascending orbit on Path 14 was formed using images from April 16 and 28, and an interferogram was formed from descending orbit on Path 94 using images from April 10 and 22. All four interferograms maintained a consistent 12-day separation between their acquisition dates.

For the Düzce-Gölyaka interferogram from the descending orbit, the ground deformation was not fully resolved (Figure 3.22). This is likely because the strike-slip motion of the earthquake is oriented primarily along the satellite's flight path, making the sensor less sensitive to this type of horizontal displacement. Additionally, residual atmospheric effects that were not fully corrected may have contributed to the incomplete deformation signal. It was also noted that there was no clear point in either the wrapped or unwrapped interferograms where the direction of deformation changed, which may be related to the fault's dip angle or the local topography.

After applying atmospheric corrections to the interferograms, we observed distinct deformation signals. The wrapped fringe patterns from the Tokat-Sulusaray event show a characteristic butterfly shape (Figure 3.28). This pattern can indicate the satellite's high sensitivity to motion parallel to its LOS, which is movement in the upward or downward direction. Despite the known right-lateral strike-slip faulting, the observed fringe patterns might suggest that the earthquake also had a dip-slip component. Analysis of the cross-sections taken perpendicular to the fault shows displacement in LOS along profiles 2 and 4 (Figure 3.27).

For the Tokat-Sulusaray Earthquake, the unwrapped interferogram from the ascending orbit revealed that the earthquake occurred on an approximately east-west trending, right-lateral strike-slip fault (Figure 3.29). When viewed in the descending orbit, the deformation appears to be oriented in a northeast-southwest direction, which is a known effect of the satellite's orbital geometry (Figure 3.36).

Therefore, in the slip modeling, interferograms obtained from ascending images for Düzce-Gölyaka and Tokat-Sulusaray earthquakes were used. The distributions of residuals between the calculated model and InSAR data are represented in Figures 3.46 and 3.47.

For the Düzce-Gölyaka earthquake, the zero-level shift was calculated to be -0.00348 m, indicating a minor overall subsidence in the interferogram. The total squared penalty from the inversion model was 0.01817 m^2, which quantifies the misfit between the model and the observed data (Figure 3.48). For the Tokat-Sulusaray earthquake, the zero-level shift was found to be 0.0056 m. The total squared penalty for this event was 0.03387 m^2 (Figure 3.49).

The total squared penalty from the regularized inversion model was calculated as 0.00908 m^2 for the Düzce-Gölyaka earthquake, and as squared penalty is 0.0884 m^2 for the Tokat-Sulusaray earthquake (Figures 3.52-3.55).

The fault parameters from the inversion for the Düzce earthquake show a strike of 254.409°, a dip of 61.575°, and a rake of -158.0°. The maximum slip was calculated to be 0.288 m. The fault plane has a substantial length of nearly 17.0 km and extends from the surface 3 km down to a bottom depth of approximately 20 km. The fault is located at the x and y coordinates of 338459.623 m and 4515264.785 m, respectively. An elastic parameter of 30 GPa was used for the model.

Our preliminary inversion provides a refined estimate of the source parameters, and a comparison with the model of Karaca et al. (2024) reveals both geometric and kinematic differences that are instructive for further refinement. Geometrically, our solution suggests a fault strike of ~254°, which is about 10° different from the 264° strike reported in the reference study. The dip angle from our model (61.6°) is slightly shallower than the 66° dip of Karaca et al., the latter being more consistent with regional geology. Kinematically, our model indicates a rake of -158°, which is similar to the -165° rake highlighted by Karaca et al. While our models are in a similar oblique-compressive regime, these minor discrepancies underscore the sensitivity of the inversion to fault geometry and highlight parameters, particularly dip and rake, that could be better constrained in future refinements.

Moreover, our inversion model indicates source parameters that show notable differences compared to the KOERI solution. Our strike estimate is approximately 254°,

differing only about 3° from KOERI's 257°. The dip angle from our model (61.6°) is shallower than KOERI's 73°. Kinematically, our rake value of -158° suggests an oblique compressional mechanism, whereas KOERI's rake of -178° indicates nearly pure right-lateral strike-slip motion. These differences emphasize the importance of refining the fault geometry constraints in future iterations.

For the Tokat earthquake, the determined fault parameters include a strike of 201.0242°, a dip of 53.973°, and a rake of 50.343°. The calculated maximum slip was 0.145 m. This fault plane has a length of approximately 9.5 km (9516.23 m) and extends from a top depth of 10.278 m to a bottom depth of about 10.9 km (10,909.996 m). The fault is centered at the coordinates 752596.619 m (x) and 4438899.618 m (y). The same elastic parameter of 30 GPa was applied to the model. We were unable to obtain a reliable slip model for the Tokat earthquake, possibly because the event was not large enough to produce deformation that could be adequately resolved.

The average slip value of 0.288 m (Figure 3.51), derived from the slip model for the Düzce earthquake, is somewhat lower than the result reported by Karaca et al. (2024). While their study reports a moment magnitude of M_w 6.1, our inversion yields M_w 6.17, which is nearly in close agreement. The estimated M_w is consistent with values obtained through different seismological methods in this study. Specifically, waveform modeling yielded a magnitude of 6.06 (Figure C.11), while coda calibration resulted in an M_w of 6.03 with a 90% confidence interval between -0.21 and 0.26 (Table B.2). The small differences between our InSAR-based estimate and the seismological results may reflect incomplete representation of the deformation field or incoherent regions within the interferogram.

In addition to the Düzce earthquake, an attempt was made to model the M_w 5.6 Tokat-Sulusaray earthquake using an elastic dislocation model (Okada) with InSAR data. However, a reliable slip model could not be constrained, likely due to the low signal-to-noise ratio in the interferogram resulting from the earthquake's moderate magnitude and potential uncorrected atmospheric artifacts. In contrast to this geodetic modeling challenge, seismological methods provided highly consistent results. The moment tensor solution indicates an M_w of 5.59 (Figure C.1), which is in excellent agreement with the M_w 5.58 (90% CI: -0.10, +0.11) obtained through our Coda Calibration Technique (CCT). This contrast

between the Düzce and Tokat case studies highlights the complementary nature of the two methodologies. While InSAR-based modeling is highly effective for capturing the rupture characteristics of larger events like Düzce, CCT proves to be a more robust tool for accurately determining the moment magnitude of small to moderate earthquakes where the geodetic signal is weak.

5. CONCLUSION

This study successfully applied the CCT to accurately estimate moment magnitudes (M_w) for earthquakes ranging from M_L 3.5 to 6.0 within the CNAFZ. The most fundamental success of the research is its multidisciplinary framework that integrates seismological (Table B.2 & Figure C.11) (CCT) and geodetic (InSAR and Okada modeling) methods (Figure 3.15 and Figure 3.51), which mutually confirm the reliability of the results. This innovative framework provides a robust and validated methodology for estimating earthquake moment magnitudes and source parameters across a broad magnitude range in the CNAFZ.

Through this integrated approach, the study generated a homogeneous and reliable M_w catalog. The CCT produced robust and stable M_w estimates, even for events too small for conventional waveform modeling. By applying 1D path corrections, the methodology proved its effectiveness by reducing interstation standard deviations to between 0.05 and 0.16. This has allowed for the creation of a complete and homogeneous earthquake catalog that includes small- to moderate-magnitude events, which is of critical importance for PSHA.

Furthermore, the research identified non-self-similar rupture behavior in the central NAFZ. It was determined that for small- and moderate-sized events, M_0 tends to increase with apparent stress (σ_A), indicating a deviation from self-similarity. This finding aligns with results from other segments of the NAFZ, suggesting that this behavior is a general characteristic of the fault zone and that larger earthquakes in the region radiate seismic energy more efficiently.

The study also helped define regional stress characteristics. The apparent stress values in the study area were found to be significantly lower than in other active tectonic regions, such as Central Italy (Morasca et al, 2022) and Ridgecrest (Mayeda et al., 2024). This points to lower seismic efficiency, which is likely related to local geophysical conditions and fault zone properties.

The successful application of CCT in this context has significant implications for regional seismic hazard assessment. The calibration parameters derived for the region in this study (Figure 4.2) can enable the near real-time estimation of source parameters such as moment magnitude, apparent stress, and corner frequency for small and moderate earthquakes. To further investigate the relationship and potential systematic biases between geodetic (InSAR) and seismic (CCT) magnitude estimates, a comprehensive analysis of a larger earthquake dataset utilizing both techniques is necessary. Therefore, this study serves as a motivating project that integrates and compares two different approaches, encouraging future research to better understanding of regional seismotectonics.

In summary, the consistency of M_w values from CCT with estimates from InSAR-based elastic dislocation modeling for moderate to large earthquakes highlights the complementary strengths of these two methods in characterizing the earthquake source. This demonstrates that for events that generate significant surface deformation (e.g., $M_w > 5.5$), both CCT and InSAR-based approaches can produce reliable results.

REFERENCES

Abercrombie, R. E., “Earthquake source scaling relationships from -1 to 5 M_L using seismograms recorded at 2.5-km depth”, *J. Geophys. Res. Solid Earth*, 100(B12), 24,015–24–036, 1995.

Abercrombie, R. E., Baltay, A., Chu, S., Taira, T., Bindi, D., Boyd, O. S., Chen, X., Cochran, E. S., Devin, E., Dreger, D., Ellsworth, W., Fan, W., Harrington, R. M., Huang, Y., Kemna, K. B., Liu, M., Oth, A., Parker, G. A., Pennington, C., & Zhang, J., “Overview of the SCEC/USGS Community Stress Drop Validation Study Using the 2019 Ridgecrest Earthquake Sequence”, *Bulletin of the Seismological Society of America*, 115(3), 734–759, 2024.

Agard, P., Omrani, J., Jolivet, L., Whitechurch, H., Vrielynck, B., Spakman, W., Monié, P., Meyer, B., & Wortel, R., “Zagros orogeny: a subduction-dominated process”, *Geological Magazine*, 148(5–6), 692–725, 2011.

Aki, K, “Scaling law of seismic spectrum”, *Journal of Geophysical Research*, 72(4), 1217–1231, 1967.

Aki, K., “Some Problems in Statistical Seismology”, *Journal of the Seismological Society of Japan. 2nd Ser.*, 8(4), 205–228, 1956.

Aki, K., & Chouet, B., “Origin of coda waves: Source, attenuation and scattering effects”, *Journal of Geophysical Research*, 80(23), 3322–3342, 1975.

Aki, K., & Richards, P. G., *Quantitative Seismology: Theory and Methods,* W.H.Freeman & Co. Ltd., San Francisco, 1980.

Aki, K., “Analysis of the seismic coda of local earthquakes as scattered waves”, *Journal of Geophysical Research*, 74(2), 615–631, 1969.

Aki, K., Tsujiura, M., Hori, M., & Goto, K., “Spectral study of near earthquake waves (1)”, *Bulletin of the Earthquake Research Institute*, 36, 71–98, 1958.

Al-Kaabi, M., Mayeda, K., Roman-Nieves, J., Chiang, A., Mahdi, H., & Al-Shukri, H., "Using a 1D Radially Symmetric Coda Envelope Model for Robust Moment Magnitude (M_w) Estimation in Iraq's Tectonically Diverse Zones", *Bulletin of the Seismological Society of America*, 115(3), 1331–1343, 2024.

Aster, R. C., Slad, G., Henton, J., & Antolik, M., "Differential analysis of coda Q using similar microearthquakes in seismic gaps. Part 1: Techniques and application to seismograms recorded in the Anza Seismic gap", *Bulletin of the Seismological Society of America*, 86(3), 868–889, 1996.

Baltay, A., Ide, S., Prieto, G., & Beroza, G., "Variability in earthquake stress drop and apparent stress", *Geophysical Research Letters*, 38(6), L06303, 2011.

Baltay, A., Prieto, G., & Beroza, G. C., "Radiated seismic energy from coda measurements and no scaling in apparent stress with seismic moment", *Journal of Geophysical Research: Solid Earth*, 115(8), 2010.

Barka, A. A., & Kadinsky-Cade, K., "Strike-slip fault geometry in Turkey and its influence on earthquake activity", *Tectonics*, 7(3), 663–684, 1988.

Barka, A. A., "Slip distribution along the North Anatolian fault associated with the large earthquakes of the period 1939 to 1967", *Bulletin of the Seismological Society of America*, 86(5), 1238–1254, 1996.

Barka, A. A., "The North Anatolian Fault Zone", *Annali Tectonicae*, 6, 164–195, 1992.

Barno, J., "LLNL/Coda-Calibration-Tool", U.S., DOE, 2017.

Bayrak, E., Yılmaz, Ş., Softa, M., Türker, T., & Bayrak, Y., "Earthquake hazard analysis for East Anatolian Fault Zone, Turkey", *Natural Hazards*, 76(2), 1063–1077, 2015.

Belin, B., Yalçin, T., Suner, F., Bozkurtoğlu, E., Gelir, A., & Güven, H., "Earthquake-related chemical and radioactivity changes of thermal water in Kuzuluk-Adapazari, Turkey", *Journal of Environmental Radioactivity*, 63(3), 239–249, 2002.

Bent, A. L., Mayeda, K., Roman-Nieves, J. I., & Barno, J., "Coda Envelope Moment Magnitudes and Source Scaling for Southeastern Canada", *Bulletin of the Seismological Society of America*, 115(3), 1318–1330, 2025.

Bianco, F., del Pezzo, E., Castellano, M., Ibanez, J., & di Luccio, F., "Separation of intrinsic and scattering seismic attenuation in the Southern Apennine zone, Italy", *Geophysical Journal International*, 150(1), 10–22, 2002.

Biswas, N. N., & Aki, K., "Characteristics of coda waves: Central and southcentral Alaska", *Bulletin of the Seismological Society of America*, 74(2), 493–507, 1984.

Bisztricsany, E., "A new method for the determination of the magnitude of earthquakes", *Geofiz. Kozlemen*, 7, 69-96, 1958.

Brune, J. N., "Tectonic stress and the spectra of seismic shear waves from earthquakes", *Journal of Geophysical Research*, 75(26), 4997–5009, 1970.

Calderoni, G., & Abercrombie, R. E., "Investigating Spectral Estimates of Stress Drop for Small to Moderate Earthquakes With Heterogeneous Slip Distribution: Examples From the 2016–2017 Amatrice Earthquake Sequence", *Journal of Geophysical Research: Solid Earth*, 128(6), 2023.

Chadha, R. K., "An M_w 7.8 Earthquake on 6 February 2023 on the East Anatolian Fault, Turkey", *Journal of the Geological Society of India*, 99(4), 449–453, 2023.

Chandrasekhar, S., *Radiative transfer,* Dover Publications, New York, 1960.

Chang, Y., Zhang, Y., & Zhang, H., "Tectonic geomorphology of Türkiye and its insights into the neotectonic deformation of the Anatolian Plate", *Earthquake Research Advances*, 4(1), 100267, 2024.

Dainty, A. M., & Toksöz, M. N, "Seismic codas on the earth and the moon - A comparison", *Physics of the Earth and Planetary Interiors*, 26(4), 250–260, 1981.

Dixon, J. E., & Robertson, A. H. F. (Eds.), "The Geological Evolution of the Eastern Mediterranean", *Geological Society of London, Special Publications*, 17, 1984.

Eken, T., Mayeda, K., Hofstetter, A., Gök, R., Örgülü, G., & Turkelli, N, "An application of the coda methodology for moment-rate spectra using broadband stations in Turkey", *Geophysical Research Letters*, 31(11), 2004.

Emre, Ö., Duman, T. Y., Özalp, S., Elmacı, H., & Olgun, Ş., "Açıklamalı Türkiye Diri Fay Haritası, Ölçek 1:1.250.000", Ankara: Maden Tetkik ve Arama Genel Müdürlüğü, 2013.

Ferretti A., Monti-Guarnieri A., Prati C., Rocca F., & Massonnet D., *InSAR Principles: Guidelines for SAR Interferometry Processing and Interpretation*, ESA Publications, Noordwijk, 2007.

Eulenfeld, T., & Wegler, U., "Crustal intrinsic and scattering attenuation of high-frequency shear waves in the contiguous United States", *Journal of Geophysical Research: Solid Earth*, 122(6), 4676–4690, 2017.

Eulenfeld, T., & Wegler, U., "Measurement of intrinsic and scattering attenuation of shear waves in two sedimentary basins and comparison to crystalline sites in Germany", *Geophysical Journal International*, 205(2), 744–757, 2016.

European Space Agency (ESA), https://sentiwiki.copernicus.eu/web/s1-mission, accessed on August 15, 2025.

Fattahi, H., & Amelung, F., "InSAR observations of strain accumulation and fault creep along the Chaman Fault system, Pakistan and Afghanistan", *Geophysical Research Letters*, 43(16), 8399–8406, 2016.

Fehler, M. C., Hoshiba, M., Sato, H., & Obara, K., "Separation of scattering and intrinsic attenuation for the Kanto-Tokai region, Japan, using measurements of S-wave energy versus hypocentral distance", *Geophysical Journal International*, 108(3), 787–800, 1992.

Frankel, A., & Wennerberg, L., "Energy-flux model of seismic coda: Separation of scattering and intrinsic attenuation", *Bulletin of the Seismological Society of America*, 77(4), 1223–1251, 1987.

Gaebler, P., Eken, T., Bektaş, H. Ö., Eulenfeld, T., Wegler, U., & Taymaz, T., "Imaging of shear wave attenuation along the central part of the North Anatolian Fault Zone, Turkey", *Journal of Seismology*, 23(4), 913–927, 2019.

Goldstein, P., Dodge, D., Firpo, M., & Minner, L., "SAC2000: Signal Processing and Analysis Tools for Seismologists and Engineers", *International Geophysics*, 81(PART B), 1613–1614, 2003.

Goldstein, R. M., & Werner, C. L., "Radar interferogram filtering for geophysical applications", *Geophysical Research Letters*, 25(21), 4035–4038, 1998.

González, P. J., & Fialko, Y., "GACOS: An operational generic atmospheric correction service for InSAR", *AGU Fall Meeting Abstracts*, G41A-0992, 2016.

Grandin, R., Vallée, M., Satriano, C., Lacassin, R., Klinger, Y., Simoes, M., & Bollinger, L., "Rupture process of the M_w = 7.9 2015 Gorkha earthquake (Nepal): Insights into Himalayan megathrust segmentation", *Geophysical Research Letters*, 42(20), 8373–8382, 2015.

Grassi, F., & Di Francesco, S., "Sentinel-1 TOPSAR acquisition mode geometry", University of Modena and Reggio Emilia, 2019.

Greber, E, "Deep circulation of CO2-rich palaeowaters in a seismically active zone (Kuzuluk/Adapazari, Northwestern Turkey)", *Geothermics*, 23(2), 151–174, 1994.

Hanks, T. C., & Kanamori, H., "A moment magnitude scale", *Journal of Geophysical Research B: Solid Earth*, 84(B5), 2348–2350, 1979.

Hanssen, R.F., *Radar Interferometry: Data Interpretation and Error Analysis*, Springer, Dordrecht, 2001.

Hartse, H. E., Phillips, W. S., Fehler, M. C., & House, L. S., "Single-station spectral discrimination using coda waves", *Bulletin of the Seismological Society of America*, 85(5), 1464–1474, 1995.

Hooper, A., Bekaert, D., Spaans, K., & Arikan, M., “Recent advances in SAR interferometry time series analysis for measuring crustal deformation”, *Tectonophysics*, 514–517, 1–13, 2012.

Hoshiba, M., “Seismic coda wave envelope in depth-dependent S wave velocity structure”, *Physics of the Earth and Planetary Interiors*, 104(1–3), 15–22, 1997.

Hoshiba, M., “Separation of scattering attenuation and intrinsic absorption in Japan using the multiple lapse time window analysis of full seismogram envelope”, *Journal of Geophysical Research: Solid Earth*, 98(B9), 15809–15824, 1993.

Hough, S. E., "Empirical Green’s function analysis: Taking the next step", *Journal of Geophysical Research: Solid Earth*, 102(B3), 5369–5384, 1997.

Ichinose, G. A., Anderson, J. G., Smith, K. D., & Zeng, Y., “Source parameters of eastern California and western Nevada earthquakes from regional moment tensor inversion”, *Bulletin of the Seismological Society of America*, 93(1), 61–84, 2003.

Ide, S., & Beroza, G. C., “Does apparent stress vary with earthquake size?”, *Geophysical Research Letters*, 28(17), 3349–3352, 2001.

Izgi, G., Eken, T., Gaebler, P., Eulenfeld, T., & Taymaz, T., “Crustal seismic attenuation parameters in the western region of the North Anatolian Fault Zone”, *Journal of Geodynamics*, 134, 101694, 2020.

Izgi, G., Eken, T., Gaebler, P., Kaya-Eken, T., & Taymaz, T., “Frequency-dependent shear wave attenuation across the Central Anatolia region, Türkiye”, *Solid Earth*, 15(6), 657–669, 2024.

Jin, A., & Aki, K., “High-resolution maps of Coda Q in Japan and their interpretation by the brittle-ductile interaction hypothesis”, *Earth, Planets and Space*, 57(5), 403–409, 2005.

Jolivet, L., & Faccenna, C., “Mediterranean extension and the Africa-Eurasia collision”, *Tectonics*, 19(6), 1095–1106, 2000.

Kanamori, H., “The energy release in great earthquakes”, *Journal of Geophysical Research*, 82(20), 2981–2987, 1977.

Kanamori, H., “Magnitude scale and quantification of earthquakes”, *Tectonophysics*, 93(3–4), 185–199, 1983.

Kanamori, H., & Anderson, D. L., “Theoretical basis of some empirical relations in seismology”, *Bulletin of the Seismological Society of America*, 65(5), 1073–1095, 1975.

Kanamori, H., & Rivera, L., “Static and dynamic scaling relations for earthquakes and their implications for rupture speed and stress drop”, *Bulletin of the Seismological Society of America*, 94(1), 314–319, 2004.

Kanamori, H., Mori, J., Hauksson, E., Heaton, T. H., Hutton, L. K., & Jones, L. M., “Determination of earthquake energy release and M_L using TERRAscope”, *Bulletin of the Seismological Society of America*, 83(2), 330–346, 1993.

Karaca, Ş. O., Erten, G., Yikmaz, B., & Özalp, S., “DInSAR analysis and geophysical modeling of 2022 November 23 Gölyaka-Düzce Earthquake”, *Turkish Journal of Earth Sciences*, 33(2), 192–207, 2024.

Ketin, I., “Über die tektonisch-mechanischen Folgerungen aus den großen anatolischen Erdbeben des letzten Dezenniums”, *Geologische Rundschau*, 36(1), 77–83, 1948.

Kopnichev, Y. F., “A model of the generation of the tail of a seismogram”, *Doklady Akademii Nauk SSSR*, 222, 333–335, 1975.

Koyanagi, S., Mayeda, K., & Aki, K., “Frequency-dependent site amplification factors using the S-wave coda for the island of Hawaii”, *Bulletin of the Seismological Society of America,* 82(3), 1151–1185, 1992.

Kuzucuoğlu, C., Çiner, A., & Kazancı, N., “The Geomorphological Regions of Turkey”, In *Landscapes and Landforms of Turkey* (pp. 41–178). Springer, 2019.

Le Pichon, X., & Angelier, J., "The Hellenic arc and trench system: a key to the neotectonic evolution of the Eastern Mediterranean area", *Tectonophysics*, 60(1–2), 1–42, 1979.

Malagnini, L., Mayeda, K., Nielsen, S., Yoo, S. H., Munafo, I., Rawles, C., & Boschi, E., "Scaling Transition in Earthquake Sources: A Possible Link Between Seismic and Laboratory Measurements", *Pure and Applied Geophysics*, 171(10), 2685–2707, 2014.

Martínez-Garzón, P., Becker, D., Jara, J., Chen, X., Kwiatek, G., & Bohnhoff, M., "The 2022 M_w 6.0 Gölyaka–Düzce earthquake: an example of a medium-sized earthquake in a fault zone early in its seismic cycle", *Solid Earth*, 14(10), 1103–1121, 2023.

Massonnet, D., & Feigl, K. L., "Radar interferometry and its application to changes in the earth's surface", *Reviews of Geophysics*, 36(4), 441–500, 1998.

Massonnet, D., Feigl, K., Rossi, M., & Adragna, F., "Radar interferometric mapping of deformation in the year after the Landers earthquake", *Nature*, 369(6477), 227–230, 1994.

Mayeda, K., "mb(LgCoda): A stable single station estimator of magnitude", *Bulletin of the Seismological Society of America*, 83(3), 851–861, 1993.

Mayeda, K., & Malagnini, L., "Source radiation invariant property of local and near-regional shear-wave coda: Application to source scaling for the M_w 5.9 Wells, Nevada sequence", *Geophysical Research Letters*, 37(7), L07303, 2010.

Mayeda, K., & Walter, W. R., "Moment, energy, stress drop, and source spectra of western United States earthquakes from regional coda envelopes", *Journal of Geophysical Research: Solid Earth*, 101(B5), 11195–11208, 1996.

Mayeda, K., Bindi, D., Roman-Nieves, J., Morasca, P., Dreger, D., Ji, C., Taira, T., Archuleta, R., Walter, W. R., & Barno, J., "Source-Scaling Comparison and Validation for Ridgecrest, California: Radiated Energy, Apparent Stress, and M_w Using the Coda Calibration Tool ($2.6 < M_w < 7.1$)", *Bulletin of the Seismological Society of America*, 115(3), 890–907, 2024.

Mayeda, K., Hofstetter, A., O'Boyle, J. L., & Walter, W. R., "Stable and transportable regional magnitudes based on coda-derived moment-rate spectra", *Bulletin of the Seismological Society of America*, 93(1), 224–239, 2003.

Mayeda, K., Malagnini, L., & Walter, W. R., "A new spectral ratio method using narrow band coda envelopes: Evidence for non-self-similarity in the Hector Mine sequence", *Geophysical Research Letters*, 34(11), L11303, 2007.

McClusky, S., Balassanian, S., Barka, A., Demir, C., Ergintav, S., Georgiev, I., Gurkan, O., Hamburger, M., Hurst, K., Kahle, H., Kastens, K., Kekelidze, G., King, R., Kotzev, V., Lenk, O., Mahmoud, S., Mishin, A., Nadariya, M., & Veis, G., "Global Positioning System constraints on plate kinematics and dynamics in the eastern Mediterranean and Caucasus", *Journal of Geophysical Research: Solid Earth*, 105(B3), 5695–5719, 2000.

McClusky, S., Reilinger, R., Mahmoud, S., Ben Sari, D., & Tealeb, A., "GPS constraints on Africa (Nubia) and Arabia plate motions", *Geophysical Journal International,* 155, 126-138, 2003.

McGarr, A., "On relating apparent stress to the stress causing earthquake fault slip", *Journal of Geophysical Research: Solid Earth*, 104(B2), 3003–3011, 1999.

McKenzie, D., "Active Tectonics of the Mediterranean Region", *Geophysical Journal of the Royal Astronomical Society*, 30(2), 109–185, 1972.

McQuarrie, N., & van Hinsbergen, D. J. J., "Retrodeforming the Arabia-Eurasia collision zone: Age of collision versus magnitude of continental subduction", *Geology*, 41(3), 315–318, 2013.

Merryman Boncori, J. P., "Measuring coseismic deformation with spaceborne synthetic aperture radar: A review", *Frontiers in Earth Science*, 7, 2019.

Morasca, P., Bindi, D., Mayeda, K., Roman-Nieves, J., Barno, J., Walter, W. R., & Spallarossa, D., "Source scaling comparison and validation in Central Italy: data intensive

direct S waves versus the sparse data coda envelope methodology", *Geophysical Journal International*, 231(3), 1573–1590, 2022.

Morasca, P., Mayeda, K., Gok, R., Phillips, W. S., & Malagnini, L., "2D coda and direct-wave attenuation tomography in northern Italy", *Bulletin of the Seismological Society of America,* 98, 1936-1946, 2008.

Morishita, Y., Lazecky, M., Wright, T. J., Weiss, J. R., Elliott, J. R., & Hooper, A., "LiCSBAS: An Open-Source InSAR Time Series Analysis Package Integrated with the LiCSAR Automated Sentinel-1 InSAR Processor", *Remote Sensing*, 12(3), 424, 2020.

Morse, P. M., & Feshbach, H, "Methods of Theoretical Physics", New York: McGraw-Hill, 1956.

Murphy, K. R., Mayeda, K., & Walter, W. R., "Lg-coda methods applied to Nevada Test Site events: Spectral peaking and yield estimation", *Bulletin of the Seismological Society of America*, 99(1), 441-448, 2009.

Nakamura, Y., "Seismic energy transmission in an intensively scattering environment", *Journal of Geophysical Research*, 82(20), 2989–2992, 1977.

Nishigami, K., "Deep crustal heterogeneity along and around the San Andreas fault system in central California and its relation to the segmentation", *Journal of Geophysical Research: Solid Earth*, 105(B4), 7983–7998, 2000.

Nocquet, J. M., "Present-day kinematics of the Mediterranean: A comprehensive overview of GPS results", *Tectonophysics*, 579, 220–242, 2012.

Okada, Y., "Surface deformation due to shear and tensile faults in a half-space", *Bulletin of the Seismological Society of America*, 75(4), 1135–1154, 1985.

Okay, A. I., & Tüysüz, O., "Tethyan sutures of northern Turkey", *Geological Society, London, Special Publications*, 156, 475–515, 1999.

Onur, T., Gök, R., Godoladze, T., Gunia, I., Boichenko, G., Buzaladze, A., Tumanova, N., Dzmanashvili, M., Sukhishvili, L., Javakishvili, Z., Cowgill, E., Bondár, I., &

Yetirmishli, G., “Probabilistic Seismic Hazard Assessment Using Legacy Data in Georgia”, *Seismological Research Letters*, 91(3), 1500–1517, 2020.

Özkan, B., Eken, T., Gaebler, P., & Taymaz, T., “Coda-derived source properties estimated using local earthquakes in the Sea of Marmara, Türkiye”, *Solid Earth*, 15(11), 1303–1317, 2024.

Paasschens, J. C. J., “Solution of the time-dependent Boltzmann equation”, *Physical Review E*, 56(1), 1135–1141, 1997.

Phillips, W. S., & Aki, K., “Site amplification of coda waves from local earthquakes in central California”, *Bulletin of the Seismological Society of America*, 76(3), 627–648, 1986.

Phillips, W. S., Stead, R. J., Randall, G. E., Hartse, H. E., & Mayeda, K. M, “Chapter 12 Source Effects From Broad Area Network Calibration of Regional Distance Coda Waves”, *Advances in Geophysics*, 50, 319–351, 2008.

Poupinet, G., Ellsworth, W. L., & Frechet, J, “Monitoring velocity variations in the crust using earthquake doublets: An application to the Calaveras Fault, California”, *Journal of Geophysical Research: Solid Earth*, 89(B7), 5719–5731, 1984.

Reilinger, R., McClusky, S., Vernant, P., Lawrence, S., Ergintav, S., Cakmak, R., Ozener, H., Kadirov, F., Guliev, I., Stepanyan, R., Nadariya, M., Hahubia, G., Mahmoud, S., Sakr, K., ArRajehi, A., Paradissis, D., Al-Aydrus, A., Prilepin, M., & Karam, G., “GPS constraints on continental deformation in the Africa-Arabia-Eurasia continental collision zone and implications for the dynamics of plate interactions”, *Journal of Geophysical Research: Solid Earth*, 111(B5), B05411, 2006.

Rousset, B., Jolivet, R., Simons, M., Lasserre, C., Riel, B., Milillo, P., Çakir, Z., & Renard, F., “An aseismic slip transient on the North Anatolian Fault”, *Geophysical Research Letters*, 43(7), 3254–3262, 2016.

Royden, L. H., “The tectonic expression of slab pull at continental convergent boundaries.” *Tectonics*, 12(2), 303–325, 1993.

Sançar, T., Zabcı, C., Karabacak, V., Yazıcı, M., & Akyüz, H. S., "Geometry and Paleoseismology of the Malatya Fault (Malatya-Ovacık Fault Zone), Eastern Turkey: Implications for intraplate deformation of the Anatolian Scholle", *Journal of Seismology*, 23(2), 319–340, 2019.

Sandwell, D. T., Mellors, R. J., Tong, X., Wei, M., & Wessel, P., GMTSAR: An InSAR processing system based on generic mapping tools, Scripps Institution of Oceanography, UC San Diego, 2016.

Sato, H., "Mean free path of S-waves under the Kanto district of Japan", *Journal of Physics of the Earth*, 26(2), 185–198, 1978.

Sato, H., "Single isotropic scattering model including wave conversions: Simple theoretical model of the short period body wave coda", *Journal of Physics of the Earth*, 25(2), 163–176, 1977a.

Sato, H., Fehler, M. C., & Maeda, T., *Seismic wave propagation and scattering in the heterogeneous earth*, [Edition 2], Springer Berlin, Heidelberg, 2012.

Scordilis, E. M., "Empirical global relations converting MS and mb to moment magnitude", *Journal of Seismology*, 10(2), 225–236, 2006.

Şengör, A. M. C., & Yilmaz, Y., "Tethyan evolution of Turkey: A plate tectonic approach", *Tectonophysics*, 75(3–4), 181–241, 1981.

Şengör, A. M. C., Gorur, N., & Saroglu, F., "Strike-slip faulting and related basin formation in zones of tectonic escape: Turkey as a case study", *SEPM Society for Sedimentary Geology*, 37, 227–264, 1985.

Şengör, A. M. C., Tüysüz, O., Imren, C., Sakinç, M., Eyidoğan, H., Görür, N., le Pichon, X., & Rangin, C., "The North Anatolian Fault: A new look." *Annual Review of Earth and Planetary Sciences*, 33, 37–112, 2005.

Sens-Schönfelder, C., & Wegler, U., "Passive image interferometry and seasonal variations of seismic velocities at Merapi Volcano, Indonesia", *Geophysical Research Letters*, 33(21), 2006.

Seyitoğlu, G., Esat, K., & Ecevitoğlu, B., "The 1 February 1944 Gerede (Bolu) earthquake and the relationship between the North Anatolian Fault Zone and the Abant and Mudurnu faults", *Turkish Journal of Earth Sciences*, 24(5), 451–466, 2015.

Shelly, D. R., Mayeda, K., Barno, J., Whidden, K. M., Moschetti, M. P., Llenos, A. L., Rubinstein, J. L., Yeck, W. L., Earle, P. S., Gök, R., & Walter, W. R., "A Big Problem for Small Earthquakes: Benchmarking Routine Magnitudes and Conversion Relationships with Coda Envelope-Derived Mw in Southern Kansas and Northern Oklahoma", *Bulletin of the Seismological Society of America*, 112(1), 210–225, 2022.

Singh, S., & Herrmann, R. B., "Regionalization of crustal coda Q in the continental United States", *Journal of Geophysical Research*, 88(B1), 527–538, 1983.

Stein, R. S., Barka, A. A., & Dieterich, J. H., "Progressive failure on the North Anatolian fault since 1939 by earthquake stress triggering", *Geophysical Journal International*, 128(3), 594–604, 1997.

Taira, T., Bürgmann, R., Nadeau, R. M., & Dreger, D. S., "Variability of fault slip behavior along the San Andreas Fault in the San Juan Bautista Region", *Journal of Geophysical Research: Solid Earth*, 119(12), 8827–8844, 2014.

Taymaz, T., Westaway, R., & Reilinger, R., "Active faulting and crustal deformation in the Eastern Mediterranean region", *Tectonophysics*, 391(1–4), 1–9, 2004.

Torres, R., Snoeij, P., Geudtner, D., Bibby, D., Davidson, M., Attema, E., Potin, P., Rommen, B. Ö., Floury, N., Brown, M., Traver, I. N., Deghaye, P., Duesmann, B., Rosich, B., Miranda, N., Bruno, C., L'Abbate, M., Croci, R., Pietropaolo, A., Huchler, M., & Rostan, F., "GMES Sentinel-1 mission", *Remote Sensing of Environment*, 120, 9–24, 2012.

Turcotte, D. L., & Schubert, G., *Geodynamics*, [Edition 3], Cambridge University Press, 2014.

Walter, W. R., & Taylor, S. R., "A Revised Magnitude and Distance Amplitude Correction (MDAC2) Procedure for Regional Seismic Discriminants: Theory and Testing at NTS", 2001.

Walter, W. R., Yoo, S. H., Mayeda, K., & Gök, R., "Earthquake stress via event ratio levels: Application to the 2011 and 2016 Oklahoma seismic sequences", *Geophysical Research Letters*, 44, 3147–3155, 2017.

Wang, H., Wright, T. J., Yu, Y., Lin, H., Jiang, L., Li, C., & Qiu, G., "InSAR reveals coastal subsidence in the Pearl River Delta, China", *Geophysical Journal International*, 191(3), 1119–1128, 2012.

Weiss, J. R., Walters, R. J., Morishita, Y., Wright, T. J., Lazecky, M., Wang, H., Hussain, E., Hooper, A. J., Elliott, J. R., Rollins, C., Yu, C., González, P. J., Spaans, K., Li, Z., & Parsons, B., "High-Resolution Surface Velocities and Strain for Anatolia From Sentinel-1 InSAR and GNSS Data", *Geophysical Research Letters*, 47(17), e2020GL087376, 2020.

Wright, T. J., "Remote monitoring of the earthquake cycle using satellite radar interferometry", *Philosophical Transactions of the Royal Society A: Mathematical, Physical and Engineering Sciences*, 360(1801), 2873–2888, 2002.

Wright, T. J., Parsons, B. E., & Lu, Z., "Toward mapping surface deformation in three dimensions using InSAR", *Geophysical Research Letters*, 31(1), 2004.

Wu, R. S., & Aki, K. "Multiple scattering and energy transfer of seismic waves—separation of scattering effect from intrinsic attenuation—II. Application of the theory to Hindu Kush region", *Pure and Applied Geophysics*, 128, 49–80, 1988.

Yague-Martinez, N., De Zan, F., & Prats-Iraola, P., "Coregistration of Interferometric Stacks of Sentinel-1 TOPS Data", *IEEE Geoscience and Remote Sensing Letters*, 14(7), 1-5, 2017.

Yague-Martinez, N., Prats-Iraola, P., Gonzalez, F. R., Brcic, R., Shau, R., Geudtner, D., Eineder, M., & Bamler, R., "Interferometric Processing of Sentinel-1 TOPS Data", *IEEE Transactions on Geoscience and Remote Sensing*, 54(4), 2220–2234, 2016.

Yoo, S. H., Rhie, J., Choi, H., & Mayeda, K., “Coda-derived source parameters of earthquakes and their scaling relationships in the Korean peninsula”, *Bulletin of the Seismological Society of America*, 101(5), 2388–2398, 2011.

Yu, C., Li, Z., Penna, N. T., & Crippa, P., “Generic atmospheric correction model for InSAR observations”, *Journal of Geophysical Research: Solid Earth*, 122(10), 8177–8189, 2017.

Chen, C. W., & Zebker, H. A., “Two-dimensional phase unwrapping with use of statistical models for cost functions in nonlinear optimization”, *Journal of the Optical Society of America*, 18(2), 338–351, 2001.

APPEDIX A

Table A.1 List of seismic stations used for calibration, detailing the network code, geographic coordinates, original and updated sampling rates, and dates of sensor replacements where applicable. A dash ("–") denotes no recorded modification.

Network	Station Name	Latitude (°)	Longitude (°)	Sampling Rate (Hz)	Sensor Changing Date (dd/mm/yyyy)	Current Sampling Rate (Hz)
KO	ADVT	40.433	29.738	100	-	100
KO	AUBOZ	39.911	30.033	100	-	100
KO	AUMIH	39.868	31.483	100	-	100
KO	BZK	41.96	34.004	50	17/04/2024	100
KO	CANT	40.606	33.62	50	17/04/2024	100
KO	CAVI	40.202	29.838	100	-	100
KO	CORM	40.179	34.63	50	17/04/2024	100
KO	DIKM	41.65	35.258	50	17/04/2024	100
KO	GEMT	40.435	29.189	100	-	100
KO	GULT	40.432	30.516	100	-	100
KO	HRTX	40.801	29.673	100	-	100
KO	KDZE	41.313	31.443	50	17/04/2024	100
KO	KURC	41.846	32.743	100	-	100
KO	LOD	39.889	32.764	50	17/04/2024	100
KO	MDUB	40.471	31.198	50	-	50
KO	SILT	41.153	29.643	100	-	100

Table A.2 List of seismic stations used for calibration, detailing the network code, geographic coordinates, original and updated sampling rates, and dates of sensor replacements where applicable. A dash ("–") denotes no recorded modification. (cont.)

Network	Station Name	Latitude (°)	Longitude (°)	Sampling Rate (Hz)	Sensor Changing Date (dd/mm/yyyy)	Current Sampling Rate (Hz)
KO	YLV	40.566	29.371	100	-	100
TU	AYAZ	40.679	34.857	100	-	100
TU	BCAM	40.816	32.066	100	-	100
TU	BILE	40.162	29.875	100	-	100
TU	BOLU	40.779	31.677	100	-	100
TU	BOYA	41.533	34.681	100	-	100
TU	BTAS	40.571	31	100	-	100
TU	CIDE	41.882	32.947	100	-	100
TU	CKRK	40.073	35.5	100	-	100
TU	CMDR	40.494	32.475	100	-	100
TU	COAL	40.255	34.986	100	-	100
TU	CTAK	40.648	34.791	100	-	100
TU	DELI	39.998	33.92	100	-	100
TU	DERS	40.852	32.551	100	-	100
TU	DEVR	41.142	31.972	100	-	100
TU	ELDT	40.489	33.427	100	-	100
TU	GEYV	40.484	30.296	100	-	100
TU	GOKD	40.073	33.475	100	-	100

Table A.3 List of seismic stations used for calibration, detailing the network code, geographic coordinates, original and updated sampling rates, and dates of sensor replacements where applicable. A dash ("–") denotes no recorded modification. (cont.)

Network	Station Name	Latitude (°)	Longitude (°)	Sampling Rate (Hz)	Sensor Changing Date (dd/mm/yyyy)	Current Sampling Rate (Hz)
TU	ILGA	41.052	33.717	50	23/06/2020	100
TU	KAGI	41.138	34.478	100	-	100
TU	KAND	41.094	30.192	100	-	100
TU	KAYN	40.965	30.341	100	-	100
TU	KBUK	41.237	32.627	100	-	100
TU	KIBS	40.42	31.852	100	-	100
TU	ODTU	39.868	32.794	100	-	100
TU	PELI	41.301	33.318	100	-	100
TU	SAHE	40.853	30.854	100	-	100
TU	SATE	41.013	29.286	100	-	100
TU	SAUV	40.74	30.327	100	-	100
TU	SEMS	40.871	29.739	100	-	100
TU	SEYI	41.636	33.742	100	-	100
TU	SUNG	40.189	34.246	100	-	100
TU	SUSU	40.34	30.844	100	-	100
TU	YENC	40.681	33.844	100	-	100
TU	YIGI	40.963	31.449	100	-	100

APPENDIX B

In this part, reference and validation events; M_w and σ_a values, obtained through independent validation and reference methods; and source parameters for validation events represented. “CI” means confidence interval.

Table B.1. Overview of reference and validation events.

192571145	192570603	180972116	163071157	161770540	Event ID
14.09.2019	14.09.2019	4.07.2018	11.02.2016	25.06.2016	Date (dd/mm/yyyy)
11:45:59	06:03:10	21:16:31	11:57:41	05:40:11	Time (hh:mm:ss) (UTC)
40.752	40.748	40.862	40.765	40.707	Latitude (°)
32.967	32.971	31.66	34.311	29.212	Longitude (°)
5	6.1	6	8.8	9.3	Depth (km)
4.38 [-0.07, 0.08]	4.93 [-0.12, 0.14]	4.50 [-0.06, 0.06]	4.52 [-0.08, 0.08]	4.14 [-0.06, 0.07]	Coda Mw [± 90% CI]
-	-	-	-	-	Reference M_w
4.38	4.87	4.53	4.43	4.1	Validation M_w
0.02 [-0.00, 0.00]	0.06 [-0.02, 0.02]	0.05 [-0.01, 0.01]	0.04 [-0.01, 0.01]	0.06 [-0.01, 0.02]	σ_A (MPa) [± 90% CI]
0.46 [-0.07, 0.07]	0.36 [-0.09, 0.09]	0.57 [-0.07, 0.07]	0.51 [-0.08, 0.09]	0.89 [-0.11, 0.16]	f_c (Hz) [± 90% CI]
-	-	-	-	-	Ref σ_A
-	-	-	-	-	Val σ_A

Table B.1. Overview of reference and validation events. (cont.)

211912153	211352306	210430337	201750554	192571903	192571808	**Event ID**
7.10.2021	15.05.2021	2.12.2021	23.06.2020	14.09.2019	14.09.2019	**Date (dd/mm/yyyy)**
21:53:25	23:06:21	03:37:53	05:54:18	19:03:31	18:08:42	**Time (hh:mm:ss) (UTC)**
40.092	40.257	41.36	40.724	40.76	40.777	**Latitude (°)**
34.473	34.453	33.542	32.941	32.932	32.956	**Longitude (°)**
2.7	5	1.7	7.2	1.6	6.6	**Depth (km)**
4.29 [-0.09, 0.09]	4.07 [-0.06, 0.07]	4.50 [-0.06, 0.06]	4.23 [-0.06, 0.07]	4.37 [-0.07, 0.07]	4.15 [-0.06, 0.07]	**Coda Mw [± 90% CI]**
4.1	-	4.46	-	-	-	**Reference M_w**
-	3.92	-	4.2	4.3	4.25	**Validation M_w**
0.01 [-0.00, 0.00]	0.01 [-0.00, 0.00]	0.10 [-0.02, 0.02]	0.02 [-0.00, 0.00]	0.01 [-0.00, 0.00]	0.01 [-0.00, 0.00]	**σ_A (MPa) [± 90% CI]**
0.44 [-0.07, 0.07]	0.54 [-0.07, 0.08]	0.68 [-0.08, 0.10]	0.51 [-0.07, 0.07]	0.42 [-0.04, 0.06]	0.48 [-0.06, 0.06]	**f_c (Hz) [± 90% CI]**
-	-	-	-	-	-	**Ref σ_A**
-	-	-	-	-	-	**Val σ_A**

Table B.1. Overview of reference and validation events.

223370459	223270350	223270108	222240607	213510928	213211240	**Event ID**
12.03.2022	23.11.2022	23.11.2022	8.12.2022	17.12.2021	17.11.2021	**Date (dd/mm/yyyy)**
04:59:19	03:50:57	01:08:15	06:07:11	09:28:31	12:40:15	**Time (hh:mm:ss) (UTC)**
40.827	40.818	40.831	40.687	40.494	40.841	**Latitude (°)**
30.942	30.921	30.998	34.858	34.217	31.031	**Longitude (°)**
5.7	5	8.3	5	2.3	7.4	**Depth (km)**
3.73 [-0.06, 0.06]	4.26 [-0.05, 0.06]	6.03 [-0.21, 0.26]	4.21 [-0.06, 0.06]	4.09 [-0.06, 0.06]	4.80 [-0.08, 0.09]	**Coda Mw [± 90% CI]**
-	-	6.06	4.19	4.1	-	**Reference M_w**
3.75	4.28	6.06	-	-	4.83	**Validation M_w**
0.02 [-0.00, 0.00]	0.04 [-0.00, 0.01]	0.22 [-0.07, 0.14]	0.04 [-0.01, 0.01]	0.03 [-0.01, 0.00]	0.10 [-0.02, 0.02]	**σ_A (MPa) [± 90% CI]**
1.00 [-0.14, 0.13]	0.69 [-0.06, 0.09]	0.16 [-0.05, 0.08]	0.70 [-0.10, 0.11]	0.73 [-0.10, 0.09]	0.49 [-0.08, 0.08]	**f_c (Hz) [± 90% CI]**
-	-	-	-	-	-	**Ref σ_A**
-	-	1.497	-	-	-	**Val σ_A**

Table B.1. Overview of reference and validation events. (cont.)

241091511	241082207	Event ID
18.04.2024	17.04.2024	Date (dd/mm/yyyy)
15:11:24	22:07:00	Time (hh:mm:ss) (UTC)
40	40	Latitude (°)
35.98	35.96	Longitude (°)
10	8.5	Depth (km)
5.58 [-0.10, 0.11]	4.59 [-0.06, 0.06]	Coda Mw [± 90% CI]
5.59	4.56	Reference M_w
-	-	Validation M_w
0.16 [-0.04, 0.03]	0.04 [-0.01, 0.01]	σ_A (MPa) [± 90% CI]
0.23 [-0.05, 0.05]	0.47 [-0.05, 0.05]	f_c (Hz) [± 90% CI]
0.16	0.04	Ref σ_A
-	-	Val σ_A

Table B.2. M_w and σ_a values, obtained through independent validation and reference methods, are compared with CCT-derived source parameters.

160010911	151221245	150170042	142951711	142470353	142152222	133282049	132091857	132022143	Event ID
1.01.2016	5.02.2015	17.01.2015	22.10.2014	9.04.2014	8.03.2014	24.11.2013	28.07.2013	21.07.2013	Date (dd/mm/yyyy)
09:11:14	12:45:57	00:42:33	17:11:04	03:53:00	22:22:44	20:49:37	18:57:55	21:43:40	Time (hh:mm:ss) (UTC)
40.066	40.845	39.877	40.407	41.644	40.607	40.785	41.02	41.135	Latitude (°)
30.519	32.493	30.395	30.115	32.512	29.165	31.876	34.356	33.492	Longitude (°)
5	1.8	7	7.5	4.5	11.5	7.6	8.5	5.3	Depth (km)
3.97 [-0.10, 0.13]	3.97 [-0.05, 0.06]	4.02 [-0.09, 0.08]	4.21 [-0.05, 0.05]	3.82 [-0.06, 0.06]	4.02 [-0.08, 0.09]	4.80 [-0.10, 0.10]	4.33 [-0.05, 0.06]	4.10 [-0.04, 0.04]	Coda Mw [± 90% CI]
-	-	-	-	-	-	-	-	-	Reference M_w
-	-	-	-	-	-	-	-	-	Validation M_w
0.03 [-0.01, 0.01]	0.02 [-0.00, 0.00]	0.03 [-0.01, 0.01]	0.03 [-0.00, 0.00]	0.03 [-0.00, 0.01]	0.03 [-0.01, 0.01]	0.07 [-0.02, 0.02]	0.03 [-0.00, 0.01]	0.02 [-0.00, 0.00]	σ_A (MPa) [± 90% CI]
0.81 [-0.18, 0.19]	0.79 [-0.10, 0.10]	0.80 [-0.15, 0.17]	0.66 [-0.07, 0.07]	1.00 [-0.12, 0.14]	0.76 [-0.13, 0.15]	0.43 [-0.09, 0.09]	0.59 [-0.06, 0.07]	0.67 [-0.06, 0.07]	f_c (Hz) [± 90% CI]
-	-	-	-	-	-	-	-	-	Ref σ_A
-	-	-	-	-	-	-	-	-	Val σ_A

Table B.2. M_w and σ_a values, obtained through independent validation and reference methods, are compared with CCT-derived source parameters. (Cont.)

190431714	182911900	180972116	163310452	163071202	163071157	162151930	161990855	161770540	Event ID
2.12.2019	18.10.2018	4.07.2018	26.11.2016	11.02.2016	11.02.2016	8.02.2016	17.07.2016	25.06.2016	**Date (dd/mm/yyyy)**
17:14:29	19:00:46	21:16:31	04:52:08	12:02:52	11:57:41	19:30:51	08:55:41	05:40:11	**Time (hh:mm:ss) (UTC)**
40.575	40.723	40.862	40.257	40.775	40.765	40.331	40.703	40.707	**Latitude (°)**
33.012	35.206	31.66	33.338	34.298	34.311	33.313	29.166	29.212	**Longitude (°)**
5	5	6	9.6	6.6	8.8	5	11.4	9.3	**Depth (km)**
4.70 [-0.08, 0.08]	3.82 [-0.06, 0.06]	4.50 [-0.06, 0.06]	3.91 [-0.06, 0.06]	3.92 [-0.06, 0.06]	4.52 [-0.08, 0.08]	4.30 [-0.07, 0.07]	3.99 [-0.09, 0.09]	4.14 [-0.06, 0.07]	**Coda Mw [± 90% CI]**
-	-	-	-	-	-	-	-	-	**Reference M_w**
-	-	4.53	-	-	4.43	-	-	4.1	**Validation M_w**
0.10 [-0.02, 0.03]	0.04 [-0.01, 0.01]	0.05 [-0.01, 0.01]	0.01 [-0.00, 0.00]	0.01 [-0.00, 0.00]	0.04 [-0.01, 0.01]	0.01 [-0.00, 0.00]	0.01 [-0.00, 0.00]	0.06 [-0.01, 0.02]	**σ_A (MPa) [± 90% CI]**
0.55 [-0.09, 0.10]	1.09 [-0.13, 0.14]	0.57 [-0.07, 0.07]	0.70 [-0.07, 0.10]	0.70 [-0.09, 0.08]	0.51 [-0.08, 0.09]	0.43 [-0.05, 0.05]	0.63 [-0.11, 0.12]	0.89 [-0.11, 0.16]	**f_c (Hz) [± 90% CI]**
-	-	-	-	-	-	-	-	-	**Ref σ_A**
-	-	-	-	-	-	-	-	-	**Val σ_A**

Table B.2. M_w and σ_a values, obtained through independent validation and reference methods, are compared with CCT-derived source parameters. (Cont.)

200230354	192831652	192571903	192571808	192571145	192570603	191531308	191021303	190431723	Event ID
23.01.2020	10.10.2019	14.09.2019	14.09.2019	14.09.2019	14.09.2019	6.02.2019	4.12.2019	2.12.2019	**Date (dd/mm/yyyy)**
03:54:11	16:52:03	19:03:31	18:08:42	11:45:59	06:03:10	13:08:46	13:03:47	17:23:23	**Time (hh:mm:ss) (UTC)**
40.113	40.695	40.76	40.777	40.752	40.748	40.761	40.69	40.571	**Latitude (°)**
33.253	29.26	32.932	32.956	32.967	32.971	30.777	30.615	33.007	**Longitude (°)**
6.2	10.3	1.6	6.6	5	6.1	9.4	12	5	**Depth (km)**
4.43 [-0.06, 0.07]	3.79 [-0.07, 0.07]	4.37 [-0.07, 0.07]	4.15 [-0.06, 0.07]	4.38 [-0.07, 0.08]	4.93 [-0.12, 0.14]	4.49 [-0.07, 0.07]	3.63 [-0.05, 0.06]	3.97 [-0.06, 0.06]	**Coda Mw [± 90% CI]**
-	-	-	-	-	-	-	-	-	**Reference M_w**
-	-	4.3	4.25	4.38	4.87	-	-	-	**Validation M_w**
0.06 [-0.01, 0.01]	0.12 [-0.03, 0.05]	0.01 [-0.00, 0.00]	0.01 [-0.00, 0.00]	0.02 [-0.00, 0.00]	0.06 [-0.02, 0.02]	0.04 [-0.01, 0.01]	0.03 [-0.00, 0.01]	0.02 [-0.00, 0.00]	**σ_A (MPa) [± 90% CI]**
0.63 [-0.08, 0.09]	1.65 [-0.25, 0.36]	0.42 [-0.04, 0.06]	0.48 [-0.06, 0.06]	0.46 [-0.07, 0.07]	0.36 [-0.09, 0.09]	0.52 [-0.08, 0.08]	1.19 [-0.13, 0.17]	0.68 [-0.09, 0.10]	**f_c (Hz) [± 90% CI]**
-	-	-	-	-	-	-	-	-	**Ref σ_A**
-	-	-	-	-	-	-	-	-	**Val σ_A**

Table B.2. M_w and σ_a values, obtained through independent validation and reference methods, are compared with CCT-derived source parameters. (Cont.)

210670909	210430337	210101953	210101952	203452226	203222305	202060219	201750554	200680421	Event ID
3.08.2021	2.12.2021	1.10.2021	1.10.2021	12.10.2020	17.11.2020	24.07.2020	23.06.2020	3.08.2020	**Date (dd/mm/yyyy)**
09:09:53	03:37:53	19:53:00	19:52:59	22:26:03	23:05:46	02:19:14	05:54:18	04:21:04	**Time (hh:mm:ss) (UTC)**
40.149	41.36	40.055	40.055	40.502	40.495	39.887	40.724	40.706	**Latitude (°)**
35.106	33.542	33.318	33.318	34.317	34.315	30.471	32.941	29.262	**Longitude (°)**
5	1.7	5	5	5	5.5	1.8	7.2	5.1	**Depth (km)**
3.84 [-0.07, 0.07]	4.50 [-0.06, 0.06]	4.52 [-0.07, 0.07]	4.53 [-0.06, 0.06]	4.03 [-0.07, 0.08]	4.23 [-0.08, 0.08]	4.00 [-0.05, 0.05]	4.23 [-0.06, 0.07]	3.89 [-0.04, 0.04]	**Coda Mw [± 90% CI]**
-	4.46	-	-	-	-	-	-	-	**Reference M_w**
-	-	-	-	-	-	-	4.2	-	**Validation M_w**
0.02 [-0.00, 0.00]	0.10 [-0.02, 0.02]	0.06 [-0.01, 0.01]	0.05 [-0.01, 0.01]	0.01 [-0.00, 0.00]	0.01 [-0.00, 0.00]	0.02 [-0.00, 0.00]	0.02 [-0.00, 0.00]	0.02 [-0.00, 0.00]	**σ_A (MPa) [± 90% CI]**
0.87 [-0.14, 0.14]	0.68 [-0.08, 0.10]	0.55 [-0.08, 0.08]	0.53 [-0.07, 0.07]	0.49 [-0.08, 0.08]	0.49 [-0.08, 0.08]	0.66 [-0.07, 0.07]	0.51 [-0.07, 0.07]	0.87 [-0.08, 0.08]	**f_c (Hz) [± 90% CI]**
-	-	-	-	-	-	-	-	-	**Ref σ_A**
-	-	-	-	-	-	-	-	-	**Val σ_A**

Table B.2. M_w and σ_a values, obtained through independent validation and reference methods, are compared with CCT-derived source parameters. (Cont.)

223270108	222240607	222011949	213510928	213211257	213211240	211912153	211352306	211011406	**Event ID**
23.11.2022	8.12.2022	20.07.2022	17.12.2021	17.11.2021	17.11.2021	7.10.2021	15.05.2021	4.11.2021	**Date (dd/mm/yyyy)**
01:08:15	06:07:11	19:49:39	09:28:31	12:57:18	12:40:15	21:53:25	23:06:21	14:06:36	**Time (hh:mm:ss) (UTC)**
40.831	40.687	40.829	40.494	40.81	40.841	40.092	40.257	40.809	**Latitude (°)**
30.998	34.858	31.346	34.217	31.026	31.031	34.473	34.453	34.803	**Longitude (°)**
8.3	5	6.7	2.3	6	7.4	2.7	5	6.4	**Depth (km)**
6.03 [-0.21, 0.26]	4.21 [-0.06, 0.06]	4.03 [-0.05, 0.05]	4.09 [-0.06, 0.06]	4.03 [-0.08, 0.09]	4.80 [-0.08, 0.09]	4.29 [-0.09, 0.09]	4.07 [-0.06, 0.07]	4.02 [-0.06, 0.06]	**Coda Mw [± 90% CI]**
6.06	4.19	-	4.1	-	-	4.1	-	-	**Reference M_w**
6.06	-	-	-	-	4.83	-	3.92	-	**Validation M_w**
0.22 [-0.07, 0.14]	0.04 [-0.01, 0.01]	0.04 [-0.01, 0.01]	0.03 [-0.01, 0.00]	0.02 [-0.00, 0.00]	0.10 [-0.02, 0.02]	0.01 [-0.00, 0.00]	0.01 [-0.00, 0.00]	0.07 [-0.01, 0.02]	**σ_A (MPa) [± 90% CI]**
0.16 [-0.05, 0.08]	0.70 [-0.10, 0.11]	0.86 [-0.09, 0.09]	0.73 [-0.10, 0.09]	0.70 [-0.12, 0.12]	0.49 [-0.08, 0.08]	0.44 [-0.07, 0.07]	0.54 [-0.07, 0.08]	1.06 [-0.12, 0.16]	**f_c (Hz) [± 90% CI]**
-	-	-	-	-	-	-	-	-	**Ref σ_A**
1.497	-	-	-	-	-	-	-	-	**Val σ_A**

Table B.2. M_w and σ_a values, obtained through independent validation and reference methods, are compared with CCT-derived source parameters. (Cont.)

241091511	241082207	223370459	223270350	**Event ID**
18.04.2024	17.04.2024	12.03.2022	23.11.2022	**Date (dd/mm/yyyy)**
15:11:24	22:07:00	04:59:19	03:50:57	**Time (hh:mm:ss) (UTC)**
40	40	40.827	40.818	**Latitude (°)**
35.98	35.96	30.942	30.921	**Longitude (°)**
10	8.5	5.7	5	**Depth (km)**
5.58 [-0.10, 0.11]	4.59 [-0.06, 0.06]	3.73 [-0.06, 0.06]	4.26 [-0.05, 0.06]	**Coda Mw [± 90% CI]**
5.59	4.56	-	-	**Reference M_w**
-	-	3.75	4.28	**Validation M_w**
0.16 [-0.04, 0.03]	0.04 [-0.01, 0.01]	0.02 [-0.00, 0.00]	0.04 [-0.00, 0.01]	**σ_A (MPa) [± 90% CI]**
0.23 [-0.05, 0.05]	0.47 [-0.05, 0.05]	1.00 [-0.14, 0.13]	0.69 [-0.06, 0.09]	**f_c (Hz) [± 90% CI]**
0.16	0.04	-	-	**Ref σ_A**
-	-	-	-	**Val σ_A**

Table B.3. Source parameters for validation events with an observed radiated energy of less than 65% were filtered out derived using the estimated calibration parameters.

Event ID	**Date (dd/mm/yyyy)**	**Time (hh:mm:ss) (UTC)**	**Latitude (°)**	**Longitude (°)**	**Depth (km)**	**Coda M_w [± 90% CI]**	**σ_A [± 90% CI]**	**f_c (Hz) [± 90% CI]**
130291838	29/01/2013	18:38:04	40.579	33.027	6	3.38 [-0.07, 0.07]	0.01 [-0.00, 0.00]	1.32 [-0.19, 0.22]
130721828	13/03/2013	18:28:11	40.111	34.35	6	3.68 [-0.06, 0.06]	0.02 [-0.00, 0.01]	1.05 [-0.12, 0.17]
132051259	24/07/2013	12:59:08	41.696	32.459	5	3.70 [-0.06, 0.06]	0.03 [-0.00, 0.01]	1.11 [-0.11, 0.15]
133521715	18/12/2013	17:15:41	40.463	34.643	5	3.80 [-0.07, 0.08]	0.02 [-0.01, 0.01]	0.92 [-0.16, 0.18]
140442123	13/02/2014	21:23:24	41.106	34.472	7.4	3.48 [-0.06, 0.06]	0.04 [-0.01, 0.01]	1.71 [-0.25, 0.28]
141041840	14/04/2014	18:40:13	40.687	34.853	1.1	3.65 [-0.06, 0.07]	0.02 [-0.00, 0.00]	1.05 [-0.15, 0.15]
141041851	14/04/2014	18:51:03	40.69	34.856	1.8	3.53 [-0.08, 0.08]	0.02 [-0.01, 0.01]	1.31 [-0.22, 0.25]
141790139	28/06/2014	1:39:19	40.086	30.385	5	3.85 [-0.05, 0.05]	0.02 [-0.00, 0.00]	0.83 [-0.09, 0.10]

Table B.3. Source parameters for validation events with an observed radiated energy of less than 65% were filtered out derived using the estimated calibration parameters. (cont.)

Event ID	**Date (dd/mm/yyyy)**	**Time (hh:mm:ss) (UTC)**	**Latitude (°)**	**Longitude (°)**	**Depth (km)**	**Coda M_w [± 90% CI]**	**σ_A [± 90% CI]**	**f_c (Hz) [± 90% CI]**
142961629	23/10/2014	16:29:10	40.409	30.122	7.4	3.41 [-0.07, 0.08]	0.04 [-0.01, 0.01]	1.73 [-0.28, 0.34]
142961733	23/10/2014	17:33:56	40.989	33.475	2	3.73 [-0.07, 0.07]	0.00 [-0.00, 0.00]	0.60 [-0.07, 0.09]
143450301	11/12/14	3:01:43	39.831	30.52	5.9	3.55 [-0.07, 0.07]	0.04 [-0.01, 0.01]	1.45 [-0.23, 0.25]
143531905	19/12/2014	19:05:43	40.704	35.303	7.3	3.36 [-0.06, 0.06]	0.02 [-0.00, 0.01]	1.55 [-0.22, 0.24]
150280339	28/01/2015	3:39:07	41.357	32.459	7.8	3.43 [-0.07, 0.08]	0.02 [-0.01, 0.01]	1.42 [-0.26, 0.28]
151281914	08/05/15	19:14:46	41.768	33.358	1.3	3.80 [-0.07, 0.06]	0.02 [-0.00, 0.01]	0.90 [-0.10, 0.16]
151312340	11/05/15	23:40:51	39.997	33.236	4.7	3.78 [-0.06, 0.06]	0.03 [-0.01, 0.01]	1.09 [-0.17, 0.20]
151820541	01/07/15	5:41:43	40.41	34.392	6.5	3.73 [-0.07, 0.07]	0.00 [-0.00, 0.00]	0.56 [-0.07, 0.07]

Table B.3. Source parameters for validation events with an observed radiated energy of less than 65% were filtered out derived using the estimated calibration parameters. (cont.)

Event ID	**Date (dd/mm/yyyy)**	**Time (hh:mm:ss) (UTC)**	**Latitude (°)**	**Longitude (°)**	**Depth (km)**	**Coda M_w [± 90% CI]**	**σ_A [± 90% CI]**	**f_c (Hz) [± 90% CI]**
151860224	05/07/15	2:24:01	40.396	34.387	1.5	3.79 [-0.07, 0.07]	0.01 [-0.00, 0.00]	0.68 [-0.10, 0.13]
151880508	07/07/15	5:08:29	40.82	31.291	5.6	3.51 [-0.06, 0.06]	0.02 [-0.00, 0.00]	1.31 [-0.17, 0.19]
153051555	01/11/15	15:55:48	40.725	32.858	2.4	3.46 [-0.07, 0.08]	0.01 [-0.00, 0.00]	1.15 [-0.20, 0.23]
153471651	13/12/2015	16:51:26	40.781	30.991	2.5	3.67 [-0.07, 0.07]	0.00 [-0.00, 0.00]	0.60 [-0.08, 0.09]
160180546	18/01/2016	5:46:31	40.717	32.75	1.7	3.39 [-0.07, 0.08]	0.03 [-0.01, 0.01]	1.60 [-0.26, 0.27]
160701749	10/03/16	17:49:17	40.547	30.635	7.4	3.37 [-0.07, 0.07]	0.03 [-0.01, 0.01]	1.62 [-0.24, 0.28]
161011506	10/04/16	15:06:51	41.101	33.844	7.3	3.72 [-0.06, 0.06]	0.01 [-0.00, 0.00]	0.76 [-0.08, 0.11]
161220255	01/05/16	2:55:30	40.858	31.71	5.4	3.48 [-0.07, 0.08]	0.03 [-0.01, 0.01]	1.53 [-0.27, 0.27]

Table B.3. Source parameters for validation events with an observed radiated energy of less than 65% were filtered out derived using the estimated calibration parameters. (cont.)

Event ID	**Date (dd/mm/yyyy)**	**Time (hh:mm:ss) (UTC)**	**Latitude (°)**	**Longitude (°)**	**Depth (km)**	**Coda M_w [± 90% CI]**	**σ_A [± 90% CI]**	**f_c (Hz) [± 90% CI]**
161511903	30/05/2016	19:03:05	40.525	34.845	5	3.73 [-0.05, 0.05]	0.03 [-0.01, 0.00]	1.17 [-0.13, 0.13]
161742335	22/06/2016	23:35:59	40.705	29.223	7.6	3.63 [-0.09, 0.09]	0.01 [-0.00, 0.00]	0.92 [-0.19, 0.22]
161911420	09/07/16	14:20:50	40.707	29.195	9.5	3.88 [-0.09, 0.10]	0.01 [-0.00, 0.00]	0.57 [-0.11, 0.12]
162660247	22/09/2016	2:47:18	40.441	29.177	5.6	3.49 [-0.06, 0.06]	0.05 [-0.01, 0.01]	1.72 [-0.30, 0.29]
162901411	16/10/2016	14:11:24	40.898	30.909	3.3	3.48 [-0.08, 0.08]	0.05 [-0.01, 0.02]	1.74 [-0.25, 0.43]
163111422	06/11/16	14:22:46	40.728	34.148	15.3	3.58 [-0.07, 0.07]	0.02 [-0.00, 0.01]	1.18 [-0.18, 0.20]
163111544	06/11/16	15:44:59	40.731	34.141	10.2	3.43 [-0.08, 0.08]	0.01 [-0.00, 0.00]	1.03 [-0.17, 0.19]
163111545	06/11/16	15:45:00	40.731	34.141	10.2	3.46 [-0.10, 0.12]	0.01 [-0.00, 0.00]	0.93 [-0.21, 0.22]

Table B.3. Source parameters for validation events with an observed radiated energy of less than 65% were filtered out derived using the estimated calibration parameters. (cont.)

Event ID	**Date (dd/mm/yyyy)**	**Time (hh:mm:ss) (UTC)**	**Latitude (°)**	**Longitude (°)**	**Depth (km)**	**Coda M_w [± 90% CI]**	**σ_A [± 90% CI]**	**f_c (Hz) [± 90% CI]**
163360011	01/12/16	0:11:15	40.78	32.777	2.4	4.06 [-0.10, 0.13]	0.00 [-0.00, 0.00]	0.38 [-0.08, 0.09]
171271344	07/05/17	13:44:12	40.58	35.258	5	3.65 [-0.06, 0.06]	0.01 [-0.00, 0.00]	0.76 [-0.10, 0.12]
171271703	07/05/17	17:03:35	40.56	35.254	5	3.81 [-0.06, 0.06]	0.01 [-0.00, 0.00]	0.71 [-0.09, 0.09]
171281319	08/05/17	13:19:15	40.579	35.257	5	3.64 [-0.06, 0.06]	0.00 [-0.00, 0.00]	0.67 [-0.09, 0.10]
171880425	07/07/17	4:25:14	40.479	34.444	5	3.86 [-0.08, 0.08]	0.01 [-0.00, 0.00]	0.58 [-0.10, 0.11]
171940919	13/07/2017	9:19:04	40.537	35.398	3.6	3.63 [-0.06, 0.05]	0.04 [-0.00, 0.01]	1.43 [-0.13, 0.19]
172070450	26/07/2017	4:50:04	40.763	32.866	5	3.78 [-0.06, 0.06]	0.01 [-0.00, 0.00]	0.81 [-0.09, 0.12]
172460323	03/09/17	3:23:13	40.143	29.94	5.5	3.69 [-0.06, 0.06]	0.02 [-0.01, 0.00]	1.09 [-0.17, 0.14]

Table B.3. Source parameters for validation events with an observed radiated energy of less than 65% were filtered out derived using the estimated calibration parameters. (cont.)

Event ID	**Date (dd/mm/yyyy)**	**Time (hh:mm:ss) (UTC)**	**Latitude (°)**	**Longitude (°)**	**Depth (km)**	**Coda M_w [± 90% CI]**	**σ_A [± 90% CI]**	**f_c (Hz) [± 90% CI]**
172922237	19/10/2017	22:37:03	40.767	33.88	5.4	3.80 [-0.06, 0.06]	0.03 [-0.00, 0.01]	1.02 [-0.11, 0.15]
173620105	28/12/2017	1:05:12	40.876	32.49	5	3.52 [-0.06, 0.07]	0.01 [-0.00, 0.00]	0.84 [-0.12, 0.12]
180870555	28/03/2018	5:55:47	40.793	31.001	10	3.71 [-0.08, 0.08]	0.01 [-0.00, 0.00]	0.66 [-0.11, 0.12]
181031338	13/04/2018	13:38:31	40.771	30.802	8.4	3.62 [-0.06, 0.06]	0.04 [-0.01, 0.01]	1.40 [-0.23, 0.22]
181230230	03/05/18	2:30:45	40.857	31.663	4.2	3.94 [-0.08, 0.08]	0.01 [-0.00, 0.00]	0.56 [-0.11, 0.10]
181230232	03/05/18	2:32:39	40.852	31.655	5	3.73 [-0.05, 0.05]	0.03 [-0.00, 0.01]	1.10 [-0.11, 0.15]
181330552	13/05/2018	5:52:40	41.489	33.726	5	3.82 [-0.06, 0.07]	0.02 [-0.00, 0.00]	0.85 [-0.12, 0.12]
181542044	03/06/18	20:44:09	41.014	33.968	5	3.67 [-0.06, 0.06]	0.01 [-0.00, 0.00]	0.90 [-0.12, 0.13]

Table B.3. Source parameters for validation events with an observed radiated energy of less than 65% were filtered out derived using the estimated calibration parameters. (cont.)

Event ID	**Date (dd/mm/yyyy)**	**Time (hh:mm:ss) (UTC)**	**Latitude (°)**	**Longitude (°)**	**Depth (km)**	**Coda M_w [± 90% CI]**	**σ_A [± 90% CI]**	**f_c (Hz) [± 90% CI]**
181590045	08/06/18	0:45:19	40.809	32.673	8.9	3.64 [-0.05, 0.05]	0.05 [-0.01, 0.01]	1.48 [-0.15, 0.20]
181841256	03/07/18	12:56:42	40.842	34.71	3.6	3.72 [-0.07, 0.08]	0.05 [-0.01, 0.02]	1.38 [-0.24, 0.27]
183062342	02/11/18	23:42:36	40.803	31.006	9.3	3.89 [-0.07, 0.08]	0.01 [-0.00, 0.00]	0.54 [-0.08, 0.08]
190490228	18/02/2019	2:28:37	40.546	33.013	5	3.59 [-0.07, 0.07]	0.01 [-0.00, 0.00]	0.99 [-0.16, 0.18]
190781741	19/03/2019	17:41:03	40.833	35.343	2	3.53 [-0.06, 0.06]	0.04 [-0.01, 0.01]	1.57 [-0.19, 0.26]
191041927	14/04/2019	19:27:41	40.547	33.022	1	3.73 [-0.06, 0.06]	0.01 [-0.00, 0.00]	0.67 [-0.08, 0.09]
191422251	22/05/2019	22:51:39	41.773	32.528	3.1	3.46 [-0.08, 0.08]	0.03 [-0.01, 0.01]	1.60 [-0.30, 0.35]
191521652	01/06/19	16:52:50	40.271	33.395	5	3.63 [-0.07, 0.07]	0.01 [-0.00, 0.00]	0.81 [-0.13, 0.13]

Table B.3. Source parameters for validation events with an observed radiated energy of less than 65% were filtered out derived using the estimated calibration parameters. (cont.)

Event ID	**Date (dd/mm/yyyy)**	**Time (hh:mm:ss) (UTC)**	**Latitude (°)**	**Longitude (°)**	**Depth (km)**	**Coda M_w [± 90% CI]**	**σ_A [± 90% CI]**	**f_c (Hz) [± 90% CI]**
191791055	28/06/2019	10:55:02	40.064	33.229	8.4	3.55 [-0.07, 0.06]	0.02 [-0.00, 0.01]	1.16 [-0.17, 0.21]
191802039	29/06/2019	20:39:09	40.44	32.951	5	3.62 [-0.07, 0.07]	0.01 [-0.00, 0.00]	0.84 [-0.12, 0.14]
191842308	03/07/19	23:08:18	40.496	34.148	8.7	3.80 [-0.05, 0.06]	0.01 [-0.00, 0.00]	0.59 [-0.07, 0.07]
192371842	25/08/2019	18:42:26	40.021	32.745	5	3.37 [-0.07, 0.07]	0.03 [-0.01, 0.01]	1.72 [-0.29, 0.31]
192542001	11/09/19	20:01:39	40.63	35.386	5	3.82 [-0.06, 0.06]	0.04 [-0.01, 0.01]	1.14 [-0.15, 0.16]
192571038	14/09/2019	10:38:50	40.741	32.966	5	3.83 [-0.09, 0.10]	0.01 [-0.00, 0.00]	0.68 [-0.12, 0.15]
192571812	14/09/2019	18:12:02	40.761	32.953	5.5	3.61 [-0.07, 0.07]	0.01 [-0.00, 0.00]	0.92 [-0.13, 0.15]
192831932	10/10/19	19:32:06	40.695	29.267	10.9	3.46 [-0.07, 0.07]	0.05 [-0.01, 0.01]	1.76 [-0.32, 0.32]

Table B.3. Source parameters for validation events with an observed radiated energy of less than 65% were filtered out derived using the estimated calibration parameters. (cont.)

Event ID	**Date (dd/mm/yyyy)**	**Time (hh:mm:ss) (UTC)**	**Latitude (°)**	**Longitude (°)**	**Depth (km)**	**Coda M_w [± 90% CI]**	**σ_A [± 90% CI]**	**f_c (Hz) [± 90% CI]**
193020636	29/10/2019	6:36:14	40.734	32.946	7.4	3.66 [-0.05, 0.05]	0.01 [-0.00, 0.00]	0.78 [-0.07, 0.09]
193402236	06/12/19	22:36:15	40.77	31.505	5	3.63 [-0.07, 0.08]	0.01 [-0.00, 0.00]	0.99 [-0.16, 0.17]
200070501	07/01/20	5:01:04	40.091	33.258	7.9	3.65 [-0.08, 0.10]	0.04 [-0.01, 0.02]	1.37 [-0.28, 0.31]
200230342	23/01/2020	3:42:46	40.108	33.267	6.8	3.86 [-0.07, 0.07]	0.03 [-0.01, 0.01]	0.94 [-0.15, 0.17]
200271051	27/01/2020	10:51:24	40.109	33.241	7.2	3.83 [-0.07, 0.07]	0.02 [-0.00, 0.00]	0.87 [-0.13, 0.13]
200932023	02/04/20	20:23:44	40.483	32.946	3.2	3.80 [-0.08, 0.09]	0.02 [-0.01, 0.01]	0.90 [-0.17, 0.21]
201172327	26/04/2020	23:27:10	40.085	33.249	7	3.79 [-0.05, 0.05]	0.01 [-0.00, 0.00]	0.80 [-0.10, 0.10]
201551311	03/06/20	13:11:10	40.535	34.897	8.3	3.76 [-0.07, 0.07]	0.05 [-0.02, 0.01]	1.30 [-0.24, 0.23]

Table B.3. Source parameters for validation events with an observed radiated energy of less than 65% were filtered out derived using the estimated calibration parameters. (cont.)

Event ID	**Date (dd/mm/yyyy)**	**Time (hh:mm:ss) (UTC)**	**Latitude (°)**	**Longitude (°)**	**Depth (km)**	**Coda M_w [± 90% CI]**	**σ_A [± 90% CI]**	**f_c (Hz) [± 90% CI]**
201971452	15/07/2020	14:52:04	40.709	32.914	5.2	3.60 [-0.06, 0.06]	0.01 [-0.00, 0.00]	0.81 [-0.10, 0.12]
202500252	06/09/20	2:52:56	40.614	33.508	1.5	3.92 [-0.09, 0.09]	0.01 [-0.00, 0.00]	0.55 [-0.09, 0.11]
202751137	01/10/20	11:37:11	41.122	34.98	5	3.57 [-0.07, 0.07]	0.03 [-0.01, 0.01]	1.34 [-0.22, 0.24]
202841146	10/10/20	11:46:06	40.7	32.989	4.4	3.76 [-0.04, 0.05]	0.02 [-0.00, 0.00]	0.96 [-0.08, 0.12]
203020204	28/10/2020	2:04:36	40.525	32.944	5	3.85 [-0.08, 0.08]	0.01 [-0.00, 0.00]	0.67 [-0.12, 0.13]
210501610	19/02/2021	16:10:53	40.564	33.02	5	3.33 [-0.07, 0.08]	0.01 [-0.00, 0.00]	1.38 [-0.21, 0.24]
212731320	30/09/2021	13:20:42	40.431	35.044	5.4	3.59 [-0.08, 0.09]	0.03 [-0.01, 0.01]	1.28 [-0.22, 0.30]
213211835	17/11/2021	18:35:41	40.834	31.028	2.6	3.73 [-0.06, 0.06]	0.04 [-0.01, 0.01]	1.23 [-0.18, 0.19]

Table B.3. Source parameters for validation events with an observed radiated energy of less than 65% were filtered out derived using the estimated calibration parameters. (cont.)

Event ID	**Date (dd/mm/yyyy)**	**Time (hh:mm:ss) (UTC)**	**Latitude (°)**	**Longitude (°)**	**Depth (km)**	**Coda M_w [± 90% CI]**	**σ_A [± 90% CI]**	**f_c (Hz) [± 90% CI]**
213541749	20/12/2021	17:49:09	40.487	34.214	1.5	3.74 [-0.05, 0.06]	0.02 [-0.00, 0.00]	0.92 [-0.10, 0.11]
213541921	20/12/2021	19:21:28	40.485	34.209	5	3.59 [-0.09, 0.10]	0.02 [-0.01, 0.01]	1.12 [-0.23, 0.25]
220221113	22/01/2022	11:13:45	40.296	29.678	6.8	3.60 [-0.06, 0.07]	0.02 [-0.00, 0.00]	1.06 [-0.15, 0.14]
220382254	07/02/22	22:54:53	40.559	33.063	6.3	3.46 [-0.06, 0.06]	0.02 [-0.01, 0.00]	1.37 [-0.21, 0.19]
220550951	24/02/2022	9:51:31	41.148	34.438	5	3.62 [-0.06, 0.06]	0.04 [-0.01, 0.01]	1.40 [-0.20, 0.23]
221150245	25/04/2022	2:45:46	40.475	33.024	5	3.75 [-0.05, 0.06]	0.01 [-0.00, 0.00]	0.77 [-0.09, 0.11]
221220316	02/05/22	3:16:13	39.991	33.978	2.2	3.67 [-0.07, 0.07]	0.03 [-0.01, 0.01]	1.25 [-0.23, 0.26]

APPENDIX C

In this section, moment tensor inversion results and the station locations used are represented.

(a) (b)

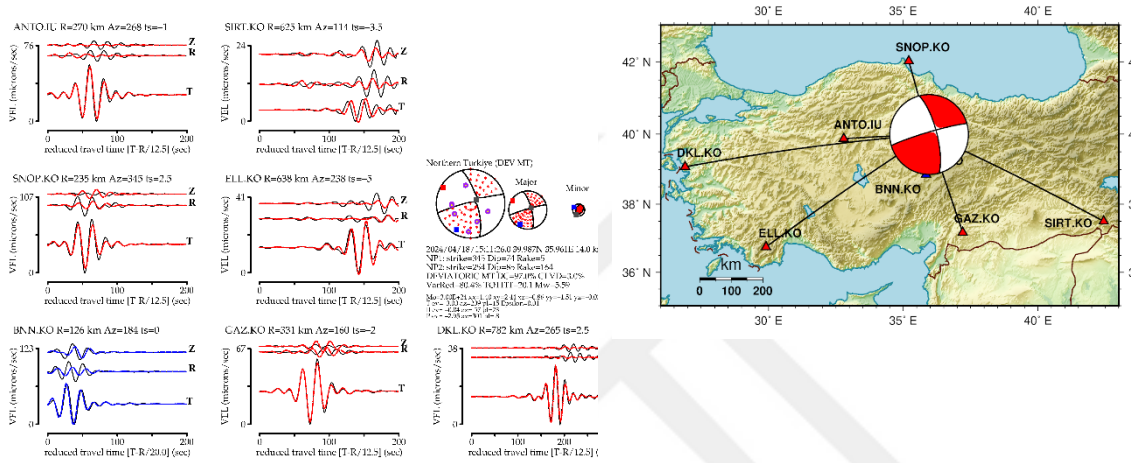


Figure C.1. (a) Moment tensor inversion results. (b) The stations used on the map and the focal mechanism are displayed for the event on 18 April 2024 at 15:11:23 UTC (Event ID: 241091511), located at 40.05°N, 35.94°E, with M_w 5.59.

(a) (b)

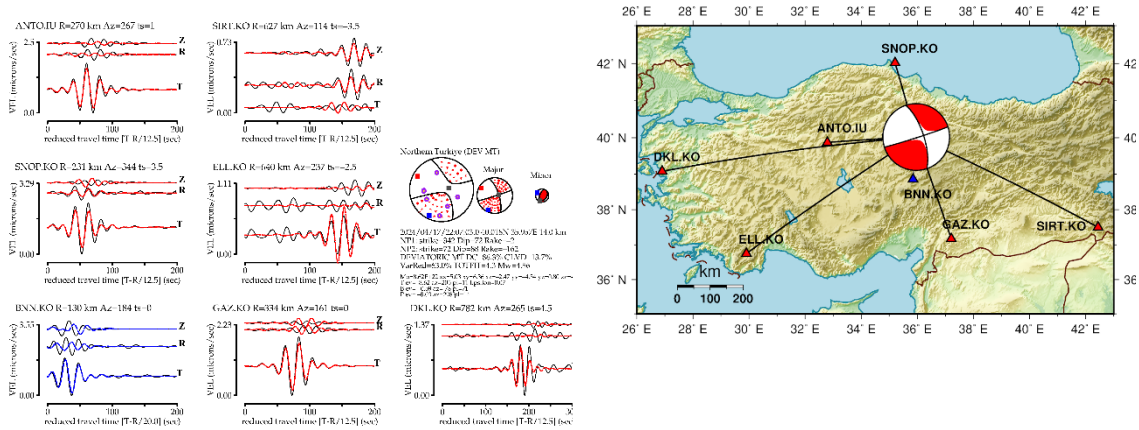


Figure C.2. (a) Moment tensor inversion results are shown in section. (b) The stations used on the map and the focal mechanism are displayed for the event on 17 April 2024 at 22:06:59 UTC (Event ID: 241082207), located at 40.06°N, 35.98°E, with M_w 4.56.

(a) (b)

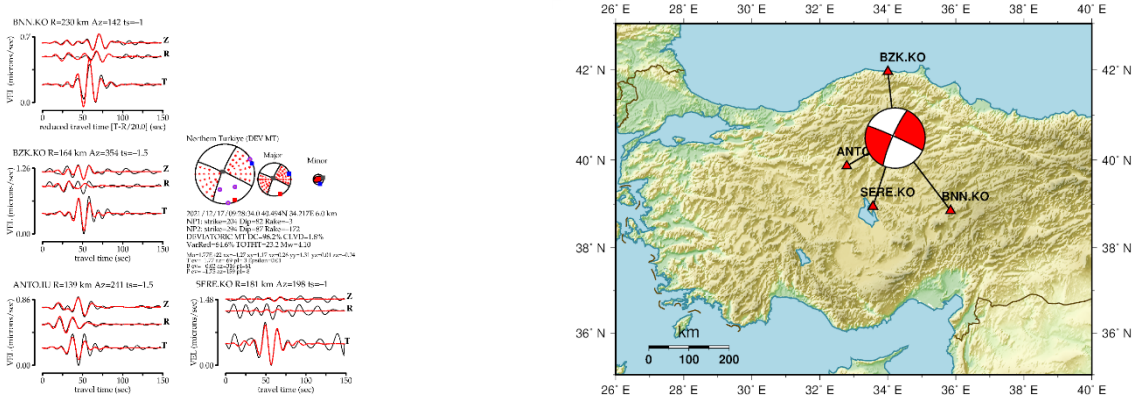


Figure C.3. Moment tensor inversion results are shown in section (a). In section (b), the stations used on the map and the focal mechanism are displayed for the event on 17 December 2021 at 09:28:32 UTC (Event ID: 213510928), located at 40.49°N, 34.22°E, with M_w 4.10.

(a) (b)

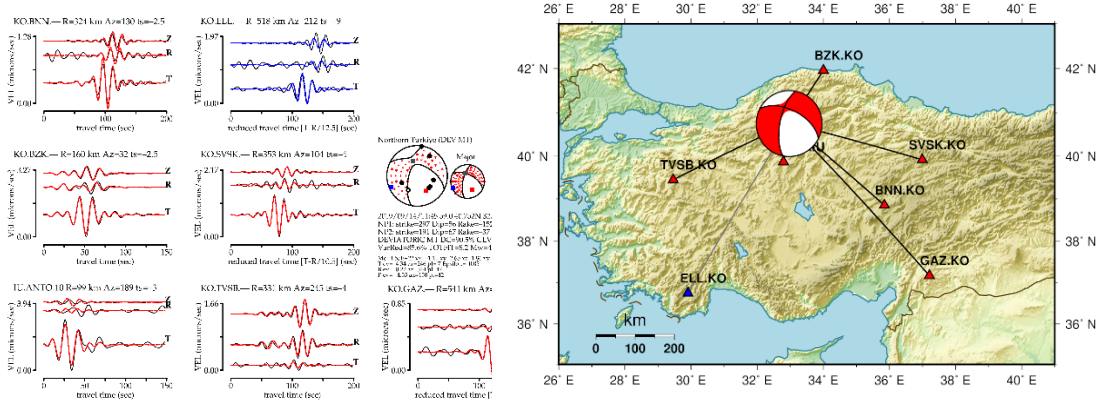


Figure C.4. Moment tensor inversion results are shown in section (a). In section (b), the stations used on the map and the focal mechanism are displayed for the event on 14 September 2019 at 11:45:59 UTC (Event ID: 192571145), located at 40.75°N, 32.97°E, with M_w 4.38.

(a) (b)

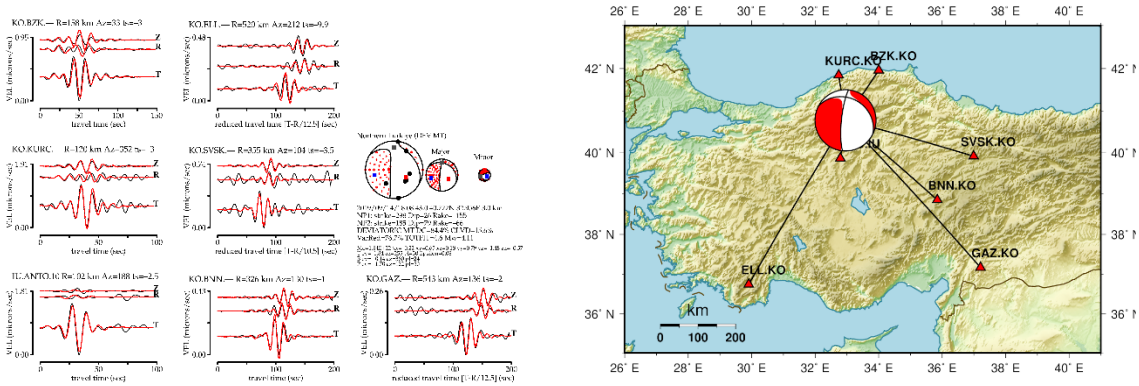


Figure C.5. Moment tensor inversion results are shown in section (a). In section (b), the stations used on the map and the focal mechanism are displayed for the event on 14 September 2019 at 18:08:43 UTC (Event ID: 192571808), located at 40.78°N, 32.96°E, with M_w 4.11.

(a) (b)

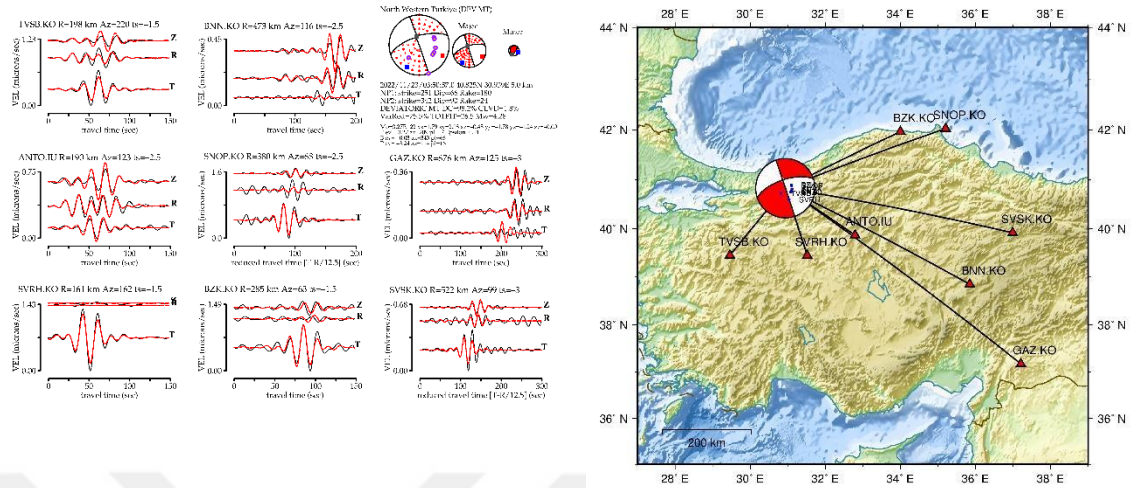


Figure C.6**.** Moment tensor inversion results are shown in section (a). In section (b), the stations used on the map and the focal mechanism are displayed for the event on 23 November 2022 at 03:50:57 UTC (Event ID: 223270350), located at 40.82°N, 30.92°E, with M_w 4.28.

(a) (b)

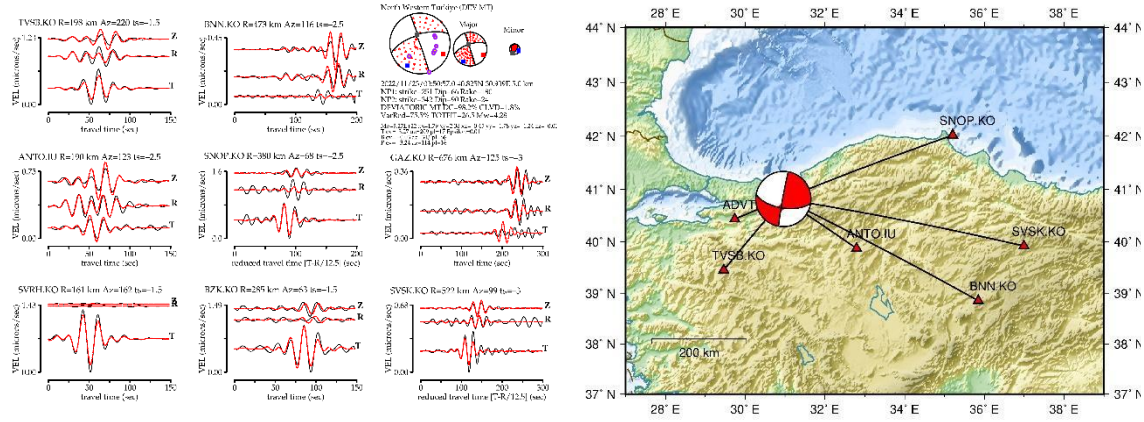


Figure C.7. Moment tensor inversion results are shown in section (a). In section (b), the stations used on the map and the focal mechanism are displayed for the event on 3 December 2022 at 04:59:20 UTC (Event ID: 223370459), located at 40.83°N, 30.94°E, with M_w 3.76.

(a) (b)

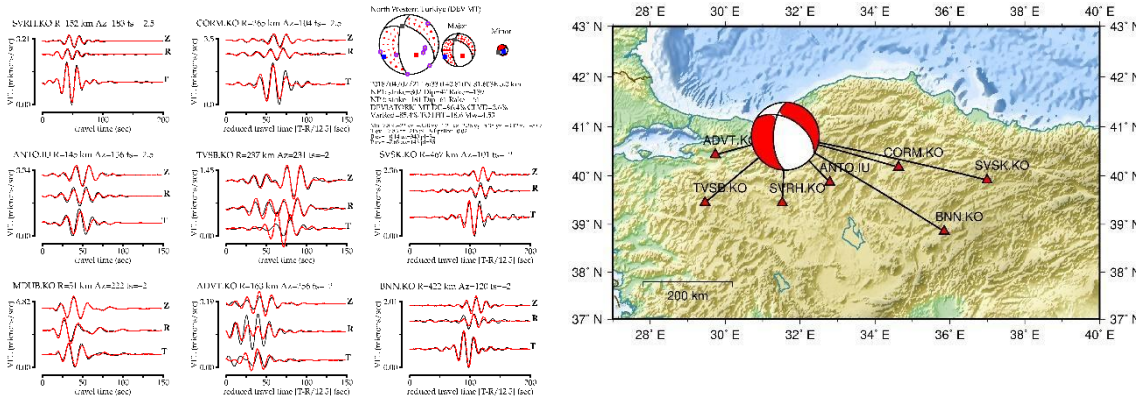


Figure C.8**.** Moment tensor inversion results are shown in section (a). In section (b), the stations used on the map and the focal mechanism are displayed for the event on 7 April 2018 at 21:16:31 UTC (Event ID: 180972116), located at 40.8617°N, 31.6603°E, with M_w 4.53.

(a) (b)

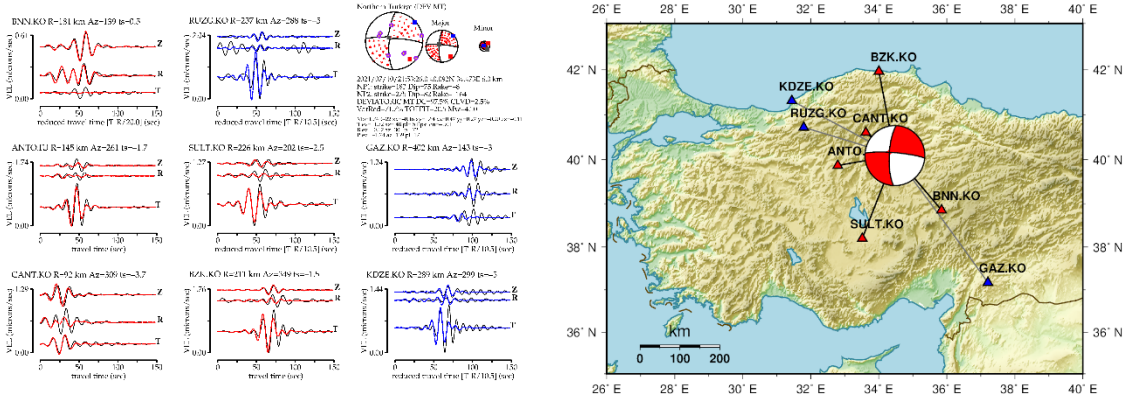


Figure C.9. (a) Moment tensor inversion results. (b) The stations used on the map and the focal mechanism are displayed for the event on 10 July 2021 at 21:53:26 UTC (Event ID: 211912153), located at 40.09°N, 34.47°E, with M_w 4.10.

(a) (b)

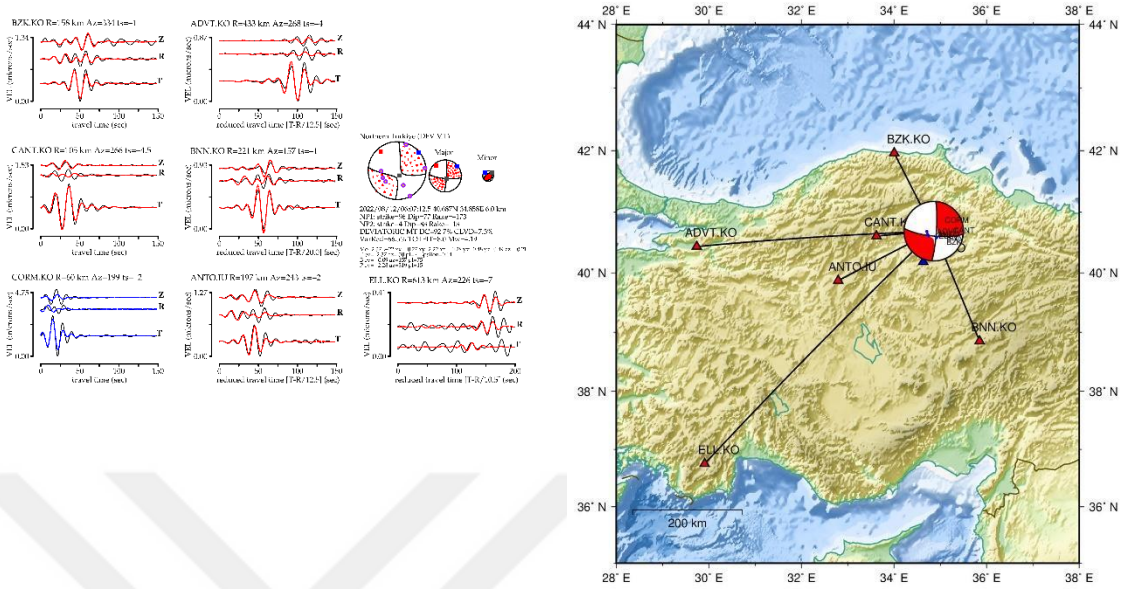


Figure C.10. Moment tensor inversion results are shown in section (a). In section (b), the stations used on the map and the focal mechanism are displayed for the event on 12 August 2022 at 06:07:11 UTC (Event ID: 222240607), located at 40.69°N, 34.86°E, with M_w 4.19.

(a) (b)

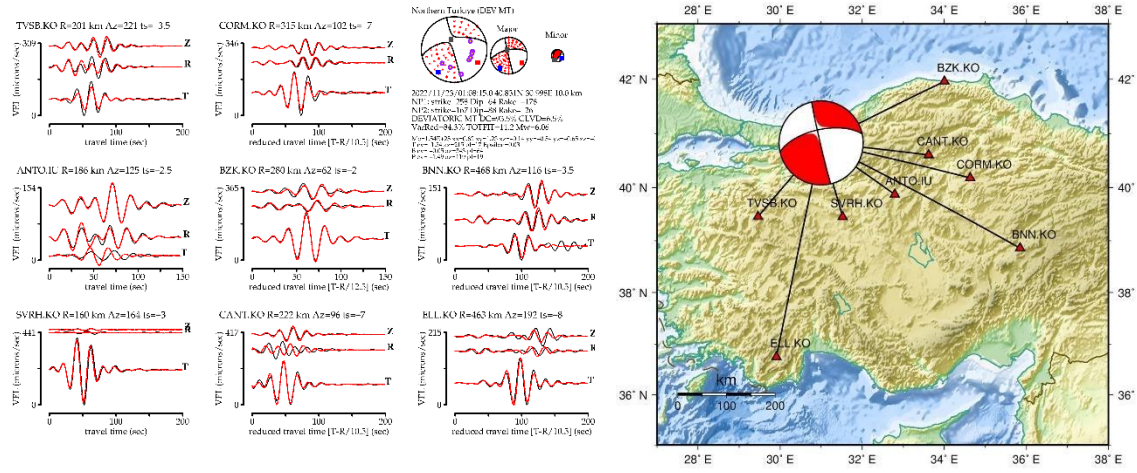


Figure C.11. Moment tensor inversion results are shown in section (a). In section (b), the stations used on the map and the focal mechanism are displayed for the event on 23 November 2022 at 01:08:14 UTC (Event ID: 223270108), located at 40.83°N, 31.00°E, with M_w 6.06.

(a) (b)

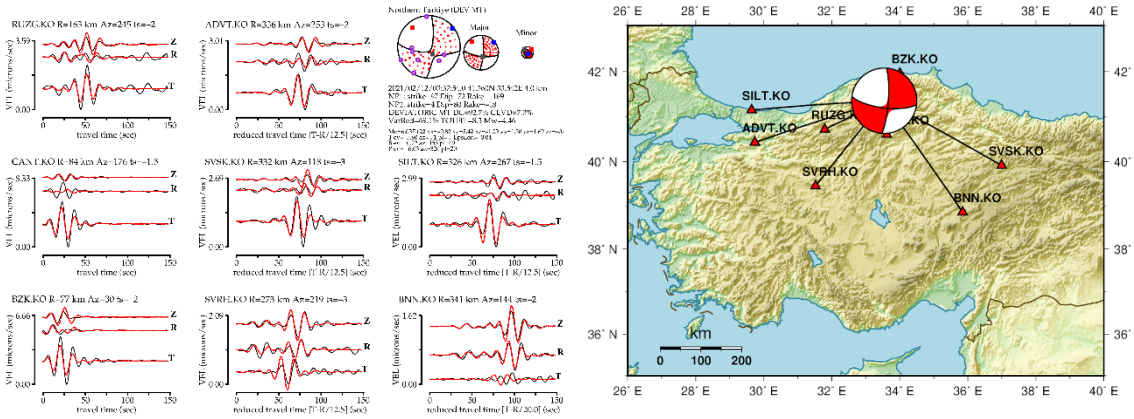


Figure C.12. Moment tensor inversion results are shown in section (a). In section (b), the stations used on the map and the focal mechanism are displayed for the event on 12 February 2021 at 03:37:54 UTC (Event ID: 210430337), located at 41.36°N, 33.54°E, with M_w 4.46.

(a) (b)

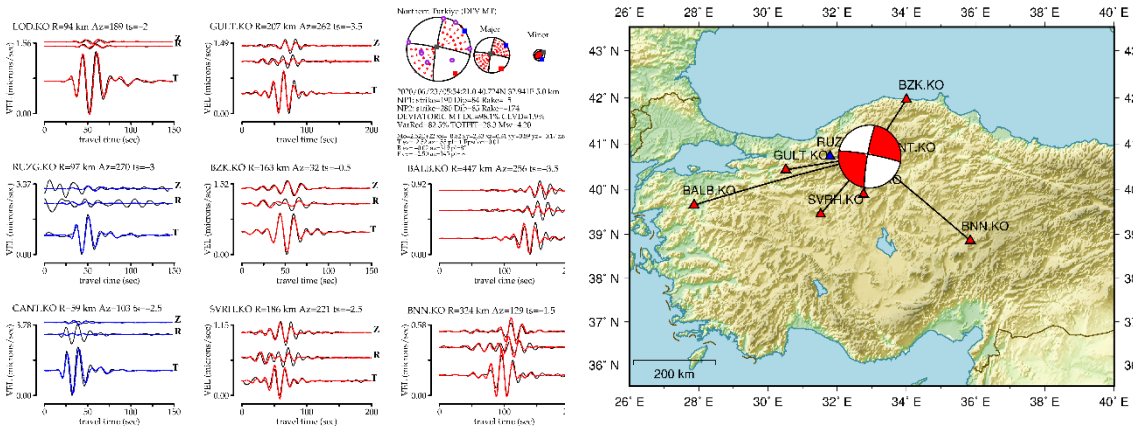


Figure C.13. Moment tensor inversion results are shown in section (a). In section (b), the stations used on the map and the focal mechanism are displayed for the event on 23 June 2020 at 05:54:19 UTC (Event ID: 201750554), located at 40.72°N, 32.94°E, with M_w 4.2.

(a) (b)

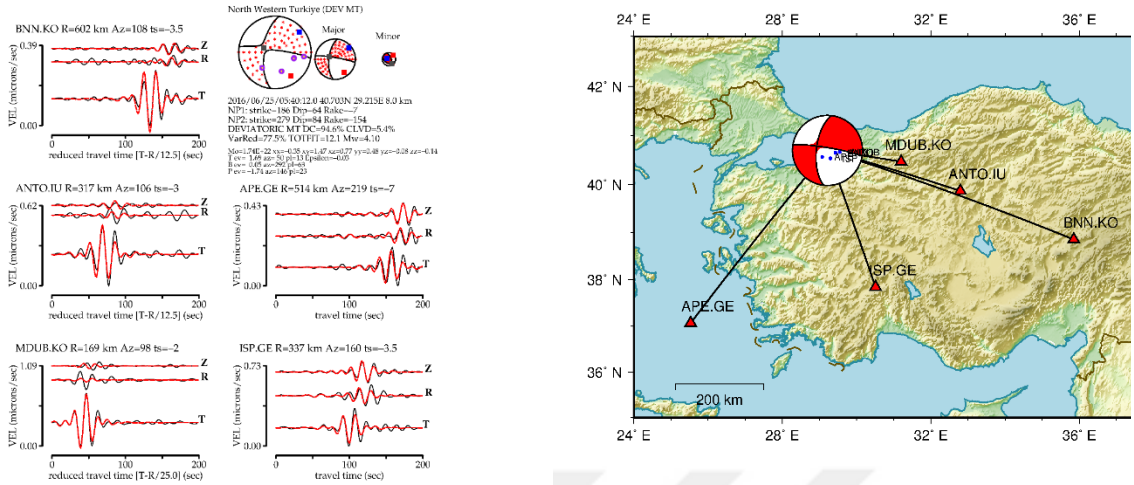


Figure C.14. Moment tensor inversion results are shown in section (a). In section (b), the stations used on the map and the focal mechanism are displayed for the event on 25 June 2016 at 05:40:11 UTC (Event ID: 161770540), located at 40.71°N, 29.21°E, with M_w 4.10.

(a) (b)

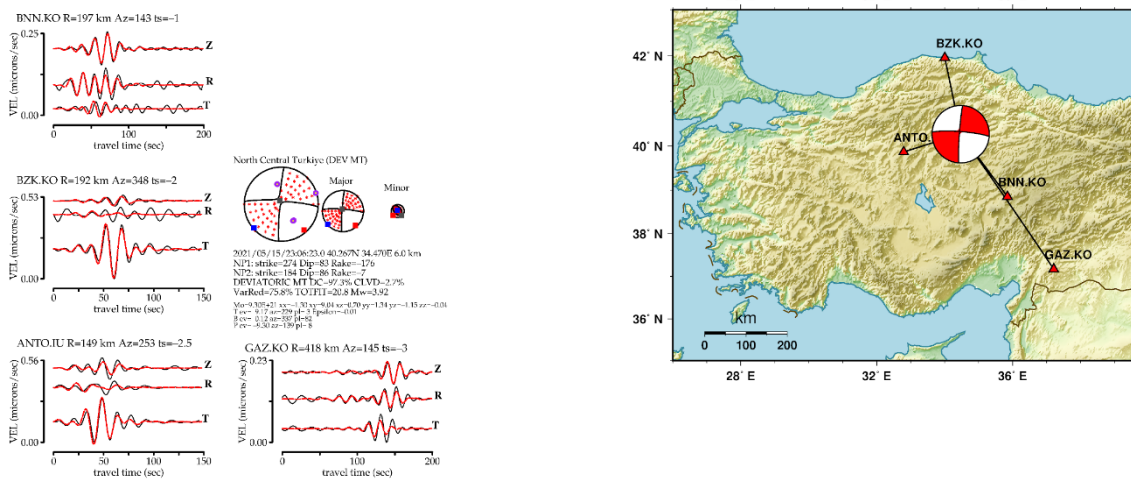


Figure C.15. (a) Moment tensor inversion results are. (b) The stations used on the map and the focal mechanism are displayed for the event on 15 May 2021 at 23:06:22 UTC (Event ID: 211352306), located at 40.26°N, 34.45°E, with M_w 4.10.

(a) (b)

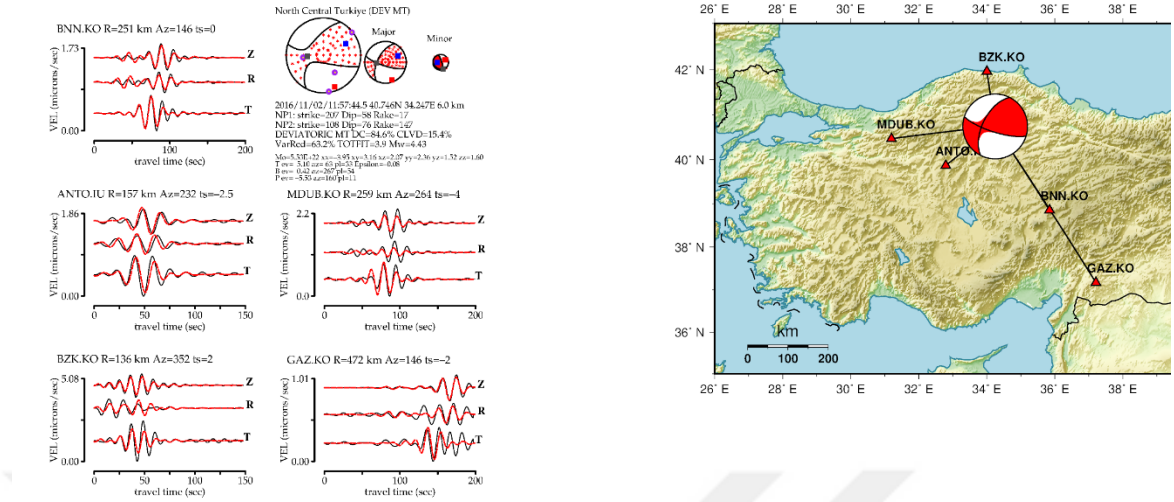


Figure C.16. (a) Moment tensor inversion results. (b), The stations used on the map and the focal mechanism are displayed for the event on 2 November 2016 at 11:57:42 UTC (Event ID: 163071157), located at 40.76°N, 34.31°E, with M_w 4.43.

(a) (b)

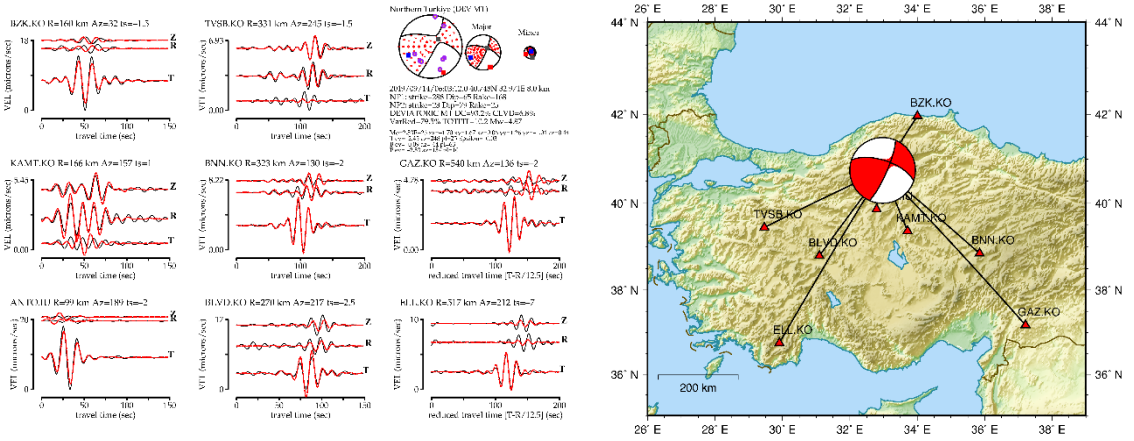


Figure C.17. Moment tensor inversion results are shown in section (a). In section (b), the stations used on the map and the focal mechanism are displayed for the event on 14 September 2019 at 06:03:11 UTC (Event ID: 192570603), located at 40.75°N, 32.97°E, with M_w 4.87.

(a) (b)

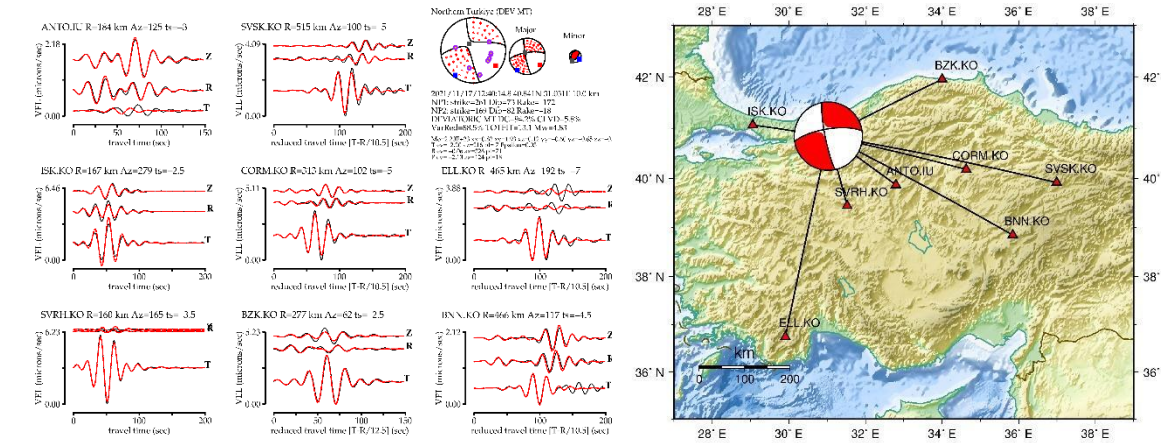


Figure C.18. Moment tensor inversion results are shown in section (a). In section (b), the stations used on the map and the focal mechanism are displayed for the event on 17 November 2021 at 12:40:15 UTC (Event ID: 213211240), located at 40.84°N, 31.03°E, with M_w 4.83.

(a) (b)

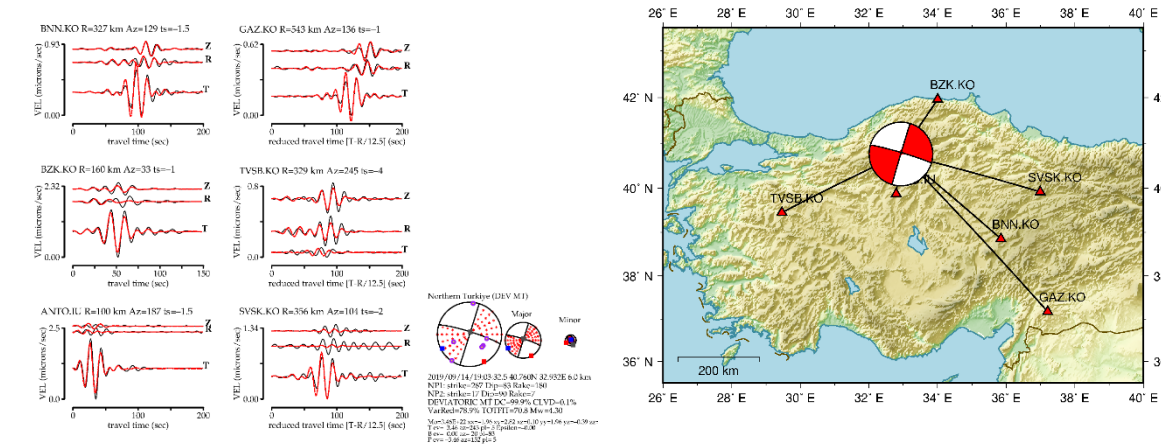


Figure C.19. Moment tensor inversion results are shown in section (a). In section (b), the stations used on the map and the focal mechanism are displayed for the event on 14 September 2019 at 19:03:31 UTC (Event ID: 192571903), located at 40.76°N, 32.93°E, with M_w 4.30.